Novel searches for top squarks at the LHC

Inauguraldissertation

der Philosophisch-naturwissenschaftlichen Fakultät

der Universität Bern

vorgelegt von

Claudia Merlassino

von Italien

Leiter der Arbeit:

Prof. Dr. Michele Weber

Albert Einstein Center for Fundamental Physics

Laboratorium für Hochenergiephysik

Physikalisches Institut

Novel searches for top squarks at the LHC

Inauguraldissertation
der Philosophisch-naturwissenschaftlichen Fakultät
der Universität Bern

vorgelegt von

Claudia Merlassino

von Italien

Leiter der Arbeit:

Prof. Dr. Michele Weber

Albert Einstein Center for Fundamental Physics
Laboratorium für Hochenergiephysik
Physikalisches Institut

Von der Philosophisch-naturwissenschaftlichen Fakultät angenommen.

Der Dekan
Prof. Dr. Zoltan Balogh

Bern, 24. October 2019

Abstract

In this thesis, I present two searches for new physics performed analysing the data collected by the ATLAS detector, during the Run 2 of the LHC. The searches are designed to target top squark pair production in Supersymmetric models which escape the traditional search approaches and are particularly sensitive to scenarios with compressed spectra or long decay chains. Both searches are characterised by the presence of multiple charged leptons (electrons or muons) and missing transverse momentum in the final state.
The results were found to be in agreement with the Standard Model predictions. The observations were interpreted to set exclusion limits significantly expanding the previous coverage on the masses of the SUSY particles under test. Models featuring direct production of either the lighter top squark ($\tilde{t}_1$) or the heavier top squark ($\tilde{t}_2$) were excluded at 95% confidence level for $\tilde{t}_1$ and $\tilde{t}_2$ masses up to about 1140 and 875 GeV, respectively, as well as neutralino ($\tilde{\chi}_1^0$) masses up to 520 GeV, depending on the model considered.
The challenges that silicon detectors will have to face in the high luminosity environment of the LHC upgrade (HL-LHC) are then presented. In this context, the effect of radiation damage on pixel sensor prototypes, designed for the ATLAS Inner Tracker upgrade (ITk), is studied, focusing on the evolution of the active region of the sensors with the increase of radiation. All the sensors measured after proton irradiation show an increase of depletion depth, reaching a maximum between 1×10^{14} and 3×10^{14} 1 MeV $\mathrm{n_{eq}/cm^2}$, when irradiated with 16.7 MeV protons, and between 1×10^{14} and 6×10^{14} 1 MeV $\mathrm{n_{eq}/cm^2}$ when irradiated with 24 GeV protons. These results present strong differences with respect to the ones obtained after neutron irradiation, demonstrating the distinct effect caused by the two particles.
In parallel, I investigated the sensitivity for future searches for electroweakino production in nearly mass degenerate scenarios, assuming an integrated luminosity of 3000 $\mathrm{fb^{-1}}$ collected during the HL-LHC data taking. This search is based on events with tracks recorded only in the innermost layers of the detector, and it is therefore key for the assessment of the physics performance of the ITk. The discovery potential of the analysis would allow for the discovery of wino-like (higgsino-like) charginos of mass 100 GeV with lifetimes between 20 ps and 700 ns (30 ps and 250 ns), or for a lifetime of 1 ns would allow the discovery of wino-like (higgsino-like) charginos of mass up to 800 GeV (600 GeV).

Contents

Introduction

The quest for new physics Beyond the Standard Model (BSM) is key for the understanding of the laws which regulates particle and their interactions on a cosmological scale. One of the proposed Standard Model extension is Supersymmetry, a theory that postulates a symmetry between bosons and fermions, so that for each known particle, a new partner is predicted with a spin difference of 1/2. In many supersymmetric models, one of these new particles is stable, neutral and weakly interacting. All of these characteristics suggest that this particle could be a good Dark Matter candidate. Moreover, the predicted particles help stabilising the Higgs boson mass from large radiative corrections. This same argument suggests that at least some of the supersymmetric particles shouldn't be too heavy. In particular the top squark (supersymmetric partner of the top quark) is foreseen to be light and could be produced in pairs in proton-proton collisions. This makes the searches for the top squark very appealing at the energies reached by the Large Hadron Collider (LHC), the largest machine ever built by humankind.
The work presented in this thesis is inserted in the framework of the analysis of the data collected from 2015 to 2018 by the ATLAS experiment. This experiment, based at CERN, records and reconstructs events arising from proton-proton collisions delivered by the LHC. The ATLAS physics program includes accurate measurements of Standard Model processes together with searches for new phenomena driven by many theories suggesting extensions of the model. Such extensions are motivated by several unexplained experimental observations, like the presence of Dark Matter or the matter-antimatter asymmetry and, at the same time, to correct some issues linked to the internal structure of the Standard Model.
My goal is to extend the previous searches for top squarks, focusing on models in which the two top squarks decay further down to a neutralino, a stable Dark Matter candidate foreseen by Supersymmetry. The production of those particles can result in final states with two or more charged leptons (electrons or muons) and significant missing transverse momentum. In this context, many searches have been performed with the data collected during the Run 1 of the LHC, looking at simpler models, and no evidence for new physics was found. For this reason, the analyses decided to develope aim to select events with two different kind complex topologies. The first one is driven by models where the mass of the neutralino is close to mass of the top squark and it is characterised by a signature with low energy leptons. The second one instead, targets models in which the SUSY particles follow long decay chains, including the emission of a Z boson. For both analyses, a new approach with respect to the searches performed during the first Run of the LHC is needed, in order to probe unexplored areas of the phase space.
The common strategy consists in isolating a kinematic selection in which the new physics signal would be enhanced and then in estimating the residual contamination due to the known Standard Model processes. A deviation from the prediction would be considered an evidence of new physics beyond the Standard Model. Particular care is given to the estimation of the background arising from events in which at least one of the lepton is not directly coming from the decay of a SM

bosons, as this is one of the major backgrounds for the signatures considered. This can arise from leptons that come from the decay of a heavy flavour quarks, electrons coming from photon conversions or in case of hadrons which are wrongly identified in the detector. This estimate is obtained with a data-driven technique, in order to avoid the use of simulation, that can't describe such processes in an accurate way, due to the involvement of low energy QCD interactions and detector effects.

In parallel with the search program, it is important to keep thinking about the future and to participate in the the effort of designing, building and commissioning upcoming detectors for future experiments. With the LHC successfully collecting data at 13 TeV, a series of upgrades is foreseen, leading to an increase of the design-luminosity in the High-Luminosity LHC (HL-LHC) project. With the upgraded accelerator, a peak instantaneous luminosity of $7.5 \times 10^{34}\mathrm{cm}^{-2}\mathrm{s}^{-1}$ will be reached, which corresponds to an average of about 200 inelastic proton-proton collisions per beam-crossing, inside ATLAS. Coping with the high instantaneous and integrated luminosity will require many changes to the detector and, in particular, a new full silicon Inner Tracker (ITk) with unprecedented radiation tolerance is being designed. In this context, this thesis investigates the effect of the radiation damage on monolithic CMOS pixel sensor, prototypes designed for the ITk. With this goal, an irradiation facility is developed at the Bern cyclotron, to emulate the effects of the HL-LHC radiation on sensors prototypes. Particular focus is then given to the study of charge collection in such sensors, performed with the Transient Current Technique.

Finally, the performances of the new ITk can be assessed, by testing the sensitivity for direct chargino production, in highly compressed mass scenarios, in proton-proton collisions at the HL-LHC conditions. In these models the chargino decays via a neutralino and a very low energy pion, which is not reconstructed. The small mass splitting between the two SUSY particles implies that the chargino has a sizeable lifetime and it can therefore decay inside the tracker. The resulting characteristic signature in the detector presents a charged track that disappears after few layers. This search is therefore the optimal benchmark to study the tracking performance of the ITk for unconventional signatures, and to motivate the search for new physics in the high luminosity environment.

This thesis is organised as follows. Chapter 1 provides an introduction to the theoretical framework in which this thesis is set, describing Supersymmetry as a possible Standard Model extension and the resulting top squark phenomenology. The status of the present limits set by previous searches is also given. Chapters 2 and 3 are dedicated to the experimental setup, with an overview of the accelerator system, of the different components of the ATLAS detector, and of the techniques employed for the reconstruction of the events produced in the proton-proton collisions, starting from the signals registered in the detector. Then, Chapters from 4 to 6 are dedicated to the analysis of the data for the top squark searches. The general strategy of the analysis is explained in Chapter 4, while the details and the results of the two searches are shown in Chapters 5 and 6. In conclusion, Chapter 7 describes the ATLAS detector upgrades foreseen for the HL-LHC program, and the effect that the resulting increased luminosity will have on the charge collection mechanism of silicon sensors, while Chapter 8 presents the prospect for the search with disappearing tracks.

Chapter 1

Supersymmetry as a Standard Model extension

The Standard Model (SM) of particle physics, developed during the 20^{th} century, is a comprehensive theory which describes the known elementary particles and their interactions. The predictions of the Standard Model have been tested by several experiments and the results have been nearly always in good agreement [1, 2], up to an energy scale of the order of 1 TeV. The discovery of a Higgs boson [3, 4], announced by the ATLAS and CMS collaborations in 2012, represents the final success of this theory, as it was the last particle needed to give self consistency to the Standard Model.

However, in spite of these great achievements, it fails to explain some open issues, like the nature and the origin of Dark Matter in our universe and the inclusion of gravity as a fundamental force; moreover some internal theoretical problems can be solved only applying a fine-tuning of the parameters, which is considered unnatural. These problems, lead to the idea that the Standard Model may only be an effective theory, which works very well at the energies tested until now, but needs to be extended to describe the particles interactions at a higher scale.

In this chapter, the main issues affecting the Standard Model are presented, together with the solutions proposed by one of the possilble extensions to the theory: Supersymmetry (SUSY).

Supersymmetric theories [5–11] were initially proposed as pure theoretical models during the second half of the 20^{th} century and only afterwards have been applied to particle physics. The basic idea is to build a model which gathers bosonic and fermionic fields under the same symmetry. One generator of this symmetry is the complex operator Q, defined by the following action on physical states:

$$\begin{cases} Q\,|\text{boson}\rangle = |\text{fermion}\rangle \\ Q\,|\text{fermion}\rangle = |\text{boson}\rangle \end{cases} \tag{1.1}$$

This operator is a spinor and each time Q is applied, the state's spin change by 1/2.

Q and its hermitian conjugate $Q^\dagger$ satisfy the following anti-commutation rules:

$$\{Q_\alpha, Q^\dagger_\beta\} = -2\sigma^\mu_{\alpha\beta} P_\mu \tag{1.2}$$

$$\{Q_\alpha, Q_\beta\} = \{Q^\dagger_\alpha, Q^\dagger_\beta\} = 0 \tag{1.3}$$

where σ^μ are the Pauli matrices and P_μ is a conserved quantity, corresponding to the generator of the space-time transformations, for the Coleman-Mandula theorem. It is also important to notice that the commutator of both generators with P^μ is zero:

$$[Q_\alpha, P^\mu] = [Q^\dagger_\alpha, P^\mu] = 0 \tag{1.4}$$

from which we derive that Supersymmetry is a global transformation.
The particles predicted by a supersymmetric theory, live in the irreducible representations of the algebra generated by Q and $Q^\dagger$, called supermultiplets. From the commutator in Equation 1.4 it's easy to derive that also P^2 commutes with the algebra's generators, therefore all the particles belonging to the same supermultiplet must have the same eigenvalue of P^2, hence the same mass. Q and $Q^\dagger$ also commute with the generators of the gauge symmetries of the Standard Model, so particles living in the same supermultiplet have the same colour, electric charge and weak isospin too.
Each supermultiplet must have the same number of bosonic and fermionic degrees of freedom. This, together with the previous considerations, means that it is not possible to complete the model using only the Standard Model's existing particles and it is necessary to include new fields in this framework: the supersymmetric partners.

1.1 Limitation of the Standard Model

This section contains an overview of the open questions in the Standard Model, focusing on the issues that can be intrinsically solved by Supersymmetry. A brief idea of how these problems can be solved is also given, while a detailed description of the Supersymmetry is discussed in the next sections.

The Higgs boson mass and naturalness

The first problem arises by comparing the mass of the Higgs boson, which is measured to be (125.10 ± 0.14) GeV [12] and compatible with the electroweak symmetry breaking scale. This consists in the bare term, a free parameter of the SM Lagrangian, and all the virtual corrections due to the contribution from each particle coupling to the Higgs propagator. In order to deal with the ultraviolet divergences arising from such contributions, a renormalisation procedure is needed, with the introduction of a cut-off value Λ which represents the energy threshold up to which the theory holds. For example, considering the correction coming from the loop containing a Dirac fermion f in Figure 1.1, which couples to the Higgs field with a Lagrangian term $-\lambda_f H\bar{f}f$, the resulting physical Higgs mass is the following:

$$m_H^2 \approx m_{H0}^2 - \frac{|\lambda_f|^2}{8\pi^2}\Lambda^2 + \dots \tag{1.5}$$

where m_{H0} is the bare Higgs mass and the omitted terms grow at most logarithmically with Λ. The presence of a cut-off scale is not a problem by itself, at the energy levels investigated until now; but if we assume the Standard Model to be valid up to the Planck scale, the correction term will be of the order of $(10^{19}\text{GeV})^2$, which forces the bare term to be equally as big, to result in the experimentally measured value. This is against the principle of naturalness [13, 14], which requires that all the relevant parameters of the theory have to be of the same order of magnitude.

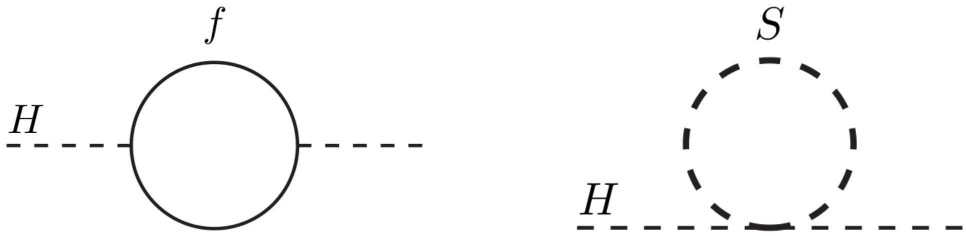

FIGURE 1.1: First order corrections to the Higgs propagator, due to a fermionic (left) or a scalar (right) field

If this is not satisfied, a tiny variation of some parameters may lead to dramatically important changes to the quantities which are several orders of magnitude smaller. This implies that a high level of fine-tuning is needed in order to obtain the physics that we observe. A commonly adopted criterion [15] to measure the fine tuning of a theory is to consider the evolution of the higgs boson mass, or equivantly m_Z or G_F, as a function of the parameters a_i of the underlying theory. The amount of fine tuning is then given by:

$$\Delta = \max \left| \frac{a_i \partial M_h^2(a_i)}{M_h^2 \partial a_i} \right| \tag{1.6}$$

Which means that a theory with $\Delta = 10$ suffers from a parameter tuning of no more than 10%, while one with $\Delta = 100$ of 1%.
One solution to avoid fine-tuning would be the cancellation of the correction terms deriving from fermions by the introduction additional opposite corrections arising from new particles. In particular, this is possible due to the fact that a generic scalar particle S in Figure 1.1, coupling to the Higgs field with a Lagrangian term $-\lambda_S |H|^2 |S|^2$, leads to an additional term equal to:

$$\Delta m_H^2 \approx + \frac{\lambda_s}{16\pi^2} \Lambda^2 + \dots \tag{1.7}$$

In Supersymmetry, which contains two scalar states for each fermion, whose coupling constants with the Higgs field follow $\lambda_S = |\lambda_f|^2$, the problem of the naturalness and the Higgs boson mass is automatically solved, as the corrections to the mass given by bosons and fermions, reported in Equations 1.5 and 1.7 cancel each other exactly.

Dark Matter and R-parity

Many astrophysical measurements, like the rotation velocities of galaxies [16], show anomalies in the gravity field, indicating the presence of a particular kind of massive, weakly interacting matter. It must be non-luminous and non-absorbing, therefore it is called Dark Matter. The presence of Dark Matter is also motivated by cosmological observations, which predict that it makes up about 25% of our universe [17].
Possible candidates for Dark Matter are the so called WIMPs (Weakly Interacting Massive Particles): these particles need to be neutral, stable and with a low cross section. In a subset of supersymmetric models the lightest supersymmetric particle (LSP) has exactly these characteristics and can be considered a Dark Matter candidate.
In the Standard Model, the conservation of the leptonic and the barionic quantum numbers is accidental and is not imposed by any symmetry, it merely comes from the absence of renormalisable interaction terms which allows these kind of processes. The same consideration cannot be applied

to Supersymmetry. All the possible interactions between particles in a supersymmetric theory are described by the Superpotential: this part of the SUSY Lagrangian can in principle contain terms which lead to the non conservation of the leptonic and barionic quantum numbers. This would allow the possibility of processes so far unobserved in nature, such as the proton decay.
The problem can be solved by imposing a new discrete symmetry, which restores the conservation of both leptonic and barionic quantum number; R-parity[18] (also called matter-parity) is defined as follow:

$$R = (-1)^{3(B-L)+2S} \tag{1.8}$$

where L and B are the leptonic and the barionic number respectively, and S is the spin of the particle. It is important to notice that $R = 1$ for every Standard Model particle, while $R = -1$ for the super-partners. The result obtained by imposing this symmetry is that every possible interaction vertex in the theory must contain an even number of supersymmetric particles. This has three important consequences:

- The lightest supersymmetric particle must be stable. In the models in which the LSP is neutral, it interacts weakly with ordinary matter, becoming a good candidate for Dark Matter[19, 20] .
- All the other supersymmetric particles must have an odd number of LSP at the end of their decay chain.
- At colliders, supersymmetric particles are always produced in an even number.

Grand Unification Theories and other unsolved issues

The unification of the electromagnetic and the weak interactions, proposed by Glashow, Weinberg and Salam [21, 22], consists in the major step toward the creation of the Standard Model. Since then, a huge effort begun in order to unify also the strong force under a unique gauge symmetry. All the models built with this goal are therefore called Grand Unification Theories (GUT).
One problem that prevents the unification is given by the running of the coupling constants of the three fundamental forces. In the context of the Standard Model, the three values don't converge, while the presence of supersymmetric particles with mass around 1 TeVwould lead to a possible unification at an energy scale of 10^{16}GeV [23–26] . The evolution of the coupling constants in the Standard Model and in supersymmetric models is shown in Figure 1.2. There are other problems affecting the Standard Model which can't be directly solved by Supersymmetry, but still motivate the search for new physics.
First of all, gravity has to be added to the picture, as the fourth fundamental force. At the Planck scale its strength becomes of the same order of the other forces, and therefore any theory describing the fundamental particles and their interactions cannot ignore gravity anymore. It is impossible to include gravity into the Standard Model by using the usual quantum field theory framework, as such theory would be non-renormalisable. To avoid this, many alternative models have been proposed, like String Theory [27] and Loop Quantum Gravity [28], but their predictions are still out of reach for current experiments.
Then, there are two physical observations which seem to be un-explained by the Standard Model predictions: the matter-antimatter asymmetry and the neutrino mass.
The first problem arises from the fact that in our universe the presence of matter is dominant

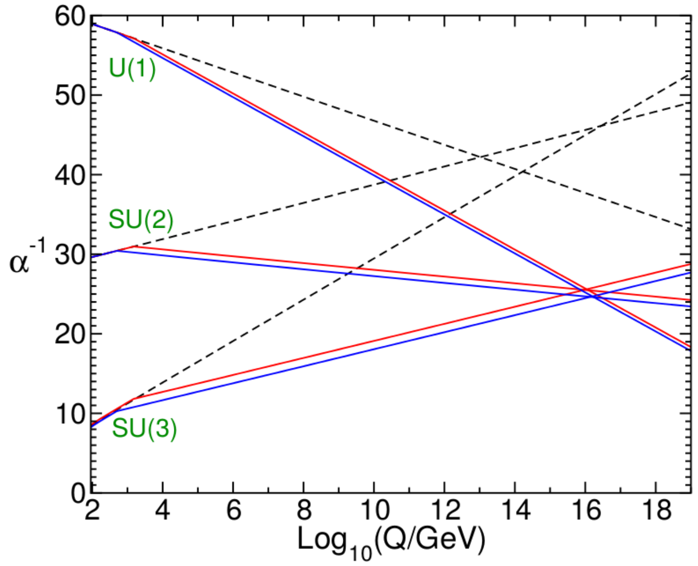

FIGURE 1.2: Running of the coupling constants in the Standard Model (dashed lines) and in supersymmetric models (solid lines) [11]. In the SUSY case, the sparticle masses are varied between 500 GeV and 1.5 TeV.

with respect to antimatter. In particular the following ratio is observed:

$$\eta = \frac{n_q - n_{\bar{q}}}{n_\gamma} \approx 10^{-10} \tag{1.9}$$

This quantity relates the overall number density difference between quarks and anti-quarks (n_q and $n_{\bar{q}}$, respectively) and the number density of cosmic background radiation photons n_γ.
If we assume a balance between matter and anti-matter immediately after the Big Bang, a process where CP is violated is needed in order to produce this kind of asymmetry. Such processes are actually allowed within the Standard Model context, thanks to the complex phase of the CKM matrix, but they are highly suppressed and can't explain the value of the ratio. Therefore, a new mechanism is needed.
The second problem regards neutrinos and their masses. In the original Standard Model formulation they are required to be massless; however, oscillations between different flavours of neutrinos have been observed by several experiments and the difference between the masses of the three neutrinos eigenstates have been measured. Several attempts to include in the Standard Model a mechanism able to give mass to neutrinos have been made since, but all the models proposed are either non renormalisable, require the introduction of new fields or the violation of the leptonic quantum number. In all these cases, this suggests that an extension of the Standard Model is necessary.

1.2 The Minimal Supersymmetric Standard Model (MSSM)

In this section, the simplest supersymmetric extension of the Standard Model, called Minimal Supersymmetric Standard Model (MSSM) [29, 30], is presented, focusing on the different particles included, their interactions and the mass spectrum.

	spin 0	spin 1/2	$SU(3)_c$, $SU(2)_L$, $U(1)_Y$
quarks & squarks ×3	$(\tilde{u}_L\ \tilde{d}_L)$	$(u_L\ d_L)$	$(\mathbf{3}, \mathbf{2}, \frac{1}{6})$
	$\tilde{u}_R$	u_R	$(\bar{\mathbf{3}}, \mathbf{1}, -\frac{2}{3})$
	$\tilde{d}_R$	d_R	$(\bar{\mathbf{3}}, \mathbf{1}, \frac{1}{3})$
leptons & sleptons ×3	$(\tilde{\nu}\ \tilde{e}_L)$	$(\nu\ e_L)$	$(\mathbf{1}, \mathbf{2}, -\frac{1}{2})$
	$\tilde{e}_R$	e_R	$(\mathbf{1}, \mathbf{1}, 1)$
Higgs & Higgsinos	$(H_u^+\ H_u^0)$	$(\tilde{H}_u^+\ \tilde{H}_u^0)$	$(\mathbf{1}, \mathbf{2}, +\frac{1}{2})$
	$(H_d^0\ H_d^-)$	$(\tilde{H}_d^0\ \tilde{H}_d^-)$	$(\mathbf{1}, \mathbf{2}, -\frac{1}{2})$

Table 1.1: Chiral supermultiplets in the MSSM.

First of all, in order to built a valid extension of the Standard Model it is necessary to fit all the known particles inside the multiplets foreseen by the theory.
The easiest way to make a supermultiplet is to gather a spin 1/2 fermion with two real scalar fields, which in turn can be arranged in a single complex scalar; this combination is called chiral (or matter) supermultiplet. In this way, the right and the left components of the fermion are still able to behave independently under the gauge transformations, therefore all the known leptons and quarks can be arranged this structure. Their scalar superpartners are called sleptons and squarks respectively and are denoted with the same symbols used for their ordinary partners, with a tilde on top.
In the MSSM, two complex Higgs doublets with weak isospin +1/2 and −1/2 are needed in order to give mass to all the particles [30]:

$$(H_u^+\ H_u^0) \quad (H_d^0\ H_d^-)$$

All together, this makes eight degree of freedom: three hidden Goldstone bosons, needed to give mass to the electroweak vector bosons, and five observable fields: two neutral scalars h and H, one pseudo-scalar A, and two charged scalar $H^\pm$. Two different chiral supermultiplets are created to cover for this Higgs sector. To fill the supermultiplets we need to add two additional spin 1/2 fermions; the name of this kind of superpartners is derived attaching the suffix "ino" to the ordinary names, in this case Higgsinos.
An inclusive list of all the ordinary and supersymmetric particles living in chiral multiplets is presented in Table 1.1.

	spin 1	spin 1/2	$SU(3)_c$, $SU(2)_L$, $U(1)_Y$
gluon & gluinos	g	$\tilde{g}$	$(\mathbf{8}, \mathbf{1}, 0)$
W bosons & winos	$W^\pm\ W^0$	$\tilde{W}^\pm\ \tilde{W}^0$	$(\mathbf{1}, \mathbf{3}, 0)$
B boson & bino	B^0	$\tilde{B}^0$	$(\mathbf{1}, \mathbf{1}, 0)$

Table 1.2: Gauge supermultiplets in the MSSM.

To complete the Standard Model particle zoo we miss the spin 1 vector bosons: they find their place in gauge supermultiplets (or vector supermultiplets). It is important to remember that these bosons are all massless before the symmetry breaking, therefore they carry only two degrees of freedom. The superpartners, called gauginos, are massless spin 1/2 fermions, again with two helicity states, so the number of fermions and bosons is matched. Table 1.2 shows the structure of the gauge supermultiplets for gluons and for the four electroweak vector bosons.
The interactions between those particles come from the terms in the superpotential and can be

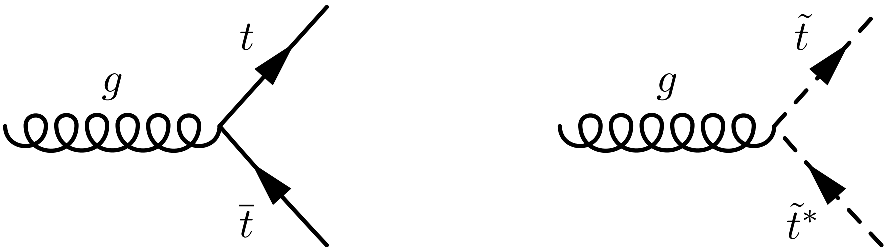

FIGURE 1.3: Example of the gluon, top, antitop vertex (left) and how it may be modified in order to obtain a stop-antistop couple (right)

easily derived from the Standard Models ones: for any interaction vertex, two lines at a time can be substituted with the respective supersymmetric partners. An example can be found in Figure 1.3

The phenomenological MSSM

The model described until now holds if particles and their super-partners are degenerate in mass. However, no particles belonging to the SUSY spectrum have been observed yet. Therefore, if Supersymmetry is realised in nature, it must be broken in a way that the new particles predicted are allowed to have a higher mass.
Ideally, Supersymmetry breaks spontaneously, with some mechanism which is still unknown. We can avoid specifying the breaking mechanism if we break the symmetry "by hand", by introducing an additional soft term to the Lagrangian:

$$\mathcal{L} = \mathcal{L}_{\text{SUSY}} + \mathcal{L}_{\text{soft}} \tag{1.10}$$

$\mathcal{L}_{\text{soft}}$ must preserve renormalisability and the Standard Model gauge invariance but breaks the supersymmetric invariance. It contains all the mass terms and any possible coupling parameter with positive energy dimension.
As a consequence of this procedure, the MSSM is characterized by more than 100 independent physical parameters: masses, phases and mixing angles.
In order to build a model that can produce a well defined phenomenology, some assumptions have to be made, while some constraints on the parameters can be applied using experimental and theoretical evidences. For example, CP violating terms and the terms which mix generations are heavily constrained by flavour physics measurements. The parameters are furthermore reduced after imposing the R-parity conservation, as illustrated before. In this way, the numbers of parameters is reduced down to 19 terms in the phenomenological MSSM model (pMSSM) [31], listed in Table 1.3.

1.3 The mass spectrum

All the supersymmetric particles listed before are not necessarily mass eigenstates and the ones with the same quantum numbers can in general mix, resulting in different observable states, listed in Table 1.4.

Parameters	Description
M_1, M_2, M_3	gaugino masses
$\tan\beta$	ratio of the VEVs of the two Higgs doublets
M_A	pseudoscalar Higgs boson mass
μ	higgsino mass
A_t, A_b, A_τ	trlinear couplings for third generation sfermions
$m_{\tilde{q}L}$, $m_{\tilde{u}R}$, $m_{\tilde{d}R}$, $m_{\tilde{\ell}L}$, $m_{\tilde{e}-\tilde{\mu}R}$	first and second generation sfermion masses
$m_{\tilde{q}3L}$, $m_{\tilde{t}R}$, $m_{\tilde{b}R}$, $m_{\tilde{\ell}3L}$, $m_{\tilde{\tau}R}$	third generation sfermion masses

Table 1.3: Free parameters of the pMSSM.

Names	Spin	Gauge Eigenstates	Mass Eigenstates
Higgs boson	0	$H_u^0\ H_d^0\ H_u^+\ H_d^-$	$h^0\ H^0\ A^0\ H^\pm$
squarks	0	$\tilde{u}_L\ \tilde{u}_R\ \tilde{d}_L\ \tilde{d}_R$ $\tilde{s}_L\ \tilde{s}_R\ \tilde{c}_L\ \tilde{c}_R$ $\tilde{t}_L\ \tilde{t}_R\ \tilde{b}_L\ \tilde{b}_R$	(same) (same) $\tilde{t}_1\ \tilde{t}_2\ \tilde{b}_1\ \tilde{b}_2$
sleptons	0	$\tilde{e}_L\ \tilde{e}_R\ \tilde{\nu}_e$ $\tilde{\mu}_L\ \tilde{\mu}_R\ \tilde{\nu}_\mu$ $\tilde{\tau}_L\ \tilde{\tau}_R\ \tilde{\nu}_\tau$	(same) (same) $\tilde{\tau}_1\ \tilde{\tau}_2\ \tilde{\nu}_\tau$
neutralinos	1/2	$\tilde{B}^0\ \tilde{W}^0\ \tilde{H}_u^0\ \tilde{H}_d^0$	$\tilde{\chi}_1^0\ \tilde{\chi}_2^0\ \tilde{\chi}_3^0\ \tilde{\chi}_4^0$
charginos	1/2	$\tilde{W}^\pm\ \tilde{H}_u^+\ \tilde{H}_d^-$	$\tilde{\chi}_1^\pm\ \tilde{\chi}_2^\pm$
gluino	1/2	$\tilde{g}$	(same)

Table 1.4: Interaction and mass eigenstates in the MSSM.

The Higgs sector

As anticipated before, the MSSM contains eight Higgs scalar fields, but only five of those are observable. They mix up in order to create the following bosons:

- a couple of charged Higgs boson H^+ and H^-
- a CP-odd neutral Higgs bosons A_0
- two CP-even neutral Higgs bosons H_0 and h_0

Between them, H^+, H^-, A_0 and H_0 may have masses far from the TeV scale, which makes them impossible to discover by present experiments. However Supersymmetry requires the lightest neutral Higgs boson h_0 mass to be below $\approx 135\,\text{GeV}$, compatible with the measurement of the Higgs mass made by ATLAS and CMS.

Charginos and neutralinos

The charged gauginos and Higgsinos mix with the following two blocks matrix in the $(\tilde{W}^\pm, \tilde{H}^\pm)$ basis:

$$\begin{pmatrix} M_2 & \sqrt{2}M_W\sin\beta & 0 & 0 \\ \sqrt{2}M_W\cos\beta & \mu & 0 & 0 \\ 0 & 0 & M_2 & \sqrt{2}M_W\sin\beta \\ 0 & 0 & \sqrt{2}M_W\cos\beta & \mu \end{pmatrix} \tag{1.11}$$

where M_W is the W boson mass and $\tan\beta$ is the ratio of the two vacuum expectation values of the Higgs doublets. The results of the mixing are four spin 1/2 particles called charginos and denoted with $\tilde{\chi}_i^{\pm}$.
For the neutral sparticles, the mixing is caused by the matrix:

$$\begin{pmatrix} M_1 & 0 & -M_Z\cos\beta\sin\theta_W & M_Z\sin\beta\sin\theta_W \\ 0 & M_2 & M_Z\cos\beta\cos\theta_W & M_Z\sin\beta\cos\theta_W \\ -M_Z\cos\beta\sin\theta_W & M_Z\cos\beta\cos\theta_W & 0 & -\mu \\ M_Z\sin\beta\sin\theta_W & -M_Z\sin\beta\cos\theta_W & -\mu & 0 \end{pmatrix} \tag{1.12}$$

in the $(\tilde{B}, \tilde{W}^0, \tilde{H}_u^0, \tilde{H}_d^0)$ basis. Here M_Z is the Z boson mass, θ_W is the Weinberg mixing angle and β is defined in the same way as before. We obtain four neutral particles called neutralinos $(\tilde{\chi}_i^0)$. The lightest neutralino $\tilde{\chi}_1^0$ is assumed to be the LSP in many supersymmetric models, as being neutral makes it an optimal Dark Matter candidate.
In both matrices, M_1, M_2 and μ are mass parameters, often called bino, wino and higgsino mass respectively and their values set the charginos and neutralinos mass spectrum.

Gluinos

Gluinos are different coloured particles and therefore cannot mix with each other. Their mass parameter M_3 can be related to the M_1 and M_2 parameters by the assumption that at the scale where unification exists, also the masses become degenerate. This leads to the following relation:

$$\frac{M_1}{\alpha_1} = \frac{M_2}{\alpha_2} = \frac{M_3}{\alpha_3} \tag{1.13}$$

The consequence is that at the TeV scale, gluinos must be havier than charginos and neutralinos; the mass parameters are expected to approximately follow these rates:

$$M_3 : M_2 : M_1 \approx 6 : 2 : 1$$

Squarks and sleptons

In principle, all the scalar superpartners with the same quantum numbers can mix, both the “left” and “right” components, leading to three 6×6 matrices for up-type and down-type squarks, and for sleptons, plus a 3×3 matrix for sneutrinos. However, the off-diagonal terms of the matrices are expected to be proportional to the sfermion mass, with the result that this left-right mixing is relevant only for sleptons and squarks of the third generation.

The SUSY spectrum and naturalness constraints

Requiring the theory to be natural, implicitly puts some constraints on the mass of the predicted SUSY particles. Needless to say, the power of such constraints is directly related to the level of fine tuning which is considered acceptable for the theory.
As shown in Equation 1.6, the amount of fine tuning can be measured as the effect that the parameters of the theory have on the value of m_h. In Supersymmetry, m_h includes the μ term at tree level. From a phenomenological point of view, this is reflected in the fact that higgsinos

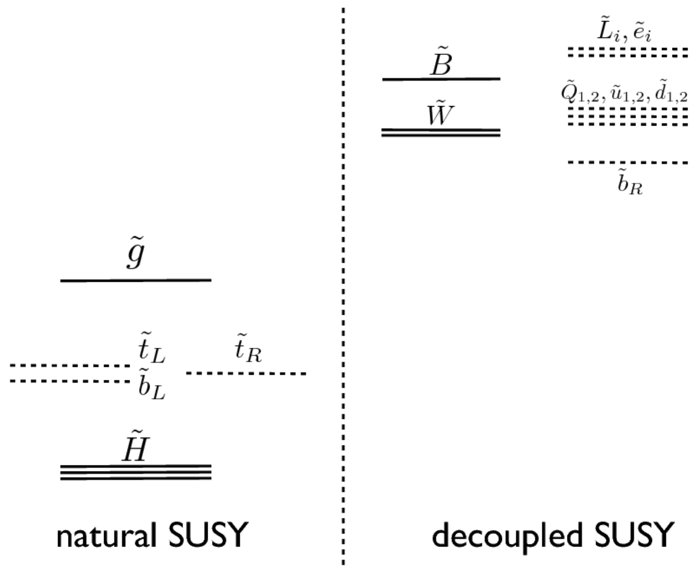

FIGURE 1.4: Hypothetical mass spectrum for the MSSM [32]. Particles on the left are constrained by the naturalness principle, while particles on the right are decoupled from the Higgs field and aren't subjected to any limit.

must be light, because their mass is directly controlled by μ. Unfortunately, the low cross-section of direct higgsinos production makes such particles very hard to find at hadrons colliders, even if realised in very light states.

Going at loop level, additional corrections arise, which correspond to more constraints to the SUSY spectrum. The Higgs potential is corrected by gauge and Yukawa interactions, with the largest contribution arising from the loop containing top and stops. Given the higher production cross-section of top squark in proton-proton collisions, this requirement makes the searches for such particles very appealing at the LHC.

Finally, further constraints arise from the gluinos, which lead to large corrections to the top squark mass and therefore enters into the Higgs term at two loops. All the other radiative contributions to the Higgs term from the other SM particles put much weaker bounds to the supersymmetric spectrum.

Figure 1.4 shows a hypothetical SUSY spectrum, built following the naturalness arguments just presented.

1.4 Top squark phenomenology

It is seen that asking for a natural SUSY spectrum requires a limit over the TeV scale for the mass eigenstates of the top squark, making those searches very appealing at the LHC. This section reviews the possible production and decay mechanisms for the two top squark mass eigenstates ($\tilde{t}_1$ and $\tilde{t}_2$) and presents the current limits on the top squark mass found by previous searches carried out by ATLAS and CMS during the first run of the LHC.

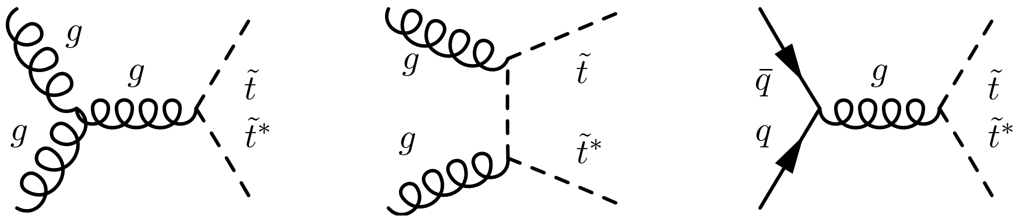

FIGURE 1.5: Leading order diagrams for stop-antistop pair production in proton-proton collisions.

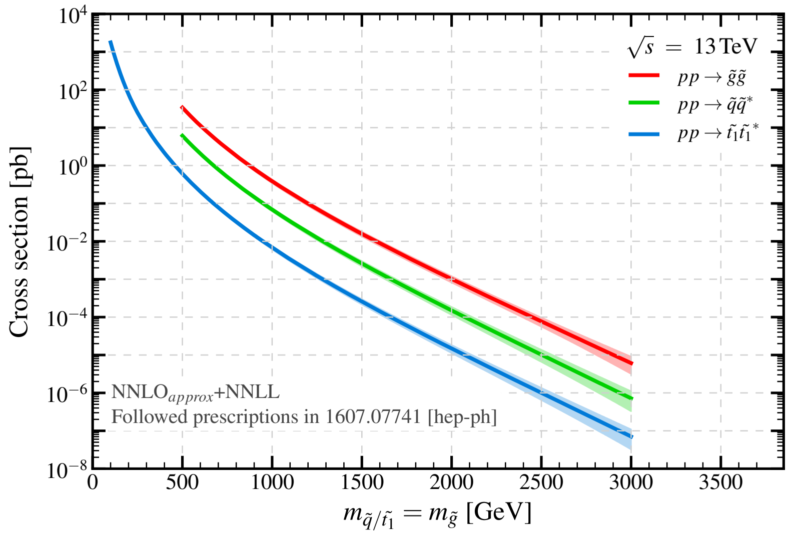

FIGURE 1.6: NNLO+NNLL prediction of the pair production cross section for stops, squarks and gluinos, at $\sqrt{s} = 13$ TeV.

Production

At the LHC, in proton proton collisions, the top squark may be mainly produced by two mechanisms:

- through the decay of gluinos, if those particles are heavy enough to decay into $t + \tilde{t}_1$ and light enough to be produced with significant rate
- direct production of a stop-antistop pair

If gluinos are very heavy, the production cross section of the first mechanism is too small and only direct production is left. The direct production's diagrams can be simply derived by the $t\bar{t}$ ones, replacing the two top quarks with the respective supersymmetric partners: the three main channels are shown in Figure 1.5.

The cross section of this process is calculated at the next-to-next-to-leading order, including soft-gluon resummation up to next-to-next-to-leading logarithmic accuracy and the resummation of Coulomb corrections ($\text{NNLO}_{\text{approx}} + \text{NNLL}$) [33]. The theoretical uncertainties are derived by the convolution with different parton density function (PDF) sets. Figure 1.6 shows the production cross section of top squark pairs at a centre of mass energy of $\sqrt{s} = 13$ TeV, as a function of the top squark mass.

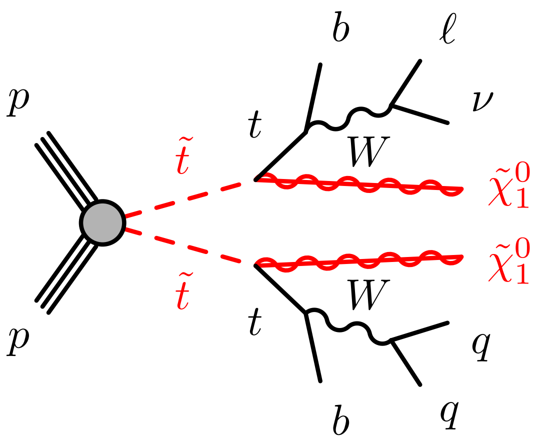

FIGURE 1.7: Diagram representing one of the possible decay modes of a pair of top squarks in the semi-leptonic channel.

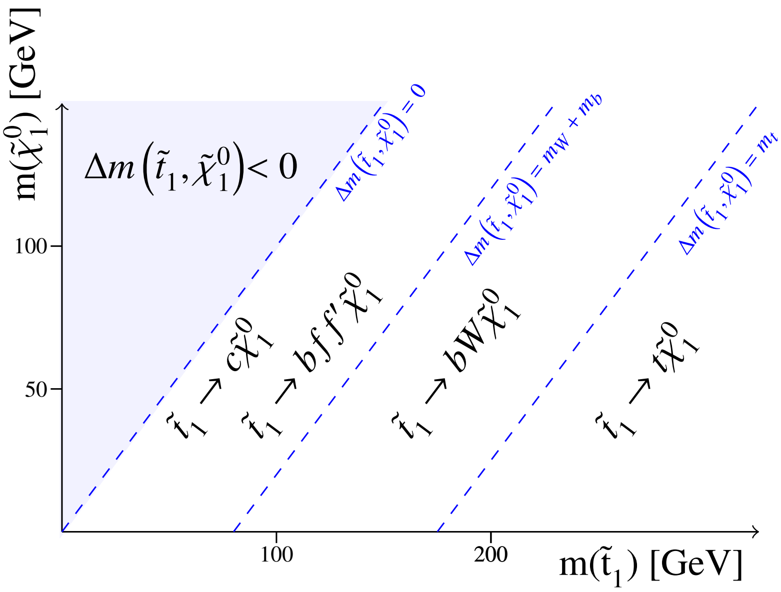

FIGURE 1.8: The figure shows the plane spanned by the $\tilde{t}_1$ and the $\tilde{\chi}_1^0$ mass, together with the $\tilde{t}_1 \to \tilde{\chi}_1^0$ decay channels dominant in each region [34].

Decay modes

All the possible decay modes of the top squark depend on the mass spectrum of the supersymmetric particles involved. For the sake of simplicity, in all the models considered here R-parity is exact and the lightest neutralino is the LSP; furthermore, all the unstable particles are expected to decay instantaneously.

First of all, let's consider the decay modes in which the $\tilde{t}_1$ directly decays to the $\tilde{\chi}_1^0$ and no other SUSY particle is involved. This is the principal decay mode if the masses of the other SUSY particles are much heavier than the $\tilde{t}_1$ mass and are therefore decoupled. If $m_{\tilde{t}_1} > m_t + m_{\tilde{\chi}_1^0}$, the light top squark can decay through:

$$\tilde{t}_1 \to t\,\tilde{\chi}_1^0 \tag{1.14}$$

In this case, the neutralino is stable, while the top quark decays further, either hadronically or leptonically. This leads to a final state with light jets, b-jets, leptons (depending on the top decay channel) and missing transverse momentum; the diagram in Figure 1.7 shows the stop-antistop decay chain in the eventuality of a semi-leptonic decay.
In case of smaller mass difference between the $\tilde{t}_1$ and the $\tilde{\chi}_1^0$, the decay can still happen, but through off-shell particles, resulting in the following three or four-body decays:

$$\tilde{t}_1 \to b\, W\, \tilde{\chi}_1^0 \tag{1.15}$$

$$\tilde{t}_1 \to b\, f f'\, \tilde{\chi}_1^0 \tag{1.16}$$

where f and f' are Standard Model fermions. Figure 1.8 shows the $\tilde{t}_1 - \tilde{\chi}_1^0$ mass plane and the region in which each decay is dominant. In the area where the $\tilde{\chi}_1^0$ mass is close to the $\tilde{t}_1$, it is present also the following two-body decay:

$$\tilde{t}_1 \to c\, \tilde{\chi}_1^0 \tag{1.17}$$

which is very rare because is one-loop mediated and is therefore competing only with the four-body decay in (1.16).
If charginos or heavier neutralinos are lighter then the $\tilde{t}_1$, intermediate decays can happen, such as:

$$\tilde{t}_1 \to b\, \tilde{\chi}_1^{\pm} \tag{1.18}$$

$$\tilde{t}_1 \to t\, \tilde{\chi}_2^0 \tag{1.19}$$

The heavier electroweakinos then decay further, emitting SM bosons (Z, h and W) down to the stable $\tilde{\chi}_1^0$. This can result in very long decay chains and consequently busy final states, with many jets and leptons, depending on the decay modes of the SM bosons. An example of two possible decay chains, including charginos and neutralinos, is presented in Figure 1.9.
The branching fraction of all decay channels depends not only on the mass spectrum of the SUSY particles but also on other free parameters of the Lagrangian, such as the mixing of the electroweakinos. This leads to many possible models, each one with more favourable decay modes. Figure 1.10 shows two examples of how the top squark phenomenology could show up in nature. The scenario on the left is motivated by gauge unification at the GUT scale, where the the bino is the LSP and the wino is the NLSP, and its two eigenstates ($\tilde{\chi}_1^{\pm}$ and $\tilde{\chi}_2^0$) are approximately twice as heavy as the $\tilde{\chi}_1^0$. The model on the right, instead, assumes that the lightest neutralinos and charginos are a mix of bino and higgsino. This scenario is motivated by naturalness arguments and provides a Dark Matter candidate with the right relic density [35, 36].

Furthermore, if the heavy top squark ($\tilde{t}_2$) is light enough to be produced at the LHC, a new set of possibilities is open, as it can decay in the same way as the $\tilde{t}_1$, but can also create longer chains, where the first step consists of:

$$\tilde{t}_2 \to \tilde{t}_1 + h/Z \tag{1.20}$$

Here, the probability of decaying in either h or Z is mostly influenced by the mixing between the the stop right and the stop left. Figure 1.11 shows instead one particular model where the heavy top squark has a mass of around 1 TeV and it can decay either in the lighter top squark or in the lighter electroweakinos.

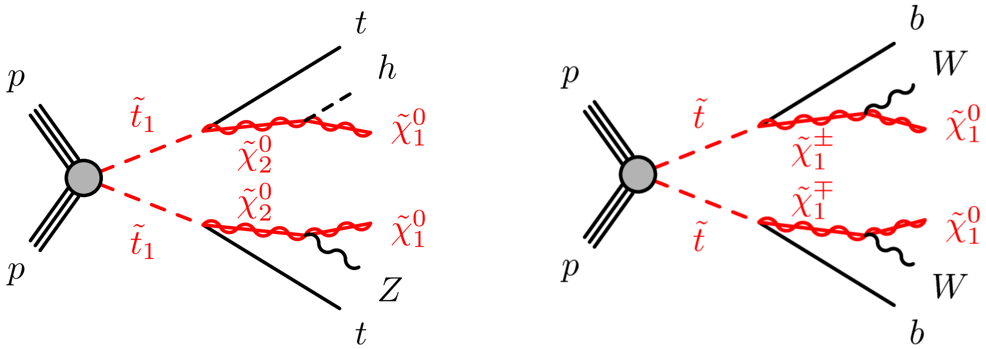

Figure 1.9: Diagrams representing two possible decay modes for the $\tilde{t}_1$, in models with light charginos and neutralinos.

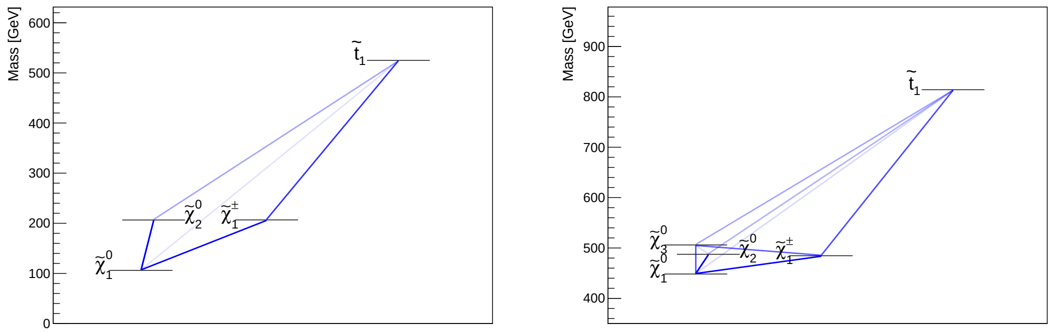

Figure 1.10: Schematic representation of the top squark decay modes in two different pMSSM models: darker lines show the decays with the higher branching ratios.

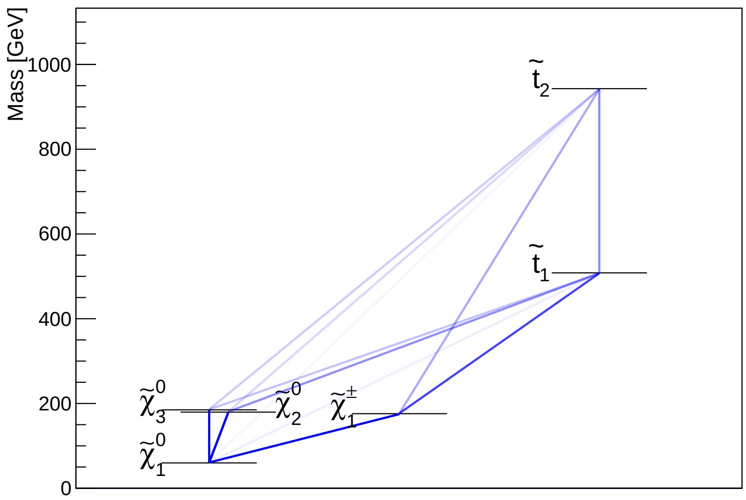

Figure 1.11: Schematic representation of the possible $\tilde{t}_2$ decay modes in one specific pMSSM model: darker lines show the decays with the higher branching ratios.

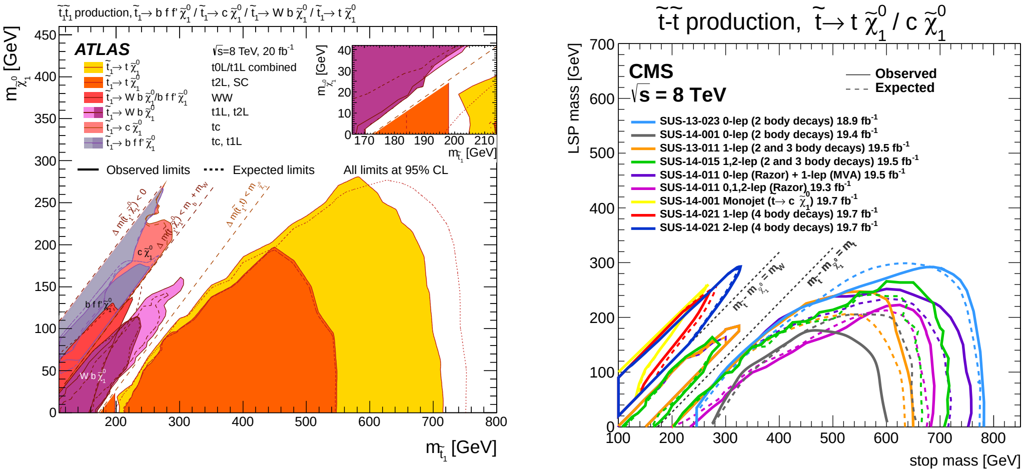

FIGURE 1.12: Summary of the limits, at 95% of CL, obtained by the searches for direct top squark pair production by ATLAS (left) [34] and CMS (right) [40–45] in models where no supersymmetric particle other than the lightest $\tilde{t}_1$ and neutralino is involved in the lightest $\tilde{t}_1$ decay. A branching ratio of 100% is assumed for the dominant decay in each region.

Simplified models

Given the multitude of possible models with different decays patterns, and the fact that many of them could produce similar signatures, a simplified approach is used. This approach helps in driving the event selection for the searches for new SUSY particles and as well to interpret their results. The so called Simplified Models [37–39] are effective models which are built in order to include the minimum number of particles necessary to produce a given final state and are usually parametrised in terms of cross sections, branching ratios and masses of on-shell particles. In such models, the phase space and the kinematics of the produced particles are calculated exactly, while the matrix element is approximated using effective parametrisations. Simplified Models are often used to present results in terms of discovery or exclusion of a certain set of SUSY particles, but it is important to connect the results obtained in such a way, to more realistic scenarios. This can be obtained by re-interpreting the analysis results over set of realistic models obtained by scanning the parameters of the SUSY Lagrangian.

1.5 Previous experimental constraints

Extensive searches for the top squark were performed by the ATLAS [34] and CMS [40–45] collaborations, using the data delivered during the Run 1 of the LHC, in proton-proton collisions at $\sqrt{s}$ = 7-8 TeV. No evidence of the top squark has been observed yet, and all the experimental efforts ended up in setting limits on the top squark mass, depending on the particular Simplified Model considered.
Figure 1.12 summarises the results obtained by the two collaborations for models where no supersymmetric particles other than the light $\tilde{t}_1$ and the $\tilde{\chi}_1^0$ are involved. It shows the same mass plane reported in Figure 1.8, together with the limits imposed by the different analysis, targeting the decay channel dominant in each area. 95% CL exclusion for a $\tilde{t}_1$ mass up to 780 GeV is obtained for a massless $\tilde{\chi}_1^0$.

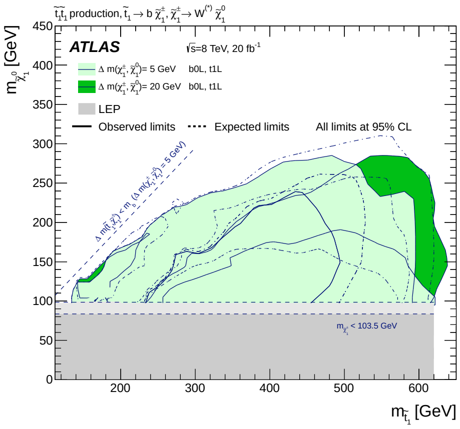

(A) $\Delta m\left(\tilde{\chi}_1^0, \tilde{\chi}_1^\pm\right) = 5\,\mathrm{GeV}$ (light blue) or $20\,\mathrm{GeV}$ (green)

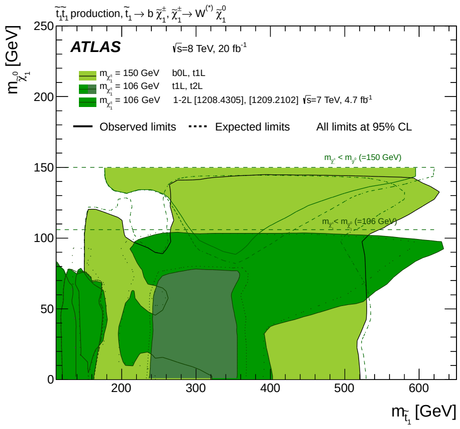

(B) $m_{\tilde{\chi}_1^\pm} = 106\,\mathrm{GeV}$ (dark green) or $150\,\mathrm{GeV}$ (light green)

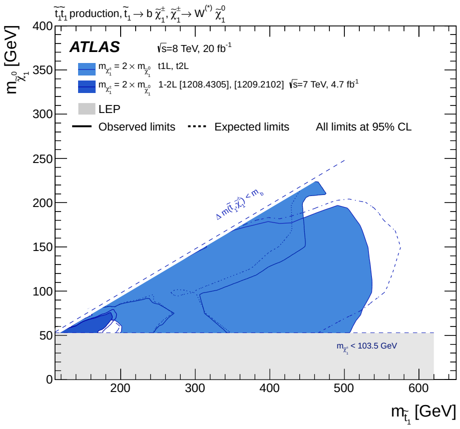

(C) $m_{\tilde{\chi}^\pm} = 2m_{\tilde{\chi}^0}$

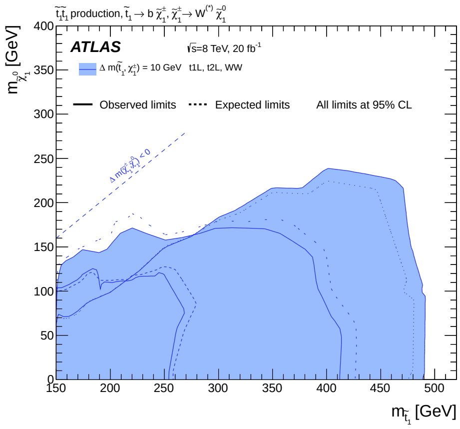

(D) $\Delta m\left(\tilde{t}_1, \tilde{\chi}_1^\pm\right) = 10\,\mathrm{GeV}$

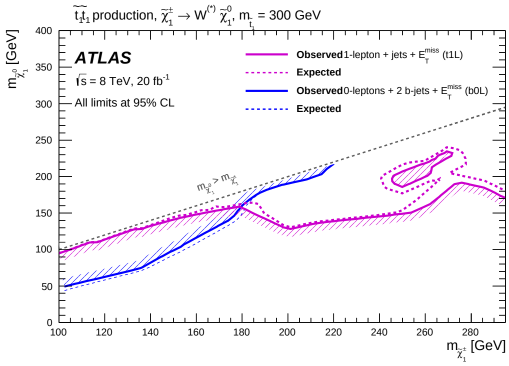

(E) $m_{\tilde{t}_1} = 300\,\mathrm{GeV}$

FIGURE 1.13: Summary of the limits, at 95% of CL, obtained by the searches for direct top squark pair production in the $\tilde{t}_1 \rightarrow \tilde{\chi}_1^\pm$ decay mode; each plot correspond to a different constrain on the mass spectrum [34].

In the more complex scenario in which the the lightest chargino is also coupled to the $\tilde{t}_1$, limits were established in selected slices of the 3D parameter space, in which one of the parameter is constrained at the time. In Figure 1.13 the results obtained by ATLAS during the first run of the LHC are reported. These have been interpreted using five different assumptions on the sparticles mass hierarchy:

- fixed chargino mass (106 GeV or 150 GeV)
- $m_{\tilde{\chi}^{\pm}} = 2m_{\tilde{\chi}^0}$ (motivated by unification, see equation 1.13)
- small splitting between the $\tilde{t}_1$ and the $\tilde{\chi}_1^{\pm}$ mass ($\Delta m\left(\tilde{t}_1, \tilde{\chi}_1^{\pm}\right) = 10\,\text{GeV}$)
- chargino and neutralino nearly degenarate ($\Delta m\left(\tilde{\chi}_1^0, \tilde{\chi}_1^{\pm}\right) = 5\text{-}20\,\text{GeV}$)
- fixed $\tilde{t}_1$ mass (300 GeV)

Summarising, in all the models considered with the $\tilde{t}_1 \rightarrow b\ \tilde{\chi}_1^{\pm}$ decay, $\tilde{t}_1$ masses up to 450 - 600 GeV are generally excluded. With the exception of highly compressed scenarios where $\tilde{t}_1$ masses as low as 200 GeV are still allowed (Figure 1.13 b) and a small unexcluded region around $(m_{\tilde{t}_1}, m_{\tilde{\chi}_1^{\pm}}, m_{\tilde{\chi}_1^0}) = (180, 100, 50)$ GeV (Figure 1.13 c), where the signal events have similar kinematics to Standard Model $t\bar{t}$ events and therefore the analysis sensitivity is much weaker.
Concerning the $\tilde{t}_2$, the search effort concentrated mostly on models where the mass splitting between the $\tilde{t}_1$ and the $\tilde{\chi}_1^0$ is equal to the top mass. This area of the phase space was not covered by the traditional $\tilde{t}_1 \rightarrow t\ \tilde{\chi}_1^0$ searches, as can be observed in Figure 1.12, due to the similarity between the signal and the $t\bar{t}$ background in term of kinematics. Exploiting the SM boson emitted by the first step of the dacay, could therefore help in resolving an possible presence of new physics in such a difficult area. Limits were placed considering the $\tilde{t}_2$ decaying 100% of the time in either $\tilde{t}_1\ h$ or $\tilde{t}_1\ Z$ and $\tilde{t}_2$ masses up to 600 GeV have been excluded in both scenarios, considering a massless $\tilde{\chi}_1^0$, as can be seen in Figure 1.14. Figure 1.15 shows instead the exclusion power for specific mass points as a function of the branching ratio of the $\tilde{t}_2$.

The results of all the searches for third generation squarks, together with other SUSY analysis in ATLAS, have been further interpreted in the context of the 19-parameter pMSSM [46]. To do so, set of realistic models have been generated by variating the parameters in the range of phase space allowed by the external experimental constraints and in order to keep the sparticles accessible the the LHC. The result, showing the excluded models as function of the $\tilde{t}_1$ and the $\tilde{\chi}_1^0$ masses, is shown in Figure 1.16. The comparison between the black area (100% excluded models) and the white line (simplified models contour) shows that in many cases using simplified models is an over-simplification and the limits obtained with them should be taken with a pinch of salt. To cover al possible models, more complex analysis strategies are needed, which cover more than the simpler signatures.

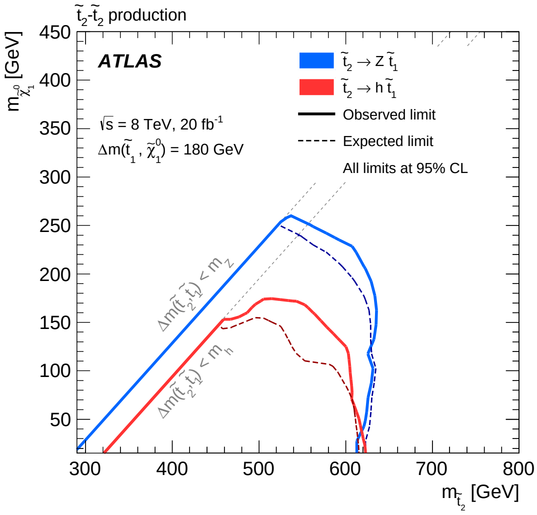

FIGURE 1.14: Exclusion limits at 95% CL in the scenario where $\tilde{t}_2$ pair production is assumed, followed by the decay $\tilde{t}_2 \rightarrow \tilde{t}_1\ Z$ (blue) or $\tilde{t}_2 \rightarrow \tilde{t}_1\ h$ (red) and then by $\tilde{t}_1 \rightarrow t\ \tilde{\chi}_1^0$ with a branching ratio of 100%, as a function of the $\tilde{t}_2$ and $\tilde{\chi}_1^0$ mass [34]. The $\tilde{t}_1$ mass is fixed by the relation $m(\tilde{t}_1) - m(\tilde{\chi}_1^0) = 180\,\text{GeV}$.

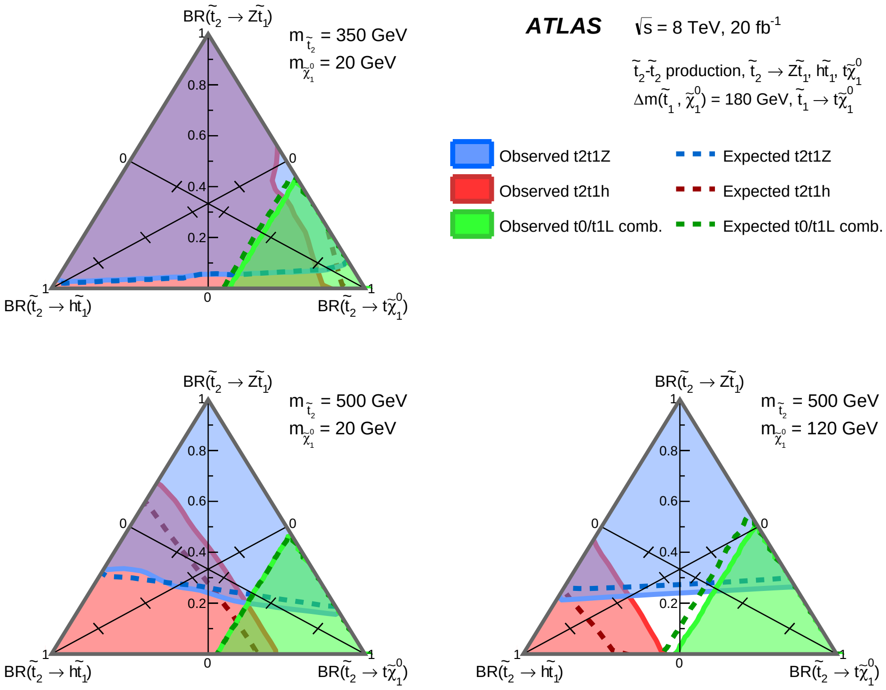

FIGURE 1.15: Exclusion limits as a function of the $\tilde{t}_2$ branching ratio for $\tilde{t}_2 \rightarrow \tilde{t}_1\ Z$, $\tilde{t}_2 \rightarrow \tilde{t}_1\ h$ and $\tilde{t}_2 \rightarrow t\ \tilde{\chi}_1^0$ [34]. The limits are given for three different values of the $\tilde{t}_2$ and $\tilde{\chi}_1^0$ masses.

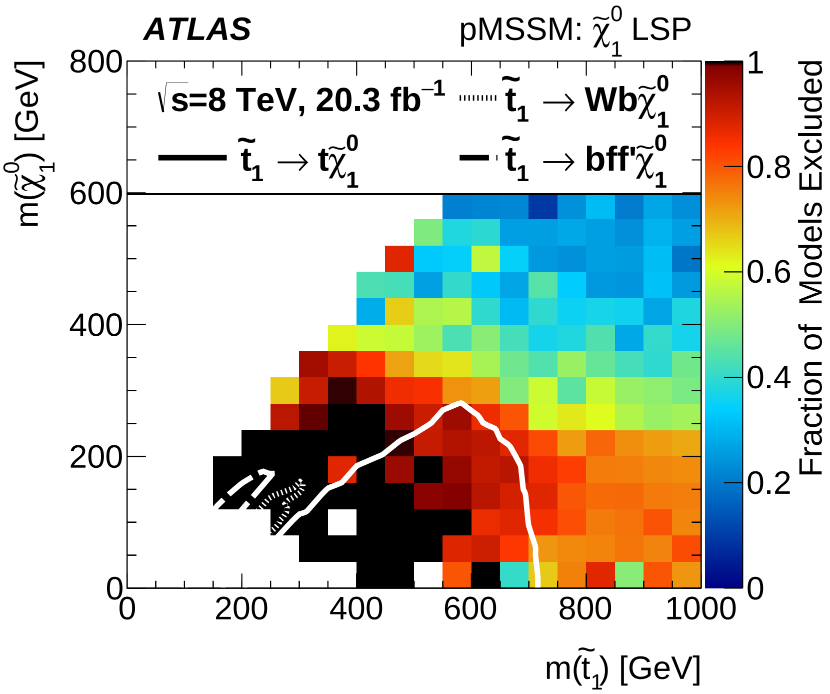

FIGURE 1.16: Fraction of pMSSM points excluded in the $(\tilde{t}_1,\tilde{\chi}_1^0)$ mass plain [46]. The simplified-model limit overlaid is set assuming directly produced top squark pairs, with each decaying to a top quark and neutralino, $\tilde{t}_1 \to t\,\tilde{\chi}_1^0$ with 100% BR. The colour scale indicates the fraction of pMSSM points excluded in each mass bin, with black squares indicating 100% of the generated models being excluded.

Chapter 2

The LHC and the ATLAS Detector

The data used in the analysis presented in this thesis come from proton-proton collisions, delivered by the LHC accelerator at CERN, and have been recorded by the ATLAS detector. In this chapter, an overview of the accelerator complex is given, together with a detailed description of ATLAS and its sub-detectors.

2.1 The Large Hadron Collider

The Large Hadron Collider (LHC) is the largest particle accelerator in the world. It has been built in order to explore a wide new range of energies, never reached before. It is created to accelerate and collide hadron beams up to a centre of mass energy of 14 TeV. The aim of the LHC is to allow experimental physicists to investigate the nature of particles interactions up to the TeV scale, study the electroweak symmetry breaking mechanism and test theories which predict new physics beyond the Standard Model.
The LHC was built into the same tunnel of the Large Electron-Positron collider (LEP) [47], the previous CERN big accelerator. For the LHC, the choice of using proton beams is closely related to the discovery power of this machine. Charged particles irradiate photons when accelerated and the rate of energy loss for a particle that covers a circular orbit with a radius R depends on its mass m in the following way:

$$\frac{dE}{dt} = \frac{E^4}{m^4 R} \tag{2.1}$$

For this reason with protons, that are two thousand times heavier than electrons, it is possible to reach a higher value of energy, keeping the same acceleration parameters.
As a side effect, protons aren't elementary objects, but are made of quarks and gluons. Therefore, the interaction takes place between two of the elementary components, which carry an unknown fraction of the momentum of the two protons. For this reason, the energy in the centre of mass of each collision is undetermined.
The project to build this huge machine started in the early nineties, and the LHC became finally operative in September 2008. The nominal design predicted bunches containing $\approx 10^{11}$ protons with an energy of 7 TeV for each beam and a bunch crossing frequency of 1/25ns. This would

have produced a nominal instantaneous luminosity $\mathcal{L} = 10^{34}$ cm^{-2}s^{-1}.
Unfortunately, nine days after the first circulating beam, an accident occurred due to an electrical fault and 53 magnets were damaged as a consequence. This caused a one year long shutdown in order to repair the damages and improve the safety conditions. During the autumn of 2009 the operations started again, with limited performance.
The first proton-proton collisions at $\sqrt{s} = 7\,\text{TeV}$ were registered on 30th March 2010 and for the following two years the experiments have been able to collect data. During 2015, after an established shutdown for repairs, upgrades and improvements, the operations have started again with an upgraded energy in the centre of mass of $\sqrt{s} = 13\,\text{TeV}$, close to the nominal target. The data taking of the Run 2 of the LHC continued until the end of 2018, with gradually increased luminosity, to finally collect a total integrated luminosity of 156 fb^{-1}. Table 2.2 shows the evolution of the LHC performances.

Year	Energy	Peak Lumi	Integrated Lumi	Bunch Spacing
2011	7 TeV	4×10^{33}cm^{-2}s^{-1}	5.61 fb^{-1}	50 ns
2012	8 TeV	8×10^{33}cm^{-2}s^{-1}	23.3 fb^{-1}	50 ns
2015	13 TeV	5×10^{33}cm^{-2}s^{-1}	4.2 fb^{-1}	25 ns
2016	13 TeV	14×10^{33}cm^{-2}s^{-1}	38.5 fb^{-1}	25 ns
2017	13 TeV	21×10^{33}cm^{-2}s^{-1}	46.9 fb^{-1}	25 ns
2018	13 TeV	21×10^{33}cm^{-2}s^{-1}	60.6 fb^{-1}	25 ns

Table 2.1: Summary of the LHC performances during the years of operation.

The accelerators complex

The LHC consists of a 27 km ring of superconducting magnets, located in the underground tunnel at the border between Switzerland and France. The proton beams travel in opposite directions in separate beam pipes and, after being accelerated to the energy limit of 6.5 TeV, are made to collide in four different points, inside the experiments: ALICE, ATLAS, CMS and LHCb.
This is only the final step of a complex acceleration chain, illustrated in Figure 2.1. The acceleration process starts from a ionised hydrogen source: protons are separated from the electrons with strong electric fields and are firstly accelerated up to an energy of 50 MeV by the linear accelerator Linac2. The proton beam is then injected into the Proton Synchrotron Booster (PSB), and reach the energy of 1.4 GeV. The next step is the Proton Synchrotron, which has been the first CERN synchrotron and during the sixties has been used as the main accelerator. Now it is part of the LHC chain and is needed to deliver proton beams with an energy of 45 GeV to the Super Proton Synchrotron (SPS), the last step before the LHC. The SPS, which made possible the discovery of the W bosons in 1983 by the UA1 and UA2 collaborations, further increases the energy of the beams up to 450 GeV before the injection in the main accelerator. Heavy ions follow a slightly different path, being accelerated by the Linac3 and by the Low Energy Ion Ring (LEIR) before entering in the PS.

LHC experiments

The main LHC experiments (ALICE, ATLAS, CMS and LHCb) are situated in caverns corresponding to the four intersection points of the LHC, shown in Figure 2.1. Three additional experiments (TOTEM, LHCf and MoEDAL) focus on forward emitted particles and are therefore

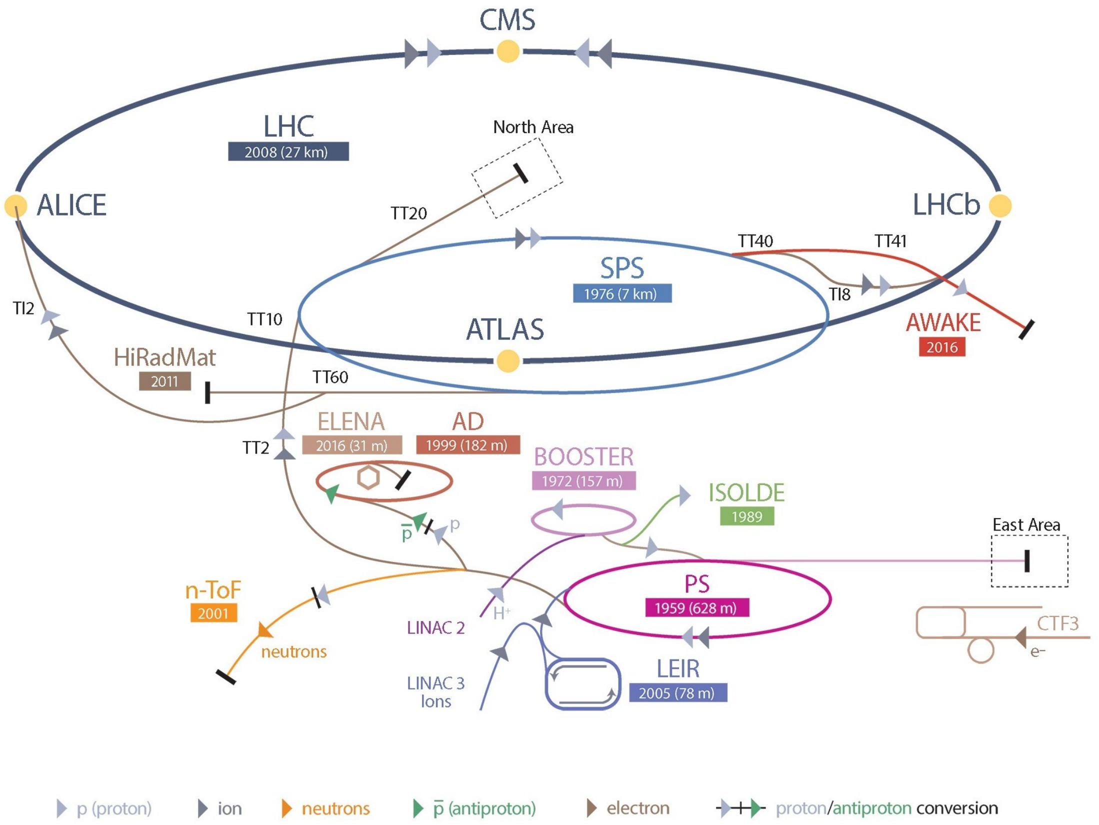

FIGURE 2.1: Scheme of the CERN accelerator complex [48].

located along the tunnel, in proximity of the main experiments. A brief list of the experiments main goals is given in this section.

- ATLAS and CMS are the two biggest experiments. They use different technologies, with the aim of discovery new particles: from the Higgs boson to the ones predicted by beyond Standard Model theories.
- LHCb is specialised in investigating the differences between matter and antimatter by studying light states containing b quarks.
- ALICE is the heavy ions detector, designed to study the physics of strongly interacting matter at extreme energy densities.
- TOTEM makes precise measurements of protons in the forward region, inaccessible by other experiments, and it is used to monitor the LHC luminosity.
- LHCf uses forward particles from the LHC as a source to simulate cosmic rays in laboratory conditions.
- MoEDAL is the newest between the LHC's experiments and it is searching for magnetic monopoles.

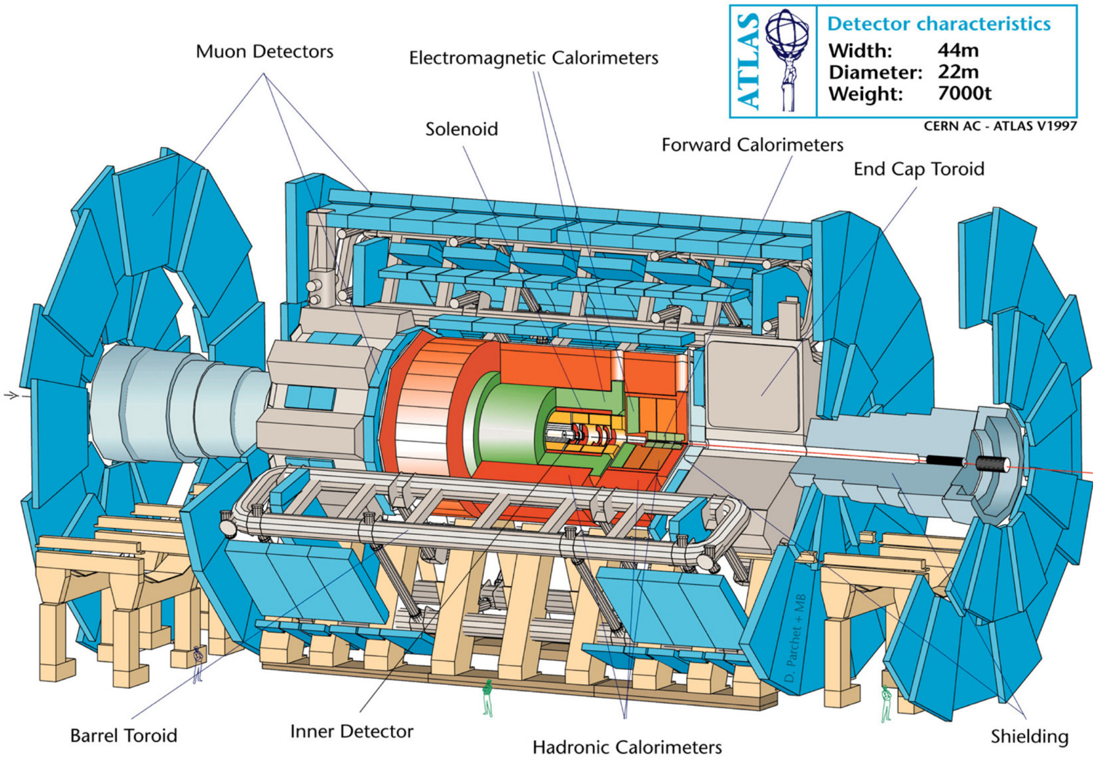

FIGURE 2.2: Schematic representation of the ATLAS detector.

2.2 The ATLAS detector

ATLAS (A Toroidal Lhc ApparatuS)[49, 50] is the largest between the LHC's detectors. It weights about 7 kTons and has a cylindrical symmetry centred on the beam axis, with a basis diameter of 25 m and a longitudinal length of 44 m. The detector design project was proposed in 1994 and it was built during the construction of the LHC accelerator. In 2008 it has been turned on for the first time, in order to be tested with cosmic ray events and in 2009 ATLAS was ready for the first LHC collisions.
ATLAS is designed to be a general-purpose detector. When the protons collide in the centre of the detector, a variety of different particles with a broad range of energies are produced. Rather than focusing on a particular physical process, ATLAS is designed to measure the broadest possible range of signals. For this reason, ATLAS is composed by different sub-detectors, each one designed and optimised for a specific task. It can be divided into three major parts: the Inner Detector (ID) that surrounds the interaction region and records the tracks left by ionising particles, the Calorimeter system to measure the energy of electrons, photons and hadronic jets in the middle, and the Muon Spectrometer in the outermost layer. The complete structure of the ATLAS detector is shown in Figure 2.2.

ATLAS coordinate system

Due to the shape of the detector, a convenient set of cylindrical coordinates has been chosen. The beam direction defines the z axis, with the origin located at the center of the detector. The transverse plane is then defined by the azimuthal angle ϕ and by the pseudorapidity η, defined as:

$$\eta = -\ln\left[\tan\left(\frac{\theta}{2}\right)\right] \tag{2.2}$$

This particular angular coordinate derives from the limit for massless particles of a quantity called rapidity (y) defined by the following equation:

$$y = \frac{1}{2}\ln\left(\frac{E+p_z}{E-p_z}\right) \tag{2.3}$$

This quantity has the propriety of being additive under a Lorentz boost β along the z axis: $y' = y + \text{arctanh}(\beta)$. Hence, the difference in rapidity and differential distributions in in this variable $\frac{dN}{dy}$ are invariant. This is really valuable at hadron colliders, where the rest frame of parton collisions is unknown.

2.3 The Inner detector

The ATLAS Inner Detector provides the reconstruction of charged particle tracks, with the aim of measuring the transverse momentum of these particles and identifying collision and decay vertexes. The structure of the detector is shown in Figure 2.3. It is composed by three concentric sub-detectors, using different technologies: the Pixel Detector, situated close to the interaction point, the Semi-Conductor Tracker (SCT) in the middle and finally the Transition Radiation Tracker (TRT) that constitutes the outermost component; all these sub-detectors are contained in the Central Solenoid, which provides a nominal field of 2 T and bends the tracks in the (R, ϕ) plane, to allow the transverse momentum measurement. The Inner Detector overall dimensions are 2.1 m in diameter and 6.2 m in length and it covers a pseudorapidity region of $|\eta| < 2.5$.
With the combination of the informations coming from the sub-detectors, it is possible to obtain a resolution on the impact parameter of a track varying with the p_T between $30 - 100$ µm in the transversal plane and between $70 - 170$ µm in the longitudinal direction [51].

Pixel Detector

The Pixel Detector is placed as close as possible to the beam pipe, in order to achieve a great resolution in vertex reconstruction. In the original design project, the cylindrical barrel contains three different layers: the B-layer (5.05 cm far from the beam axis), the L1 (8.85 cm) and the L2 (12.25 cm), These layers are 80 cm long and the two end-caps have three disks each, needed to cover the remaining η region. It is made up of 1744 partially overlapping modules (1456 in the barrel plus 288 in the end-caps), consisting in a 250 µm thick silicon sensor with n^+ pixels implanted on a n-doped bulk, 16 front-end chips and one controller chip. Each module has an active area of $16.4 \times 60.8\,\text{mm}^2$ consisting of 47232 (328×144) pixels. The typical pixel size is $50 \times 400\,\mu\text{m}^2$, while in the regions between two front-end chips a size of $600 \times 50\,\mu\text{m}^2$ has been chosen to guarantee a full angular coverage. This leads to a position resolution better than 15 µm in the (R, ϕ) plane and of 72 µm and 115 µm in the z direction, for the first layer and the others respectively.
In May 2014, during the shutdown, an additional innermost layer, the Insertable B-Layer (IBL) [52] with a radius of 3.3 cm, has been inserted in ATLAS in order to improve the tracking precision.

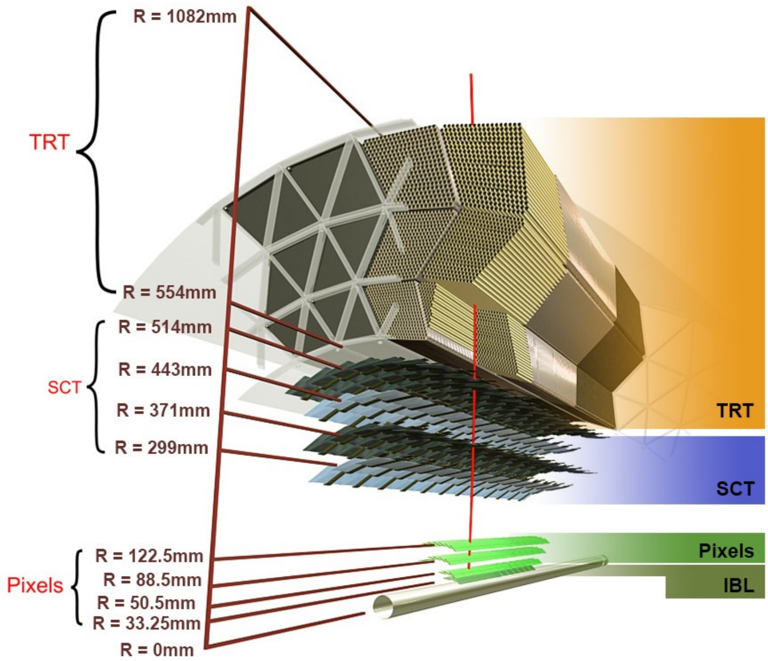

FIGURE 2.3: View of the transverse section of the ATLAS Inner Detector.

Two different technologies have been used for the upgrade: improved planar sensors in the middle and 3D sensors in the forward region, with a reduced pixel size of $50 \times 250\,\mu\text{m}^2$ in order to improve the longitudinal resolution.

Semi-Conductor Tracker

The SCT is the second system of the Inner Detector. It is composed by four cylinders in the barrel region, covering the pseudorapidity range $1.1 < |\eta| < 1.4$, with a radial extension between 299 mm and 514 mm, and a length of ≈ 1.5 m, plus two end-caps consisting in nine disks covering the remaining region of $|\eta| < 2.5$. It uses a semiconducting silicon technology, like the Pixel Detector, with larger strip (80 µm pitch) sensors in order to cover a bigger area. In the end-cap disks, slightly different sizes are needed in order to accommodate the more complex geometry, with strip pitch ranging from 56.9 to 90.4 µm. Over all, the SCT counts 61 m^2 of silicon sensors with around 6.3 million readout channels and deliver position measurement with an accuracy of 17 µm and 580 µm in the azimuthal and z directions respectively.

Transition Radiation Tracker (TRT)

The TRT is the outermost system of the Inner Detector and covers a radial distance from 563 mm to 1066 mm. It consists of straw tubes with a 4 mm diameter filled with a gas mixture of 70% Xe, 27% CO_2 , and 3% O_2. In the centre of each tube there is a gold-plated tungsten wire at ground potential while the wall are kept at a voltage of -1.5 kV, therefore each tube acts as a small proportional counter.
In addition to this, the spaces between the straws are filled with polymer, therefore transition radiation is emitted by highly relativistic charged particles as they pass through the material

boundary; these soft X-rays can be absorbed by Xe atoms and then detected by the tubes. This effect has a dependence on the factor $\gamma = E/m$ and can be used to discriminate electrons from heavier particles like pions.

The TRT barrel region contains 52544 straw tubes 1.5 m long, parallel to the beam axis. They cover a radius from 0.5 m to 1.1 m and a pseudorapidity range of $|\eta| < 1$. The end-caps contain 0.4 m long straws organised perpendicular to the beam axis, covering the following geometrical range: $0.8\,\text{m} < |z| < 2.7\,\text{m}$ and $1 < |\eta| < 2$.

The performances of the TRT go in the opposite direction of the silicon-based tracking devices: the single-point resolution is worst ($\approx 120\,\mu\text{m}$), but this is compensated by a larger number of hits per track (typically more than 30) and a long lever arm.

2.4 The Calorimeters

The second layer of the ATLAS detector is occupied by the calorimeter system, shown in Figure 2.4, dedicated to the measurement of the energy of photons, electrons and hadronic particles. This is possible when the particles release all their energy inside the material and are arrested before the end of the calorimeter. Electromagnetic and hadronic showers have a different behaviour inside matter and, therefore, two different calorimeters are needed: the Electromagnetic Calorimeter (ECAL) is collocated right after the solenoid and allows the measurement of photon and electrons energy, while the Hadronic Calorimeter (HCAL) is placed immediately after and needs more powerful absorbers to deal with the deeper development of hadronic jets. For both calorimeters a "sampling" strategy has been adopted: most of the energy of the particles is absorbed in high density metals, while the measurement is based on a periodical detection of the shape of the resulting showers, in some active materials. This leads to a worse energy resolution, due to the fluctuations that affect the energy release processes, but allows to build more compact calorimeters and, above all, the segmentation makes also possible position measurements. This is especially important for neutral particles, like photons, that don't leave tracks inside the Inner Detector. The performances of the ATLAS calorimeter system, in terms of energy resolution, are shown in Table 2.2.

Electromagnetic Calorimeter

The Electromagnetic Calorimeter uses lead layers as absorbing material and liquid argon ionisation chambers for the shower sampling. This sub-detector is designed with the characteristic accordion geometry shown in Figure 2.5: such configuration allows for good energy and space resolution, together with a full azimuthal coverage, while it has the disadvantage of having a time resolution longer than the nominal separation between two events. The total thickness is more than 22 radiation lengths (X_0) in the barrel and more than 24 X_0 in the end-caps, in order to contain

Calorimeter	Resolution (σ_E/E)
ECAL	$10\%\sqrt{E} \oplus 0.7\%$
HCAL	$50\%\sqrt{E} \oplus 3\%$
FCAL	$100\%\sqrt{E} \oplus 3.1\%$

TABLE 2.2: Energy resolution obtained by the ATLAS calorimeter system.

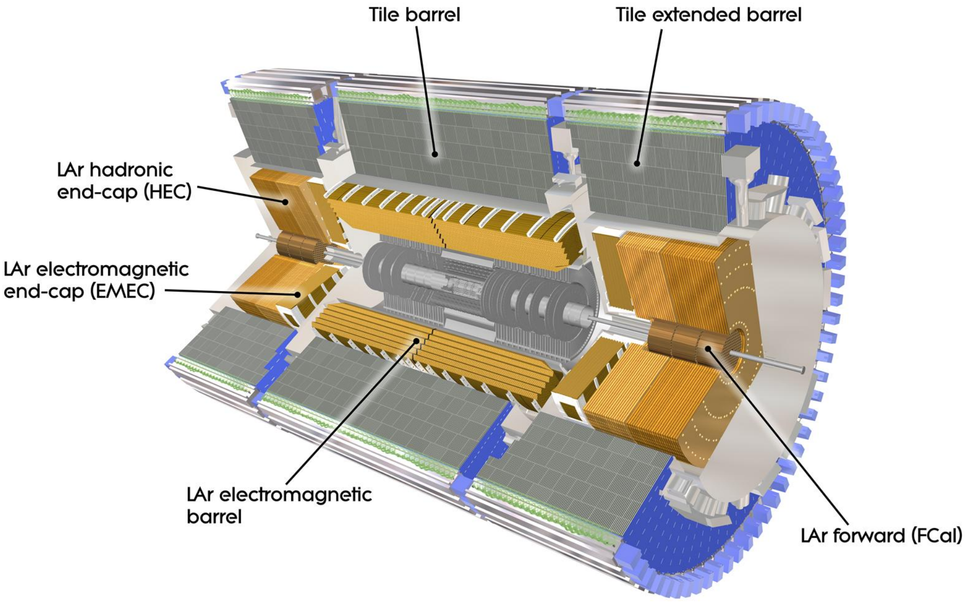

FIGURE 2.4: Schematic description of the calorimeter system of the ATLAS detector.

almost every electromagnetic shower and about 2/3 of the hadronic ones.
The barrel is divided in three layers, called strips, middle and back. The strip section is 6 X_0 long and has high segmentation in the η direction, in order to discriminate between photons and π_0. The middle part extends up to 22 X_0 and contains most of the energy of the showers originated by photon and electrons with energy up to 50 GeV. Finally, the back provides 2 additional X_0 and is used to estimate the energy leakage in the hadronic cells. In order to study the shower development before the start of the calorimeter and estimate the energy loss inside the Inner Detector, an additional pre-sampler layer of liquid argon is added inside the solenoid. Because of the transitions between the different components, there are regions in η (called crack) where the performances of the EM calorimeter are worse. In particular, this happens at $\eta = 0$, between 1.37 and 1.52 , and at $|\eta| = 2.5$.

Hadronic Calorimeter

The Hadronic Calorimeter makes use of different absorbers and active materials for the barrel region and for the end-caps.
The Tile Calorimeter is placed in the central region and uses a sampling technique with steel and scintillators. It extends from a radius of 2.28 m to 4.25 m and is longitudinally segmented in three layers; the pseudorapidity coverage is $|\eta| < 1.0$ for the barrel and $0.8 < |\eta| < 1.7$ for the extended barrel.
The Hadronic End-cap Calorimeter (HEC), instead, consists of two independent wheels per end-cap, covering the region $1.5 < |\eta| < 3.1$, and uses a copper-liquid argon sampling technique. Each wheel is divided into two longitudinal segments, for a total of four layers per end-cap.

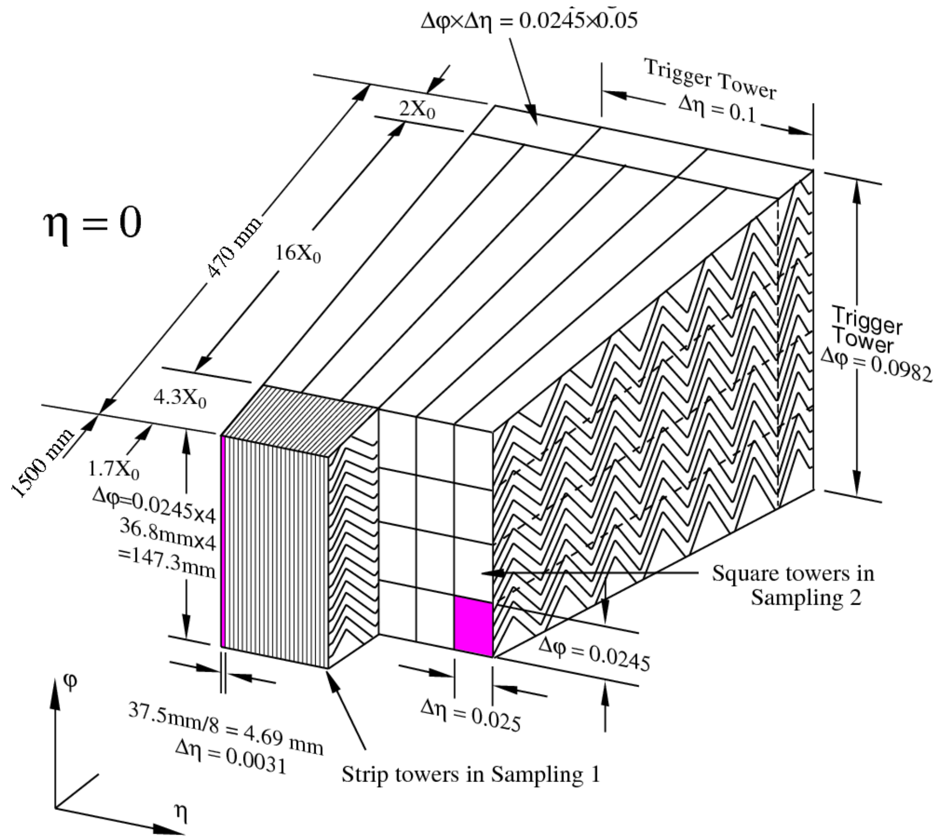

Figure 2.5: 3D view of the accordion geometry of the ECAL.

Forward Calorimeter

Finally, the Forward Calorimeter (FCal) covers the $3.1 < |\eta| < 4.9$ region and allows both electromagnetic and hadronic energy measurements. This system, based on liquid argon technologies, is not used for precision measurements, but provides information for the missing transverse energy evaluation and the reconstruction of very forward jets. It is built in order to have an high tolerance to radiation, which is extremely important in this region close to the beam pipe.

2.5 The Muon Spectrometer

The Muon Spectrometer (MS), shown in Figure 2.6, is in the outermost part of ATLAS: muons lose a negligible amount of energy by ionisation in the materials of the calorimeters, therefore they are not absorbed and can reach this region of the detector almost unperturbed. The muon system has two different functions: it needs to provide high precision tracking, for which high granularity is needed, and to serve as trigger for the recording of the events, requiring the employiment of fast detectors. Different technologies have been exploited to satisfy these requirements.
The muon tracks measurement is provided in the central η region by the Monitored Drift Tubes (MDT), while at large η, the higher segmented Cathode Strip Chambers (CSC) are used. The two systems can provide hit measurements with a resolution of 80 µm and 60 µm respectively. The magnetic field used for the momentum measurement derives from the external toroids system,

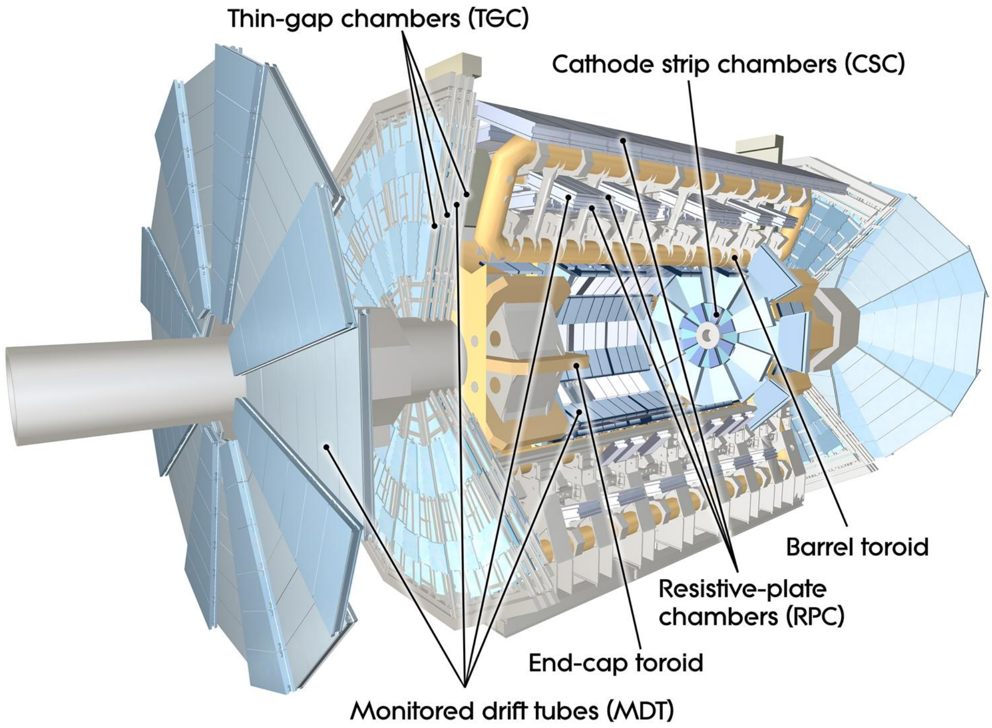

FIGURE 2.6: Location of the Muon Spectrometer inside the ATLAS detector.

which provides a field of 0.5 T and 1 T in the barrel and end-caps respectively. The field's lines are circumferences centred on the beam axis and bends the particle trajectories in the (R, z) plane. In order to reduce multiple scattering affecting the tracking precision, the whole system is placed in air.
The detectors participating to the trigger decisions need a very fast response: the Resistive Plate Chambers (RPC) are used in the barrel region, while the Thin Gap Chambers (TGC) are used in the end-cap. Together they cover the region for $|\eta| < 2.4$.

2.6 Triggers and Data Acquisition

Considering a bunch-spacing of 25 ns, bunches filled with protons collide inside the ATLAS detector with a rate of roughly 40 MHz. This large amount of data can't be fully reconstructed and stored; therefore, the number of events collected by the detector has to be reduced down to approximately 1 kHz in a very short time frame. The ATLAS trigger system has been designed to reduce the initial data rate by several orders of magnitude, selecting only the small fraction of events interesting for the ATLAS physics programme.
The trigger system consists of two trigger levels, a hardware-based first level trigger (Level-1) and a software-based high-level trigger (HLT), as illustrated in Figure 2.7. The Level-1 trigger is implemented to determine Regions-of-Interest (RoIs) in the detector, exploiting informations coming from the calorimeters and from the Muon Spectrometer; it reduces the event rate from the LHC bunch crossing rate down to 100 kHz. The RoIs are then passed to the HLT which uses the full detector information in either the RoI or the entire event to form a decision. In the HLT, reconstruction algorithms similar to the ones used for the off-line analysis of the data run in a

large farm of ≈ 40.000 processor cores and a decision is formed typically within 300 ms. The output rate of the HLT is around 1 kHz.
The increased luminosities, above 1.5×10^{34} cm^{-2}s^{-1}, recorded during the Run 2 of the LHC, are responsible for severe limitations on the ATLAS TDAQ system due to the increased trigger rate. In order to guarantee the stable running of the system, either additional pre-scale factors or an increase of the trigger thresholds would be needed. However, this would reduce the physics acceptance, counteracting the gain of the higher luminosities. Therefore, the L1 topological trigger (L1Topo) upgrade has been commissioned. The L1Topo trigger decision is derived from combinations of trigger objects identified by the calorimeters and the Muon Spectrometer L1 triggers, and can be based on topological quantities such as angular distances and invariant masses, at the LHC bunch crossing rate. Topological triggers have the benefit of allowing lower energy thresholds for multi-object final states without increasing the trigger rates.
After an event is accepted by the L1 trigger, the data are transferred off the detector to the Readout Drivers (RODs). Digitised signals are formatted as raw data and then transferred to the Data Acquisition System (DAQ). The events that pass also the HLT selection are then moved to permanent storage at the CERN computing centre.
During all these processes, the Detector Control System (DCS) permits the safe operation of the ATLAS detector hardware. It monitors and archives the operational parameters (like magnetic field, temperatures and humidity), points out any abnormal behaviour, and allows any automatic or manual corrective action that has to be taken.

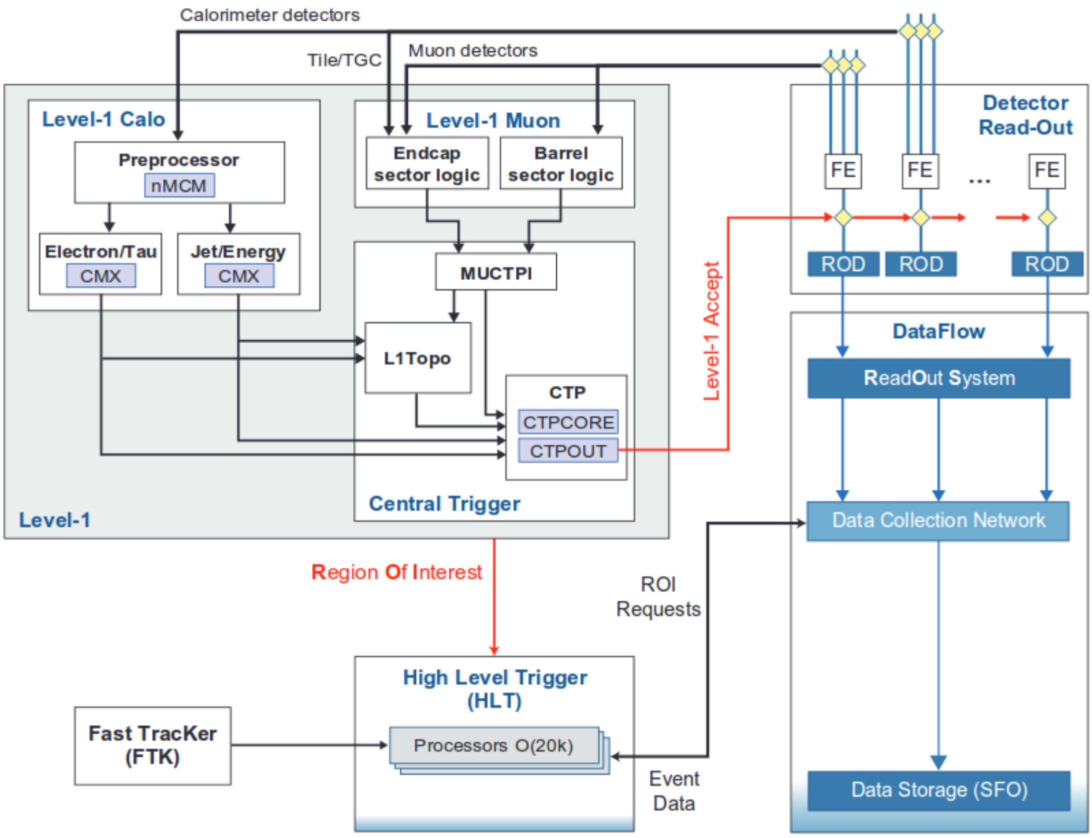

FIGURE 2.7: Schematic overview of the Run 2 ATLAS trigger and data acquisition system [53].

Chapter 3

Particles reconstruction and identification

The interactions in the detector of the particles produced in proton-proton collisions and of their decay products are stored in term of the electric signals acquired in the various ATLAS sub-detectors. For each event stored by the data acquisition system, the information coming from the sub-detectors is elaborated in order to reconstruct all the particles contained in the final state such as photons, leptons and hadrons. This Chapter will focus on the reconstruction and identification techniques for the particles used in the searches presented in this thesis: electrons, muons, and jets arising from quarks and gluons. Section 3.6 is dedicated to the description of the missing transverse momentum, a global quantity which indicates the presence of weakly interacting particles in the final state.

3.1 Tracks and primary vertex

The reconstruction of the charged particles trajectories (called tracks) with $p_{\mathrm{T}} > 0.4\,\mathrm{GeV}$ and $|\eta| < 2.5$ is performed exploiting the information coming from the Inner Detector [54]. Hits found in the Pixel Detector, are used as seeds for the reconstruction algorithm. Then, the combination with the information coming from the SCT leads to a set of track candidates and finally the results are further combined with the TRT measurements. This procedure can also be applied backwards, starting from reconstructed segments inside the TRT. This is particularly useful to recover the tracks corresponding to converted photons, if no hit inside the Pixel Detector is registered.

The tracks reconstructed in this way are then used as input for the primary vertex identification algorithm [55]. It follows an iterative procedure that can be divided in two major steps:

- a "finding" algorithm is used to isolate the vertex seed by looking for the mode of the z-coordinates of tracks at their respective points of closest approach to the beam spot;
- then the "vertex fitting" algorithm, which takes as input the seed position and the available tracks, determines the position of the vertex and evaluates the compatibility of each track with the defined interaction coordinates.

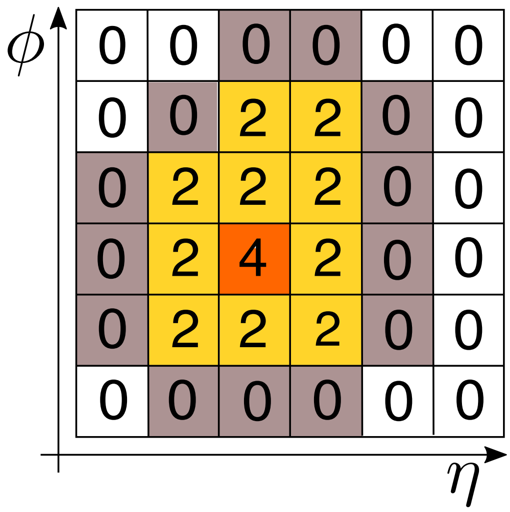

FIGURE 3.1: Schematic representation of a Topocluster. The numbers inside the cells indicate the signal-to-noise ratio threshold.

If some tracks are found to be incompatible with the vertex (at a distance of more than three standard deviations), they are used to seed a new vertex and the procedure is repeated until each track in the event belongs to one vertex, or no more vertices can be found. After this procedure, the parameters of the tracks are re-evaluated adding the constrains of the vertex coordinates.
During Run 2, the average number of interactions per bunch crossing is more than 30, so many vertices are reconstructed in each event. The vertex associated to the group of tracks for which the squared p_{T} sum has the highest value is called primary vertex and it is considered the origin of the different particles arising from the hard scatter.

3.2 Jets

Gluons and quarks arising from the hard scatter are coloured particles and can't exist in free states. Other coloured quarks and gluons are therefore created to form colourless hadrons: a jet is a cone of particles produced by this hadronisation process.
At first, it is necessary to identify the clusters of the energy deposits in the calorimeter cells left by the particles in the jet and to associate to those clusters the relative four-momentum vector; for this purpose a "TopoCluster" algorithm is used [56]. Calorimeter cells with a signal-to-noise ratio $\gamma = E_{\mathrm{cell}}/\sigma_{\mathrm{cell}}^{\mathrm{noise}}$ above a threshold ($|\gamma| > 4$) are chosen as seed to start the clustering, then all the neighbouring cells with $|\gamma| > 2$ are added. Finally, a ring of guard cells, with signal significances above the basic threshold is also considered when forming the cluster. A schematic representation of the calorimeter cells belonging to a Topocluster is shown in Figure 3.1.
After the initial cluster is formed, a search for the local maximum considering the energy in the cells is performed: if more than one maximum is found, the cluster is split. Finally, a zero-mass four-vector, built using the direction with respect to the primary vertex and the sum of the energy in its cells is associated to the cluster.
When all the clusters are identified, a complex algorithm is exploited to gather them and build the corresponding jet, in ATLAS the jet candidates are reconstructed using the anti-k_{T} jet clustering algorithm [57]. The first step consists in the calculation of the distance between two clusters (d_{ij})

and the distance between each cluster and the beam (d_{iB}), defined as follows:

$$d_{iB} = p_{\mathrm{T}i}^{2n} \tag{3.1}$$

$$d_{ij} = \min\left(p_{\mathrm{T}i}^{2n}, p_{\mathrm{T}j}^{2n}\right) \frac{\Delta R_{ij}^2}{R^2} \tag{3.2}$$

where $\Delta R_{ij}^2 = (y_i - y_j)^2 + (\phi_i - \phi_j)^2$, y_i is the rapidity of the cluster i and $p_{\mathrm{T}i}$ is its transverse momentum. n is equal to -1 for anti-k_{T} algorithms, while the value of the R parameter defines the width of the final reconstructed jets, a choice of $R = 0.4$ has been made for the jets used in the searches presented in this thesis.
The algorithm works in the following way:

- a set containing all the possible distances is considered;
- if the smallest element of the set is a d_{iB} the related cluster becomes a jet and it is removed from the procedure;
- if the smallest element is a d_{ij}, the objects i and j are combined, with $p_{\mathrm{T}}^{\mathrm{new}} = p_{\mathrm{T}i} + p_{\mathrm{T}j}$ and a new set is created with the new object replacing i and j.

The algorithm is iterated until all the clusters are classified as jets.
The transverse momentum of the resulting jet needs to be corrected in order to take into account the fraction of the hadronic shower that can't be recorded by the calorimeters (soft neutrons, neutrinos, energy used to break nuclear binding...) and energy loss in the inactive material. This correction is made by applying calibration factors, based on Monte Carlo simulations.
The uncertainties relative to the scale and the resolution of the jet energy (JES and JER) are derived as a function of the p_{T} and η of the jet, as well as of the pile-up conditions and the jet flavour composition (more quark-like or gluon-like) of the selected jets in the events. They are determined using a combination of data and MC simulated samples, comparing the jet response asymmetry in di-jet, Z+jet and γ+jet events [58, 59].
In the set of reconstructed jets, some misidentified jets having non-collision origin can emerge. These jets arise from Beam Induced Background (BIB), cosmic showers and calorimeter noise. To discriminate collision jets from these backgrounds, a set of different variables divided in three categories is used: variables based on signal pulse shape in the EM calorimeters, energy ratio variables, and track-based variables. Pulse shape variables provide good discrimination against the noise. The energy ratio variables and track-based ones are instead mainly used to reject the BIB and cosmic muon showers.
Further discrimination is needed to suppress jets arising from pile-up events. The Jet Vertex Fraction variable (JVF) [60] helps to remove jets which are not associated to the primary vertex (PV) and is defined as the sum of the scalar transverse momentum of the tracks that are associated with the jet and originated from the PV, divided by the scalar p_{T} sum of all the tracks associated to the jet. Applying a lower cut on JVF rejects the majority of pile-up jets, but leads to a selection efficiency that depend on the number of reconstructed primary vertices in the event (N_V). A multivariate combination of JVF and (N_V) called the Jet Vertex Tagger (JVT) [61] is constructed in such a way that the resulting jet efficiency is stable as a function of (N_V).

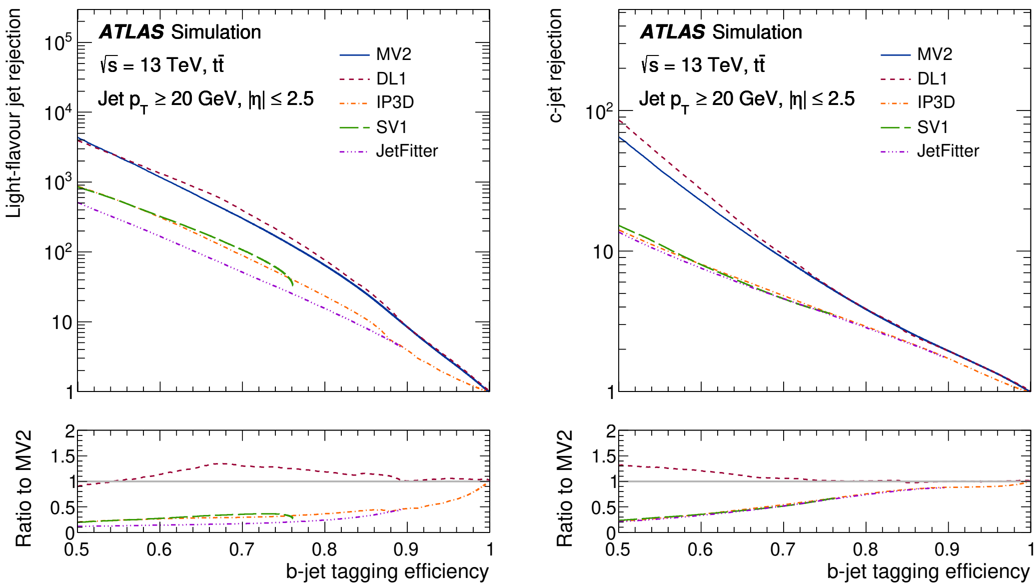

FIGURE 3.2: The light-flavour jet (left) and c-jet (right) rejections versus the b-jet tagging efficiency for the IP3D, SV1, JetFitter, MV2 and DL1 b-tagging algorithms evaluated on $t\bar{t}$ simulated events [65].

Identification of b-hadron initiated jets

The identification of jets originating from bottom quark fragmentation (b-jets), called b-tagging, exploits the specific features of the b-quark of having a relatively long lifetime (of the order of 1.5 ps) that results in a observable displacement of the decay vertex from the centre of the beam-spot.
In ATLAS, three kind of b-tagging algorithms are used in order to produce a set of variables that can discriminate between different jet flavours:

- the impact parameter based algorithm (IP2D and IP3D), which make use of the signed impact parameter significance of the tracks matched to the jet [62];
- the inclusive secondary vertex reconstruction algorithm (SV1), that tries to reconstruct an inclusive displaced vertex within the jet [63];
- the decay chain multi-vertex reconstruction algorithm (JetFitter), which aims to reconstruct the full decay chain (primary vertex $\rightarrow b \rightarrow c$) [64];

Finally, the variables obtained from the three algorithms are combined using multivariate classifiers to discriminate b-jets from light (u, d, s or gluon) jets and c-jets. Two high-level tagging algorithms have been developed [62]. The first one, MV2, is based on a boosted decision tree (BDT) discriminant, while the second one, DL1, is based on a deep feed-forward neural network (NN). The light-flavour jet and c-jet rejections as a function of the b-jet tagging efficiency are shown in Figure 3.2 for the various low- and high-level b-tagging algorithms [65].

The b-tagging efficiency can differ in MC simulation and data. MC simulated events are then corrected with the scale factors derived as the ratio of the efficiency in data and in MC. The scale factors are derived on a per-jet basis in a parametric form based on the jet p_{T}, η and truth

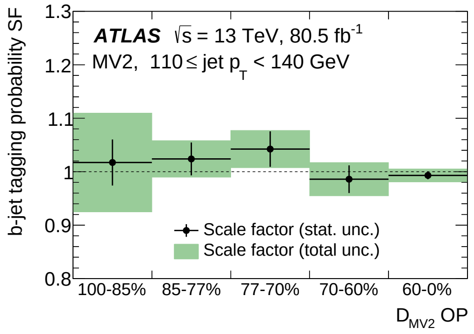

FIGURE 3.3: The b-jet tagging probability simulation-to-data scale factors for the MV2 tagger for jets with $110 \leq p_{\mathrm{T}} \leq 140$ GeV divided in efficiency bins [65]. Vertical error bars include data statistical uncertainties only while the green bands correspond to the sum in quadrature of statistical and systematic uncertainties.

flavour.
Systematic uncertainties on the b-tagging efficiencies are estimated by varying the η, p_{T} and flavour-dependent scale factors that corrects the tagging rate in simulation to match with the data, within a range that reflects the uncertainty in the measured tagging efficiency and mis-tag rates in data [66, 67]. Figure 3.3 shows the measurement of the uncertainties on the b-tagging probabilities for the output of the MV2 algorithm.

3.3 Electrons

Electrons are identified using information coming from the electromagnetic calorimeter and from the ID. At first, the corresponding tracks and electromagnetic clusters are reconstructed in an independent way, following the procedures described in Section 3.1 and 3.2 respectively. Then, variables (see Table 3.1) describing the shape of the electromagnetic shower, track-cluster matching, and the quality of the track are used to form a likelihood discriminator [68]. The selection on this discriminator is chosen in order to obtain a large background rejection and high and uniform efficiency over the full acceptance of the detector and it is therefore depending on η; this cut is also corrected depending on the number of primary vertices in the event.
Finally, three standard working point (loose, medium and tight) are chosen, corresponding to a reconstruction efficiency respectively of 95%, 90% and 80% for electrons with $E_{\mathrm{T}} \approx 40\,\mathrm{GeV}$. Figure 3.4 shows the efficiency of electrons reconstruction for the three different working points.

A calibration of the electrons energy is necessary in order to consider effects like energy losses in passive materials, EM shower leakages and fluctuations in the energy deposited in the calorimeters. The corrections of the electrons energy scale and resolution are evaluated using a number of well know SM processes as reference, such as $Z \to e^+e^-$ and $J/\psi \to e^+e^-$, which cover a wide range of values. The corrective parameters are evaluated from a fit over the invariant mass distributions of di-electron events, with the goal of obtaining the correct peak value for the resonances and at the same time, minimise the experimental width. The agreement between data and Monte Carlo simulations obtained after the calibration is illustrated in Figure 3.5.
Uncertainties on the energy calibration, as well as the ones on reconstruction and identification efficiency, are computed considering the error on the scale factors applied to match the MC simulations and the data.

Type	Description
Hadronic leakage	Ratio of E_{T} in hadronic calorimeter to E_{T} in the EM cluster
EM third layer	Ratio of the energy in the third layer to the total energy in the EM calorimeter
EM second layer	Lateral shower width Ratio of the energy in 3×3 cells over the energy in 3×7 cells centred at the electron cluster position Ratio of the energy in 3×7 cells over the energy in 7×7 cells centred at the electron cluster position
EM first layer	Lateral shower width Fraction of energy outside core of three central cells but within seven cells Difference between the energy of the cell associated with the second maximum, and the energy reconstructed in the cell with the smallest value found between the first and second maxima Ratio of the energy difference between the maximum energy deposit and the energy deposit in a secondary maximum in the cluster to the sum of these energies Ratio of the energy measured in the first layer of the electromagnetic calorimeter to the total energy of the EM cluster
Track quality	Number of hits in the IBL Number of hits in the Pixel Detector Total number of hits in the pixel and SCT detectors Transverse impact parameter relative to the beam-line Significance of transverse impact parameter Momentum lost by the track between the first and the last measured point divided by the original momentum Likelihood probability based on transition radiation in the TRT
Track-cluster matching	$\Delta\eta$ between the cluster position in the first layer and the extrapolated track $\Delta\phi$ between the cluster position in the second layer and the extrapolated track Ratio of the cluster energy to the track momentum

TABLE 3.1: Main variables used for the electron identification.

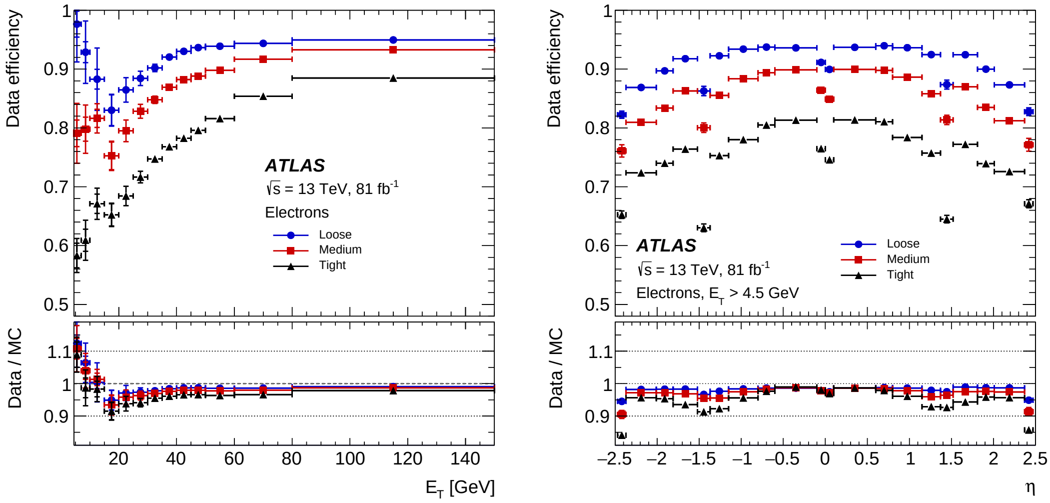

FIGURE 3.4: The electron identification efficiency measured in $Z \to e^+e^-$ events as a function of E_{T} (left) and η (right) for the Loose, Medium and Tight operating points [68]. For both plots, the bottom panel shows the data-to-simulation ratios.

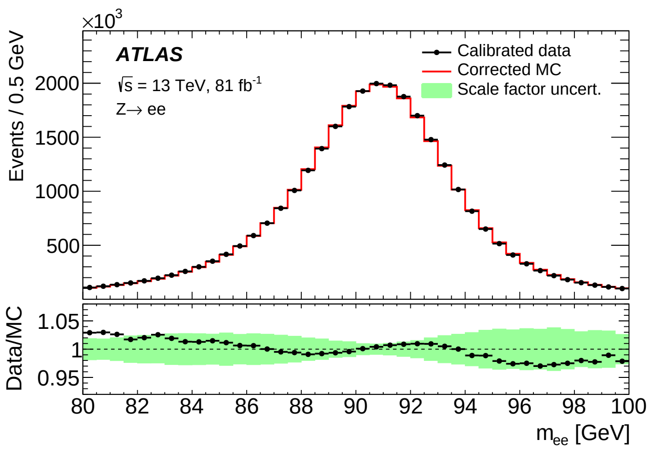

FIGURE 3.5: Comparison between data and simulation of the invariant mass distribution of the two electrons in selected $Z \to e^+e^-$ events, after the calibration and resolution corrections are applied [68]. The uncertainty band of the bottom plot represents the impact of the uncertainties in the calibration and resolution correction factors.

3.4 Muons

Muon identification [69] is based on the information provided by the Inner Detector, the Muon Spectrometer and, in minor part, from the calorimeters. Four different types are defined, depending on which sub-detectors are used in reconstruction:

- Combined muons (CB), identified by the matching of a MS track with an ID track. For muons of this type, the momentum is recalculated with a global fit using information from both sub-detectors.
- Segment-Tagged muons (ST), resulting from the combination of tracks in the ID with at least one partially reconstructed track in the MDT or CSC chambers.
- Calorimeter-Tagged muons (CT), originating from tracks in the ID matched to an energy deposit in the calorimeter compatible with a minimum ionising particle.
- Extrapolated muons (ME), for which the trajectory is reconstructed based only on the MS track and a loose requirement on compatibility with originating from the IP.

Then, following the same model used for electrons, different sets of requirements are defined in order to create four working points (Loose, Medium, Tight and High-p_{T}) with the aim to suppress fake tracks reconstructed from spurious hits, non-prompt muons originating from in-flight decays of charged hadrons and signals detected in the MS caused by jets not contained by the calorimeters.

- The Loose identification criteria are designed to maximise the reconstruction efficiency. All muon types are used, and the only cuts applied are to discard the η regions where the MS looses efficiency.
- Medium muons follow the default selection in ATLAS and are built in order to minimise the systematic uncertainties. Only CB and ME muons are used, in different $|\eta|$ regions, and a very loose selection is applied on the compatibility between ID and MS momentum measurements in order to suppress the contamination due to misidentified hadrons.
- Tight muons are selected to optimise the purity of the sample. Only CB tracks with a good quality of reconstruction and good compatibility between the momenta measurements are chosen.
- The High-p_{T} selection is defined to maximise the momentum resolution for muons over 100 GeV. CB muons passing the Medium selection and having at least three hits in three MS stations are selected.

The η dependence of the muons reconstruction efficiencies for the different working points is shown in Figure 3.6. The efficiency drastically decreases around $|\eta| \approx 0$ because of the presence of service cables that reduce the detector acceptance in the low ϕ region. The Loose selection allows the mitigation of these losses by filling the MS acceptance gap using the calorimeter and segment-tagged muons contributions.

The momentum scale and resolution for the muons are studied using reference processes such as $Z \to \mu^+\mu^-$ and $J/\psi \to \mu^+\mu^-$. These measurements allow for comparison on how the procedure

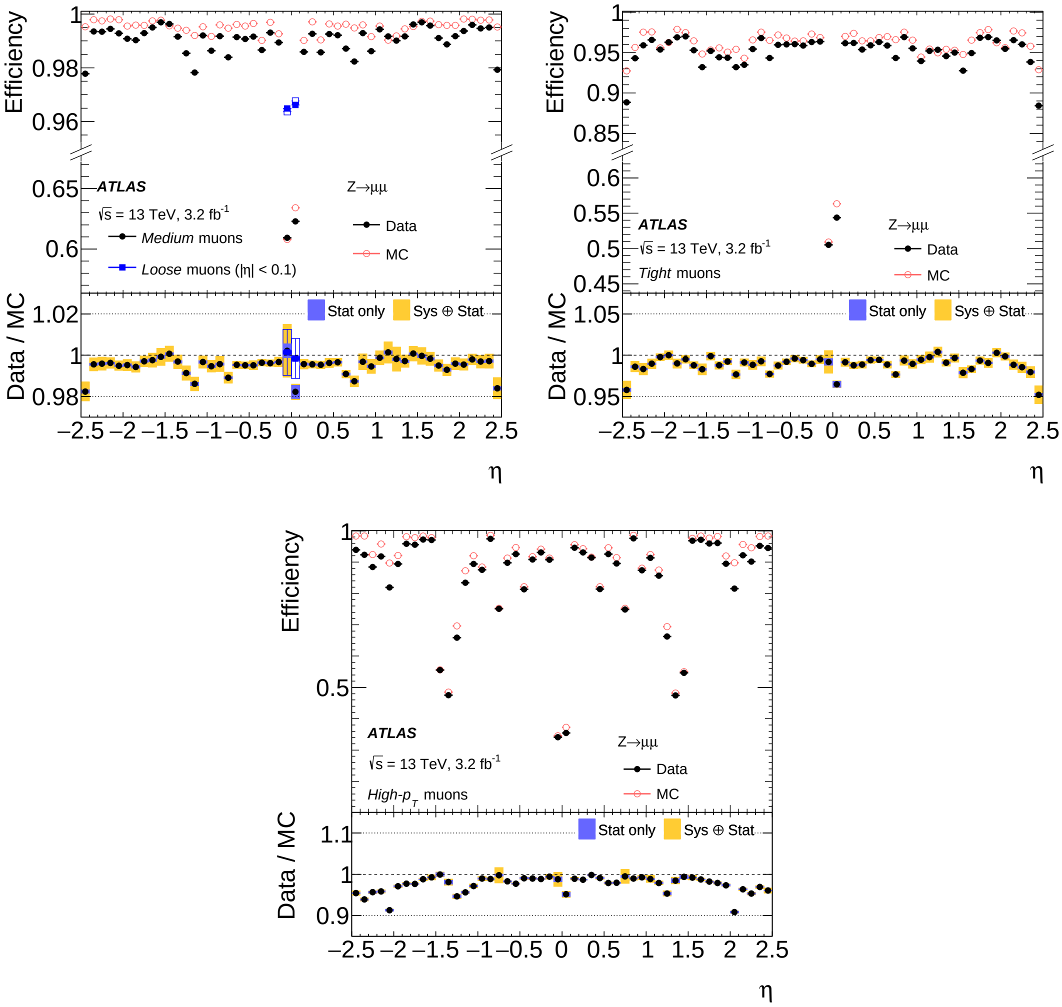

FIGURE 3.6: Muon reconstruction efficiencies for the four identification working points, measured in $Z \to \mu\mu$ events as a function of η [69].

behaves when applied to data and Monte Carlo samples, in order to derive the scale factors needed to correct the discrepancies arising from the energy losses in the detector materials and the possible distortions in the magnetic field, which aren't accurately described in the simulation. The invariant mass distributions for the $Z \to \mu^+\mu^-$ and $J/\psi \to \mu^+\mu^-$ candidates events are shown in Figure 3.7 and compared with uncorrected (dashed black line) and corrected (solid red line) MC simulation. The systematic uncertainty associated to the momentum resolution is obtained by varying the fit parameters for the ID and MS tracks. Uncertainties on the reconstruction efficiency are computed considering the error on the scale factors applied to match the MC simulations to the data [70].

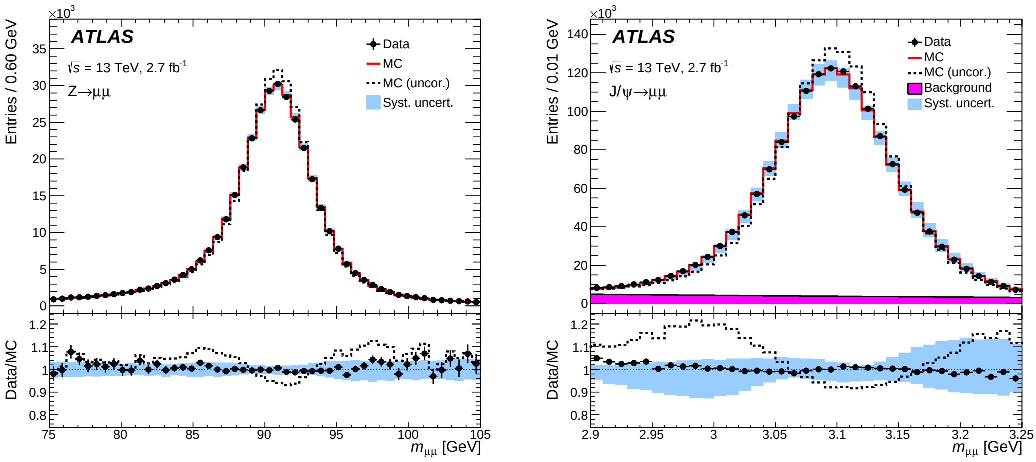

FIGURE 3.7: Dimuon invariant mass distribution of $Z \to \mu^+\mu^-$ (left) and $J/\psi \to \mu^+\mu^-$ (right) candidate events reconstructed with CB muons [69].

3.5 Lepton Isolation

Leptons originating from the prompt decay of heavy bosons must be discriminated from the ones deriving from the decay of quarks, from converted photons inside hadronic jets or from the ones which are misidentified hadrons. All of these are generated in proximity of a jet and are surrounded by high detector activity; on the contrary, prompt leptons tends to be well separated from other particles in the event. The measurement of the detector activity around a leptons candidate, referred to as isolation, is therefore a powerful tool for background rejection in many physics analyses. The presence of other particles near electrons and muons can be quantified from the tracks of nearby charged particles and from the energy deposits in the calorimeters, leading to two classes of isolation variables [68, 69].
The track-based isolation variable $p_{\mathrm{T}}^{\mathrm{varcone}R_{\mathrm{max}}}$ is defined as the sum of the transverse momenta of the tracks measured in a cone built around the track, excluding the momentum of lepton-track itself. The solid angle which define the cone dimensions depends on the lepton transverse momentum p_T^ℓ ($\min(10\,\mathrm{GeV}/p_T^\ell, R_{\mathrm{max}})$) to improve the efficiency for leptons coming from boosted particle decays. The tracks considered in the sum must originate from the primary vertex associated to the lepton track, have $p_{\mathrm{T}} > 1\,\mathrm{GeV}$ and $|\eta| < 2.5$, and at least seven hits in the two silicon sub-detectors.
The calorimeter-based isolation variable $E_T^{\mathrm{topo}R_{\mathrm{max}}}$ is computed by adding the energy of the topological clusters around the lepton deposit in a cone of radius $\Delta R = R_{\mathrm{max}}$. The energy deposit from the muons is removed by excluding clusters within $\Delta R < 0.1$, while for electrons the energy measured in the cells in the middle of the cluster (3 in the η direction and 5 along ϕ) is excluded. As an example, the distributions of the two variables for medium quality muons are shown in Figure 3.8. With the combination of the two it is possible to define several working points, either with fixed cuts or with adjustable cuts in order to obtain a specific efficiency of reconstruction. Table 3.2 show the existing working points with their characteristics.

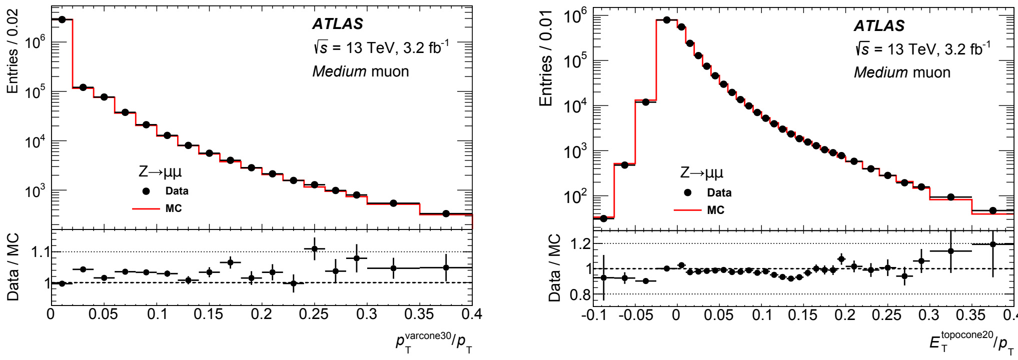

FIGURE 3.8: Distribution of the track-based (left) and calorimeter-based(right) isolation variables measured in $Z \to \mu^+\mu^-$ events [69].

Working point	Particle	Calorimeter isolation	Track isolation
FCLoose	e	$E_T^{\text{topo20}}/p_{\text{T}} < 0.15$	$p_{\text{T}}^{\text{varcone20}}/p_{\text{T}} < 0.2$
FCLoose	μ	$E_T^{\text{topo20}}/p_{\text{T}} < 0.15$	$p_{\text{T}}^{\text{varcone30}}/p_{\text{T}} < 0.3$
FCTight	e	$E_T^{\text{topo20}}/p_{\text{T}} < 0.06$	$p_{\text{T}}^{\text{varcone20}}/p_{\text{T}} < 0.06$
FCTight	μ	$E_T^{\text{topo20}}/p_{\text{T}} < 0.04$	$p_{\text{T}}^{\text{varcone30}}/p_{\text{T}} < 0.15$
FCTightTrackOnly	μ	-	$p_{\text{T}}^{\text{varcone30}}/p_{\text{T}} < 0.06$
Gradient	e	$E_T^{\text{topo20}} < 0.1143 \times p_{\text{T}} + 92.14\%$	$0.1143 \times p_{\text{T}} + 92.14\%$
FCHighPtTrackOnly	μ	-	$p_{\text{T}}^{\text{varcone20}} < 1.25$ GeV
FCHighPtCaloOnly	e	$E_T^{\text{topo20}} < \max(0.015 \times p_{\text{T}}, 3.5 \text{ GeV})$	-

TABLE 3.2: Table showing the available isolation working points.

3.6 Missing Transverse Momentum

Presuming the conservation of momentum, the transverse momentum recorded by the detector in each event should sum to zero. Any measured imbalance is known as missing transverse momentum ($E_{\text{T}}^{\text{miss}}$) [71] and may indicate the presence of weakly-interacting particles in the final state. In the SM, this quantity arises from neutrinos, but it may also come from particles predicted in theories beyond the SM, making the $E_{\text{T}}^{\text{miss}}$ a very important variable in searches for new physics.
The x and y components of the $E_{\text{T}}^{\text{miss}}$ are calculated as:

$$E_{x(y)}^{\text{miss}} = E_{x(y)}^{\text{miss},e} + E_{x(y)}^{\text{miss},\gamma} + E_{x(y)}^{\text{miss},\tau} + E_{x(y)}^{\text{miss,jets}} + E_{x(y)}^{\text{miss},\mu} + E_{x(y)}^{\text{miss,soft}} \quad (3.3)$$

where each term is given by the negative vectorial sum of the momenta of the respective particles. Then, the absolute value and the direction of the vector can be calculated:

$$E_T^{\text{miss}} = \sqrt{(E_x^{\text{miss}})^2 + (E_y^{\text{miss}})^2} \quad (3.4)$$

$$\phi^{\text{miss}} = \arctan\left(E_y^{\text{miss}}/E_x^{\text{miss}}\right) \quad (3.5)$$

The soft term in Equation 3.3 consists in all the energy deposits in detector not associated with any reconstructed particle or jet. These deposits can be in the form of be tracks in the Inner Detector (track-based soft term) or signals from the calorimeters (calorimeter-based soft term). Since tracks can be matched to the primary vertex, the track-based soft term is more robust in case of a high number of pile-up interactions, and it is chosen for the $E_{\text{T}}^{\text{miss}}$ calculation in Run 2.

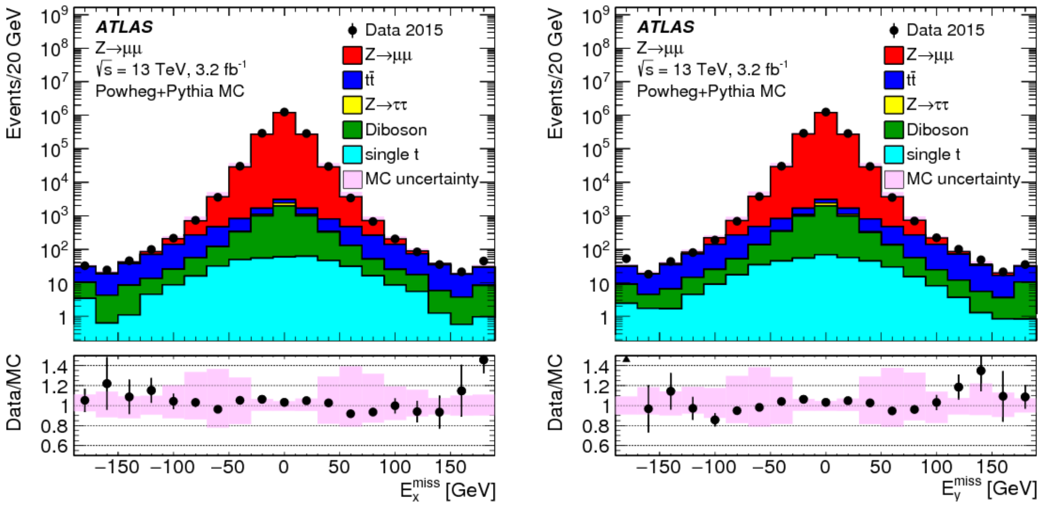

FIGURE 3.9: Distributions of $E_x^{\rm miss}$ (left) and $E_y^{\rm miss}$ (right) for an inclusive sample of $Z \to \mu^+\mu^-$ events extracted from data and compared to MC simulations [72].

The resolution of the $E_{\rm T}^{\rm miss}$ measurement can be evaluated using $Z \to \mu\mu$ events, where very little invisible contribution is expected. Figure 3.9 shows the distributions for x and the y components measured in such events: the value of the resolution is estimated from the root-mean square of the combined $E_x^{\rm miss}$ and $E_y^{\rm miss}$, parametrised as a function of the scalar sum of the energy recorded ($\Sigma E_{\rm T}$) and of the number of primary vertices.
The systematic effects arising from the energy scale and resolution of the soft term are computed from comparisons of data to MC simulated events [71]. The systematics arising from the reconstructed particles are calculated separately and consequently propagated to the $E_{\rm T}^{\rm miss}$ calculation.

Chapter 4

Supersymmetry searches

This Chapter presents the common strategy for the searches for SUSY particles presented in this thesis. Furthermore, the common tools and techniques used in the analyses will be discussed. A description of the dataset collected by ATLAS between 2015 and 2018, and the simulated events used to aid the background estimation and to model the SUSY signals is given, together with an illustration of all the steps toward the event selection optimisation, the background estimation, the evaluation of the systematic uncertainty and the statistical interpretation of the results. Details specific to only one analysis are described in the dedicated Chapters.

4.1 Dataset and Monte Carlo simulation

This Section describes the dataset collected by the ATLAS detector and the collection of simulated events analysed in the searches presented in this Thesis.

ATLAS dataset

The data analysed in this thesis were collected by the ATLAS detector during Run 2 of the LHC, between 2015 and 2018. The collision conditions vastly changed during this period, going from a peak instantaneous luminosity of $\mathcal{L} = 5.1 \times 10^{33}$ cm^{-2}s^{-1} in 2015, up to $\mathcal{L} = 2.1 \times 10^{34}$ cm^{-2}s^{-1} in 2018, resulting in a mean number of pp interactions per bunch crossing of $\langle \mu \rangle = 34$. Figure 4.1 shows the distribution of the mean number of interactions per crossing in the four years of the data taking, along with the total one.

Data quality requirements are applied to the recorded data, to ensure that all subdetectors were operating at nominal conditions and that the LHC beams were in stable-collision mode. The integrated luminosity resulting after this cleaning procedure is 36.1 fb^{-1}, with an uncertainty of 3.2%, for the 2015/2016 dataset (exploited in the analysis presented in Chapter 5) and 139 fb^{-1}, with an uncertainty of 1.7%, for the full Run 2 set. The evolution of the integrated luminosity during the years is presented in Figure 4.2. The uncertainty on the integrated luminosity was derived from the calibration of the luminosity scale using x-y beam-separation scans and using the LUCID-2 detector for the baseline luminosity measurements [74].

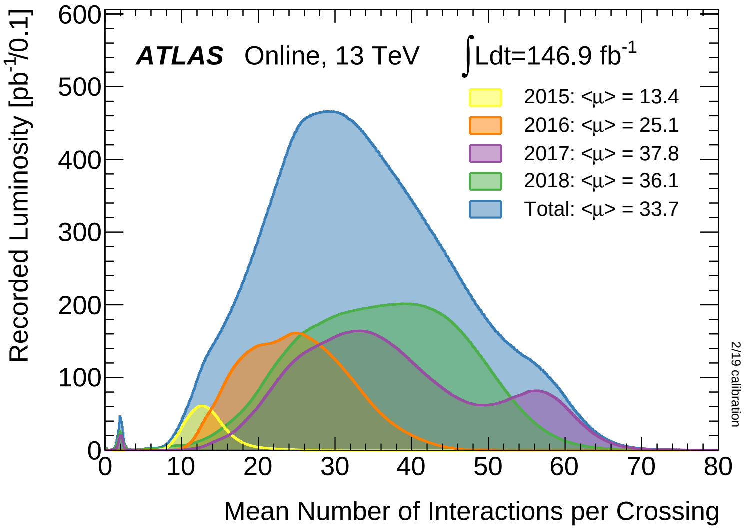

FIGURE 4.1: Distribution of the mean number of interactions per bunch crossing for the proton-proton collision data at 13 TeV centre-of-mass energy recorded by ATLAS during Run 2 [73].

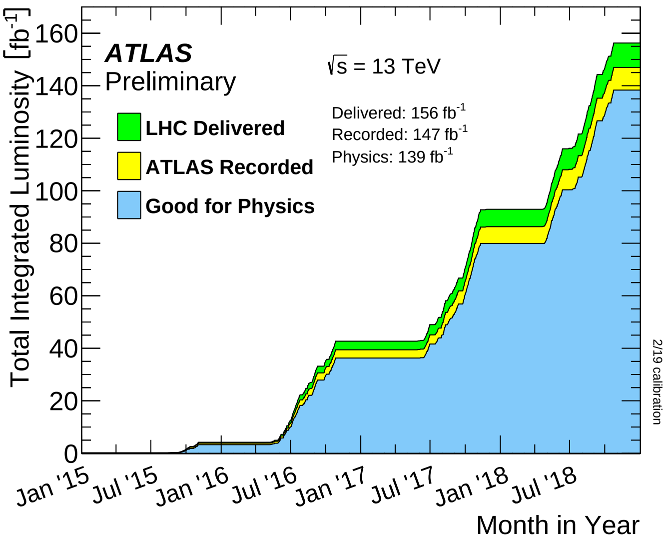

FIGURE 4.2: Cumulative luminosity versus time delivered by the LHC (green), recorded by ATLAS (yellow), and certified to be good quality data (blue) during stable beams for proton-proton collisions at 13 TeV centre-of-mass energy during the Run 2 [73].

Simulated samples

Simulated events, generated with the Monte Carlo (MC) technique, are used for the estimation of the background arising from SM processes and to model the SUSY signal. The goal of the simulations is to describe, as accurately as possible, the characteristics of the physics processes of interest and how they appear in the detector. The production of simulated events can be decomposed into the following steps:

- matrix element calculation, parton showering and hadronisation;

- addition of pile-up and underlying events;
- simulation of the particle interactions inside the detector;
- reconstruction.

The first part consists in the evaluation of the production cross section of the targeted physics process. This includes the choices of the parton distribution function (PDF), to extract from the protons the two partons participating to the hard scattering, the factorisation and the renormalisation scales. The parton showering instead, simulates soft and co-linear QCD emissions from the interacting partons produced in the hard scatter. In order to avoid the double counting between the extra jets obtained with the parton shower, and the ones arising from the matrix element calculation at higher QCD orders, a careful matching procedure is needed [75–77]. Finally, the hadronisation stage allows quarks and gluons obtained in this way, to form the observable hadronic jets.
The secondary interactions arising from other protons in the same bunch crossing (pile-up) are generated separately and then overlaid to each generated hard scatter event.
The last step of event generation consists in relating the set of generated particles to the response obtained by the detector; this is performed simulating the full ATLAS detector with Geant [78]. After this procedure, the simulated events have the same format of the real data and the same particle reconstruction can be applied to both.

4.2 Analysis strategy

The goal of this Section is to illustrate the general strategy for a search for SUSY particles. The techniques presented here are then applied in two searches for top squark, presented in the next chapters.

Event selection

In order to extract a potential new signal from the SM background, it is necessary to select events with kinematic properties that would enhance the sought for signal. In spite of the generally tiny cross section of the SUSY processes, this is achievable exploiting selections over particular kinematic discriminants, which show different distributions in the two cases. The area of the phase-space selected in this way is called Signal Region (SR). The choice of the optimal set of selections for the SR is obtained comparing the kinematic distributions of simulated events for the physics processes involved. Figure 4.3 shows, as an example, the difference in the $E_{\mathrm{T}}^{\mathrm{miss}}$ distribution for $t\bar{t}Z$ production (one of the main backgrounds in top squark searches with many leptons in the final state) and a signal model considering the $\tilde{t}_1$ decaying via $\tilde{t}_1 \to t + \tilde{\chi}_2^0$. The two distributions are normalised to unit area, in order to better show the difference in shape. In a realistic analysis, many kinematic variables are considered at the same time, and the discovery potential of the SR is tested for each possible set of cuts, using a statistical significance Z defined in Equation 4.1.

$$Z = \sqrt{2\left(n \ln\left(\frac{n(b+\sigma^2)}{b^2+n\sigma^2}\right) - \frac{b^2}{\sigma^2}\ln\left(1+\frac{\sigma^2(n-b)}{b(b+\sigma^2)}\right)\right)} \tag{4.1}$$

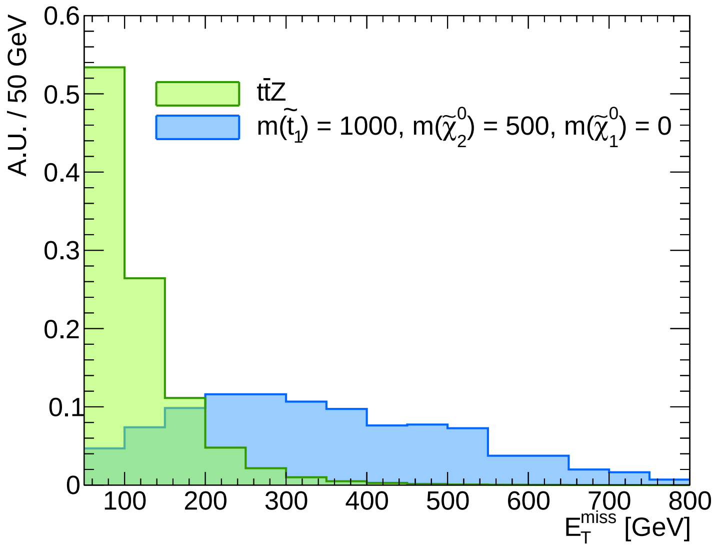

FIGURE 4.3: $E_{\mathrm{T}}^{\mathrm{miss}}$ distribution normalised to unit area for simulated $t\bar{t}Z$ (green) and $\tilde{t}_1$ pair production (light blue) events. The events are selected requiring at least three leptons in the final state.

Here, b is the number of expected background events, σ is the uncertainty on this number and n is corresponding to the sum of the expected background and signal events. Since a collection of signal samples with different parameters (usually the masses of the SUSY particles) is targeted in each analysis, the optimal SR may differ for different models considered. For this reason, SUSY searches usually include more than one SR, each one optimised over a class of models with similar kinematic features.

Background estimation

Once the SR is defined, it is necessary to estimate the SM backgrounds which populate such a region, with as much accuracy as possible. This goal can be achieved with different techniques:

- estimated the background the prediction using simulated MC events, normalised to their cross-section;
- exploiting simulated MC events, but constraining them with data, in kinematic regions close in term of phase space to the SR;
- with data-driven methods.

The first method is the most straightforward, however it often comes with higher systematics uncertainties and it is therefore reserved for the minor processes participating in the SR. The third one is mostly used for backgrounds that require a very large number of simulated events to obtain a prediction which doesn't suffer from statistical fluctuations, or which enter in the SR due to detector effects, which are harder to simulate. This is the case for the background events arising from non-prompt of mis-identified leptons, which will be comprehensively presented in Chapter 5. The second method, instead, is used for the backgrounds which present an identical signature in the detector with respect to the new physics signal (often called irreducible backgrounds) and is

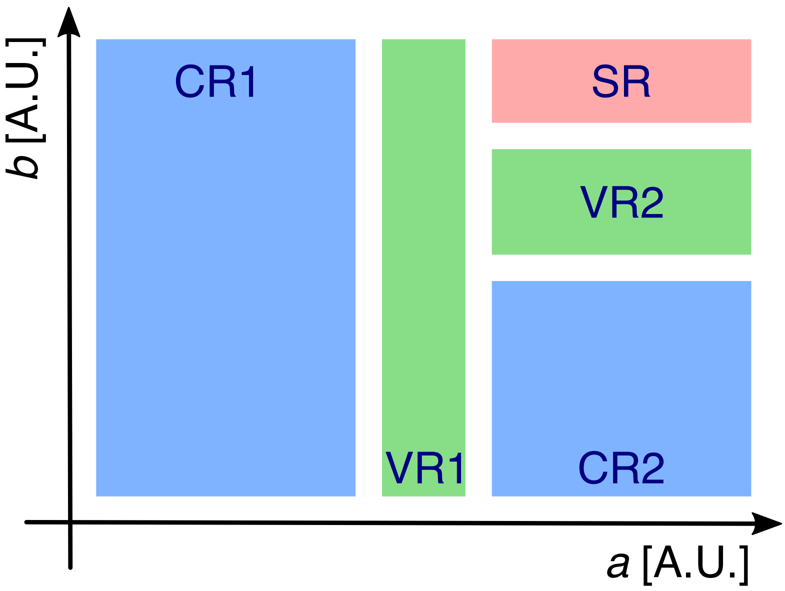

FIGURE 4.4: Scheme illustrating a simplified configuration for CRs, VRs and SR. All the regions here are made orthogonal using cuts on the two kinematic variables a and b.

the focus of this section.
The extreme phase space of the SRs, is can be very different from a kinematically point of view from the regions where the MC simulation have been tuned and validated. For this reason, the simulation might poorly model the data in the tails of the kinematic distributions and provide an inaccurate prediction. In order to improve the modelling and to reduce the related uncertainties, the MC simulated events of a specific process can be normalised to the data using a kinematic selection enriched with the SM process itself, called Control Region (CR). The normalisation factor obtained in this way is then propagated to the SR, for the final prediction. For the reasons explained before, the CR needs to be close to the SR in term of phase space. At the same time, it has to contain very low signal contamination, in order not to over-estimate the background prediction, hiding eventual new physics phenomena. Additionally, a high purity for the background process of interest is favoured, to avoid fluctuation of the normalisation factor.
Typically, multiple CRs are defined, each one targeting a specific background. In this case, a simultaneous fit is performed considering all the orthogonal CRs. The parameters of interest of the fit are the scale factors for each process, which are subsequently applied to all the regions of interest in the search. Finally, the background estimation is validated in additional regions of the phase space, called Validation Regions (VR). The VRs are defined in a similar fashion of the CRs, presenting similar kinematic cuts to the ones used for the SRs, while keeping a low signal contamination. The main difference is that the VRs don't take part in the background fit, instead are used to check the validity of the normalisation in an independent way.
An example of the design of control and validation regions is presented in Figure 4.4, where a simplified SR is defined through two arbitrary variables a and b, and the CRs and the VRs are placed orthogonally.

The Likelihood fit

The extraction of the normalisation factors is performed by maximising the probability that the observed data in the CRs and the SRs would agree with the given background model. To do so, a likelihood function is built as the product of the poissonian distributions of the event counts in the the regions and of additional gaussian distributions that implement the constraints on systematic uncertainties. It can be written as:

$$
\begin{aligned}
L\left(\boldsymbol{n}, \boldsymbol{\theta}^0 | \mu_{\text{sig}}, \mu_{\text{SF}}, \boldsymbol{b}, \boldsymbol{\theta}\right) &= P_{\text{SR}} \times P_{\text{CR}} \times C_{\text{syst}} = \\
&= P(n_{\text{SR}} | \lambda_{\text{SR}}(\mu_{\text{sig}}, \boldsymbol{b}, \boldsymbol{\theta})) \times \prod_{i \in \text{CR}} P(n_i | \lambda_i(\mu_{\text{sig}}, \mu_{\text{SF}}, \boldsymbol{b}, \boldsymbol{\theta})) \times C_{\text{syst}}(\boldsymbol{\theta}^0, \boldsymbol{\theta})
\end{aligned}
\quad (4.2)
$$

The first two terms (P_{SR} and P_{CR}) reflect the measurements of the number of observed events in the SR and in each CR i. The Poisson expectation valuses λ_{SR} and λ_i are functions depending on: the predictions b of the backgrounds, the nuisance parameters which model the systematic uncertainties ($\boldsymbol{\theta}$), the normalisation factors for background processes (μ_{SF}), and the signal strength parameter (μ_{sig}). μ_{sig} is fixed at 0, when testing the background-only hypothesis.
The third term takes into account the systematic uncertainties, which are included using the probability density function C_{syst}. For each independent nuisance parameter, C_{syst} is the product of the distributions corresponding to the auxiliary measurements describing the systematic uncertainties, where $\boldsymbol{\theta}^0$ are the mean values around which $\boldsymbol{\theta}$ can be varied.

4.3 Statistical interpretation of the results

Following the careful evaluation of the SM backgrounds, the number of the expected events in each SR is compared with the observed data. The distance between the observed data and the prediction is measured using a test statistic. The p-value is then the probability that the test statistic would have been at least as large as its observed value, given that the hypothesis H is correct:

$$
p\text{-value} = \int_{q_{\text{obs}}}^{+\infty} f(q|H)dq \quad (4.3)
$$

where f is the probability density function of the test statistic given the hypothesis H and q_{obs} is the value of the test statistic obtained with the observed data.
The hypothesis can be considered excluded if its observed p-value is below a specified threshold. In addition, the significance Z corresponding to a given p-value is defined as the number of standard deviations at which a normal distributed random variable, with mean of zero, would give a one-sided tail area equal to the p-value. In the particle physics community, the threshold for the rejection of the background hypothesis has been set at a significance of Z = 5, which corresponds to a p-value of 2.8×10^{-7}. For the exclusion of a new a signal hypothesis, a threshold p-value of 0.05, which corresponds to Z = 1.64, is instead used.
If we consider a situation where the background only hypothesis (H_0) and the alternative hypothesis (H_1) give similar a distribution of the test statistic (which may be the case for SUSY signals with very low cross-section), a down-fluctuation in data could result in the exclusion of the signal hypothesis, even if it is almost indistinguishable from the background only one. To

avoid this problem, the modified confidence level (CL_s) [79] is defined as:

$$CL_\mathrm{s} = \frac{p_\mu}{1-p_b} = \frac{\int_{q_\mathrm{obs}}^{+\infty} f(q|H_1)dq}{1-\int_0^{q_\mathrm{obs}} f(q|H_0)dq} \tag{4.4}$$

With this method, the situation described above will result in small numbers for not only the numerator but also the denominator, with a consequently higher CL_s to prevent the exclusion of the alternative hypothesis. Requiring for the CL_s to be less then 0.05 is the default procedure used in this thesis to reject the new signal model hypothesis.
The test statistic used for this procedure is the log-likelihood ratio, defined as:

$$q_{\mu_\mathrm{sig}} = -2\ln\left(\frac{L(\mu_\mathrm{sig},\bar{\boldsymbol{\theta}})}{L(\mu_\mathrm{sig},\boldsymbol{\theta})}\right) \tag{4.5}$$

where L is the likelihood function defined in Equation 4.2 and $\bar{\boldsymbol{\theta}}$ is the the set of values of the parameters which maximise the likelihood for the specific signal hypothesis.

Null hypothesis test and model independent limits

As a first step, the background-only hypothesis is tested, fixing $\mu_\mathrm{sig} = 0$, and a p-value is associated to each SR, representing the discrepancy between the observed number of events and the predicted background. By convention, if the significance of this p-value reaches the 5 sigma, a claim of discovery can be made. If this is not the case and there is no (or moderate) excess, the results are used to place upper limits on the presence of new physics in the phase-pace considered by the analysis. This is done by scanning the number of events that could enter the SR selection for a general new signal, with the goal to find the number which gives a CL_s of exactly 0.05. The upper limit calculated in this way, can also be scaled by the integrated luminosity, in order to express the result in terms of effective cross-section.

Model dependent limits

As a second step, the observation is compared with specific SUSY signal models. The alternative hypothesis is defined including all the SM backgrounds and the signal model under test (with signal strength $\mu_\mathrm{sig} = 1$) in all regions, in order to account for possible signal contamination in the CRs. A simultaneous fit is performed and the observed data in the CRs and SRs are used as constraints. This procedure is performed multiple times, for every signal scenario under consideration. If the models are defined scanning over two parameters, usually masses of the sparticles considered, a grid in the 2D phase space is defined. For each point of the grid (corresponding to one signal model) the CL_s is calculated, converted in significance, and the results are interpolated between models, in order to obtain an exclusion contour at 95% confidence level in the parameters phase space. Figure 4.5 illustrates this procedure.

Combination of multiple Signal Regions

When a specific SUSY model is tested, stronger limits can be obtained combining orthogonal SRs. This can be useful, for example, to target different signal scenarios at the same time, by

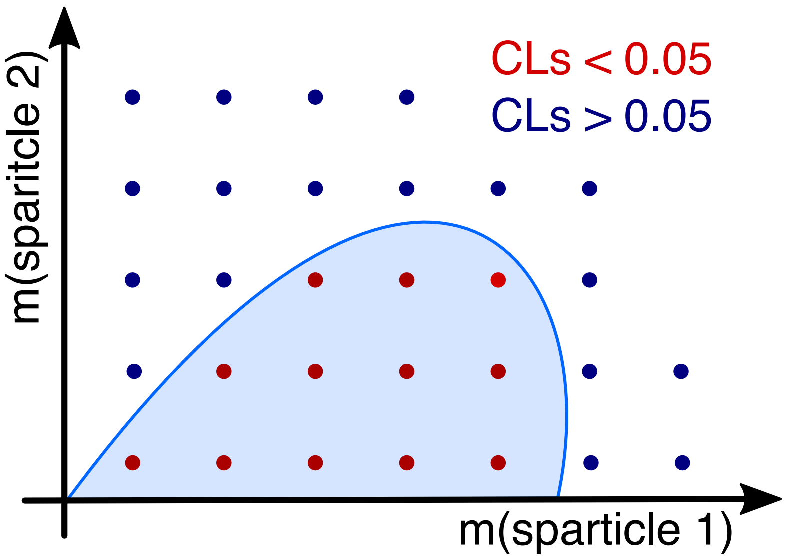

FIGURE 4.5: Sketch showing the 2D grid defined by the signal models considered for the statistical interpretation. The red dots represent the models with a $CL_s < 0.05$, which are therefore excluded. The light blue area marks the excluded slice of the phase space obtained with the interpolation of the significance for each signal point.

defining a dedicated region for each channel. Alternatively, it can be useful when signal and background present different shapes for a key kinematic variable. In this case the SRs can be by defined dividing the distribution in multiple bins, with the goal to provide more information to the likelihood, compared to the use of only the integrated signal region. This technique is called shape fit.
In both cases, the likelihood function presented in Equation 4.2 is modified to in order consider the additional SRs.

4.4 Systematics uncertainties

The effect of the systematic uncertainties is evaluated for all the signal and background processes. They are defined in order to cover for uncertainties related to the detector effects and theoretical modelling of the physics processes. The experimental and theoretical uncertainties are implemented in the MC simulated events as the variation of quantities, such as the reconstructed particles four-momenta or the cross section. Consequently, they are incorporated in the background fit as nuisance parameters, each of them described by a gaussian centred on zero and of width one. Zero corresponds to the nominal rate in all regions, while ± 1 correspond to the "up" and "down" systematic variations. Different nuisance parameters are treated as uncorrelated. Then, the final error on the fitted total background in the CRs and SRs properly takes into account the correlation matrix between the different errors.
The experimental uncertainties include all the effects relative to the reconstruction of particles and jet in the detector, such as the uncertainty on the energy scale and resolution, and the differences in term of reconstruction efficiencies obtained in data and MC simulated events. The evaluation of these uncertainties is specific to the particles considered and it was presented in Chapter 3.

Regarding the theoretical modelling of the MC simulations, the following uncertainties are considered:

- Generator choice: each step of the simulation chain can be performed using different softwares and this can result in not identical final predictions. In these cases a systematic uncertainty evaluated comparing the results obtained with different generator is applied.
- Factorisation and renormalisation scales: the computation of the production cross section for any physics process is performed with perturbation expansions and this implies that a choice over a factorisation and renormalisation scales has to be made. These scales are arbitrary and should not affect the all-order computation, but since the truncated approximation of the calculation is considered, some difference can be observed when varying such scales. These differences are taken as an uncertainty.
- Matrix element and parton shower matching: the extra jets arising from the matrix element computation and the ones from the parton shower need to be matched to avoid double counting of the radiation. Different matching procedures are available and the uncertainty cover for the differences observed;
- PDF choice: the PDFs are obtained by fitting experimental data. Several PDF sets are available, exploiting data from different experiments or employing different parametrisations in the fit. The modelling variations observed changing the PDF set is also considered as an uncertainty.
- Cross section: given that the cross-section computation is not an exact calculation, it also comes with its theoretical error. This uncertainty can however be totally absorbed when background processes are normalised in CRs.

Chapter 5

Search for top squarks in compressed scenarios

In this Chapter, a search for direct top squark pair production is presented, selecting events with two isolated leptons (electrons or muons) and missing transverse momentum. The search exploits 36.1 fb^{-1} of proton-proton collision data collected by the ATLAS experiment in 2015 and 2016, at a centre-of-mass energy $\sqrt{s} = 13$ TeV.
Depending on the mass splitting between the top squark and the lightest SUSY particle, different decay channels become dominant. In case of mass differences smaller then 80 GeV, the energy is not enough to produce neither an on-shell top quark or a W boson and the four body decay ($\tilde{t} \to bff'\tilde{\chi}_1^0$, where f and f' are two generic fermions) can be the most important one. The analysis presented in this Chapter is optimised to target such cases. The characteristic signature for these kind of signal models is the presence of low p_{T} fermions, arising from he virtual W boson decays, that in the case considered here will be respectively a charged leptons and a neutrino. Signal events can be distinguished from SM processes by requiring a high-p_{T} jet from initial state radiation (ISR), which leads to a sizable transverse boost of the sparticle system and enhances the $E_{\mathrm{T}}^{\mathrm{miss}}$.
Previous ATLAS searches [34] have set exclusion limits at 95% confidence level on the signal scenarios considered here, using the data collected during the first Run of the LHC, at a centre-of-mass energy of $\sqrt{s} = 8$ TeV. The analysis presented here exploits the higher center of mass energy and the improved reconstruction techniques for leptons with low momentum, to enhance the sensitivity for scenarios with higher $\tilde{t}_1$ masses.

5.1 Targeted models

The analysis is optimised and interpreted using simplified models, considering $\tilde{t}_1$ pair production, with the $\tilde{t}_1$ decaying into $bff'\tilde{\chi}_1^0$ with 100% branching ratio, as illustrated in the diagram in Figure 5.1. While the Figure shows the leptonic decay of the off-shell W boson, as an illustration of the targeted final state, the SM branching fraction of the W is considered for the event generation. The $\tilde{\chi}_1^0$ is considered the LSP and it is therefore stable. All the other SUSY particles are treated as decoupled and don't participate to the decay.

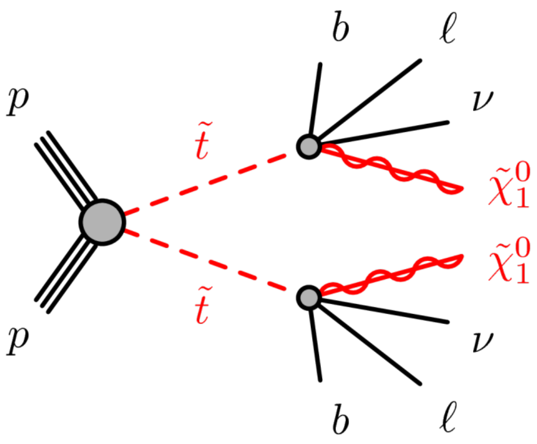

FIGURE 5.1: Diagram representing the four-body decay of the $\tilde{t}$ to a b-quark, a charge lepton ℓ, a neutrino and the $\tilde{\chi}_1^0$ (LSP).

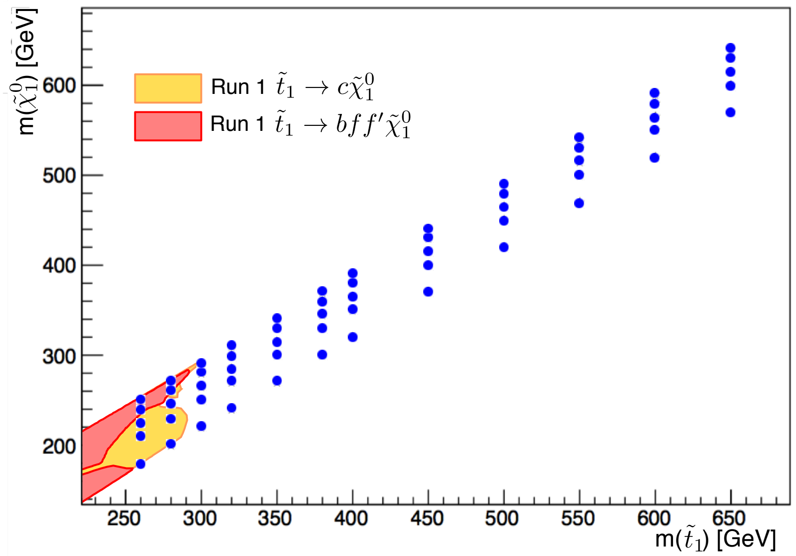

FIGURE 5.2: Schematic view of the generated signal models, as a function of the $\tilde{t}_1$ and $\tilde{\chi}_1^0$ masses. The shaded regions represent the exclusion obtained by previous ATLAS searches [80, 81].

A set of signal models has been generated in the area of the phase space where the four body decay of the $\tilde{t}_1$ is dominant, considering different values of $m(\tilde{t}_1)$, ranging from 260 to 650 GeV, with the $\Delta m(\tilde{t}_1, \tilde{\chi}_1^0)$ set to 80, 50, 35, 20 and 10 GeV. A representation of the signal models considered is presented in Figure 5.2, together with the limits placed by the ATLAS searches with Run 1 data [80, 81]. The red area shows the region excluded at 95% confidence level when interpreting the analysis with simplified models defined in the same way as the one used in this thesis. The orange area instead, is obtained considering the competitive decay of the $\tilde{t}_1$ into $c\tilde{\chi}_1^0$, with a 100% branching fraction.

5.2 Leptons and jets selection

The selection criteria for jets, electrons and muons used specifically in this analysis are provided in this section. More details on how such quantities are reconstructed in ATLAS are discussed in Chapter 3.

Electron candidates are required to have their pseudorapidity $|\eta| < 2.47$, $p_{\mathrm{T}} > 7\,\mathrm{GeV}$, and to pass the Loose likelihood-based identification requirement [82]. The likelihood input variables include measurements of calorimeter shower shapes and of track properties from the ID. In order to pass the signal selection, electrons are further required to pass the GradientLoose [83] isolation criteria and the following cuts on the impact parameters: $|d_0/\sigma(d_0)| < 5$ and $|z_0 \cdot \sin(\theta)| < 0.5$.

Muon candidates are selected in the pseudorapidity region $|\eta| < 2.4$, must have $p_{\mathrm{T}} > 7\,\mathrm{GeV}$ and to pass the Medium identification, based on requirements on the number of hits in the different ID and muon spectrometer subsystems, and on the significance of the charge to momentum ratio (q/p) measurement [70]. Signal muons have the further requirement to pass the GradientLoose [83] isolation criteria and to respect the following impact parameter prescription: $|d_0/\sigma(d_0)| < 5$ and $|z_0 \cdot \sin(\theta)| < 0.5$.

Jets are reconstructed from energy clusters in the calorimeter [84] with the anti-k_t jet clustering algorithm [57] with a radius parameter $R = 0.4$. Only jet candidates with $p_{\mathrm{T}} > 20\,\mathrm{GeV}$ and $|\eta| < 2.8$ are considered. Additional selections are applied on jets with $p_{\mathrm{T}} < 60\,\mathrm{GeV}$ and $|\eta| < 2.4$ in order to reject jets produced in pileup collisions: a significant fraction of the tracks associated with each jet is required to have an origin compatible with the primary vertex, by asking the JVT discriminant [61] to be less then 0.59. Events are discarded if they contain any jet with $p_{\mathrm{T}} > 20\,\mathrm{GeV}$ failing basic quality selection criteria that reject detector noise and non-collision backgrounds [85].

Jets resulting from the hadronisation of b-quarks are identified using the MV2c10 b-tagging algorithm. This algorithm is used at a working point that provides 77% b-tagging efficiency in simulated $t\bar{t}$ events, and a rejection factor of 134 for light-quark flavours and gluons and 6 for charm initiated jets.

Leptons and jets can have similar signature in the detector, and in case of ambiguities the same mark in the detector can be reconstructed as both categories. In order to avoid this problem and to assign each signature to the correct particle, an algorithm for the removal of the ambiguities is applied on candidate leptons and jets.

- Non-b-tagged jets which are at $\Delta R = \sqrt{\Delta y^2 + \Delta\phi^2} < 0.2$ (here y stands for the rapidity) from an electron candidate are removed;
- Removal occours also for jets which lie close to a muon candidate and are consistent with the characteristics of jets produced by muon bremmstrahlung;
- Any lepton candidate within $\Delta R < 0.4$ from the direction of a surviving jet candidate is removed, in order to reject leptons from the decay of a b or c hadron;
- Electrons which share an ID track with a muon candidate are also removed.

5.3 Event selection

Events are required to have exactly two signal leptons (electrons or muons) which must be of opposite charge, with an invariant mass $m_{\ell\ell}$ greater than 10 GeV, in order to remove leptons

	SR
Leptons	2, opposite charge
$E_{\mathrm{T}}^{\mathrm{miss}}$ [GeV]	> 200
$p_{\mathrm{T}}(\ell_1)$ [GeV]	$7 - 80$
$p_{\mathrm{T}}(\ell_2)$ [GeV]	$7 - 35$
$m_{\ell\ell}$ [GeV]	> 10
n_{jets}	≥ 2
$p_{\mathrm{T}}(j_1)$ [GeV]	> 150
$p_{\mathrm{T}}(j_3)/E_{\mathrm{T}}^{\mathrm{miss}}$	< 0.14
$R_{2\ell 4j}$	> 0.35
$R_{2\ell}$	> 12
$n_{b-\mathrm{jets}}$	veto on j_1 and j_2

TABLE 5.1: Signal region definition.

from low mass resonances. Furthermore, upper limits on $p_{\mathrm{T}}(\ell_1)$ and $p_{\mathrm{T}}(\ell_2)$, respectively of 80 GeV and 35 GeV, are applied.

Those events are selected using an $E_{\mathrm{T}}^{\mathrm{miss}}$-based trigger and presents an additional offline cut at $E_{\mathrm{T}}^{\mathrm{miss}} > 200$ GeV, to ensure constant efficiency. Using this trigger strategy, allows to lower the p_{T} threshold of the leptons down to 7 GeV, increasing the acceptance for the signal models considered. Using dileptonic triggers, instead, would have meant requiring both leptons with $p_{\mathrm{T}} > 20$ GeV, strongly affecting the final sensitivity.

The momentum imbalance in signal events is actually moderate, since the two $\tilde{\chi}_1^0$ can be produced back-to-back, cancelling each other's contributions. The $E_{\mathrm{T}}^{\mathrm{miss}}$ can then be enhanced by requiring the presence of a high-p_{T} jet from initial state radiation (ISR) recoiling against the sparticle pair system. This further helps to discriminate against SM events.

The leading jet is then considered to be the ISR jet and required to have $p_{\mathrm{T}} > 150$ GeV. Since the jets resulting from $\tilde{t}$ decays tend to have low p_{T} in this scenario, at most one more energetic jet is permitted in the event and the transverse momentum of the third jet (if present) must satisfy $p_{\mathrm{T}}(j_3)/E_{\mathrm{T}}^{\mathrm{miss}} < 0.14$. Furthermore, the two most energetic jets in the event must not be identified as b-jets.

Finally, the missing transverse momentum and the p_{T} of the leading leptons and jets are used to define two useful ratio variables :

$$R_{2\ell} = E_{\mathrm{T}}^{\mathrm{miss}}/(p_{\mathrm{T}}(\ell_1) + p_{\mathrm{T}}(\ell_2)), \tag{5.1}$$

$$R_{2\ell 4j} = E_{\mathrm{T}}^{\mathrm{miss}}/(E_{\mathrm{T}}^{\mathrm{miss}} + p_{\mathrm{T}}(\ell_1) + p_{\mathrm{T}}(\ell_2) + \sum_{i=1,\ldots,N\leq 4} p_{\mathrm{T}}(j_i)), \tag{5.2}$$

where $p_{\mathrm{T}}(\ell_1)$ and $p_{\mathrm{T}}(\ell_2)$ are the leading and subleading lepton transverse momenta respectively and $p_{\mathrm{T}}(j_{i=1,\ldots,N\leq 4})$ are the transverse momenta in decreasing order of up to the four leading jets. A summary of all the cuts applied to define the SR can be found in Table 5.1, while the expected background yields are shown in Table 5.2. The dominant contribution is arising from events with fake or non-prompt leptons, followed by $t\bar{t}$ and diboson (VV) production.

	SR
Expected SM events	29 ± 6
$Z_{\tau\tau}$ events	1.0 ± 0.5
VV events	6 ± 1
$t\bar{t}$ events	8 ± 3
$t\bar{t}Z$ events	0.03 ± 0.01
Wt events	1.1 ± 0.3
Z_{ee}, $Z_{\mu\mu}$ events	0.21 ± 0.09
FNP	13 ± 5
Others	0.8 ± 0.3
$m(\tilde{t}_1, \tilde{\chi}_1^0) = (350, 300)$ GeV	23 ± 2

TABLE 5.2: Expected SM yields in the signal region for an integrated luminosity of 36.1 fb^{-1}.

5.4 Standard Model background estimation

The irreducible SM backgrounds satisfying the SR requirements illustrated above are all the processes with two leptons in the final states, mostly $t\bar{t}$, diboson production and the Z boson decaying into $\tau\tau$ with both τ leptons decaying leptonically. These backgrounds are estimated via MC, with the aid of three CRs to constrain the simulation in data. A simultaneous "background" fit is performed to the number of events found in the three CRs, as described in Section 4. In the fit, the normalisations of $t\bar{t}$, diboson and $Z \to \tau\tau$ are allowed to float, while the other backgrounds are determined directly using simulation or from additional independent studies in data. The agreement of the background prediction with data is compared in three additional VRs, which are not used to constrain the background normalisation or nuisance parameters in the fit and are defined to be enriched with the background of interest. The background due to fake and non-prompt leptons, collectively referred to as "FNP", mostly consisting of semi-leptonic $t\bar{t}$ and W+jets events, requires a dedicated data-driven estimation, described in Section 5.5.

Irreducible backgrounds

Dedicated control regions are defined the for the largest SM background contributions with two prompt leptons in the final state: $t\bar{t}$, diboson, and $Z \to \tau\tau$ events. The selections criteria of the three regions ($\mathrm{CR}_{t\bar{t}}^{4-\mathrm{body}}$, $\mathrm{CR}_{VV}^{4-\mathrm{body}}$ and $\mathrm{CR}_{Z\tau\tau}^{4-\mathrm{body}}$) are described in Table 5.3.
The CRs for diboson and $Z \to \tau\tau$ production are made orthogonal to the SR by requiring the presence of exactly one jet. This jet is requested to have $p_{\mathrm{T}} > 150$ GeV to keep a similar topology with the ISR. The two regions are then made mutually exclusive by applying opposite cuts to the invariant mass of the two leptons. On the other end, the $t\bar{t}$ CR keeps the same jet multiplicity requirements of the SR, but lowers the p_{T} range of its leading jet putting an upper threshold at 150 GeV.

The background prediction is then tested in three validation regions that are defined to be kinematically similar, but disjoint, to both the CRs and the SR. This is achieved varing the cuts on $R_{2\ell 4j}$ and $R_{2\ell}$, as shown in Table 5.4.

	$\mathrm{CR}_{t\bar{t}}^{4-\mathrm{body}}$	$\mathrm{CR}_{VV}^{4-\mathrm{body}}$	$\mathrm{CR}_{Z\tau\tau}^{4-\mathrm{body}}$
$E_{\mathrm{T}}^{\mathrm{miss}}$ [GeV]	> 200	> 200	> 200
Leading lepton p_{T} [GeV]	(7,80)	(7,80)	> 20
Sub-leading lepton p_{T} [GeV]	(7,35)	(7,35)	> 20
n_{jets}	≥ 2	$= 1$	$= 1$
Leading jet p_{T} [GeV]	(100,150)	> 150	> 150
$m_{\ell\ell}$ [GeV]	> 10	> 45	(10,45)
$R_{2\ell}$	-	< 54	-
$n_{b-\mathrm{jets}}$	-	$= 0$	$= 0$

TABLE 5.3: Definition of the three CRs for the irreducible backgrounds normalisation.

	$\mathrm{VR}_{t\bar{t}}^{4-\mathrm{body}}$	$\mathrm{VR}_{VV}^{4-\mathrm{body}}$	$\mathrm{VR}_{Z\tau\tau}^{4-\mathrm{body}}$
$E_{\mathrm{T}}^{\mathrm{miss}}$ [GeV]	> 200	> 200	> 200
Leading lepton p_{T} [GeV]	(7,80)	(7,80)	> 50
Sub-leading lepton p_{T} [GeV]	(7,35)	(7,35)	(7,20)
n_{jets}	≥ 2	$= 1$	$= 1$
Leading jet p_{T} [GeV]	> 150	> 150	> 150
$m_{\ell\ell}$ [GeV]	> 10	> 45	(10,45)
$R_{2\ell 4j}$	< 0.35	-	-
$R_{2\ell}$	< 12	> 5	-
$n_{b-\mathrm{jets}}$	-	$= 0$	$= 0$

TABLE 5.4: Validation regions definition for the main irreducible backgrounds.

Normalisation Factor	value
$\mu_{t\bar{t}}$	1.03 $\pm$ 0.32
μ_{VV}	0.79 $\pm$0.46
$\mu_{Z_{\tau\tau}}$	1.07 $\pm$ 0.38

TABLE 5.5: Normalisation factors for $t\bar{t}$, dibosons and $Z_{\tau\tau}$ background processes.

Table 5.6 shows the expected and observed number of events in each of the control regions after the background fit, while the normalisation factors obtained for the three normalised background processes are presented in Table 5.5.

Excellent agreement between data and the SM predictions is observed in the validation regions, as shown in Table 5.7. Figures 5.3 and 5.4 show a selected number of distributions in the control and validation regions for this analysis after applying the normalisation factors provided by the background fit.

	$\mathrm{CR}_{t\bar{t}}^{4-\mathrm{body}}$	$\mathrm{CR}_{VV}^{4-\mathrm{body}}$	$\mathrm{CR}_{Z\tau\tau}^{4-\mathrm{body}}$
Observed events	1251	110	106
Total SM events	1251 ± 35	110 ± 10	106 ± 10
Fit output, $t\bar{t}$	960 ± 50	47 ± 20	10 ± 6
Fit output, VV	37 ± 22	40 ± 22	18 ± 11
Fit output, $Z_{\tau\tau}$	22 ± 8	$0.00^{+0.17}_{-0.00}$	54 ± 16
$t\bar{t}Z$	5.6 ± 0.8	0.08 ± 0.01	0.05 ± 0.02
Wt	62 ± 19	9.0 ± 2.7	2.7 ± 2.4
Z_{ee}, $Z_{\mu\mu}$	0.7 ± 0.5	$0.2^{+0.4}_{-0.2}$	1.6 ± 0.6
FNP	154 ± 14	13.1 ± 2.0	16 ± 7
Others	11.2 ± 1.6	0.51 ± 0.12	3.2 ± 0.6
Fit input, $t\bar{t}$	931	46	10
Fit input, VV	47	51	23
Fit input, $Z_{\tau\tau}$	20	0	51

TABLE 5.6: Background fit results in the three CRs. The nominal expectations from MC simulation are given for comparison for those backgrounds ($t\bar{t}$, diboson and $Z_{\tau\tau}$) that are normalised to data. Events with fake or non-prompt leptons are estimated with the data-driven technique described in Section 5.5.

	$\mathrm{VR}_{t\bar{t}}^{4-\mathrm{body}}$	$\mathrm{VR}_{VV}^{4-\mathrm{body}}$	$\mathrm{VR}_{Z\tau\tau}^{4-\mathrm{body}}$
Observed events	2698	21	43
Total SM events	2900 ± 500	24 ± 5	57 ± 8
Fit output, $t\bar{t}$	2300 ± 500	5.2 ± 2.7	5.3 ± 2.8
Fit output, VV	80 ± 40	8 ± 5	9 ± 5
Fit output, $Z_{\tau\tau}$	89 ± 33	$0.00^{+0.04}_{-0.00}$	25 ± 9
$t\bar{t}Z$	14.2 ± 0.8	0.01 ± 0.01	0.01 ± 0.01
Wt	150 ± 60	1.4 ± 0.7	1.7 ± 0.4
Z_{ee}, $Z_{\mu\mu}$	8.6 ± 3.0	0.08 ± 0.02	0.62 ± 0.34
FNP	260 ± 40	9.6 ± 1.1	14 ± 4
Others	30.6 ± 2.3	0.01 ± 0.01	1.09 ± 0.22
Fit input, $t\bar{t}$	2200	5	5.1
Fit input, VV	99	10.1	11.9
Fit input, $Z_{\tau\tau}$	83	0.00	23

TABLE 5.7: Background fit results in the three VRs. The nominal expectations from MC simulation are given for comparison for those backgrounds ($t\bar{t}$, diboson and $Z_{\tau\tau}$) that are normalised to data. Events with fake or non-prompt leptons are estimated with the data-driven technique described in Section 5.5.

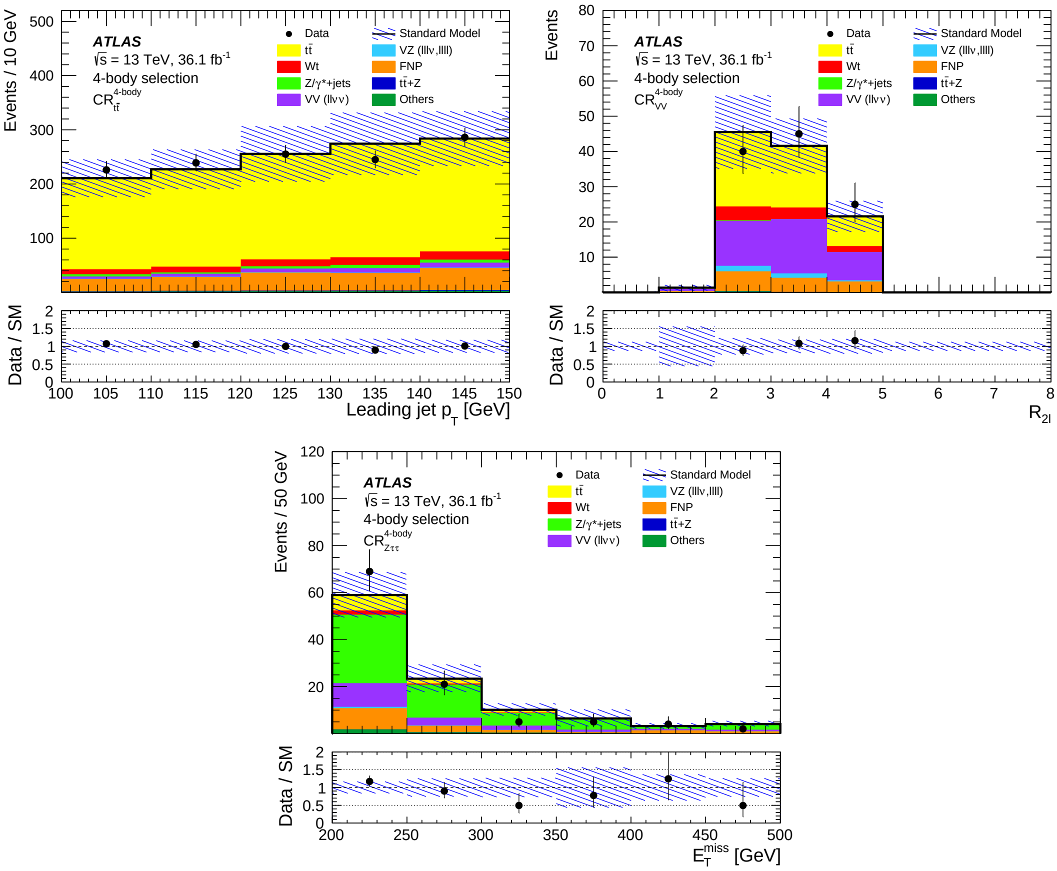

FIGURE 5.3: Distributions of the $p_{\mathrm{T}}(j_1)$ in $\mathrm{CR}_{t\bar{t}}^{4-\mathrm{body}}$, $R_{2\ell}$ in $\mathrm{CR}_{VV}^{4-\mathrm{body}}$ and $E_{\mathrm{T}}^{\mathrm{miss}}$ in $\mathrm{CR}_{Z\tau\tau}^{4-\mathrm{body}}$ after the background fit.

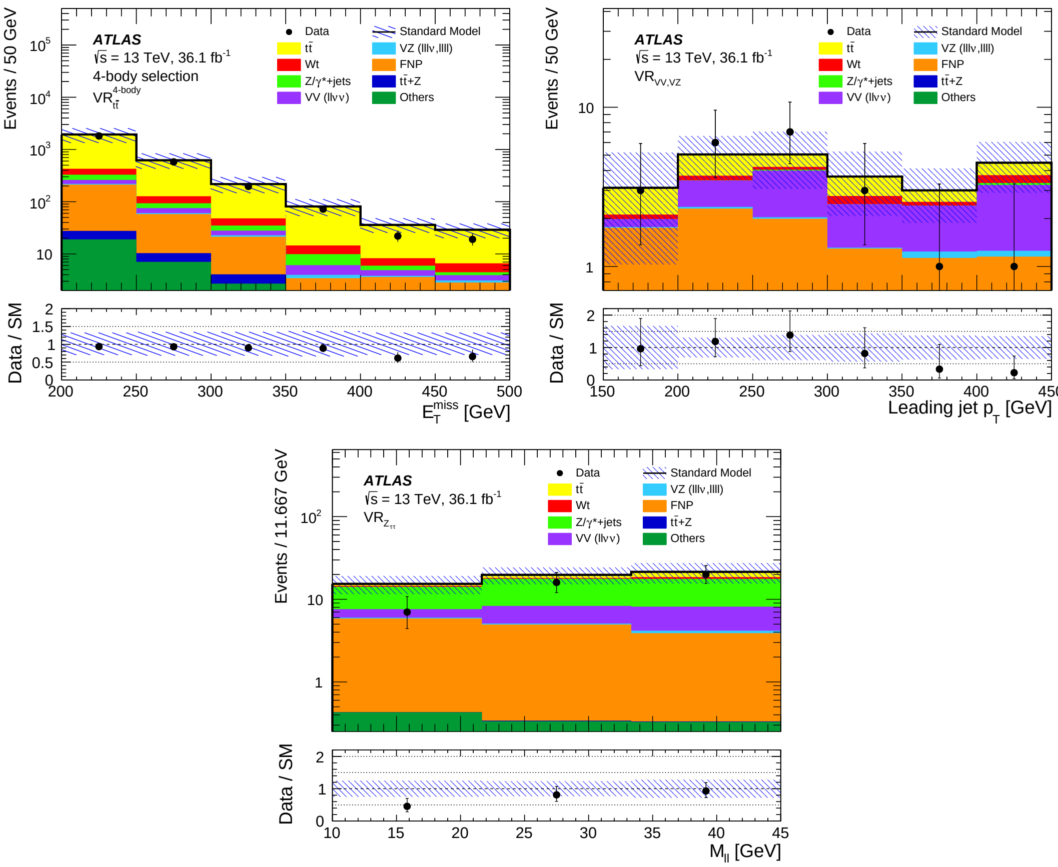

FIGURE 5.4: Distributions of the $E_{\mathrm{T}}^{\mathrm{miss}}$ in $\mathrm{VR}_{t\bar{t}}^{4-\mathrm{body}}$, of the leading jet p_{T} in $\mathrm{VR}_{VV}^{4-\mathrm{body}}$ and of the invariant mass of the two leptons in $\mathrm{VR}_{Z\tau\tau}^{4-\mathrm{body}}$, after the background fit.

5.5 Estimation of the background from non-prompt or misidentified leptons

The subject of this section is the study of a data driven technique to estimate the background arising from events with one or more non-prompt or misidentified leptons (often referred as fake leptons). These events comes from SM processes which should not enter the analyses selection, because they present fewer prompt leptons in the final state. However, due to errors in the identification of the reconstructed particles, the lepton multiplicity can be artificially increased and those processes can contaminate the analysis regions of interest. This background is particularly dominant in analyses selecting leptons with low momenta and it requires therefore a dedicated estimation.
Fake and non-prompt leptons (FNP) mainly arise from three sources:

- when a hadron inside a jet decays into a lepton;
- when a lepton is reconstructed from the conversion of a photon;
- if a hadron inside a jets is wrongly associated to a lepton by the reconstruction algorithms.

Most of these processes strongly depend on the showering development of the jets and can't be well modelled by Monte-Carlo simulations, as non perturbative QCD is involved. Furthermore, since the probability to obtain a FNP lepton is quite low, a unsustainable large number of events needs to be generated and reconstructed in order to obtain a sufficient amount of statistics in the extreme corner of the phase space targeted by the searches. Achieving an accurate simulation of this kind of events requires therefore a large computational power. For all these reasons, it becomes necessary to develop a method to estimate the FNP leptons background which relies on data as much as possible.
The Matrix Method allows to predict the rate of events with FNP leptons using the probability of identification for both real and FNP leptons, measured from data in dedicated control regions. In this Section the description of the method is presented, as well as the calculation of needed inputs. For sake of simplicity, all the examples illustrated here are relative to the search with two leptons presented in this Chapter, but can be easily extended to other signatures.

The Matrix Method

The aim of this method is to build a matrix which relates the number of leptons selected in a generic kinematic region with the number of fake or not prompt leptons which have wrongly passed the selection.
First of all, two different identification selections of leptons are defined. The *tight* selection matches the main analysis selection, while the *loose* one has some relaxed constrain and includes therefore more candidates. In particular, electrons are asked to pass looser identification criteria and no isolation is asked for both electrons and muons. This selection criteria corresponds to the ones used for the definition of baseline leptons candidates
In case of a selection with two *loose* leptons, all the events can be divided in four categories (*loose-loose*, *loose-tight*, *tight-loose* and *tight-tight*), with respect to the number of leptons which also pass the *tight* selection. In parallel, the same events can be categorised regarding the true nature of the leptons: *real-real* events containing two prompt leptons, *real-fake* and *fake-real*

events with one real and one FNP lepton and finally *fake-fake* events in which both leptons are wrongly identified.
The number of events in each category can be connected by the equation:

$$\begin{pmatrix} N_{TT} \\ N_{TL} \\ N_{LT} \\ N_{LL} \end{pmatrix} = M \begin{pmatrix} N^{RR} \\ N^{RF} \\ N^{FR} \\ N^{FF} \end{pmatrix} \tag{5.3}$$

with:

$$M = \begin{pmatrix} r_1 r_2 & r_1 f_2 & f_1 r_2 & f_1 f_2 \\ r_1(1-r_2) & r_1(1-f_2) & f_1(1-r_2) & f_1(1-f_2) \\ (1-r_1)r_2 & (1-r_1)f_2 & (1-f_1)r_2 & (1-f_1)f_2 \\ (1-r_1)(1-r_2) & (1-r_1)(1-f_2) & (1-f_1)(1-r_2) & (1-f_1)(1-f_2) \end{pmatrix} \tag{5.4}$$

In the matrix M, r_i is the probability for a real lepton which pass the *loose* selection to pass also the *tight* one, while f_i is the same probability for a FNP lepton, as shown in the equation:

$$\begin{cases} r_i = \frac{\text{\# of real tight leptons}}{\text{\# of real loose leptons}} \\ f_i = \frac{\text{\# of FNP tight leptons}}{\text{\# of FNP loose leptons}} \end{cases} \tag{5.5}$$

The index $i = 1, 2$ refers to the two p_{T}-ordered leptons selected in the event. In the general case, for events with n leptons, the matrix dimension is extended to 2^n, to acomodate for all the possible combinations. The fake rates f_i and the real efficiencies r_i are calculated in dedicated control regions, selected in order to obtain samples enriched with fake or real leptons respectively. When the matrix is constructed to parametrise the *loose*-to-*tight* probabilities for a generic single event, the components of the vector in right term of Equation 5.3 can be interpreted as the probability of the single event to belong to each of the four categories and they are denoted as p_{rr}, p_{rf}, p_{fr} and p_{ff}. Those probabilities can be obtained by inverting the system of equations. In the two lepton channel, we are interested in how many events with at least one FNP lepton are selected by the analysis requirements, so identified as *tight-tight* events. Therefore, for each event the following weight w_{fake} is calculated:

$$w_{\mathrm{fake}} = r_1 f_2 \cdot p_{rf} + f_1 r_2 \cdot p_{fr} + f_1 f_2 \cdot p_{ff} \tag{5.6}$$

The estimate of the fake events in each region is carried out by considering the events with two *loose* leptons satisfying the selection requirements, weighted with w_{fake}.

Measurement of the real efficiencies

This measurement must be performed on a sample of real *loose* leptons.
A pure sample of such leptons can be obtained in data by using the *tag and probe* method on Z boson candidate events. To apply this method, events with exactly two same flavour, opposite charge leptons and with an invariant mass close to the Z boson resonance (81 GeV $< m_{ll} <$ 101 GeV) are selected. These events are additionally required to have fired single lepton triggers. Then, tight selection requirements are applied to select one of the two leptons, to ensure that it is a prompt lepton coming from the decay of the Z boson. If the lepton passes all the requirements,

it is considered as *tag* and its partner can be used as a *probe* to evaluate the real efficiencies. The probe lepton has a high probability of coming from the Z decay, but no constrains have been put directly on the lepton, allowing to build a pure sample of prompt leptons without any bias.
To pass the *tag* selection a lepton has to:

- be identified as a *tight* lepton;
- satisfy more stringent isolation requirements, placed on the energy of the tracks surrounding the leoptons ($p_{\mathrm{T}}^{\mathrm{varcone20}}/p_{\mathrm{T}} < 0.01$ for electrons and $p_{\mathrm{T}}^{\mathrm{varcone30}}/p_{\mathrm{T}} < 0.01$ for muons);
- have $p_T > 30$ GeV;
- be the lepton that has fired the trigger.

The last requirement is added because the trigger decision is based on the leptons kinematics and their isolation. Thus, this can introduce a bias in the sample if the *probe* lepton is matched with the trigger, buy applying an involuntary selection to the leptons used to populate the *loose* sample.
The efficiencies can strongly depend on the kinematics properties of the leptons, and are therefore parametrised as a function of p_T and η. The size of the parametrisation bins is chosen in order to take into account the variation of the *loose*-to-*tight* probabilities with the value of these variables, yet being careful to avoid to be dominated by statistical uncertainties. The probabilities are parametrised over five p_T bins [GeV]:

$$(7;12), (12;20), (20;35), (35;50), > 50$$

and over five bins of $|\eta|$:

$$(0;0.7), (0.7;1.37), (1.37;1.52), (1.52;2), (2;2.5)$$

Consequently, the efficiencies are parametrised in a total of 15 different bins.
The results of the measurement, as a function of one variable individually and integrating over the other one, are shown in Figure 5.5 and Figure 5.6 for electrons and muons respectively. The ratio in the lower pad displays the real efficiencies used as input for the Matrix Method.

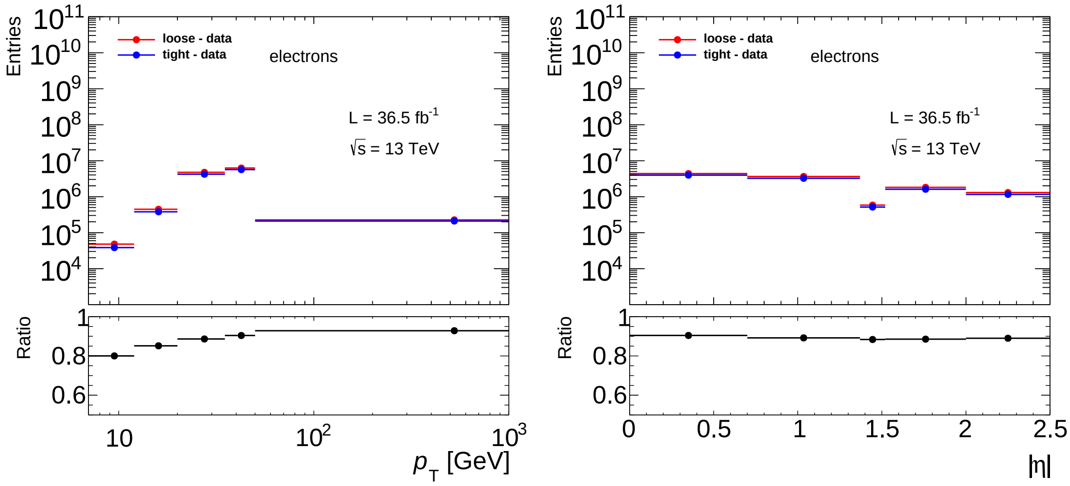

FIGURE 5.5: Measurement of the prompt electron efficiencies as a function of p_{T} and η. In both figures, the upper pad shows the distribution obtained for *loose* and *tight* electrons, in the bin considered for the parametrisation, while the lower pad presents the ratio used as input for the Matrix Method.

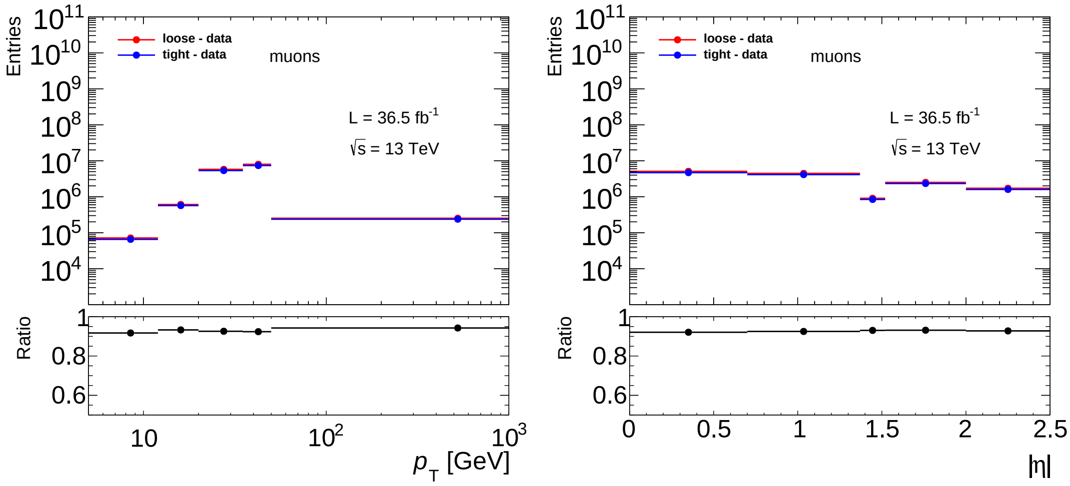

FIGURE 5.6: Measurement of the prompt muon efficiencies as a function of p_{T} and η. In both figures, the upper pad shows the distribution obtained for *loose* and *tight* muons, in the bin considered for the parametrisation, while the lower pad presents the ratio used as input for the Matrix Method.

Measurement of the fake probabilities

The fake rate is measured in a selection in which the presence of prompt leptons is expected to be very rare, thus any reconstructed lepton can be considered to be FNP.
To obtain such a sample, a modified *tag and probe* technique is adopted, developed in a similar to the one used for the real efficiencies, but with the opposite goal. This is achieved selecting events with two same-charge leptons, a very rare signature in the SM. In such selection, making sure that one lepton is a real, increases the probability for the other one to be fake. Events are therefore selected with one electron and one muon with the same charge. Then, the leading lepton is asked to have $p_T > 30$ GeV, to be *tight* and to pass stringent isolation requirements. If the prompt lepton passes this selection, his partner can be used as a *probe* to evaluate the fake rate. The most relevant Standard Model process which may contains one real electron and one real muon with the same charge is the WZ production, in which both electroweak bosons decay leptonically. To remove the real contamination deriving from this process, it is asked that each event must contain exactly two leptons; the remaining events which meet the selection requirements are the ones in which one of lepton is not reconstructed and are subtracted using MC simulated events.
An additional source of real contamination is given by those processes that may have two different flavour, opposite-charge leptons in the final state, like $t\bar{t}$ and $Z \to \tau\tau$, but pass the selection because the charge of the lepton is wrongly measured. This phenomenon, called *charge flip*, is dominated by cases when an electron irradiates a photon, which then converts rapidly: if one of the two electrons of the conversion carries most of the momentum, it can be reconstructed as the main electron and therefore the wrong charge may be assigned. The radiation is emphasised inside the detector's materials. For this reason the charge flip contribution is more important for electrons at high η. In order to reduce the contamination due to this kind of events an additional cut of $|\eta| < 1.3$ is imposed for the electrons passing the *tag* requirements. This operation is not needed for muons because being heavier particles, the emission of photons is suppressed, and therefore the charge flip is really rare. The remaining contamination due to charge-flip is subtracted using MC simulated events.
After the subtraction of the real contaminations from the *loose* and the *tight* leptons samples, the fake rate is computed parametrised in a similar way as the real efficiencies, as a function of p_{T} and η of the leptons. The results are shown in Figure 5.7 and Figure 5.8 for electrons and muons respectively. In all the Figures, the distributions for *loose* (red) and *tight* (blue) leptons observed in data are represented by the dotted histograms in the upper pad, while the real contamination simulated with MC is shown with the histograms filled in the same colours. It can be noticed that such contamination is negligible for soft leptons, while it start to become important when the p_{T} of the lepton reaches over 30 GeV. In the lower pad of the Figures, instead, the ratio calculated after the real contamination subtraction is shown: this is the final fake rate, used as input for the Matrix Method.

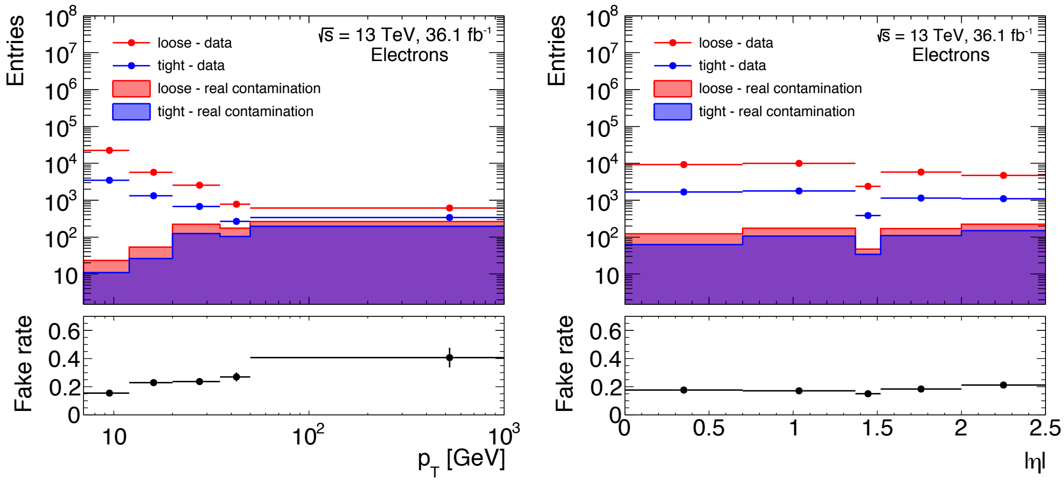

FIGURE 5.7: Measurement of the electrons fake rate as a function of p_T and η. In both figures, the upper pad shows the distribution obtained for *loose* and *tight* electrons in data as well as the real contamination extracted from MC, while the lower pad presents the ratio used as input for the Matrix Method.

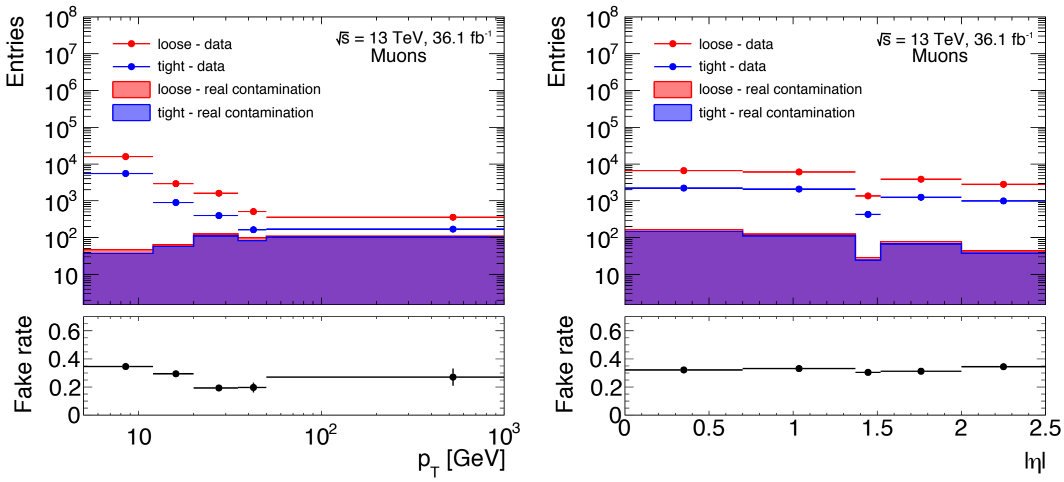

FIGURE 5.8: Measurement of the electrons fake rate as a function of p_T and η. In both figures, the upper pad shows the distribution obtained for *loose* and *tight* electrons in data as well as the real contamination extracted from MC, while the lower pad presents the ratio used as input for the Matrix Method.

Validation

The estimation of the number of events with FNP leptons can be validated defining kinematic regions enriched with such background. These regions must be defined taking into account the origin of the FNP leptons in the SRs, trying to match the relative composition of the different sources.

In this search, the FNP estimation is validated using a selection requiring two leptons with the same charge, where the FNP contribution is expected to dominate. Two different validation regions are established for this purpose. The first one, called $\mathrm{VRF_{tight}}$, is defined by keeping all the SR selections, apart from the inverted charge requirement (in the SR the leptons are required to have opposite charge); this VR has the goal to validate the fake estimation in an identical area of the phase space. In the second VR ($\mathrm{VRF_{loose}}$) some of the requirements of the SR are dropped, in order to increase the statistics of the selection and check the modelling of the main analysis variables. The definitions of the two validation regions can be found in Table 5.8. The expected and observed yields are found to be comparable, with less than two sigma deviations, as shown in in Table 5.9. Finally, the distributions of $R_{2\ell 4j}$ and $R_{2\ell}$ for the events in the $\mathrm{VRF_{loose}}$ selection are presented in Figure 5.9, as an example. The modelling was found to be accurate for all the distributions exploited in the analysis.

	$\mathrm{VRF_{loose}}$	$\mathrm{VRF_{tight}}$
Leptons	2 same-sign leptons (ee, $e\mu$, $\mu\mu$)	
b-veto	veto on b-tagget jets for jet_1 and jet_2	
$E_{\mathrm{T}}^{\mathrm{miss}}$ [GeV]	> 200	> 200
Leading lepton p_{T} [GeV]	(7,80)	(7,80)
Sub-leading lepton p_{T} [GeV]	(7,35)	(7,35)
m_{ll} [GeV]	> 10	> 10
n_{jets}	≥ 2	≥ 2
Leading jet p_{T} [GeV]	> 150	> 150
$R_{2\ell 4j}$	–	> 0.35
$R_{2\ell}$	–	> 12

TABLE 5.8: Event selection applied for the definition of the two regions designed for the validation of the FNP leptons estimate.

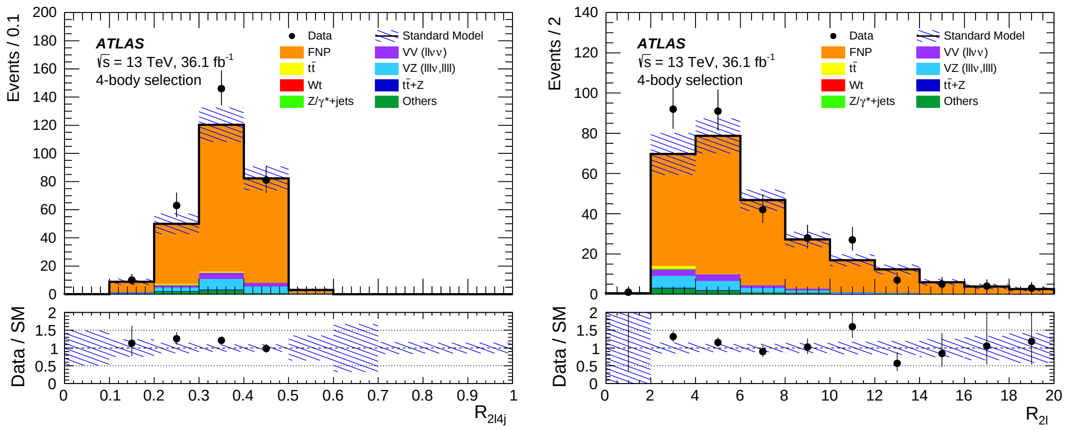

FIGURE 5.9: Distributions of $R_{2\ell 4j}$ and $R_{2\ell}$ for events passing the $\mathrm{VRF_{loose}}$ requirements.

	$\text{VRF}_{\text{loose}}$	$\text{VRF}_{\text{tight}}$
Observed events	300	10
Fitted bkg events	264 ± 24	14 ± 3
Fit output, $t\bar{t}$	$1.6^{+3.2}_{-1.6}$	$0.02^{+0.02}_{-0.02}$
Fit output, VV	24 ± 11	0.7 ± 0.4
Fit output, $Z_{\tau\tau}$	0.4 ± 0.2	–
$t\bar{t}Z$	0.94 ± 0.09	0.01 ± 0.00
Wt	$0.02^{+0.13}_{-0.02}$	–
FNP	230 ± 20	13 ± 2
Others	6.3 ± 0.4	0.03 ± 0.01
Fit input, $t\bar{t}$	1.6	0.02
Fit input, VV	31	0.9
Fit input, $Z_{\tau\tau}$	0.4	–

Table 5.9: Expected and observed yields in two regions designed for the validation of FNP leptons estimation.

5.6 Systematic Uncertainties

The effect of the systematic uncertainties is evaluated for all signal samples and background processes. For the background processes for which the normalisation is extracted in dedicated control regions, the systematic uncertainties only affect the extrapolation to the signal regions. Table 5.10 summarises the contributions of the different sources of systematic uncertainty in the total SM background predictions in the SR. The primary sources of uncertainties for this analysis are related to the estimation of the FNP leptons background and the theoretical uncertainties on the modelling of the backgrounds determined using CRs. The statistical uncertainties of the simulated event samples are also taken into account. The major contribution to the experimental systematic uncertainties, described in Chapter 3, arises from the jet energy scale.
Systematic uncertainties are assigned to the FNP background estimate to account for potentially different compositions (heavy flavour, light flavour or conversions) between the signal and control regions. Two different measurements of the fake rate are independently derived from the same-charge dilepton samples, selecting either W+jets or $t\bar{t}$ events and enriched by fakes from light flavour decays and photon conversions or from heavy flavour decays respectively. The first measurement, obtained vetoing events with b-tagged jets, is used to derive the nominal parametrisation. The full difference between the prediction derived from the W+jets (nominal) and the $t\bar{t}$ (alternative) parameterisations is assigned as a symmetrised systematic uncertainty on the central FNP prediction. The uncertainty on contamination from prompt leptons in the regions used to measure the probabilities for fake and non-prompt leptons to pass the signal criteria is evaluated by varying the expected MC contribution by 30%. Finally, the one-sigma statistical variations of the nominal parametrisation are also considered. Figure 5.10 shows the uncertainties on the fake rate as a function of the p_{T} of the lepton: the composition uncertainty is dominant for soft leptons, while the real lepton contamination and the statistical uncertainties start to become important as the energy increases. All these uncertainties related to the fake efficiencies have been propagated independently through the Matrix Method, to provide the final uncertainty on the FNP estimation.
The uncertainties on the modelling of the $t\bar{t}$ and single-top backgrounds in simulation are estimated by varying the renormalisation and factorisation scales, as well as the amount of initial and

	SR
Total background systematic	20%
Diboson theoretical uncertainties	2.7%
$t\bar{t}$ theoretical uncertainties	8.1%
Fake and non-prompt leptons	14%
MC statistical uncertainties	10%
VV normalisation	9.2%
$t\bar{t}$ normalisation	8.6%
$Z_{\tau\tau}$ normalisation	1.5%
Jet energy scale	4.4%
Jet energy resolution	1.0%
$E_{\mathrm{T}}^{\mathrm{miss}}$ modelling	1.3%
b-tagging	2.2%
Pile up reweighting	1.4%
Lepton modelling	2.5%

TABLE 5.10: Sources of systematic uncertainty on the SM background estimates, evaluated after the background fit. The values are given as relative uncertainties on the expected background event yields in the SR.

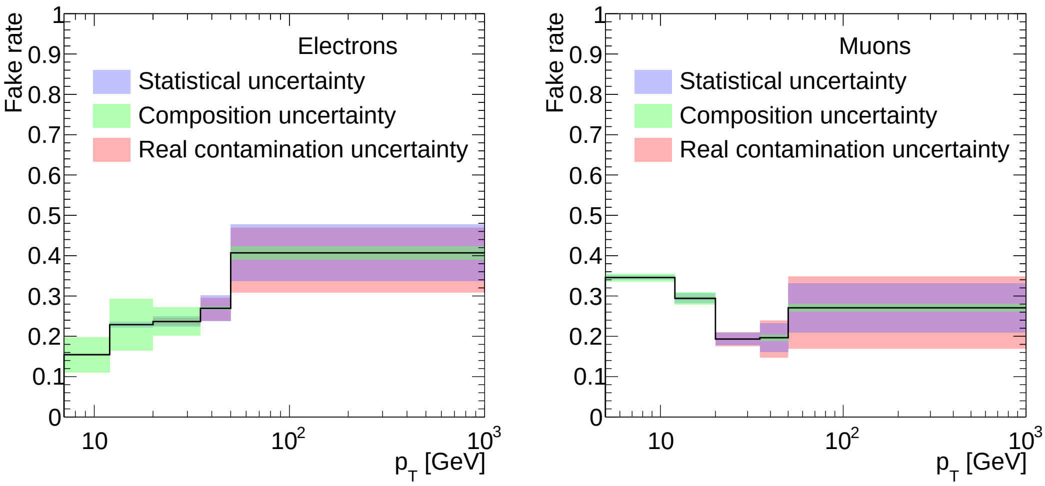

FIGURE 5.10: Uncertainties on the fake rate for electrons (left) and muons (right).

final state radiation [86]. Additional uncertainties on the parton shower modelling are assessed as the difference between the predictions from PYTHIA and HERWIG, and on the generator choice by comparing POWHEG and MADGRAPH5_aMC@NLO [86]. An additional uncertainty on the interference between $t\bar{t}$ and single top quark Wt production is assigned by comparing the predictions of dedicated LO $WWbb$ MADGRAPH 2.5 sample, where the same $t\bar{t}$ and Wt production diagrams are included, but top quarks are not required to be on-shell.
The diboson background MC modelling uncertainties are estimated by varying the renormalisation, factorisation and resummation scales [87]. For $t\bar{t}Z$ production, the predictions from the MADGRAPH5_aMC@NLO and SHERPA generators are compared, and the uncertainties related to the choice of the renormalisation and factorisation scales are assessed by varying

the corresponding generator parameters up and down by a factor of two around their nominal values [88].
The uncertainties related to the choice of the QCD renormalisation and factorisation scales in $Z/\gamma^* + $jets events are assessed by varying the corresponding generator parameters up and down by a factor of two around their nominal values. Uncertainties on the resummation scale and the matching scale between the matrix element and the parton shower are evaluated by varying up and down by a factor of two the corresponding parameters in SHERPA.
The cross-sections used to normalise the MC samples are varied according to the uncertainty on the cross-section calculation, that is, 5.3% uncertainty for single top quark in the Wt-channel [89], 13% for $t\bar{t}W$ and 12% for $t\bar{t}Z$ production [77]. For $t\bar{t}WW$, tZ, tWZ, $t\bar{t}h$, $t\bar{t}t$, $t\bar{t}t\bar{t}$, and tribosons production processes, which constitute a small background, a 50% uncertainty on the event yields is assumed.

5.7 Results

The data are compared to the background prediction in the SR and good agreement with the predicted number of events is observed, with no significant excess over the SM expectation. Figure 5.11 shows the distributions of $R_{2\ell 4j}$ and $R_{\ell\ell}$ for events satisfying the SR requirement apart from the ones on the represented variable, which is well modelled in both cases. The total number of observed events in the SR is compared with the background-only fit results in Table 5.11. The observed yield is within one standard deviation of the background prediction in the SR.

Two different sets of exclusion limits for new physics beyond the SM are derived from these results. A model-independent upper limit on the visible cross-section σ_{vis} of new physics, defined as cross-section times acceptance times efficiency, is derived by performing a fit which includes the observed yield in the SR as a constraint, and a free signal yield in the SR as an additional process. These limits assume negligible signal contamination in the CRs. Model independent upper limits at 95% confidence level are presented in Table 5.12.
Finally, model dependent limits (at 95% confidence level) are computed on $\tilde{t}_1$ pair production scenarios. A profile likelihood fit is performed including the expected signal yield for each signal

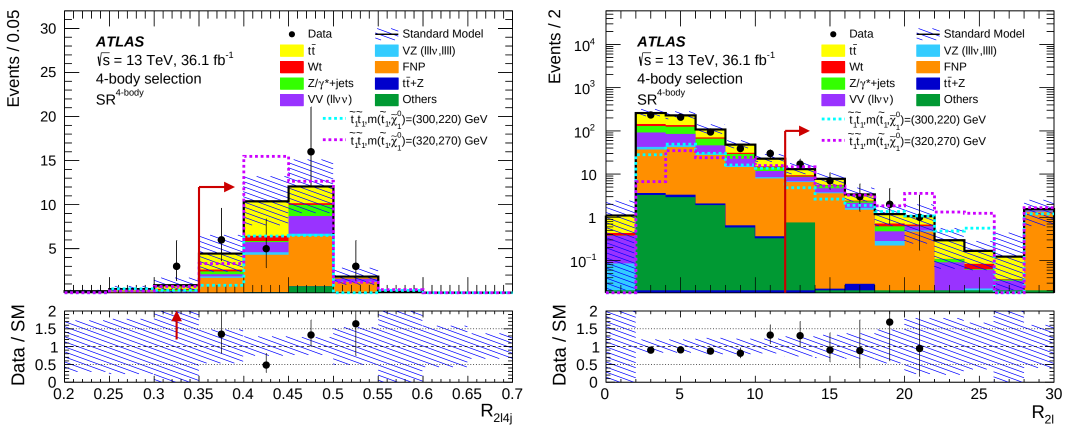

FIGURE 5.11: Distributions of $R_{2\ell 4j}$ (left) and $R_{2\ell}$ (right) for events satisfying all the SR selections except for the one on the variable shown in the figure, after the background fit. Red arrows indicate the signal region selection criteria.

	$\mathrm{SR}^{4-\mathrm{body}}$
Observed events	30
Total SM events	28 ± 6
Fit output, $t\bar{t}$	7.9 ± 2.0
Fit output, VV	4.5 ± 2.3
Fit output, $Z_{\tau\tau}$	1.2 ± 0.6
$t\bar{t}$ +Z	0.03 ± 0.01
Wt	1.08 ± 0.27
Z_{ee}, $Z_{\mu\mu}$	0.21 ± 0.09
Others	0.80 ± 0.30
Fake and non-prompt	12.8 ± 4.3
Fit input, $t\bar{t}$	7.7
Fit input, VV	5.7
Fit input, $Z_{\tau\tau}$	1.1

TABLE 5.11: Background fit results in the SR. The nominal expectations from MC simulation are given for comparison for those backgrounds ($t\bar{t}$, VV and $Z_{\tau\tau}$) that are normalised to data in dedicated CRs.

σ_{vis} [fb]	S^{95}_{obs}	S^{95}_{exp}	$p(s=0)$
0.48	17.4	16^{+7}_{-5}	0.37

TABLE 5.12: Model-independent 95% CL upper limits on the visible cross-section (σ_{vis}) of new physics, the visible number of signal events (S^{95}_{obs}), the number of signal events (S^{95}_{exp}) given the expected number of background events (and $\pm 1\sigma$ excursions on the expectation), and the discovery p-value ($p(s=0)$).

model considered and its associated uncertainties in the CRs and in the SR. Limits for simplified models in which pair-produced $\tilde{t}_1$ decay with 100% branching ratio into $bff'\tilde{\chi}^0_1$ are shown in the $\tilde{t}_1$–$\tilde{\chi}^0_1$ mass plane in Figure 5.12. In the four-body decay regime, top squark masses are excluded up to 400 GeV for $m_{\tilde{t}_1} - m_{\tilde{\chi}^0_1} = 40$ GeV. In Figure 5.13 the same result is shown in combination with the sensitivity obtained by other searches targeting different signal models in the two lepton channel [90]. For each signal model the search with the highest expected sensitivity is considered for the calculation of the limit. Comparing with the blue area, which shows the observed exclusion from the ATLAS $\sqrt{s} = 8$ TeV analyses [34], it can be noticed how the sensitivity in the compressed region has been extended by nearly 200 GeVwith respect to the previous results.

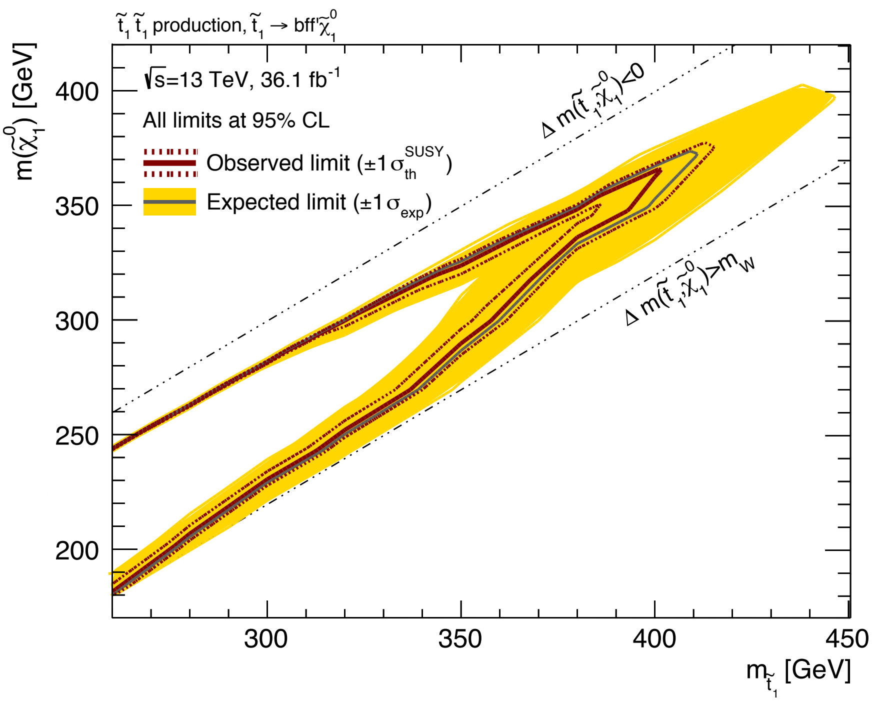

FIGURE 5.12: Exclusion limits at the 95% confidence level for a simplified model assuming $\tilde{t}_1$ pair production, decaying via $\tilde{t}_1 \rightarrow bff'\tilde{\chi}_1^0$ with 100% branching ratio. The dashed grey line and the yellow band are the expected limit and its $\pm 1\sigma$ uncertainty. The thick solid red line is the observed limit for the central value of the signal cross-section.

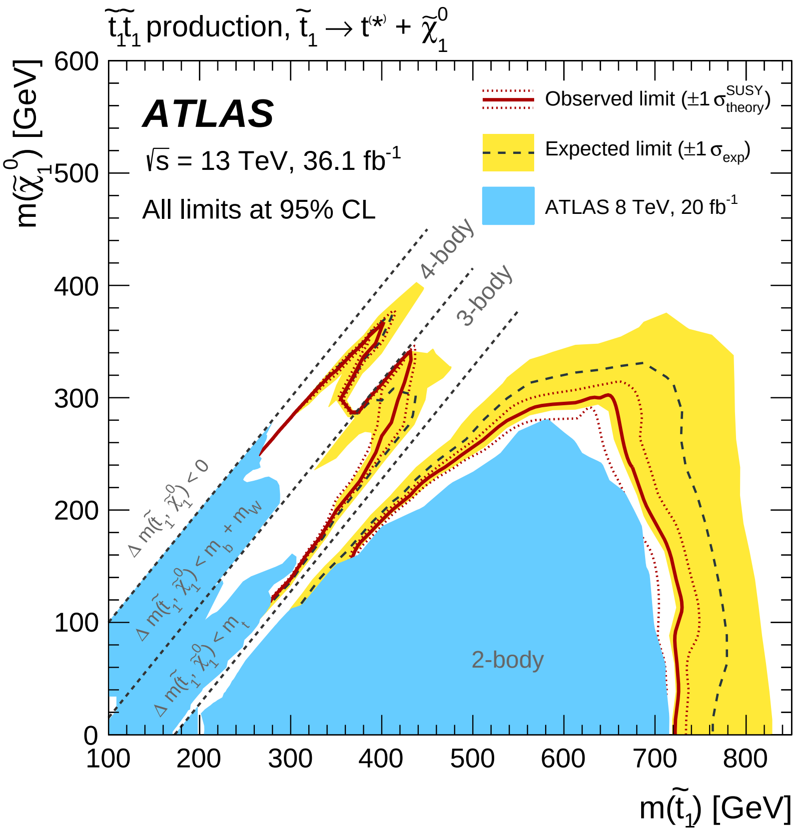

FIGURE 5.13: Exclusion limits at the 95% confidence level for a simplified model assuming $\tilde{t}_1$ pair production, decaying via $\tilde{t}_1 \rightarrow bff'\tilde{\chi}_1^0$ with 100% branching ratio, obtained considering different searches in the two-lepton channel.

Chapter 6

Search for top squarks in final states containing a Z boson

Z bosons can appear in the decay chain of top squarks. This can happen either in the decay of the $\tilde{t}_2$, via $\tilde{t}_1 \to t\tilde{\chi}_2^0$ or through the decay of intermediate produced sparticles, like for example when the $\tilde{t}_1$ dacays to t and $\tilde{\chi}_2^0$, with the $\tilde{\chi}_2^0$ consequently decaying via $\tilde{\chi}_2^0 \to Z\tilde{\chi}_1^0$. Both examples are illustrated in Figure 6.1. The presence of the Z boson allows to efficiently discriminate these signal from the SM top quark pair production ($t\bar{t}$) background by requiring a same-flavour opposite-sign (SF-OS) lepton pair originating from the $Z \to \ell^+\ell^-$ decay. The presence of an additional lepton which could be produced in the decay of the top quarks in the event can further increase the discriminating power of the search, given the rarity of SM processes with three leptons in the final state.

This Chapter presents the results of a search for top squarks in final states with Z bosons at $\sqrt{s} = 13$ TeV using the complete data set collected by the ATLAS experiment in proton–proton (pp) collisions during Run-2 (2015-2018), corresponding to 139 fb^{-1}of integrated luminosity. Searches for top squark production in events involving Z bosons have been previously performed by both ATLAS [91, 92] and CMS [93, 94], with no evidence for new physics yet.

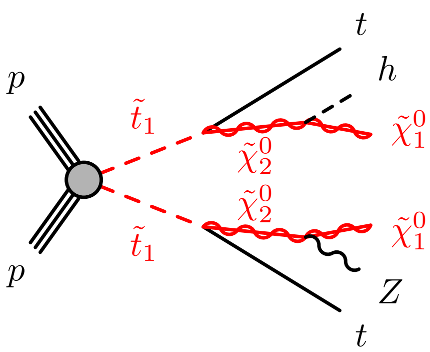

(A)

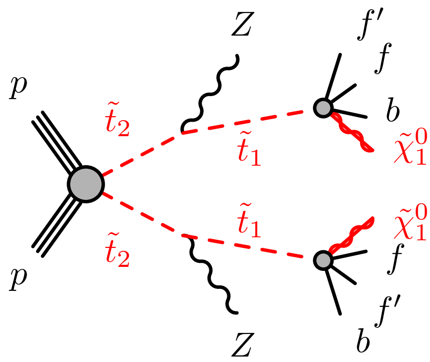

(B)

FIGURE 6.1: Diagrams for the top squark pair production processes considered in this analysis: (a) $\tilde{t}_1 \to t\tilde{\chi}_2^0$ with $\tilde{\chi}_2^0 \to h/Z\tilde{\chi}_1^0$ decays, and (b) $\tilde{t}_2 \to Z\tilde{t}_1$ with $\tilde{t}_1 \to bff'\tilde{\chi}_1^0$ decays.

6.1 Targeted models

Two classes of simplified models are used for the analysis optimisation and the interpretation of the results. In both classes, direct top squark pair production is considered, with all SUSY particles are decoupled except for the top squarks and the neutralinos involved in their decay. In all cases the $\tilde{\chi}_1^0$ is assumed to be the LSP.
The first set of models features direct $\tilde{t}_1$ production with $\tilde{t}_1 \rightarrow t\tilde{\chi}_2^0$, with the $\tilde{\chi}_2^0$ which decays either via Z ($\tilde{\chi}_2^0 \rightarrow Z\tilde{\chi}_1^0$) or h ($\tilde{\chi}_2^0 \rightarrow h\tilde{\chi}_1^0$) bosons with a 50% branching ratio. In these models, the $\tilde{\chi}_1^0$ is assumed to be very light, while the $\tilde{\chi}_2^0$ and the $\tilde{t}_1$ masses are varied, keeping the $\tilde{\chi}_2^0 - \tilde{\chi}_1^0$ mass difference to be large enough to allow on-shell Z or Higgs boson decays. The set of sparticle masses chosen for the signal models generated in this way are shown in Figure 6.2.

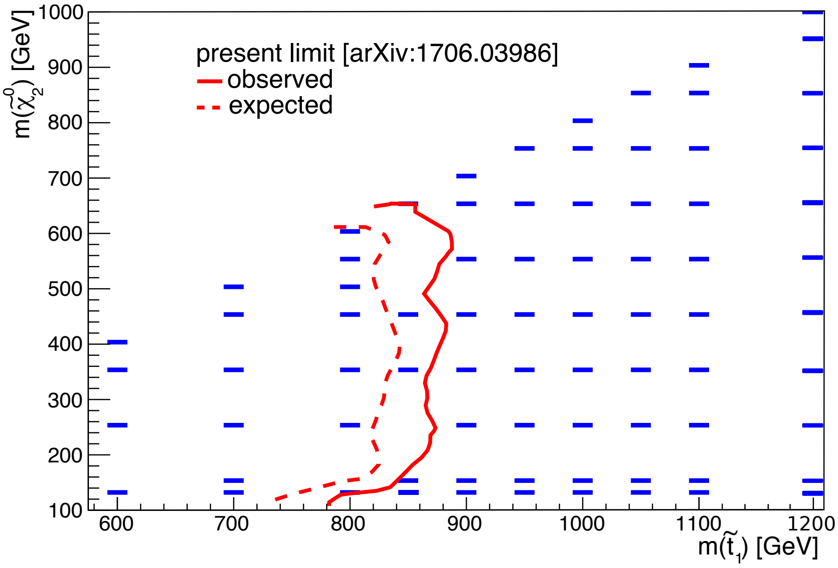

FIGURE 6.2: Signal samples investigated for the $\tilde{t}_1\tilde{t}_1 \rightarrow t\bar{t}\tilde{\chi}_2^0\tilde{\chi}_2^0$ models. The BR of the $\tilde{t}_1$ decay is fixed to 50% in Z and 50% in h. The figure shows also the limits placed on such models by the analysis performed on this channel with the intermediate Run 2 dataset [91].

Additional simplified models featuring direct $\tilde{t}_2$ production with $\tilde{t}_2 \rightarrow Z\tilde{t}_1$ decays and $\tilde{t}_1 \rightarrow t^{(*)}\tilde{\chi}_1^0$ are also considered. Being heavier, the $\tilde{t}_2$ has a lower cross-section than that of the $\tilde{t}_1$, and their decay properties can be similar. However, searches for the latter can provide additional sensitivity in regions where the $\tilde{t}_1$ falls in a phase space difficult to experimentally discriminate from the background due to the similarities in kinematics. This can be the case in scenarios where the lighter top squark is only slightly heavier than the sum of the masses of the top quark and the lightest neutralino ($\tilde{\chi}_1^0$). To target this kind of models, the mass difference between the $\tilde{t}_1$ and $\tilde{\chi}_1^0$ is set to 40 GeV, and the four-body decay channel $\tilde{t}_1 \rightarrow bff'\tilde{\chi}_1^0$ is assumed to occur, where f and f' are two fermions from the W^* decay. Figure 6.3 shows the values of the $\tilde{t}_2$ and $\tilde{\chi}_1^0$ masses considered, for this scenario. All the simulated signal sample are generated as described in Section 4.1.

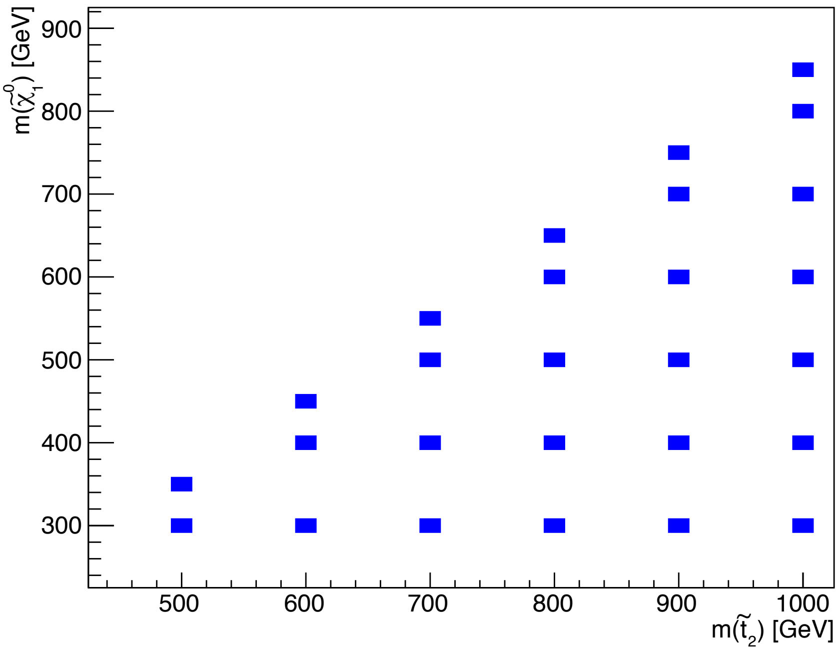

FIGURE 6.3: Signal generated for the $\tilde{t}_2 \to \tilde{t}_1 Z$, $\tilde{t}_1 \to bff\tilde{\chi}_1^0$ models.

6.2 Selection of particles and jets

In this section the definitions of the reconstructed particles and jets used specifically in this analysis are provided. More details on how jets, electrons, muons and the transverse missing energy are reconstructed in ATLAS were given in Chapter 3. Identification criteria for Jets, Electron and Muon are summarised in Table 6.1.

Jets

Jets are reconstructed using the anti-k_t jet algorithm [57] with the distance parameter R set to 0.4 and topological clusters as input. They are selected if they have $p_{\mathrm{T}} > 30$ GeV and lie within $|\eta| < 2.8$. To mitigate the effects of pileup, the JVT [61] requirement is applied and jets are rejected in case they have $p_{\mathrm{T}} < 120$ GeV, $|\eta| < 2.5$ and JVT< 0.59. This requirement reduces the fraction of jets from pile-up down to 1%, with an efficiency for pure hard scatter jets of about 90%. In order to remove events with fake $E_{\mathrm{T}}^{\mathrm{miss}}$ arising from the mis-measurement of a jet, an event is vetoed when a jet (with $|\eta| < 4.9$) is judged as bad according to quality selection criteria that reject detector noise and non-collision backgrounds.
The b-jets are tagged using the MV2c10 tagging algorithm [62], using the calibrated bins of the BDT score. A jet is consider tagged, if it lays in the last three bins, equivalent to 77% b-tagging efficiency.

Electrons

Two levels of electron selections are defined: baseline leptons have to pass a first loose selection, while signal leptons are subject to more stringent cuts. Baseline electrons must satisfy the Loose identification [68], have $E_{\mathrm{T}} > 4.5$ GeV and $|\eta| < 2.47$ and pass following requirements on the longitudinal impact parameter: $|z_0 \cdot sin(\theta)| < 0.5$ mm and on the transverse impact parameter: $|d_0/\sigma(d_0)| < 5$. Signal electrons are additionally required to pass the Medium identification [68] and the FCTight isolation working point, similar to the one described in [68].

Muons

Muon candidates must have $p_{\mathrm{T}} > 4$ GeV and $|\eta| < 2.4$ and must be identified as Medium [69]. Additionally, they need to pass the requirements on the longitudinal impact parameter: $|z_0 \cdot sin(\theta)| < 0.5$ mm and on the transverse impact parameter: $|d_0/\sigma(d_0)| < 3$.
Finally, signal muon are required to pass the FCTightTrackOnly isolation working point, similar to the one described in [69].
Events containing cosmic muons are vetoed; these particles are identified in cse they satisfy the following conditions on the longitudinal and transverse impact parameters with respect to the primary vertex: $|z_0| < 1$ mm and $|d_0| < 0.2$ mm.

Removal of reconstruction ambiguities

When all the jets, electrons and muons are reconstructed, some ambiguities can arise in the classification, and the same reconstructed object can occur in different categories. The overlap removal (OR) is an algorithm applied to candidate leptons and jets, to remove such ambiguities and is defined as follow.

- Jet candidates with $p_{\mathrm{T}} < 100$ GeV within $\Delta R = \sqrt{(\Delta y)^2 + (\Delta\phi)^2} = 0.2$ of a baseline electron are discarded, unless the jet has a value of the b-tagging discriminant larger than the value corresponding to approximately 85% b-tagging efficiency, in which case the lepton is discarded since it is likely to have originated from a semileptonic b-hadron decay.
- Jet candidates within $\Delta R = 0.2$ of a baseline muon are discarded, irrespective of the jet p_{T}.
- Any remaining electron candidate within $\Delta R = 0.4$ of a jet, and any muon candidate within $\Delta R = \min\{0.4, 0.04 + p_{\mathrm{T}}(\mu)/10\,\mathrm{GeV}\}$ of jet is discarded. In case of the muon, if the jet has fewer than three associated tracks, the muon is retained and the jet is discarded instead to avoid inefficiencies for high-energy muons undergoing significant energy loss in the calorimeter.
- Finally, any baseline electron sharing an Inner Detector track with a remaining baseline muon is also removed.

	Selection
Jets	$p_{\mathrm{T}} > 30$ GeV $\lvert\eta\rvert < 2.8$ JVT > 0.59 if $p_{\mathrm{T}} < 120$ GeV and $\lvert\eta\rvert < 2.5$
B-jets	$p_{\mathrm{T}} > 30$ GeV $\lvert\eta\rvert < 2.5$ MV2c10 > 0.63 ($\epsilon_b \sim 77\%$)
Baseline Electrons	$E^{\mathrm{clust}}/\cosh(\eta) > 4.5$ GeV $\lvert\eta\rvert < 2.47$ Loose identification $\lvert z_0 \sin\theta\rvert < 0.5\,\mathrm{mm}$ and $\lvert d_0/\sigma\rvert < 5$
Signal Electrons	$E^{\mathrm{clust}}/\cosh(\eta) > 5$ GeV Medium identification FCTight isolation $\lvert z_0 \sin\theta\rvert < 0.5\,\mathrm{mm}$ and $\lvert d_0/\sigma\rvert < 5$
Baseline Muons	$p_{\mathrm{T}} > 4$ GeV $\lvert\eta\rvert < 2.4$ $\lvert z_0 \sin\theta\rvert < 0.5\,\mathrm{mm}$ and $\lvert d_0/\sigma\rvert < 3$
Signal Muons	$p_{\mathrm{T}} > 5$ GeV Medium identification FCTightTrackOnly isolation $\lvert z_0 \sin\theta\rvert < 0.5\,\mathrm{mm}$ and $\lvert d_0/\sigma\rvert < 3$

TABLE 6.1: Sumamry of jet, electron and muon selection criteria.

6.3 Event selection

Events are accepted if they have fired a trigger requiring either two electrons, two muons or one electron and one muon. The trigger-level requirements on the p_{T}, identification and isolation of the leptons involved in the trigger decision are looser than those applied offline to the candidate leading and subleading leptons. This ensures constant trigger efficiencies in the relevant phase space [95].

A pre-selection of events of interest is performed by requiring the presence of at least three signal leptons (electrons or muons), with at least one SF-OS lepton pair whose invariant mass is compatible with the Z boson mass ($|m_{\ell\ell} - m_Z| < 15$ GeV, with $m_Z = 91.2$ GeV). The leading lepton is required to have $p_{\mathrm{T}} > 40$ GeV and the subleading to have $p_{\mathrm{T}} > 20$ GeV. In addition, at least three jets with $p_{\mathrm{T}} > 30$ GeV are required in each event and a preliminary cut of $E_{\mathrm{T}}^{\mathrm{miss}} > 50$ GeV is applied. These requirements are summarised in Table 6.2 and are applied throughout the analysis unless stated otherwise. Figure 6.4 shows the distributions of the variables used for the preliminary selection of events. The observed events are compared with the expected SM distributions. These are obtained with MC simulated events for the irreducible backgrounds and with the data-driven method discussed in Chapter 5 for the events with at least one fake or non prompt lepton (FNP). Two sets of SRs are optimised for the best discovery sensitivity, using the significance reported in Equation 4.1, for the two classes of models discussed in Section 6.1. The kinematic variables and the list of cuts used for each SR definition are illustrated in the following.

Variable	Pre-selection
Number of signal leptons	≥ 3
Number of SF-OS pairs	≥ 1
Leading lepton p_{T} [GeV]	> 40
Subleading lepton p_{T} [GeV]	> 20
$\lvert m_{\ell\ell}^{\text{SF-OS}} - m_Z \rvert$ [GeV]	< 15
n_{jets} ($p_{\mathrm{T}} > 30$ GeV)	≥ 3
$E_{\mathrm{T}}^{\mathrm{miss}}$ [GeV]	> 50

Table 6.2: Definition of the event pre-selection used in the analysis.

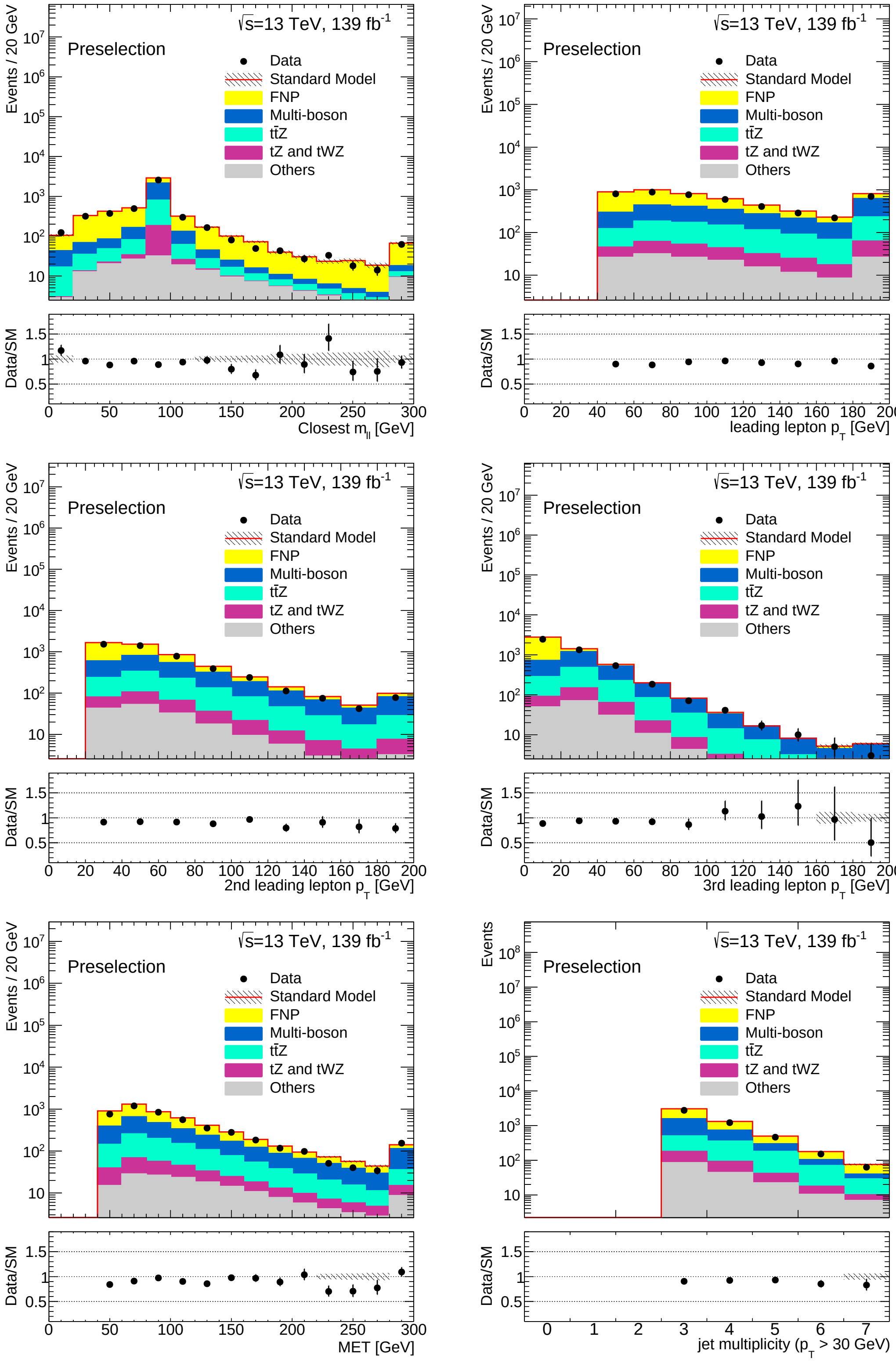

Figure 6.4: Comparison between the distribution of observed data and the expected SM prediction, for an integrated luminosity of 139 fb^{-1}. The contribution from all SM backgrounds is shown as a histogram stack, all the backgrounds come from MC, apart form the fake and non prompt leptons, which are estimated as explained in Chapter 5; the bands represent the statistical uncertainty. The lower panels show the ratio of the observed data to the total SM background prediction.

Signal regions targeting the $\tilde{t}_1$ models

Two signal regions are defined, in order to have optimal sensitivity for different signal scenarios, depending on the mass splitting between $\tilde{\chi}_2^0$ and $\tilde{\chi}_1^0$.
Signal region $\mathrm{SR_{1A}}$ is optimised for large $\tilde{\chi}_2^0 - \tilde{\chi}_1^0$ mass splitting. It includes requirements on $m_{\mathrm{T2}}^{3\ell}$, a variation of the stransverse mass m_{T2}, which is used to bound the masses of a pair of particles that are presumed to have each decayed semi-invisibly into one visible and one invisible particle [96, 97]:

$$m_{\mathrm{T2}}(\boldsymbol{p}_{\mathrm{T}}^{\alpha}, \boldsymbol{p}_{T}^{\beta}, \boldsymbol{p}_{\mathrm{T}}^{\mathrm{miss}}) = \min_{\boldsymbol{q}_{\mathrm{T}}^{1}+\boldsymbol{q}_{\mathrm{T}}^{2}=\boldsymbol{p}_{\mathrm{T}}^{\mathrm{miss}}} \max(m_{\mathrm{T}}^{2}(\boldsymbol{p}_{\mathrm{T}}^{\alpha}, \boldsymbol{q}_{\mathrm{T}}^{1}), m_{\mathrm{T}}^{2}(\boldsymbol{p}_{\mathrm{T}}^{\beta}, \boldsymbol{q}_{T}^{2})) \tag{6.1}$$

In the formula, $\boldsymbol{p}_{\mathrm{T}}^{\mathrm{miss}}$ is the vector sum of the transverse momenta of the two invisible particles, m_{T} indicates the transverse mass of two vectors (defined as $m_{\mathrm{T}}^2 = (E_{\mathrm{T1}} + E_{\mathrm{T2}})^2 - (\boldsymbol{p}_{\mathrm{T1}} + \boldsymbol{p}_{\mathrm{T2}})^2$), $\boldsymbol{p}_{\mathrm{T}}^{\alpha}$ and $\boldsymbol{p}_{\mathrm{T}}^{\beta}$ are the momenta of the two leptons, and $\boldsymbol{q}_{T}^{1}$ and $\boldsymbol{q}_{\mathrm{T}}^{2}$ are vectors which satisfy $\boldsymbol{q}_{\mathrm{T}}^{1} + \boldsymbol{q}_{\mathrm{T}}^{2} = \boldsymbol{p}_{\mathrm{T}}^{\mathrm{miss}}$. The minimum is taken over all the possible choices of $\boldsymbol{q}_{\mathrm{T}}^{1}$ and $\boldsymbol{q}_{\mathrm{T}}^{2}$.
In the case of $m_{\mathrm{T2}}^{3\ell}$, the two visible legs of the two semi-invisible decays are set to be the system of the SF-OS lepton pair with an invariant mass closest to m_Z, and the third lepton. Further important discriminating variables are the $E_{\mathrm{T}}^{\mathrm{miss}}$, and the jet and b-jet multiplicity. Figure 6.5 presents the distribution of the $E_{\mathrm{T}}^{\mathrm{miss}}$ and the $m_{\mathrm{T2}}^{3\ell}$variables, in a selection with all the $\mathrm{SR_{1A}}$ cuts applied, apart from the plotted variable itself; the upper pad in each plot illustrates the expected distribution for the SM background and for three representative signal samples, while the lower pad shows the significance obtained by selecting events over the value of each bin.

Models with small mass differences between the $\tilde{\chi}_2^0$ and the $\tilde{\chi}_1^0$ are targeted with $\mathrm{SR_{1B}}$, which instead features requirements on the transverse momentum of the SF-OS lepton pair ($p_{\mathrm{T}}^{\ell\ell}$), tighter cuts on the jet multiplicity and less stringent cuts on the $E_{\mathrm{T}}^{\mathrm{miss}}$ with respect to $\mathrm{SR_{1A}}$. The distributions of the first two variables are shown in Figure 6.6; the lower pad shows the significance obtained cutting on each variable, as described before.
The requirements of $\mathrm{SR_{1A}}$ and $\mathrm{SR_{1B}}$ are summarised in Table 6.3.

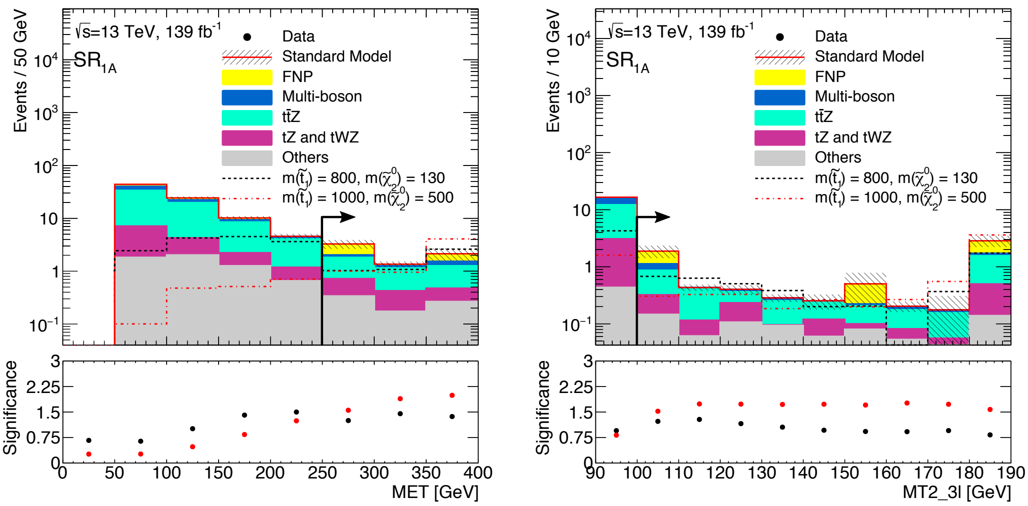

FIGURE 6.5: Distributions of the main discriminating variables for signal and backgrounds, with all the $\mathrm{SR_{1A}}$ cuts applied, apart from the one on the plotted variable. The lower pad shows the significance obtained by selecting events at each value of the histogram's bins.

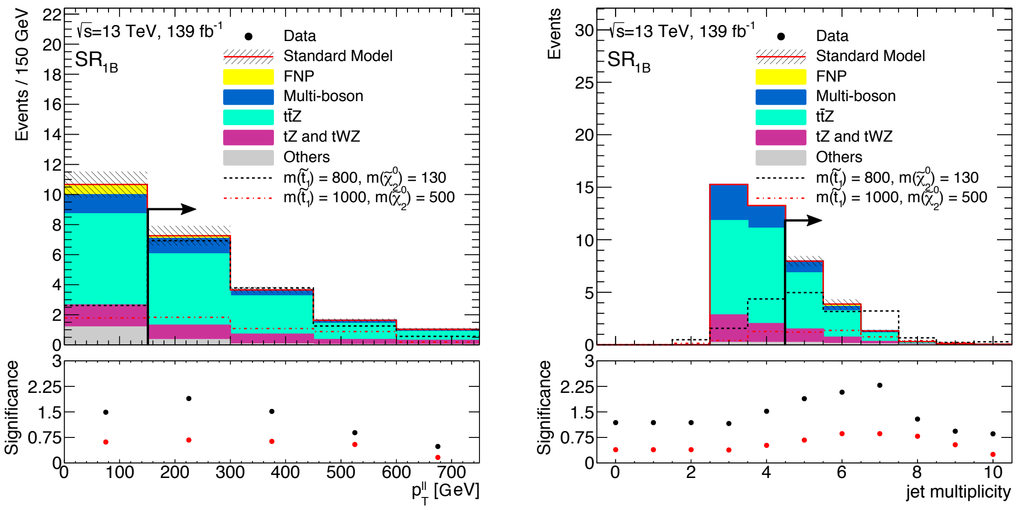

FIGURE 6.6: Distributions of two of the main discriminating variables for signal and backgrounds, with all the $\mathrm{SR_{1B}}$ cuts applied, apart from the one on the plotted variable. The lower pad shows the significance obtained by selecting events at each value of the histogram's bins.

Requirement / Region	$\mathrm{SR_{1A}}$	$\mathrm{SR_{1B}}$
Third leading lepton p_T [GeV]	> 20	> 20
n_jets ($p_\mathrm{T} > 30$ GeV)	≥ 4	≥ 5
$n_{b-\mathrm{tagged\,jets}}$ ($p_\mathrm{T} > 30$ GeV)	≥ 1	≥ 1
Leading b-tagged jet p_T [GeV]	–	> 100
$E_\mathrm{T}^\mathrm{miss}$ [GeV]	> 250	> 150
$p_\mathrm{T}^{\ell\ell}$ [GeV]	–	> 150
$m_\mathrm{T2}^{3\ell}$[GeV]	> 100	–

TABLE 6.3: Definition of the signal region selections used to target the $\tilde{t}_1$ models.

To further improve the exclusion power of the analysis, two multi-bin fit are defined. $\mathrm{SR_{1A}}$ and $\mathrm{SR_{1B}}$ are additionally split in four $E_\mathrm{T}^\mathrm{miss}$ bins and four $p_\mathrm{T}^{\ell\ell}$ bins respectively. In the case of $\mathrm{SR_{1A}}$, an additional bin in the range of $E_\mathrm{T}^\mathrm{miss}$ (200,250) is added to improve the exclusion depth for low-mass signal models. Tables 6.4 and 6.5 present the expected background and signal yields obtained in each bin.

The expected sensitivity achieved with this strategy, presented in Figure 6.7, allows to increase the range of sparticle masses tested in these kind of models, particularly improving in the case of high $\tilde{\chi}_2^0$ masses.

	$\mathrm{SR_{1A}}$ bin1	$\mathrm{SR_{1A}}$ bin2	$\mathrm{SR_{1A}}$ bin3	$\mathrm{SR_{1A}}$ bin4
$E_{\mathrm{T}}^{\mathrm{miss}}$ [GeV]	$(200-250)$	$(250-300)$	$(300-350)$	>350
Total SM events	5.2 ± 0.7	2.3 ± 0.4	1.4 ± 0.3	1.9 ± 0.4
Multi-boson	0.5 ± 0.1	0.21 ± 0.07	0.12 ± 0.04	0.27 ± 0.07
$t\bar{t}Z$	2.9 ± 0.4	1.1 ± 0.2	0.7 ± 0.2	0.8 ± 0.2
FNP	0.6 ± 0.3	0.3 ± 0.2	0.18 ± 0.03	0.3 ± 0.2
tZ and tWZ	0.5 ± 0.3	0.4 ± 0.2	0.3 ± 0.2	0.2 ± 0.1
Others	0.7 ± 0.2	0.34 ± 0.09	0.17 ± 0.06	0.27 ± 0.07
$m(\tilde{t}_1)=1000$ GeV, $m(\tilde{\chi}_2^0)=350$ GeV	0.71 ± 0.07	0.84 ± 0.09	0.74 ± 0.08	2.9 ± 0.2
$m(\tilde{t}_1)=1000$ GeV, $m(\tilde{\chi}_2^0)=500$ GeV	0.71 ± 0.07	1.0 ± 0.1	1.0 ± 0.1	4.1 ± 0.3
$m(\tilde{t}_1)=1000$ GeV, $m(\tilde{\chi}_2^0)=800$ GeV	0.36 ± 0.04	0.43 ± 0.05	0.62 ± 0.07	3.9 ± 0.3

TABLE 6.4: Expected yields in the four $E_{\mathrm{T}}^{\mathrm{miss}}$ bins of $\mathrm{SR_{1A}}$, for an integrated luminosity of $139\,\mathrm{fb}^{-1}$.

	$\mathrm{SR_{1B}}$ bin1	$\mathrm{SR_{1B}}$ bin2	$\mathrm{SR_{1B}}$ bin3	$\mathrm{SR_{1B}}$ bin4
$p_{\mathrm{T}}^{\ell\ell}$ [GeV]	$(150-300)$	$(300-450)$	$(450-600)$	>600
Total SM events	7.1 ± 0.9	3.7 ± 0.6	1.6 ± 0.3	1.02 ± 0.22
Multi-boson	1.0 ± 0.3	0.42 ± 0.09	0.22 ± 0.06	0.16 ± 0.06
$t\bar{t}Z$	4.8 ± 0.6	2.5 ± 0.4	1.1 ± 0.2	0.58 ± 0.12
FNP	$--$	0.04 ± 0.02	$--$	$--$
tZ and tWZ	1.0 ± 0.5	0.6 ± 0.3	0.3 ± 0.2	0.3 ± 0.2
Others	0.32 ± 0.08	0.04 ± 0.01	$--$	$--$
$m(\tilde{t}_1)=800$ GeV, $m(\tilde{\chi}_2^0)=130$ GeV	6.9 ± 0.5	3.8 ± 0.3	1.3 ± 0.1	0.56 ± 0.07
$m(\tilde{t}_1)=850$ GeV, $m(\tilde{\chi}_2^0)=130$ GeV	6.6 ± 0.4	1.9 ± 0.1	1.4 ± 0.2	1.0 ± 0.1
$m(\tilde{t}_1)=900$ GeV, $m(\tilde{\chi}_2^0)=130$ GeV	3.4 ± 0.2	1.8 ± 0.1	0.7 ± 0.1	1.1 ± 0.1

TABLE 6.5: Expected yields in the four $p_{\mathrm{T}}^{\ell\ell}$bins of $\mathrm{SR_{1B}}$, for an integrated luminosity of $139\,\mathrm{fb}^{-1}$.

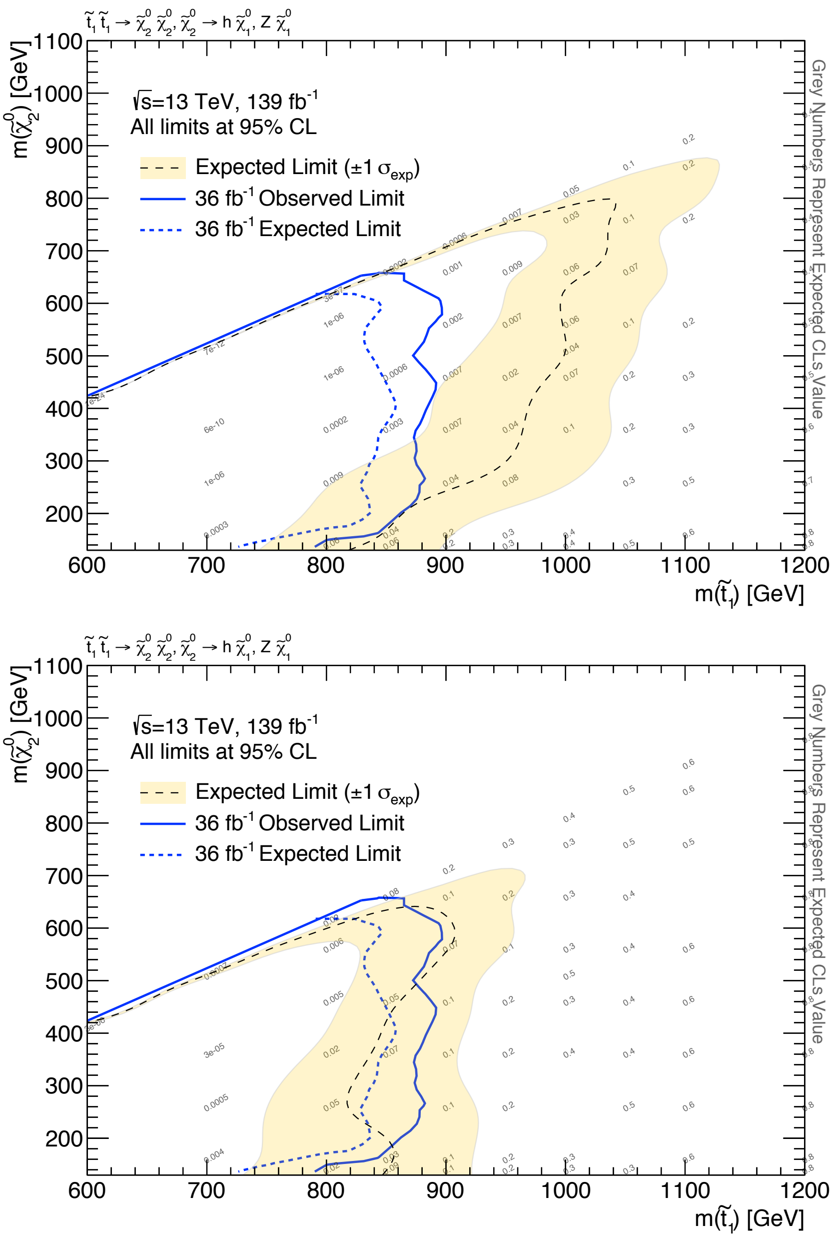

FIGURE 6.7: Expected exclusion obtained with SR$_{1A}$ (top) and SR$_{1B}$ (bottom). In the latter, the expected sensitivity is improved in the difficult scenarios where the $\tilde{\chi}_2^0$ mass is low and there is just enough phase space to produce an on-shell Z boson. I both plots, the grey numbers show the CL_s obtained for each signal model tested; the black dashed line and the yellow band are the expected limit obtained with the interpolation and its $\pm 1\sigma$ uncertainty, respectively. The blue lines show the previous results obtained looking at this phase space with the partial Run 2 dataset [91].

Signal regions targeting the $\tilde{t}_2$ models

Two SRs are optimised for the $\tilde{t}_2 \to Z\tilde{t}_1$ with $\tilde{t}_1 \to bff'\tilde{\chi}_1^0$ models, $\mathrm{SR_{2A}}$ and $\mathrm{SR_{2B}}$, targeting small and large mass splittings between the $\tilde{t}_2$ and the $\tilde{\chi}_1^0$ respectively. Due to the overall soft kinematics of the particles in compressed $\tilde{t}_2$ signals, $\mathrm{SR_{2A}}$ features upper bounds on the p_T of the third leading lepton and on $p_\mathrm{T}^{\ell\ell}$, as well as no requirement on the number of b-tagged jets since they are likely to be soft in this scenario and can be missed. On the opposite side, when $\Delta m(\tilde{t}_2, \tilde{t}_1)$ is large, both the Z and the $\tilde{t}_1$ acquire some momentum, and all the decay products are in average more energetic; this is reflected in the choice of cuts for the $\mathrm{SR_{2B}}$ definition, which features higher $E_\mathrm{T}^\mathrm{miss}$ and $p_\mathrm{T}^{\ell\ell}$ requirements, and relax the upper cut on the third lepton p_T. The list of cuts applied to both SRs is presented in Table 6.6, two examples of kinematic variables are instead shown in Figure 6.8.

In order to extend the sensitivity for less energetic signal models, $\mathrm{SR_{2B}}$ is supplemented with three more independent regions, defined by relaxing the cuts on the $E_\mathrm{T}^\mathrm{miss}$ and on the $p_\mathrm{T}^{\ell\ell}$ distributions, as sketched in Figure 6.9. This allows for an increase in the sensitivity, especially at lower $\tilde{t}_2$

Requirement / Region	$\mathrm{SR_{2A}}$	$\mathrm{SR_{2B}}$
Third leading lepton p_T [GeV]	< 20	< 60
n_jets ($p_\mathrm{T} > 30$ GeV)	≥ 3	≥ 3
$n_{b-\mathrm{tagged\,jets}}$ ($p_\mathrm{T} > 30$ GeV)	–	≥ 1
Leading jet p_T [GeV]	> 150	–
$E_\mathrm{T}^\mathrm{miss}$ [GeV]	> 200	> 350
$p_\mathrm{T}^{\ell\ell}$ [GeV]	< 50	> 150

TABLE 6.6: Definition of the signal regions used to target the $\tilde{t}_2$ models.

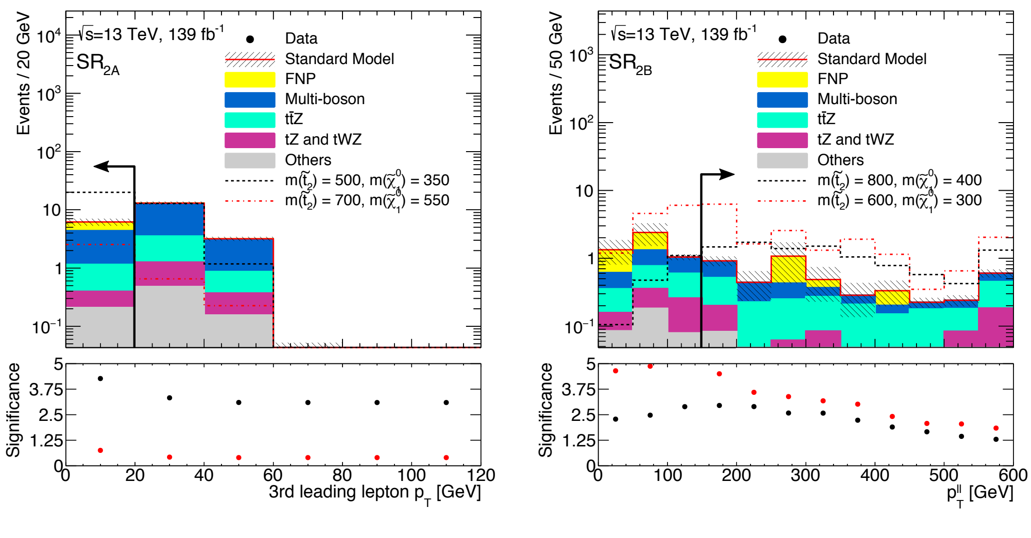

FIGURE 6.8: Distribution of the third lepton p_T in $\mathrm{SR_{2A}}$ (left) and $p_\mathrm{T}^{\ell\ell}$ in $\mathrm{SR_{2B}}$ (right), for signal and backgrounds. The SRs cuts are applied, apart from the one on the plotted variable. The lower pad shows the significance obtained by selecting events at each value of the histogram's bins, in the direction of the arrow.

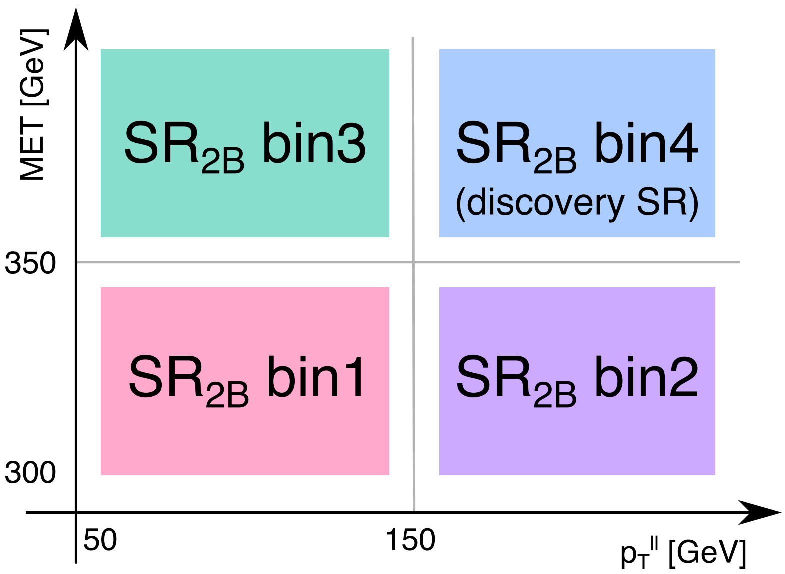

FIGURE 6.9: The four different kinematic selections applied to increase the sensitivity of SR_{2B}.

	SR_{2A}
Total SM events	6.2 ± 1.6
Multi-boson	3.2 ± 0.9
$t\bar{t}Z$	0.8 ± 0.3
FNP	1.8 ± 1.1
tZ and tWZ	0.2 ± 0.1
Others	0.21 ± 0.06
$m(\tilde{t}_2) = 500$ GeV, $m(\tilde{\chi}_1^0) = 350$ GeV	13.8 ± 1.4
$m(\tilde{t}_2) = 700$ GeV, $m(\tilde{\chi}_1^0) = 550$ GeV	2.0 ± 0.2
$m(\tilde{t}_2) = 800$ GeV, $m(\tilde{\chi}_1^0) = 400$ GeV	0.20 ± 0.02
$m(\tilde{t}_2) = 600$ GeV, $m(\tilde{\chi}_1^0) = 300$ GeV	1.3 ± 0.1

TABLE 6.7: Expected yields in the SRs targeting $\tilde{t}_2$ models, for an integrated luminosity of $139\,\text{fb}^{-1}$. The errors shown are the statistical uncertainties only.

masses, and it is particularly important as this is the first search at the LHC for this specific signal topology.

All five SRs defined in this way, are orthogonal in terms of $p_T^{\ell\ell}$ or E_T^{miss}, making them statistical independent and therefore easily combinable for the final interpretation. The expected sensitivity obtained in this way is shown in Figure 6.10, as a function of the $\tilde{t}_2$ and the $\tilde{\chi}_1^0$ masses. To produce the exclusion contours the full systematics uncertainties, as described if Section 6.5 have been considered for the backgrounds.
The expected exclusion is compared with the limits obtained from the analysis presented in Chapter 5, for the correct combination of masses ($\Delta m(\tilde{t}_1, \tilde{\chi}_1^0) = 40$ GeV). Using the $\tilde{t}_2$ decay products as proxy to discriminate from the SM background, it is possible to reach sensitivity to higher $\tilde{\chi}_1^0$ masses, with respect to the traditional searches.

	SR_{2B} bin1	SR_{2B} bin2	SR_{2B} bin3	SR_{2B} bin4
E_T^{miss} [GeV]	$(300-350)$	$(300-350)$	>350	>350
$p_T^{\ell\ell}$ [GeV]	$(50-150)$	>150	$(50-150)$	>150
Total SM events	4.1 ± 0.6	4.7 ± 0.7	4.9 ± 0.8	5.7 ± 0.9
Multi-boson	1.1 ± 0.3	1.0 ± 0.3	1.5 ± 0.4	1.8 ± 0.4
$t\bar{t}Z$	1.4 ± 0.2	2.4 ± 0.4	1.2 ± 0.2	2.2 ± 0.4
FNP	0.8 ± 0.2	0.73 ± 0.08	1.2 ± 0.2	0.7 ± 0.1
tZ and tWZ	0.4 ± 0.2	0.5 ± 0.3	0.7 ± 0.4	1.0 ± 0.5
Others	0.4 ± 0.1	0.12 ± 0.03	0.36 ± 0.08	0.16 ± 0.03
$m(\tilde{t}_1) = 500$ GeV, $m(\tilde{\chi}_1^0) = 350$ GeV	5.0 ± 0.5	1.10 ± 0.08	11.7 ± 0.9	4.3 ± 0.2
$m(\tilde{t}_1) = 700$ GeV, $m(\tilde{\chi}_1^0) = 550$ GeV	0.63 ± 0.07	0.13 ± 0.01	0.84 ± 0.06	0.27 ± 0.01
$m(\tilde{t}_1) = 800$ GeV, $m(\tilde{\chi}_1^0) = 400$ GeV	0.34 ± 0.04	2.5 ± 0.2	1.3 ± 0.1	8.9 ± 0.5
$m(\tilde{t}_1) = 600$ GeV, $m(\tilde{\chi}_1^0) = 300$ GeV	4.7 ± 0.5	12.1 ± 0.9	8.6 ± 0.7	14.2 ± 0.7

TABLE 6.8: Expected yields in the SRs targeting $\tilde{t}_2$ models, for an integrated luminosity of 139 fb^{-1}. The errors shown are the statistical uncertainties only.

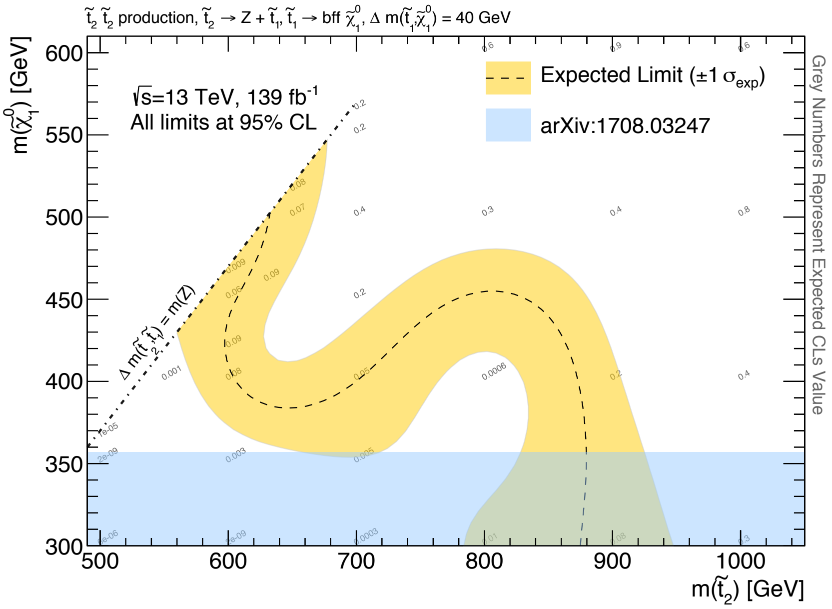

FIGURE 6.10: Expected exclusion obtained combining the 5 signal regions targeting the $\tilde{t}_2$ models. The grey numbers show the CL_s obtained for each signal model tested, the black dashed line and the yellow band mark the expected exclusion contour and its its $\pm 1\sigma$ uncertainty. The light blue already excluded area is derived from the constraints obtained from the analysis presented in Chapter 5 for the correct mass combinations.

6.4 Background estimation

As shown in Tables 6.4, 6.5, 6.7 and 6.8, the dominant SM background contribution in all the SRs is expected to originate from $t\bar{t}Z$ production, from multi-boson production (mainly WZ) and from backgrounds containing at least one non-prompt or mis-identified (fakes) lepton. The normalisation of the $t\bar{t}Z$ and multi-boson backgrounds is obtained by fitting the yield from MC simulation to the observed data in dedicated CRs enhanced in one of the two background components, and then extrapolating this yield to the SRs, with the mechanism explained in Chapter 4. The estimation of the background arising from fake or non-prompt leptons is estimated with the Matrix Method, a data driven techniques which is comprehensively described in Chapter 5.

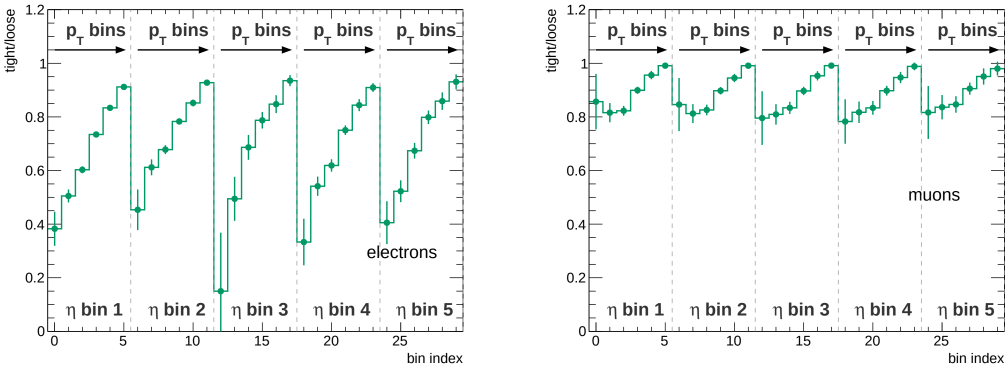

FIGURE 6.11: The probability for prompt *loose* leptons to satisfy the *tight* selection. The Figure shows the efficiencies parametrised as a function of p_{T} and η, as they are used in the Matrix Method, for electrons (left) and muons (right). The p_{T} distribution is divided in the following bins: $(5;7), (7;12), (12;20), (20;35), (35;50), > 50$.

Backgrounds from other sources (mostly tZ, tWZ, $t\bar{t}W$ and other rare SM processes), which provide a subdominant contribution to the SRs, are determined from MC simulation only.
For each set of signal regions, a simultaneous “background fit” is performed to the numbers of events found in the CRs, where the normalisations of the $t\bar{t}Z$ and the multi-boson backgrounds are allowed to float freely, while the other backgrounds are fixed to the estimate from simulation or data-driven techniques. The impact of the systematic uncertainties considered in the fit is described in Section 6.5. The level of agreement of the predictions for the main backgrounds is compared with data in dedicated validation regions (VRs).

Fake and non-prompt lepton background

The background from fake and non-prompt leptons (FNP) is estimated from data with the Matrix Method; the description of this procedure is given in Chapter 5, while this section is dedicated to its application to this analysis.
Two types of lepton identification criteria are defined for this evaluation: *tight* and *loose*, corresponding to the signal and baseline electrons and muons described in Section 6.2. The method relates the number of events containing FNP leptons to the number of observed events with *tight* or *loose* leptons using the probability for *loose* prompt or FNP leptons to satisfy the *tight* criteria.
The probability for prompt *loose* leptons to satisfy the *tight* selection is determined from $t\bar{t}Z$ MC simulation, corrected to model the data. The events are selected with a similar topology to the analysis CRs and SRs: at least 4 jets with $p_{\mathrm{T}} > 30$ GeV and at least one b-jet. Prompt leptons are selected using truth matching, to remove any possible contamination from fake leptons, and proper correction factors, obtained by comparing $Z \to \ell^+\ell^-$ ($\ell = e, \mu$) events in data and MC simulation, are applied to both the *loose* and *tight* selection. The results, parametrised as a function of p_{T} and η, are shown in Figure 6.11, for both electrons and muons.

The equivalent probability for *loose* FNP leptons to pass the *tight* selection is measured in a data sample enhanced in $t\bar{t}$ using events with one electron and one muon with the same charge plus at least one b-tagged jet. The contamination from prompt leptons, which could bias the measurement, is evaluated from MC simulations and subtracted from both the *loose* and the *tight*

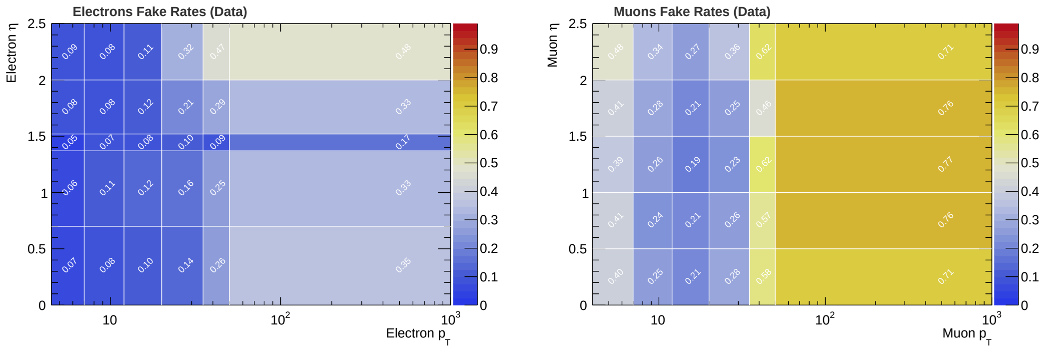

FIGURE 6.12: Probability for FNP *loose* leptons to satisfy the *tight* selection, calculated in $e\mu$ SS events. The Figure shows the efficiencies parametrised as a function of p_{T} and η, as they are used in the Matrix Method, for electrons (left) and muons (right).

Requirement / Region	$\mathrm{VR}_{1\mathrm{F}}$	$\mathrm{VR}_{2\mathrm{F}}$
	No SF-OS pair	
	At least one DF-OS pair	
Third leading lepton p_{T} [GeV]	> 20	< 60
n_{jets} ($p_{\mathrm{T}} > 30$ GeV)	≥ 3	≥ 3
$n_{b-\mathrm{tagged\,jets}}$ ($p_{\mathrm{T}} > 30$ GeV)	≥ 1	–
$E_{\mathrm{T}}^{\mathrm{miss}}$ [GeV]	> 50	> 150

TABLE 6.9: Definition of the regions used to validate the FNP lepton estimation.

samples, before the computation of the rates. The results obtained with the lepton definition used for this analysis are presented in Figure 6.12, for both electrons and muons.

The estimation for the FNP background is validated in dedicated validation regions, which are enriched in these events and at the same time reflect the SRs selections in terms of kinematics and composition. Two VRs are defined in Table 6.9, with $\mathrm{VR}_{1\mathrm{F}}$ probing the lepton p_{T} regime in $\mathrm{SR}_{1\mathrm{A}}$ and $\mathrm{SR}_{1\mathrm{B}}$, while $\mathrm{VR}_{2\mathrm{F}}$ includes soft lepton requirements as in $\mathrm{SR}_{2\mathrm{A}}$ and $\mathrm{SR}_{2\mathrm{B}}$. These VRs are made orthogonal to the CRs and SRs thanks to a veto on events with SF-OS dilepton pairs and require to have at least one different flavour and opposite sign (DF-OS) dilepton pair; in this way, the FNP component is also enhanced. The similarity in terms of composition (leptons arising from hadron decays, photon conversions, etc. . .) of the FNP leptons between the SRs and the respective VRs is studied looking at the truth information of $t\bar{t}$ and $Z \rightarrow \ell^+\ell^-$ simulated events, which enter the region selections, as illustrated in Figure 6.13.

The observed and expected yields in these VRs are shown in Table 6.10, with a purity of FNP leptons above 55% and with good agreement between data and the background estimation. The data-driven estimation allows for a good modelling of the kinematic variables exploited in the analysis, as can be seen in Figures 6.14 and 6.15, which show an example of the main distributions of the events in the $\mathrm{VR}_{1\mathrm{F}}$ and $\mathrm{VR}_{2\mathrm{F}}$ respectively.

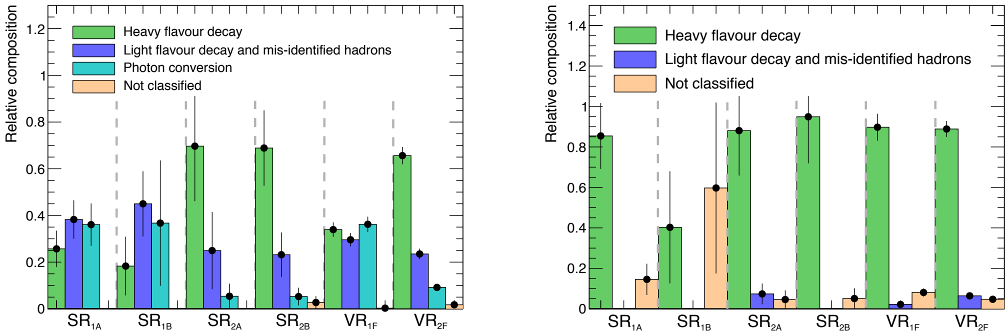

FIGURE 6.13: Origin of the fake electrons (left) and muons (right) in SRs and VRs, studied with $t\bar{t}$ and $Z \to \ell^+\ell^-$ simulated events.

	$\mathrm{VR_{1F}}$	$\mathrm{VR_{2F}}$
Observed events	84	98
Total (post-fit) SM events	98 ± 28	95 ± 33
Post-fit, multi-boson	0.7 ± 0.2	2.8 ± 0.7
Post-fit, $t\bar{t}Z$	8.7 ± 1.6	2.9 ± 0.6
Fake/non-prompt leptons	54 ± 27	76 ± 32
tZ, tWZ	0.9 ± 0.5	0.40 ± 0.21
Others	33 ± 5	13.4 ± 2.6

TABLE 6.10: Background fit results it the FNP validation regions. The number of $t\bar{t}Z$ and multi-boson background events is estimated as described in Section 6.4 and uncertainties quoted already include both statistics and systematic errors, as described in Section 6.5.

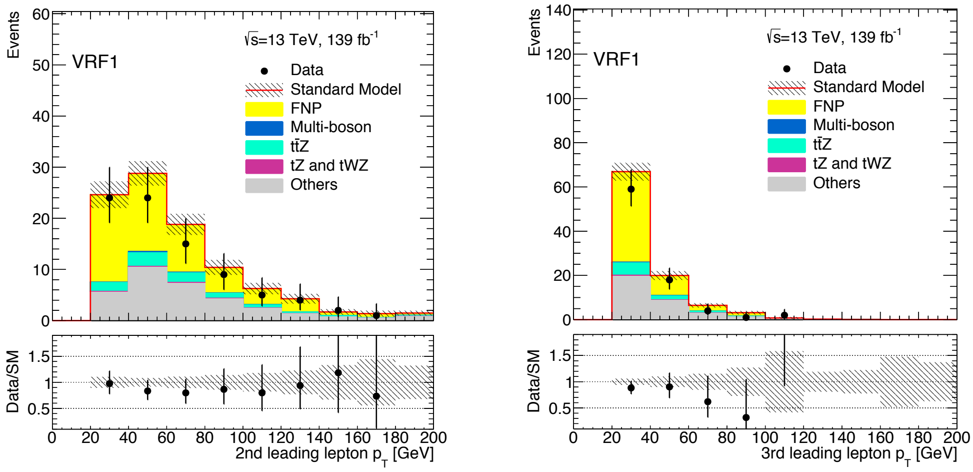

FIGURE 6.14: Distributions of the second (left) and the third (right) lepton p_{T} in $\mathrm{VR_{1F}}$. The contribution from all SM backgrounds is shown as a histogram stack and the striped the bands represent the total uncertainty in the background prediction. The fake and non-prompt lepton background is estimated from data, the other backgrounds are estimated with MC simulation. The lower panels show the ratio of the observed data to the total SM background prediction.

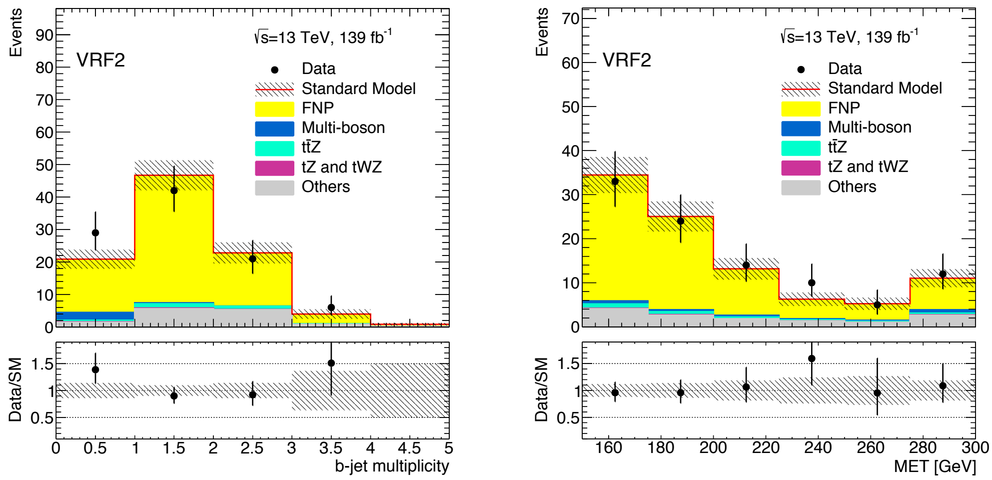

FIGURE 6.15: b-jet multiplicity (left) and $E_{\mathrm{T}}^{\mathrm{miss}}$ (right) distributions in $\mathrm{VR_{2F}}$. The contribution from all SM backgrounds is shown as a histogram stack and the striped the bands represent the total uncertainty in the background prediction. The fake and non-prompt lepton background is estimated from data, the other backgrounds are estimated with MC simulation. The lower panels show the ratio of the observed data to the total SM background prediction.

$t\bar{t}Z$ and multi-boson background

The two dedicated control regions, used for the $t\bar{t}Z$ ($\mathrm{CR}_{t\bar{t}Z}$) and multi-boson (CR_{VV}) background estimation, are defined in Table 6.11. To ensure orthogonality with the SRs, only events with $E_{\mathrm{T}}^{\mathrm{miss}} < 100$ GeV are included in $\mathrm{CR}_{t\bar{t}Z}$, while a b-tagged jet veto and $E_{\mathrm{T}}^{\mathrm{miss}} < 200$ GeV requirements are applied in CR_{VV}.
To validate the background estimation procedure, three validation regions are defined, in a corner of the phase space suitable to check the extrapolation towards the SRs, as show in Table 6.12. The $\mathrm{VR}_{t\bar{t}Z}$ region primarily validates the $t\bar{t}Z$ background estimation in an intermediate $E_{\mathrm{T}}^{\mathrm{miss}}$ region (100 GeV$< E_{\mathrm{T}}^{\mathrm{miss}} < 150$ GeV.) The $\mathrm{VR}_{VV}^{\text{n-jet}}$ and $\mathrm{VR}_{VV}^{b\text{-tag}}$ regions, instead, are designed for the validation of the multi-boson background, the former focusing on the extrapolation in jet multiplicity and the latter on the extrapolation from events without to events with b-tagged jets. These regions are not independent (their overlap is around 50%) but they are useful to provide a validation in the two different regimes of the CRs and the SRs. The normalisation factor obtained for the $t\bar{t}Z$ sample is $\mu_{ttZ} = 0.97 \pm 0.17$ and for the multi-boson backgrounds $\mu_{VV} = 0.84 \pm 0.20$. Table 6.13 shows the observed and expected yields in the CRs and VRs for each background source before and after the fit, while Figure 6.16 and Figure 6.17 show the jet multiplicity distribution after the background fit for the CRs and VRs, respectively. The post-fit agreement with data is good in all the regions and the distributions are well modelled.

Requirement / Region	$\mathrm{CR}_{t\bar{t}Z}$	CR_{VV}
Second lepton p_T [GeV]	> 20	> 20
Third lepton p_T [GeV]	> 20	> 20
$n_\mathrm{jets}(p_\mathrm{T} > 30$ GeV$)$	≥ 4	≥ 3
$n_{b-\mathrm{tagged\,jets}}$ $(p_\mathrm{T} > 30$ GeV$)$	≥ 1	0
$E_\mathrm{T}^\mathrm{miss}$ [GeV]	$50 - 100$	$50 - 200$

TABLE 6.11: Definition of the control regions used for the $t\bar{t}Z$ and multi-boson background estimation.

Requirement / Region	$\mathrm{VR}_{t\bar{t}Z}$	$\mathrm{VR}_{VV}^{\text{n-jet}}$	$\mathrm{VR}_{VV}^{b\text{-tag}}$
Second lepton p_T [GeV]	> 20	> 40	> 40
Third lepton p_T [GeV]	> 20	> 40	> 40
$n_\mathrm{jets}(p_\mathrm{T} > 30$ GeV$)$	≥ 3	≥ 3	3
$n_{b-\mathrm{tagged\,jets}}$ $(p_\mathrm{T} > 30$ GeV$)$	≥ 1	0	≥ 0
$E_\mathrm{T}^\mathrm{miss}$ [GeV]	$100 - 150$	$200 - 300$	$200 - 300$

TABLE 6.12: Definition of the validation regions for the $t\bar{t}Z$ and multi-boson background estimation.

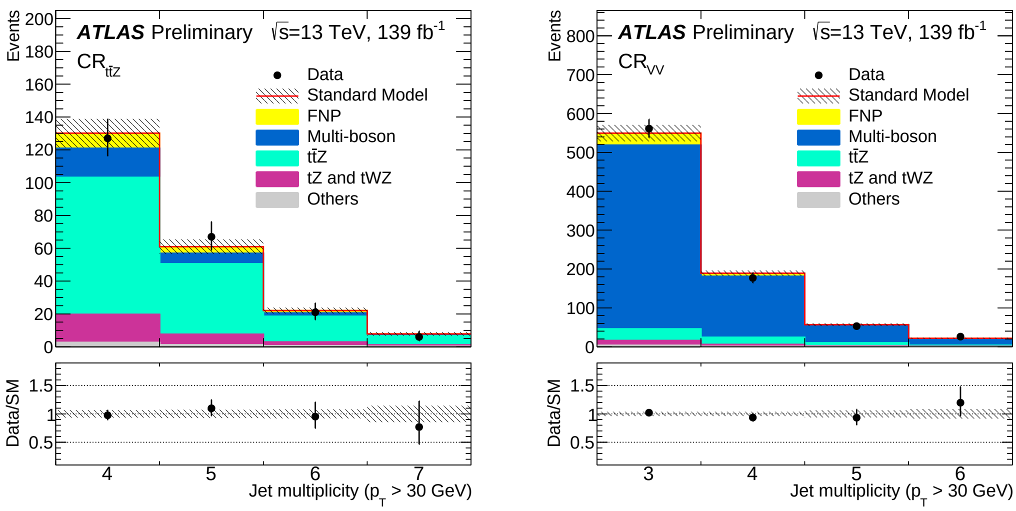

FIGURE 6.16: Jet multiplicity distributions in control regions $\mathrm{CR}_{t\bar{t}Z}$ (left) and CR_{VV} (right), after the normalisation of the $t\bar{t}Z$ and multi-boson background processes.

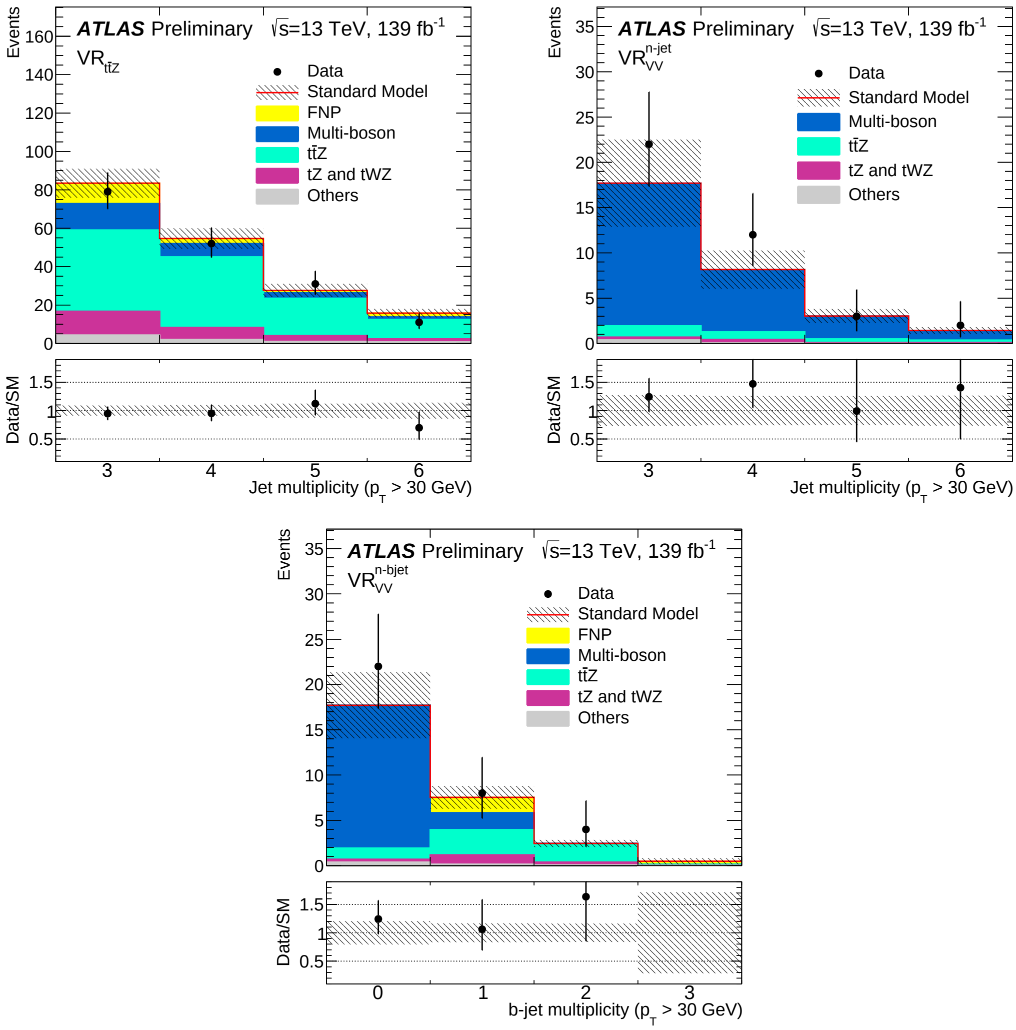

FIGURE 6.17: Jet and b-jet multiplicity distributions in the three validation regions, after the normalisation of the $t\bar{t}Z$ and multi-boson background processes.

	$\mathrm{CR}_{t\bar{t}Z}$	$\mathrm{VR}_{t\bar{t}Z}$	CR_{VV}	$\mathrm{VR}_{VV}^{\text{n-jet}}$	$\mathrm{VR}_{VV}^{b\text{-tag}}$
Observed events	221	173	817	39	34
Total (post-fit) SM events	221 ± 15	182 ± 16	817 ± 29	30 ± 8	27 ± 6
Post-fit, multi-boson	27 ± 7	25 ± 8	693 ± 34	26 ± 8	18 ± 6
Post-fit, $t\bar{t}Z$	148 ± 22	109 ± 19	59 ± 11	2.7 ± 0.5	6.1 ± 1.2
Fake/non-prompt leptons	15.1 ± 1.7	16.7 ± 1.9	41 ± 15	<1.5	$0.9^{+1.1}_{-0.9}$
tZ, tWZ	27 ± 14	23 ± 12	19 ± 10	0.9 ± 0.5	1.7 ± 0.9
Others	4.6 ± 0.8	8.0 ± 1.5	5.5 ± 2.0	0.42 ± 0.08	0.59 ± 0.11
Pre-fit, multi-boson	32.1 ± 3.1	30 ± 7	830 ± 190	31 ± 6	21 ± 4
Pre-fit, $t\bar{t}Z$	153 ± 13	112.2 ± 2.5	61.3 ± 2.7	2.82 ± 0.20	6.3 ± 0.4

TABLE 6.13: Background fit results for the control and validation regions. The nominal predictions from MC simulation are given for comparison for those backgrounds ($t\bar{t}Z$, multi-boson) that are normalised to data.

6.5 Systematic uncertainties

The effects of the systematic uncertainties are evaluated for all signal samples and background processes, as described in Section 4.4.
The modelling uncertainties on the diboson MC are estimated varying the renormalisation, factorisation, resummation and matching scales used for the generation of the nominal sample [87]. An additional uncertainty on the heavy flavour composition was tested in order to account for the extrapolation in number of b-jets between the CR and some of the SRs. The contribution from gluons splitting into $b\bar{b}$ pairs (studied at truth level) was varied by 30%, but the impact was found to be negligible. For $t\bar{t}Z$, the uncertainties related to the choice of renormalisation and factorisation scales are assessed by varying the corresponding event generator parameters up and down by a factor of two around their nominal values. The radiation uncertainties are evaluated comparing the nominal sample to dedicated samples with α_s varied [88]. The cross-sections used to normalise the MC samples (which are not normalised to data) are varied according to the uncertainty in the cross-section calculation, i.e. 13% for $t\bar{t}W$ production [77]. For $t\bar{t}WW$, tZ, tWZ, $t\bar{t}h$, Wh, Zh, $t\bar{t}t$, $t\bar{t}t\bar{t}$, and triboson production processes, which constitute a small background, a 50% uncertainty in the event yields is assumed.
Additional systematic uncertainties are assigned to the estimation of the background arising from non-prompt and mis-identified leptons. Those are evaluated to account for potentially different compositions (heavy flavour, light flavour or conversions) between the SRs and the regions were the efficiencies, input for the Matrix Method, are measured, as well as the contamination from prompt leptons in the regions used to measure such efficiencies.
The main sources of systematic uncertainty affecting this analysis are related to the background theoretical and modelling uncertainties, the uncertainties on the data-driven estimation of the FNP background, as well as the jet energy scale and resolution. Other detector-related systematic uncertainties, such as those related to the $E_{\mathrm{T}}^{\mathrm{miss}}$ modelling, as well as lepton reconstruction efficiency, energy scale and energy resolution are found to have a small impact on the results.
Table 6.14 summarises the contributions from the different sources of systematic uncertainty to the total SM background predictions in the signal regions.

	$\mathrm{SR_{1A}}$	$\mathrm{SR_{1B}}$	$\mathrm{SR_{2A}}$	$\mathrm{SR_{2B}}$
Total systematic uncertainty (%)	13	13	29	15
Diboson theoretical uncertainties (%)	2	3	11	5
$t\bar{t}Z$ theoretical uncertainties (%)	3	6	4	5
Other theoretical uncertainties (%)	6	9	2	9
MC and FNP statistical uncertainties (%)	6	<1	14	7
Diboson normalisation (%)	2	3	11	6
$t\bar{t}Z$ normalisation (%)	5	9	2	7
Fake/non-prompt leptons efficiency (%)	4	<1	14	2
Jet energy resolution (%)	4	3	2	2
Jet energy scale (%)	1	4	<1	1
b-tagging (%)	3	5	1	5

TABLE 6.14: Summary of the main systematic uncertainties and their impact (in %) on the total SM background prediction in each of the signal regions studied. The total systematic uncertainty can be different from the sum in quadrature of individual sources due to the correlations effects. The quoted theoretical uncertainties include both modelling and cross-section uncertainties.

6.6 Results

The observed number of events and expected yields are shown in Table 6.15 for each of the four inclusive SRs, and Figure 6.18 shows kinematic distributions after applying all the SR selection requirements except those on $E_{\mathrm{T}}^{\mathrm{miss}}$ or $p_{\mathrm{T}}^{\ell\ell}$. The data have been found to be in good agreement with SM background prediction in all the SRs.
The results obtained in the inclusive SRs are then interpreted as exclusion limits for new physics scenarios. Table 6.16 shows upper limits (at the 95% confidence level) on the visible BSM cross-section $\sigma_{\mathrm{vis}} = S_{\mathrm{obs}}^{95}/\mathcal{L}dt$, defined as the product of cross-section, SR acceptance and selection efficiency.

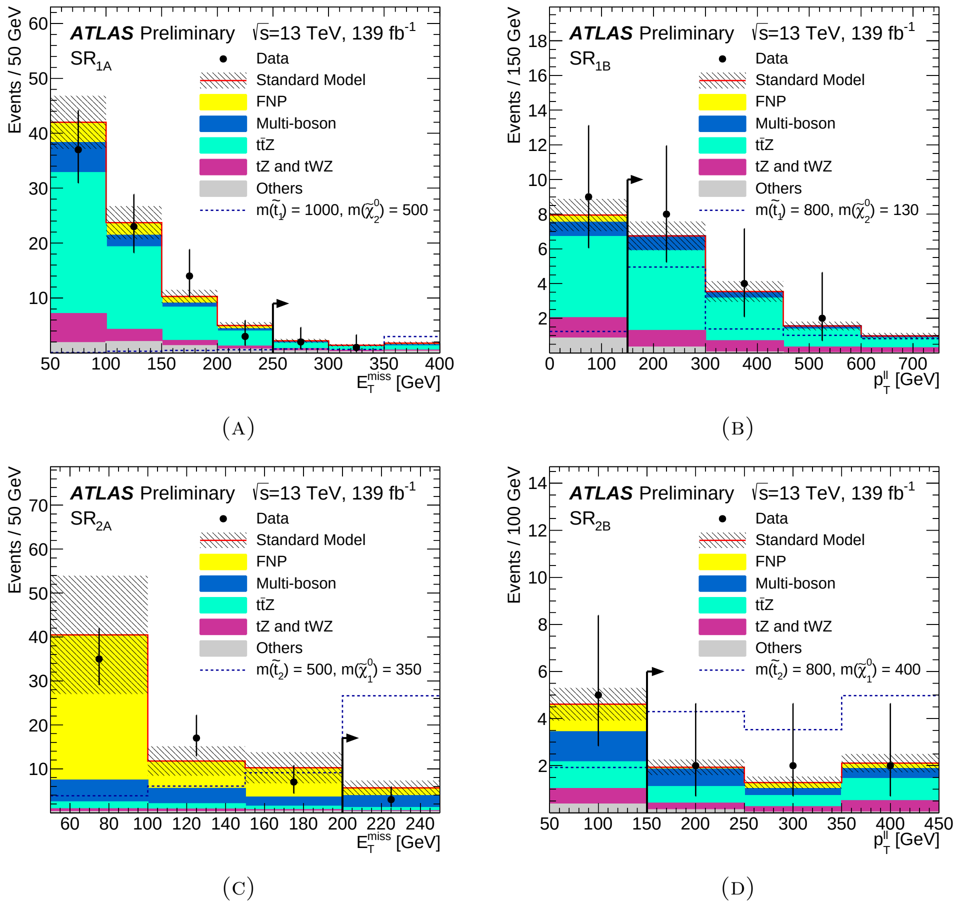

FIGURE 6.18: Distributions of (A) $E_{\mathrm{T}}^{\mathrm{miss}}$ in SR$_{1\mathrm{A}}$, (B) $p_{\mathrm{T}}^{\ell\ell}$ in SR$_{1\mathrm{B}}$, (C) $E_{\mathrm{T}}^{\mathrm{miss}}$ in SR$_{2\mathrm{A}}$, and (D) $p_{\mathrm{T}}^{\ell\ell}$ in SR$_{2\mathrm{B}}$ for events passing all the SR requirements except those on the variable shown (which are indicated by the arrows). The expected distributions for selected signal models are also shown as dashed lines.

Model-dependent limits are set for the two classes of SUSY models considered. For each signal hypothesis, the background fit is redone taking into account the signal contamination in the CRs, which is found to be below 12% for the signals with the higher cross-section. Correlations of the uncertainties between the SM backgrounds and the signals are taken into account. To enhance the exclusion power in the considered SUSY models, the binned versions of the SRs are used; a summary of the observed number of events and expected yields in all these bins is shown in Figure 6.19.

	SR_{1A}	SR_{1B}	SR_{2A}	SR_{2B}
Observed events	3	14	3	6
Total (post-fit) SM events	5.4 ± 0.7	12.8 ± 1.6	5.7 ± 1.7	5.4 ± 0.8
Post-fit, multi-boson	0.50 ± 0.22	1.5 ± 0.5	2.7 ± 1.0	1.5 ± 0.6
Post-fit, $t\bar{t}Z$	2.5 ± 0.5	8.7 ± 1.6	0.73 ± 0.29	2.1 ± 0.5
FNP	0.74 ± 0.24	0.04 ± 0.02	1.8 ± 1.1	0.65 ± 0.11
tZ, tWZ	0.9 ± 0.4	2.2 ± 1.2	0.19 ± 0.11	1.0 ± 0.5
Others	0.78 ± 0.17	0.37 ± 0.08	0.21 ± 0.06	0.16 ± 0.03
Pre-fit, multi-boson	0.59 ± 0.18	1.8 ± 0.5	3.2 ± 0.9	1.8 ± 0.4
Pre-fit, $t\bar{t}Z$	2.6 ± 0.4	8.9 ± 1.0	0.76 ± 0.27	2.2 ± 0.4

TABLE 6.15: Observed and expected numbers of events in the four inclusive signal regions. The pre-fit predictions from MC simulation are given for comparison for those backgrounds ($t\bar{t}Z$, multi-boson) that are normalised to data in the CRs.

	SR_{1A}	SR_{1B}	SR_{2A}	SR_{2B}
S^{95}_{obs}	4.6	10.9	4.9	7.0
S^{95}_{exp}	$6.1^{+2.5}_{-1.5}$	$9.4^{+3.3}_{-1.9}$	$6.2^{+2.5}_{-1.7}$	$6.5^{+2.5}_{-1.8}$
σ_{vis} [fb]	0.03	0.08	0.03	0.05
p_0	0.5	0.37	0.50	0.38

TABLE 6.16: Model-independent upper limits (at 95% confidence level) obtained using the four inclusive SRs. The limits are expressed in terms of the visible number of BSM events (S^{95}_{obs}), the number of BSM events given the expected number of background events (S^{95}_{exp}) and the visible BSM cross-section (σ_{vis}), as well as the discovery p-value (p_0) for the background-only hypothesis. The value of p_0 is capped at 0.5 if the number of observed events is below the number of expected events.

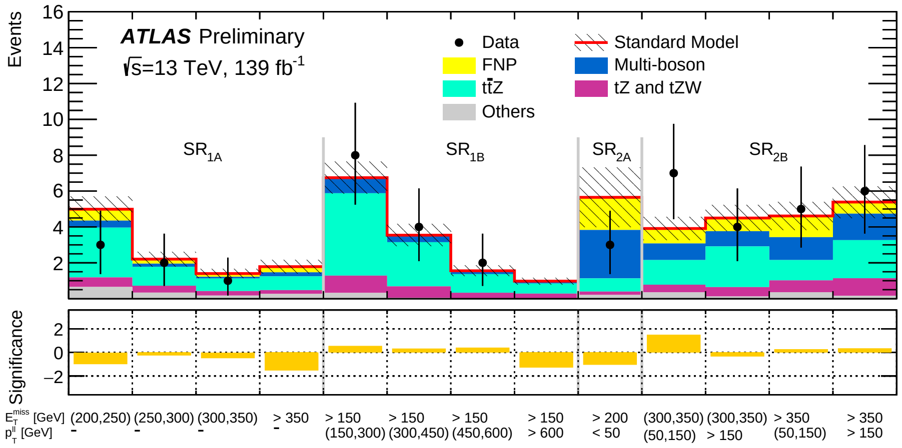

FIGURE 6.19: Comparison of the observed and expected event yields in all the SRs and bins used for the model-dependent exclusion limits. The lower panel shows the significance in each SR bin, computed as described in Equation 4.1.

Figure 6.20 shows the exclusion limits in the $\tilde{t}_1 \rightarrow t\tilde{\chi}_2^0$ with $\tilde{\chi}_2^0 \rightarrow h/Z\tilde{\chi}_1^0$ simplified model. Since $\mathrm{SR}_{1\mathrm{A}}$ and $\mathrm{SR}_{1\mathrm{B}}$ are not orthogonal, the two likelihood fit are performed separately for each combination of sparticle masses. The SR with the best expected sensitivity is considered to produce the final exclusion contour. For $\tilde{\chi}_2^0$ masses above 250 GeV, $\tilde{t}_1$ masses up to about 1050 GeV are excluded at 95% CL, while $\tilde{t}_1$ masses below 1140 GeV are excluded for a $\tilde{\chi}_2^0$ mass of 850 GeV. These results improve the existing limits on the $\tilde{t}_1$ mass in this model by approximately 200 GeV [91]. The observed exclusion limit is enhanced with respect to the expected one due to the under-fluctuation of data observed in the high-$E_{\mathrm{T}}^{\mathrm{miss}}$ bin of $\mathrm{SR}_{1\mathrm{A}}$.

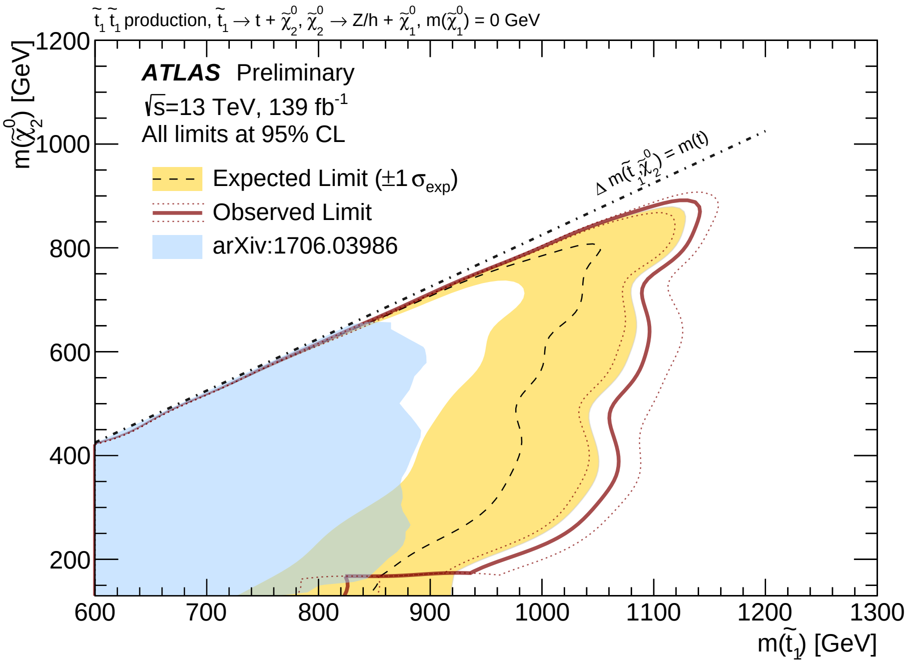

FIGURE 6.20: Exclusion limits at 95% CL on the masses of the $\tilde{t}_1$ and $\tilde{\chi}_2^0$, for a fixed massless $\tilde{\chi}_1^0$, assuming $\mathcal{B}(\tilde{\chi}_2^0 \rightarrow Z\tilde{\chi}_1^0) = 0.5$ and $\mathcal{B}(\tilde{\chi}_2^0 \rightarrow h\tilde{\chi}_1^0) = 0.5$. The dashed line and the yellow band are the expected limit and its $\pm 1\sigma$ uncertainty, respectively. The thick solid line is the observed limit for the central value of the signal cross-section. The dotted lines show the effect on the observed limit when varying the signal cross-section by $\pm 1\sigma$. Results are compared with the observed limits obtained by the previous ATLAS search in Ref. [91].

Figure 6.21 shows the exclusion limits in the $\tilde{t}_2 \rightarrow Z\tilde{t}_1$ with $\tilde{t}_1 \rightarrow bff'\tilde{\chi}_1^0$ simplified model. These results are obtained from the statistical combination of $\mathrm{SR}_{2\mathrm{A}}$ and the extended version of $\mathrm{SR}_{2\mathrm{B}}$. The shape of the contour is driven by $\mathrm{SR}_{2\mathrm{A}}$ and $\mathrm{SR}_{2\mathrm{B}}$ being most sensitive to respectively small and large splittings between the $\tilde{t}_2$ and the $\tilde{\chi}_1^0$. $\tilde{t}_2$ masses up to 875 GeV are excluded at 95% CL for a $\tilde{\chi}_1^0$ mass of about 350 GeV and $\tilde{\chi}_1^0$ masses of approximately 520 (450) GeV are excluded for $\tilde{t}_2$ masses of 650 (800) GeV, extending the previous limits on the $\tilde{\chi}_1^0$ mass, obtained with the analysis presented in Chapter 5, by up to 160 GeV.

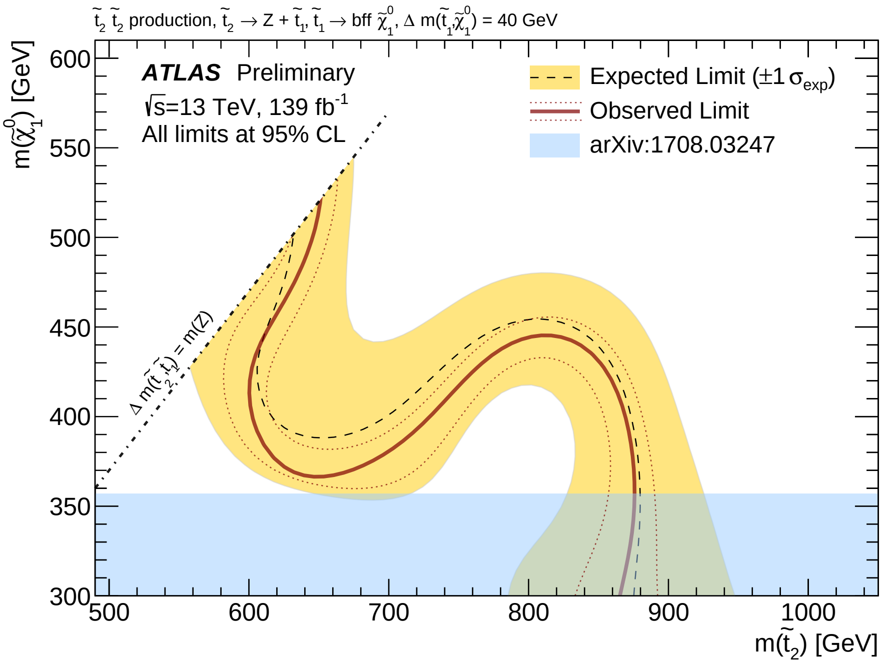

FIGURE 6.21: Exclusion limits at 95% CL on the masses of the $\tilde{t}_2$ and $\tilde{\chi}_1^0$, for a fixed $m(\tilde{t}_1) - m(\tilde{\chi}_1^0) = 40$ GeV and assuming $\mathcal{B}(\tilde{t}_2 \to Z\tilde{t}_1) = 1$. The dashed line and the yellow band are the expected limit and its $\pm 1\sigma$ uncertainty, respectively. The thick solid line is the observed limit for the central value of the signal cross-section. The dotted lines show the effect on the observed limit when varying the signal cross-section by $\pm 1\sigma$. Results are compared with the observed limits obtained by the search with two soft leptons in the final state, presented in Chapter 5.

Chapter 7

The ATLAS detector upgrades

The scientific programme of the LHC will continue, spanning over the next 20 years. It includes a series of upgrades to the accelerator complex, aimed at coolecting a total integrated luminosity for proton-proton collisions up to 4000 fb^{-1}. This represents more than an order of magnitude more data than what has been collected until now. The improvements necessary to achieve this performance will be realised during two long shutdowns, which are scheduled according to the time-line presented in Figure 7.1.

During the Long Shutdown 2 (LS2), which started in 2019 and will last until 2021, the accelerator injection chain is foreseen to be modified to allow for instantaneous luminosities up to 5×10^{34} $cm^{-2}s^{-1}$. The LHC dipole magnets will be prepared for an energy increase up to 14 TeV in the centre of mass, the nominal LHC value. In parallel, some detector upgrades are foreseen, to cope with the expected data-taking conditions. These upgrades include the introduction of the New Small Wheels (NSW) [98], a dedicated muon detector to improve the trigger efficiency in the forward region, and an improved hardware-level trigger system for the calorimeters [99].
The Long Shutdown 3 (LS3), starting at the end of 2023, will include major upgrades to the accelerator for the high-luminosity phase (HL-LHC). The HL-LHC environment, with a an instantaneous luminosity of 7.5×10^{34} $cm^{-2}s^{-1}$ and an average of 200 inelastic proton-proton collisions per beam-crossing, will be much beyond the specification for which the current ATLAS experiment was designed for. The increase of luminosity, along with the associated data rate and accumulated radiation damage, particularly affects the inner tracker, which would become inoperable. For this reason, the current Inner Detector will be replaced with a new all-silicon tracker (called ITk) to maintain optimal performances in this high-occupancy environment and

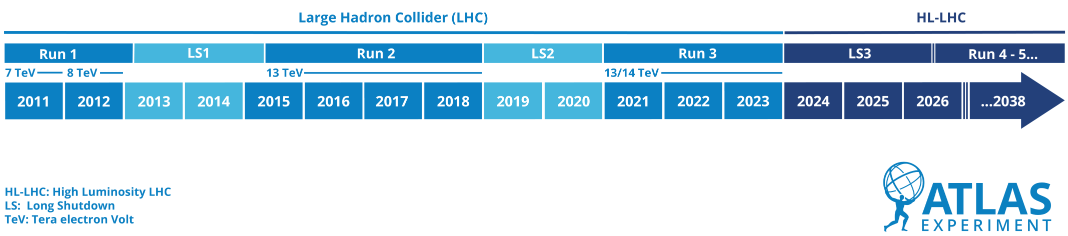

FIGURE 7.1: Expected timeline for the LHC and its upgrades.

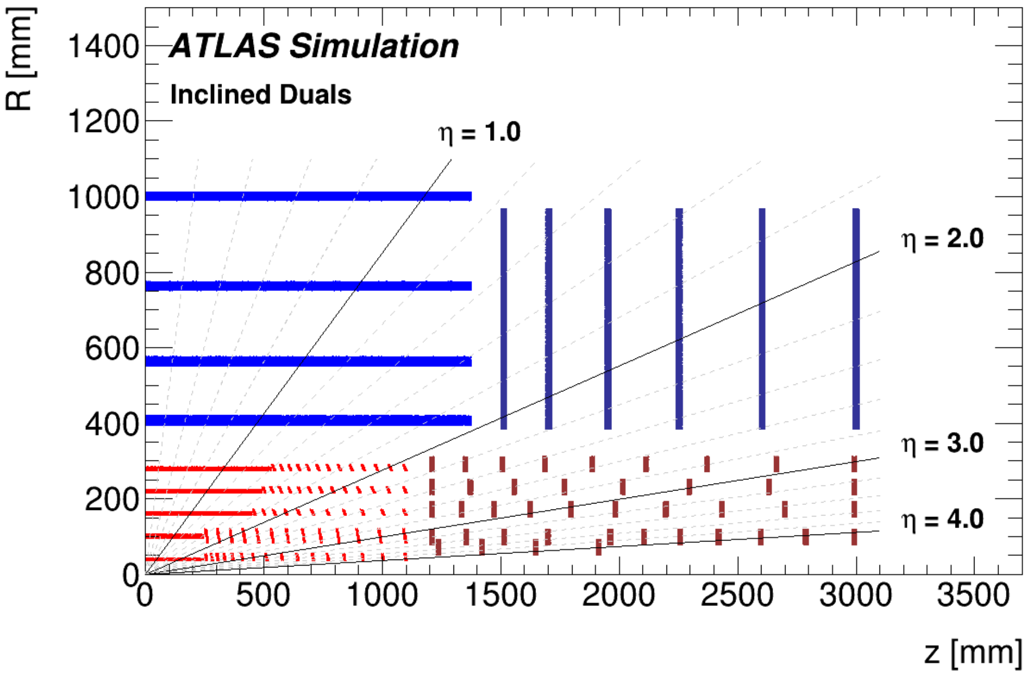

FIGURE 7.2: A schematic view of the proposed ITk layout [101].

to cope with the increase of the integrated radiation dose.
This Chapter is dedicated to the description of the ITk, the consequence of high levels of radiations on silicon sensors, and the measurements performed to study this effect on a pixel sensor prototypes.

7.1 The Inner Tracker (ITk)

The ITk [100, 101] is designed to be a fully silicon based detector, with the goal of delivering good tracking performances during the 10 years of data taking in the HL-LHC environment while extending the tracking coverage to a pseudorapidity of 4. The ITk will be inserted in the space currently occupied by the ID and will consists of two subsystems: a Strip Detector on the outside, which surrounds an internal Pixel Detector. The Strip Detector design foresees four barrel layers and six end-cap disks, both composed of double modules. The Pixel Detector will instead be composed by 5 layers. The combination of Strip and Pixel Detectors provides a total of 13 hits for $|\eta| < 2.7$, with the exception of the barrel/end-cap transition of the Strip Detector, where the hit count is 11. The Pixel Detector layout is then optimised to supply at least 13 hits from the end of the strip coverage in pseudorapidity up to $|\eta| < 4$, exploiting an inclined loyout of the external modules. Figure 7.2 illustrates the proposed layout, showing the pixel layers in red and the strip ones in blue.

Fluence and Radiation Dose in the ITk pixel detector

During the HL-HLC data-taking, the expected radiation levels in the ITk will increase by more than an order of magnitude compared to the present Inner Detector. When discussing the effect of radiation on silicon sensors, the damage arising from two different kind of effects has to be considered: the Total Ionising Dose (TID) and the Non-Ionising Energy Loss (NIEL).
The TID arises from charged particles which release their energy inside the detector through ionisation. The charges produced in this way inside silicon bulk are collected to the edge of the sensor, thanks to the electric potential difference applied, and are responsible for the defects on the surface of the sensor [102].
The NIEL, instead, is responsible for the displacement of atoms, producing defects in the lattice and altering the properties of charge mobility inside the sensor. The amount of non-ionising energy released in the silicon depends on the type and the energy of the particles considered. For this reason, to compare the damage due to different particles or different energies, the NIEL is expressed as the fluence of 1 MeV neutrons. This normalised fluence is obtained by reweigthing the effective fluence by a factor accounting for the differences in energy loss, with the so-called "hardness factor" κ defined in Equation 7.1 [103].

$$\kappa = \frac{\int D(E) \cdot \phi(E) dE}{D(E_n = 1 \text{ MeV}) \cdot \int \phi(E) dE} \tag{7.1}$$

Here $\phi(E)$ is the flux of the particles responsabile for the energy loss, $D(E)$ is the density of the non-ionising energy deposited by such particles and $D(E_n = 1 \text{ MeV})$ is the same quantity, defined for neutrons with an energy of 1 MeV.
To precisely assess the value of expected radiation damage arising from both effect in the ITk, simulations have been performed for using the PYTHIA [104] event generator and the FLUKA [105] particle transport code. The predictions of particle fluences and ionising doses are calculated considering the proposed layout and for an integrated luminosity of 4000 fb^{-1}. In Figure 7.3 the fluence and dose distributions for the Pixel Detector are shown. While fluences in the innermost layers of the ITk pixel barrel region are dominated by particles coming directly from the interaction point, the fluences in the outer barrel layers and the pixel end-cap region are increasingly dominated by particles coming from secondary interactions in the calorimeter, beam-line and pixel service material. In the baseline scenario, the outer pixel barrel and end-cap detector will be operated until the end of the data-taking, to collect the total integrated luminosity of up to 4000 fb^{-1}, while the inner barrel and end-caps will be replaced after 2000 fb^{-1}. A summary of the expected 1 MeV neutron equivalent fluences and the ionising dose are given in Table 7.1, in different part of the detector. All the sensors expected to populate the detector will have to respect these specifications, multiplied by a safety factor of 1.5 [101], to ensure optimal operations.

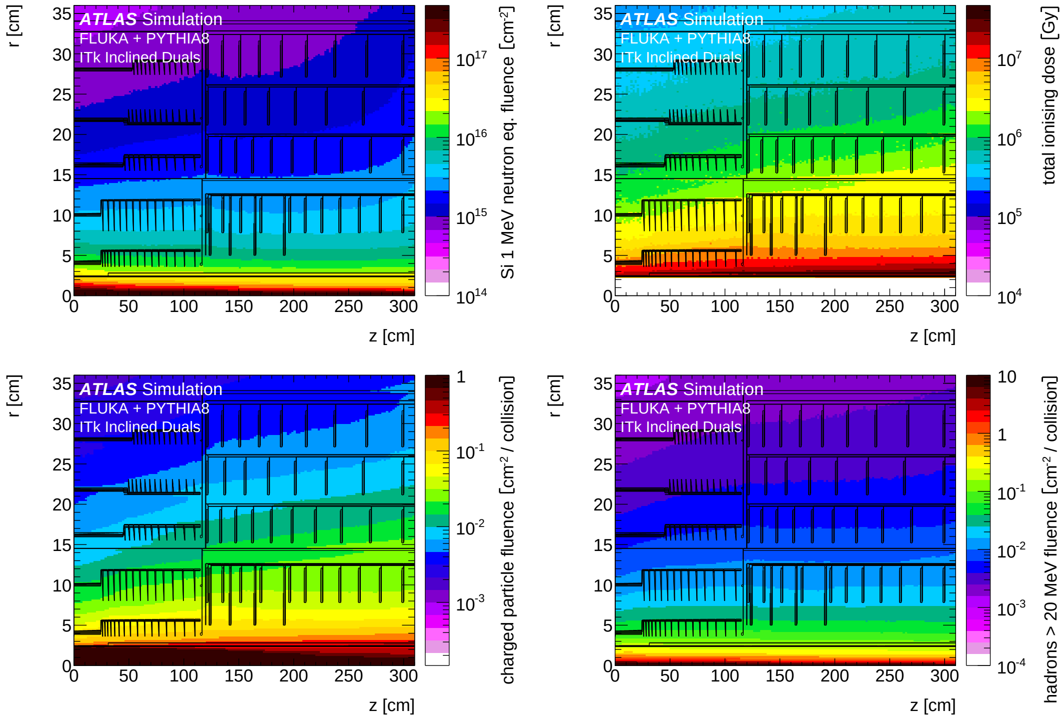

FIGURE 7.3: Expected fluence and dose distributions for the Pixel Detector. Top left: 1 MeV neutron equivalent fluence [101]. Top right: Total ionising dose. Bottom left: Charged particle fluence. Bottom right: Hadron fluence for energies greater than 20 MeV. The top two lots are normalised to 4000 fb-1, while the bottoms ones show the fluence per collision.

Location	r [cm]	z [cm]	fluence [10^{14} cm^{-2}]	TID [MGy]
Layer 0	3.9	121.0	147.7	11.57
Layer 1	7.5	121.0	58.9	6.46
Layer 2	15.5	72.0	16.8	0.93
Layer 3	21.3	72.0	10.9	0.59
Layer 4	27.1	72.0	8.0	0.38

TABLE 7.1: The 1 MeV neutron equivalent fluence and the total ionising dose for different parts of the Pixel Detector.

Pixel modules

Different sensor technologies have been proposed for the the ITk Pixel Detector, according for the different specifications in terms of radiation tolerance, size and number of channels required in each layer.

Thanks to its radiation tolerance, the 3D sensor technology is the baseline option for the innermost layer (Layer 0 and Ring 0), and a possible alternative for Layer 1. Such sensors are already exploited within the the ATLAS experiment, both for the IBL [52] and for the AFP [106]. The ITk will require further development of the 3D sensor technology [107]: a smaller pixel size, thinner active area and extreme radiation tolerance.

Planar pixel sensors have been proposed for the layers between 1 to 4. In constrast with the sensors presently used in the Pixel Detectors, the n-in-p technology has been chosen instead

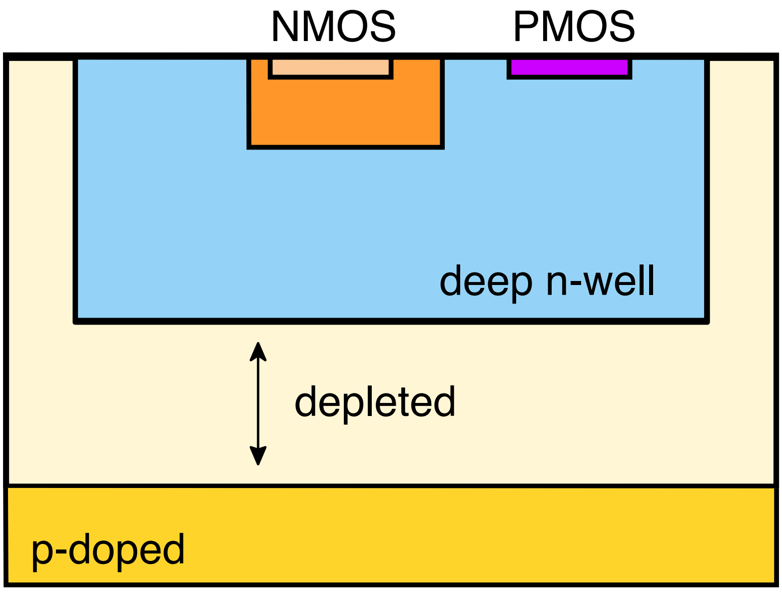

FIGURE 7.4: A schematic view a HV-CMOS sensor cross-section.

of n-in-n implants, because it doesn't undergo through type-inversion [108] when subject to radiation, simplifying the detector operations. The active sensor thickness will be 100 µm in Layer 1 and Ring 1, and 150 µm elsewhere, with an option to deploy 100 µm sensors in Layer 2 and Ring 2, 200 µm sensors in the end-caps and 300 µm sensors as an option restricted to Layer 4 and Ring 4.
Finally, an alternative approach is the use of a monolithic module, with pixel sensor and read-out chip being one entity. The monolithic CMOS sensor technology was investigated for the outer layers of the pixel detector of ITk. This region presents looser requirements on radiation tolerance and hit rate, making a fully monolithic design a viable option. The benefit of this approach are the reduction of the pixel size, of the power consumption and consequently of the material budget in front of the calorimeter system, thanks to the reduction of the space dedicated to services and cooling. Furthermore, the possibility to use commercial processes would cut the production costs and increase the production efficiency. The monolithic CMOS technology foresees charge collection, analog amplification and digital electronics in the same silicon wafer. To improve the radiation hardness of the sensors, the charge collection is obtained by applying a reverse bias voltages (HV) of the order of 100 V; this results in fast signal obtained by charge drift. The combination of high voltage and CMOS is called HV-CMOS technology and is a new concept for a monolithic devices in particle physics [109]. The analog and digital circuitries are protected by the high electric potential difference by being implemented in deep n-wells, decoupled from the charge collection region in the p-substrate, as illustrated in Figure 7.4.

7.2 Irradiation facility at the Bern Cyclotron

In order to prove the functionality of the ITk in the high luminosity environment, the functionality of its active sensors and of all the electronic components have to proved after irradiation, reaching the doses expected from simulation at the end of the HL-LHC data tacking. The various components can be irradiated by directly exposing them in front of a proton beam. In particular,

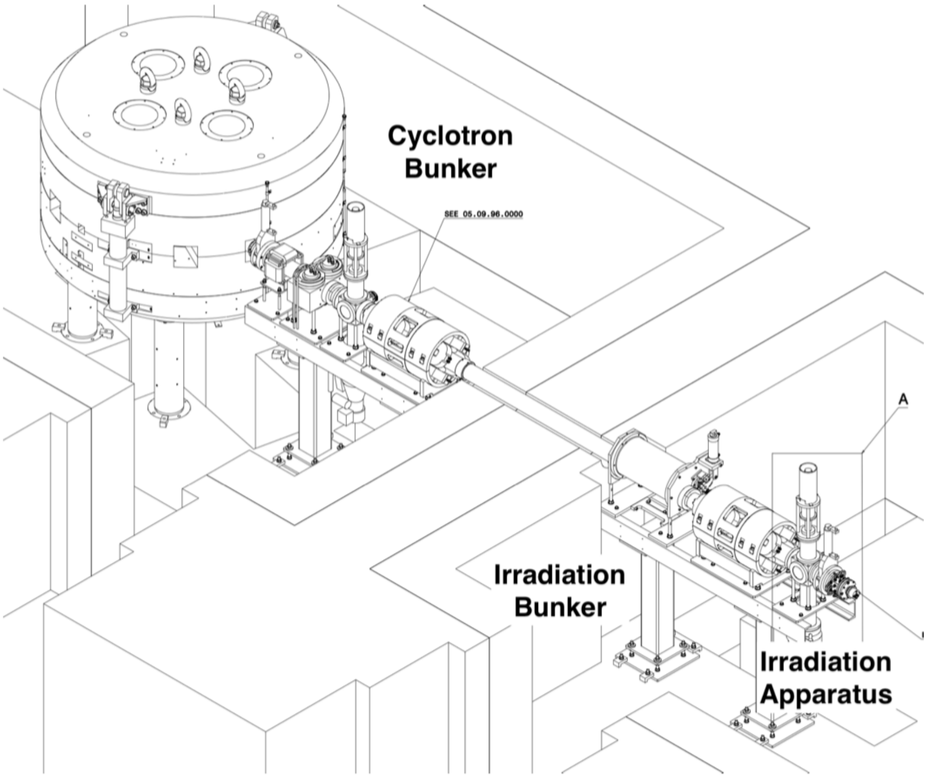

FIGURE 7.5: Diagram of the cyclotron facility.

the high stopping power for low energy protons can be exploited to obtain the high level of dose foreseen, in very limited time. To this purpose, an irradiation facility has been developed at the Bern Cyclotron.

The Bern Cyclotron

The Bern Cyclotron is a medical cyclotron in operation at the Bern University Hospital (Inselspital) [110]. It is a commercial IBA18/18 cyclotron, accelerating H^- to 18 MeV. Proton extraction is achieved by stripping off the electrons from the negative H^- ions with 5 µm thick pyrolytic carbon foils. The machine is equipped with an external 6.5 m long Beam Transfer Line (BTL), which delivers the beam in a second bunker, as illustrated in Figure 7.5. This allows for the operation of the cyclotron for research activities during the day time, while the radio isotope production for medical purpose is running over-night.

The beam is transported to the second bunker, called irradiation bunker, with a transfer efficiency greater than 95%. The accelerated protons are steered by an X-Y magnet system and are directed towards a collimator. The focusing of the beam is realised using two horizontal-vertical quadrupole doublets; the first is located in the cyclotron bunker and the second in the irradiation bunker. Beam currents from few pA up to 150 µA can be achieved, by varing operation settings for the ion source, the main coil, the radio-frequency systems and the BTL magnets.
A 1.8 m thick wall divides the irradiation bunker from the cyclotron bunker, to stop the neutron flux generated during the isotope production. For the same reason, a movable cylindrical neutron

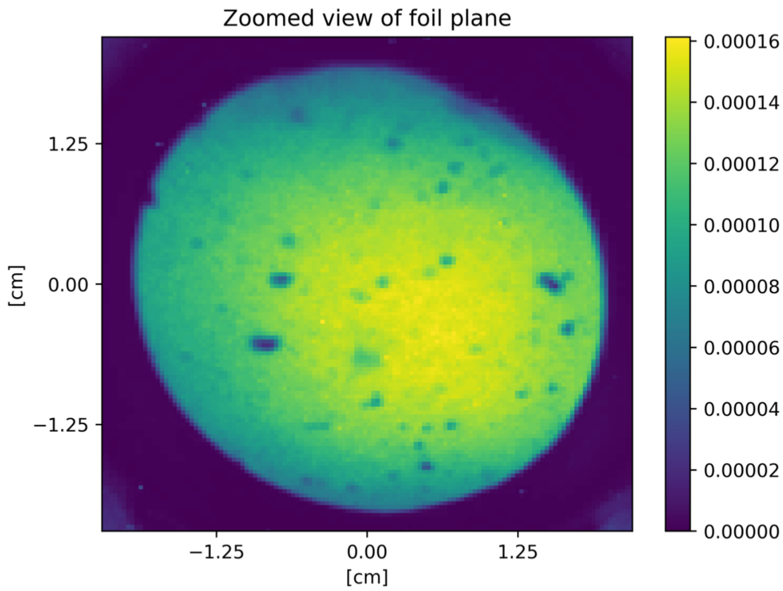

FIGURE 7.6: Beam shape obtained with the two-dimensional beam profiler. The colour scale is in arbitrary units.

shutter is located inside the beam pipe while the BTL is not in use. As a consequence, the research bunker has a low level of activity, below 2 µSv per hour, allowing access to the beam area a few minutes after the beam is switched off. The possibility to operate interventions inside the bunkers is a fundamental feature of the irradiation facility.

Dose measurement

When irradiating test sensors to qualify them for the ITk upgrade, it is necessary to have an accurate control on the given dose along the total irradiation process. The key quantity to measure both the ionising and not ionising dose given by the protons to the device under test (DUT), is the flux of proton reaching the DUT itself. The flux can be measured starting from the the beam current $j(t)$:

$$\phi = \int_{t_{\text{start}}}^{t_{\text{stop}}} \frac{j(t)}{Q_e} dt \tag{7.2}$$

A dedicated irradiation setup was developed for the measurement of $j(t)$. The method relies on the extraction of the central part of the beam to irradiate the device, while dumping the outermost part of the beam thanks to a collimator to measure the current density.
To be able to use this methodology it is important to have a constant intensity on the transverse plane. In order to obtain the required beam profile, the downstream quadrupole doublets of the BTL are switched off. In this way the beam profile is flat within 20% up to a radius of 40 mm. A two-dimensional beam profiler is then used to monitor the uniformity of the beam. It consists of a matrix of silicon dioxide enriched with ytterbium: protons hitting the matrix produce fluorescence, which is monitored by a camera. A two-dimensional image of the beam, obtained from the beam profiler, is presented in Figure 7.6.

A schematic view of the collimator is shown in Figure 7.7. It consists of three aluminium rings:

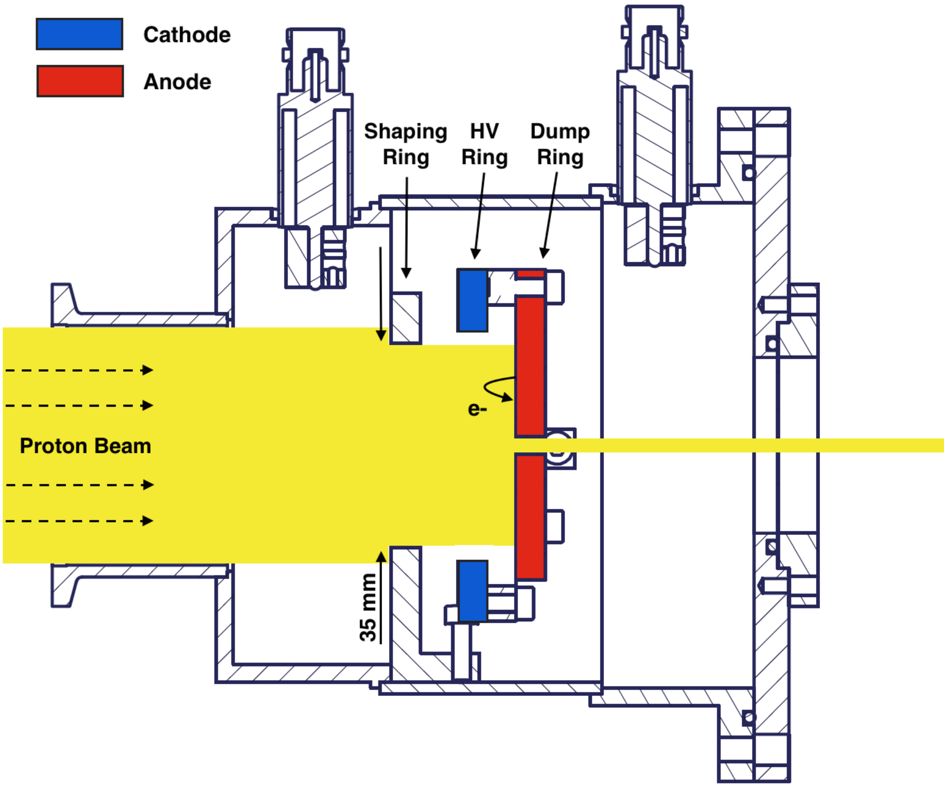

FIGURE 7.7: Cross section of the collimator system.

the shaping ring, the high-voltage ring and the beam dump. Each of the rings is 5 mm thick: this value was optimised considering that 18 MeV protons have a range of 1.6 mm in aluminium. The proton beam coming from the BTL enters the system of collimators through a 40 mm diameter opening and is further shaped through the shaping ring of 35 mm inner diameter. After the shaping ring, the proton beam hits a dump ring, which also acts as additional collimator. The part of the beam absorbed by the beam dump is used for the current density measurement, as defined in Equation:

$$j(t) = \frac{i(t)}{A_{\mathrm{bd}}} \cdot \Lambda \tag{7.3}$$

where $i(t)$ is the current measured on the beam dump, A_{bd} is the area of the beam dump collimator and Λ is a correcting factor for eventual inhomogeneities of the two-dimensional beam profile measured with the beam profiler.

When the protons hit the aluminium surface of the beam dump, they extract secondary electrons. This phenomenon is the cause of an overestimation of the current by up to 20%. To avoid this effect, an intermediate high voltage ring is placed between the shaping ring and the dump ring. The high-voltage ring has an inner diameter of 37.5 mm and it is placed at a difference of potential of -100 V with respect to the dump ring. This prevents the loss of secondary electrons in the dump ring and the consequent overestimation of the beam current.

The entire system is operated in vacuum in order to prevent air ionisation and the beam is extracted into air through a 300 µm aluminium window. A picture of the full setup is presented in Figure 7.8.

The energy of the protons, after passing trough the extraction window, is estimated with

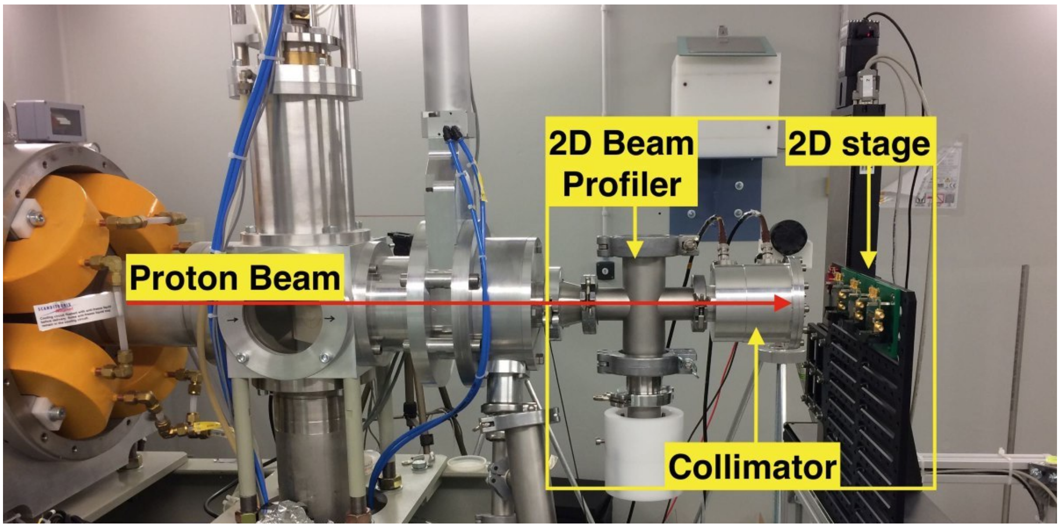

FIGURE 7.8: View of the extraction beam line and of all the elements developed for the irradiation facility.

$\frac{1}{\rho}\frac{dE}{dX}$ [MeV cm^2/g]	κ
23.25	3.6

TABLE 7.2: Stopping power and hardness factor in silicon for the 16.7 MeV proton beam.

simulations [111] and is found to be 16.7 ± 0.5 MeV. The ionising and not ionising dose can finally be calculated from the proton flux in the following way:

$$\text{fluence} = \kappa \cdot \phi_{\text{protons}} \tag{7.4}$$

$$\text{TID} = \frac{dE}{\rho dX} \cdot \phi_{\text{protons}} \tag{7.5}$$

The values of the stopping power $\frac{dE}{\rho dX}$ and the hardness factor κ for 16.7 MeV protons into silicon are presented in Table 7.2.

Figure 7.9 shows the beam current measured by the dump ring and the relative dose measured during a typical irradiation taken as an example.

As an independent offline measurement of the delivered dose, radiochromic films are exploited. During each irradiation, a film is positioned between the extraction window and the DUT and it is measured at the end of the run. The radiochromic films used are made from hexa(hydroxyethyl) aminotriphenylacetonitrile (HHEVC) dyes and become blue when exposed to ionising radiation. The TID received by the film is anticorrelated with its optical absorbance, which can me measured with infra-red light. Figure 7.10 shows the film calibration provided by the production company (FWT [112]) in black, compared with the red points showing the measurement performed at the Bern Cyclotron. The uncertainty on the measured optical absorbance takes in account an uncertainty of 5 µm on the film thickness.

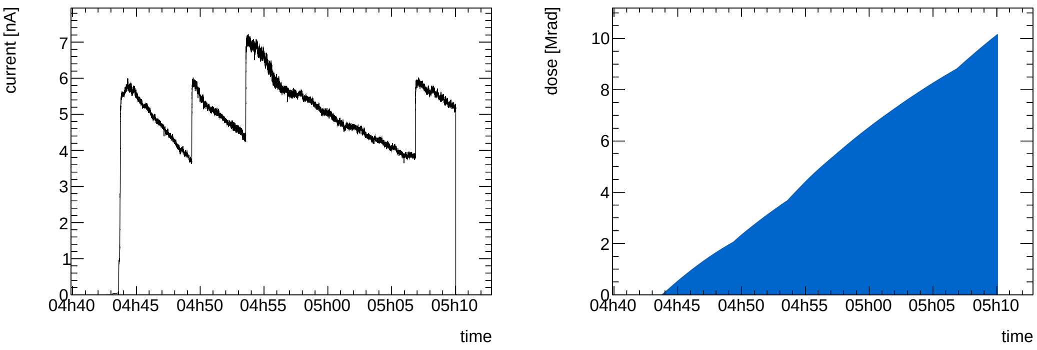

FIGURE 7.9: Observed beam current during an irradiation with the estimated delivered dose given a test silicon device

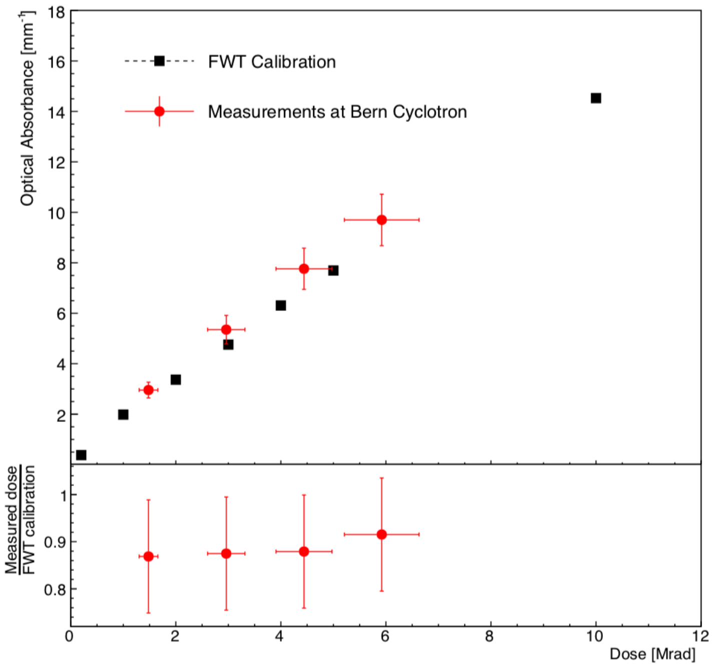

FIGURE 7.10: Comparison between the film calibration and the dose measurement at the Bern Cyclotron. The two measurements techniques are compatible within 15% as showed by the ratio in the bottom of the plot.

7.3 Characterisation of charge collection processes

This section is dedicated to study of the modification of charge collection process under irradiation, for HV-CMOS prototypes. To achieve this, the size of the depletion depth is studied with the Transient Current Technique (TCT) before and after proton irradiation.

The H35DEMO ASIC

The sensor chose for the characterisation is the H35DEMO ASIC [113], a chip produced in the 350 nm technology at ams AG [114]. The area of the chip is 18.49×24.40 mm^2 and has been produced on substrates with four different nominal resistivities: 20, 80, 200 and 1000 $\Omega \cdot$cm. The

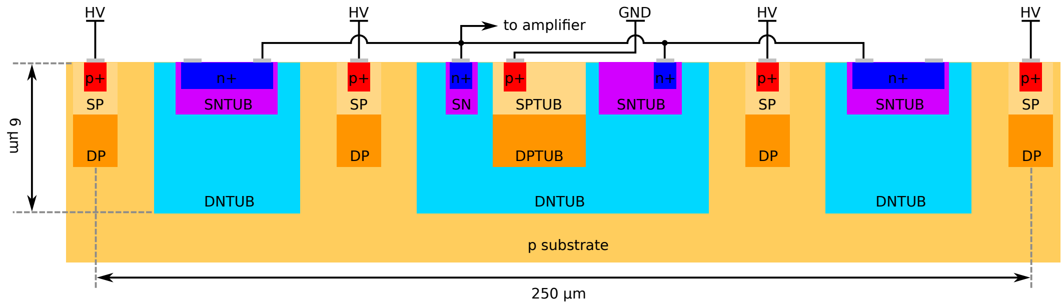

FIGURE 7.11: Simplified cross section of a test structure pixel. It is split into three n-wells connected together and the sensor pn junction is formed between the deep n-well (DNTUB) and the p substrate. SNTUB/SN is the shallow n-well, while DPTUB/DP and SPTUB/SP are the deep and shallow p-wells respectively.

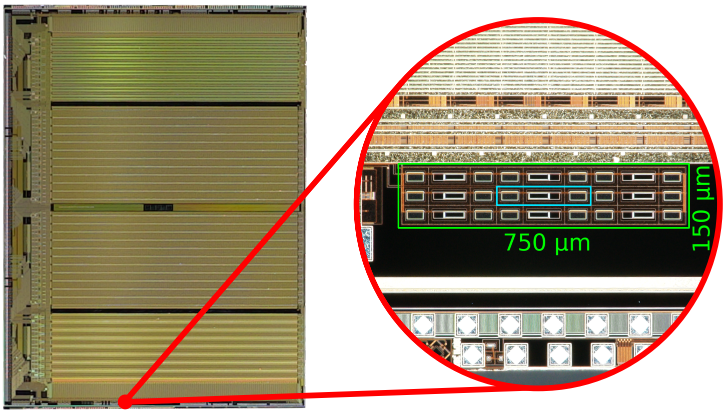

FIGURE 7.12: The H35DEMO and the test structure used for TCT measurements.

pixels of this ASIC have an area of 50×250 µm^2 and the electrode is split into three n-wells, as shown in Figure 7.11. The pn junction of the sensor is between the p-doped substrate and the deep n-well. The high voltage is provided by a dedicated pad and it is delivered from the top of the chip with $p+$ implants passing in between each n-well.

In order to characterise the properties of the silicon bulk, the chip contains several test structures on one edge. The structure used for the depletion zone charactesiation is a 3×3 pixel matrix (circled in Figure 7.12), with no electronics, where the n-wells of the pixel are connected directly to a pad: the central pixel (circled in blue) and the surrounding ones are connected to two different lines, so it is possible to measure the charge collected by each of them separately.

Experimental setup

The depletion depth of the tested sensors is measured with a Transient Current Technique. This technique consists in illuminating the edge of the sensor with an infrared laser beam to generate electron-hole pairs inside the silicon bulk. The laser position with respect to the sensor is controlled using a micrometric xyz stage system. The current pulse induced by the laser is amplified, digitised and integrated to estimate the total charge collected inside the sensor. Two-dimensional scans in the plane perpendicular to the laser beam are performed to measure the depletion depth.
The TCT measurements are carried with the setup produced by Particulars [115], illustrated

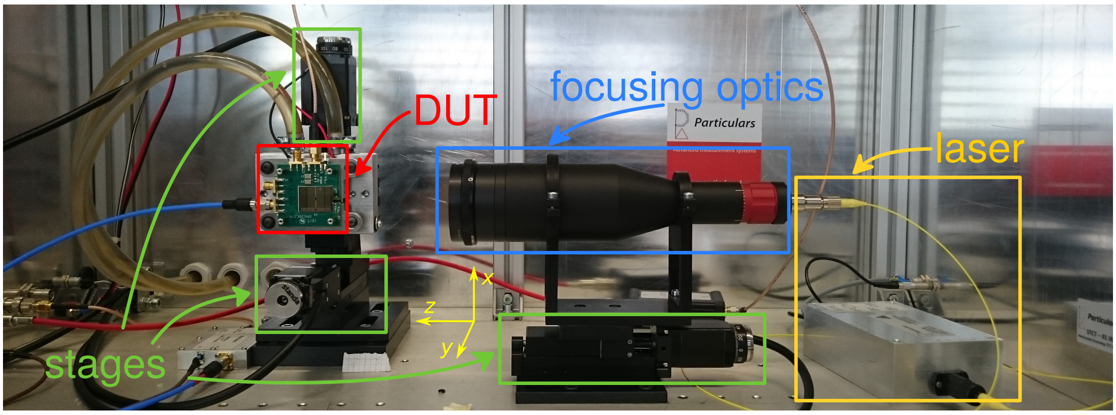

FIGURE 7.13: A picture of the TCT setup. The laser beam is supplied to the optics through an optical fiber and focalised on the device under test (DUT).

in Figure 7.13. It consists of three moving stages: two used to position the Device Under Test (DUT) and a third to adjust the focus of the laser. The stages can be positioned with 1 µm precision. A right-handed coordinate system is defined by picking y is the direction perpendicular to the DUT surface, z in the direction of the laser beam and x perpendicular to y and z. A laser with a wavelength of 1064 nm, generating pulses $\sim$ 500 ps long with a rate of 1 kHz, is focused using dedicated optics. The laser also provides the trigger signal for the oscilloscope. The output signals of the detector are read with two 53 dB current amplifiers [115], digitised with a DRS4 oscilloscope [116] and acquired with a dedicated data acquisition software.

The DUT is cooled with a Peltier cell and a chiller: the temperature is controlled by software and dry air is supplied to the setup to avoid the formation of dew or frost.
The laser has a gaussian profile, which is measured by performing a scan perpendicular to the silicon-metal edge of a test sensor. The charge profile of this scan is modelled with an error function, whose σ parameter is used to estimate the laser beam width. This procedure is repeated at different focus positions (z direction) and the results are shown in Figure 7.14. With this method, the laser profile was found to have a minimum Full Width at Half Maximum (FWHM) of 15 ± 2 µm.
When the laser is pointed to the silicon, charge is generated along its full profile, as illustrated in Figure 7.15. For this reason it is important to focus the laser before taking measurements. The laser width also influences the minimum depletion depth that can be measured.

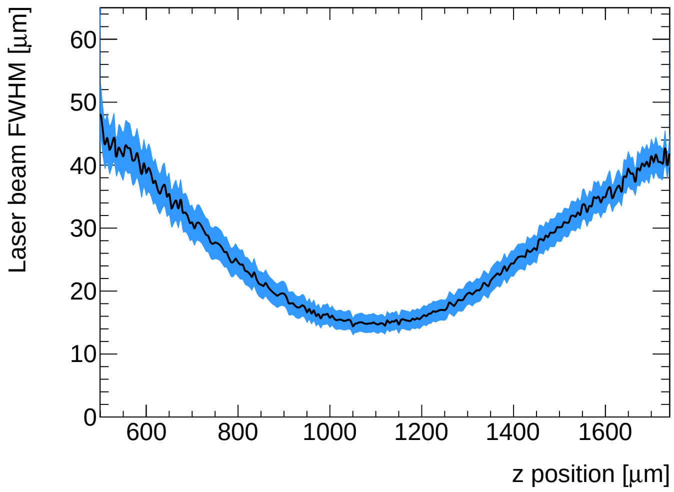

FIGURE 7.14: Distribution of FWHM, obtained shifting the the laser beam around the focus. The region around the minimum is the best focus achievable and the aim is to position it exactly below the test structures.

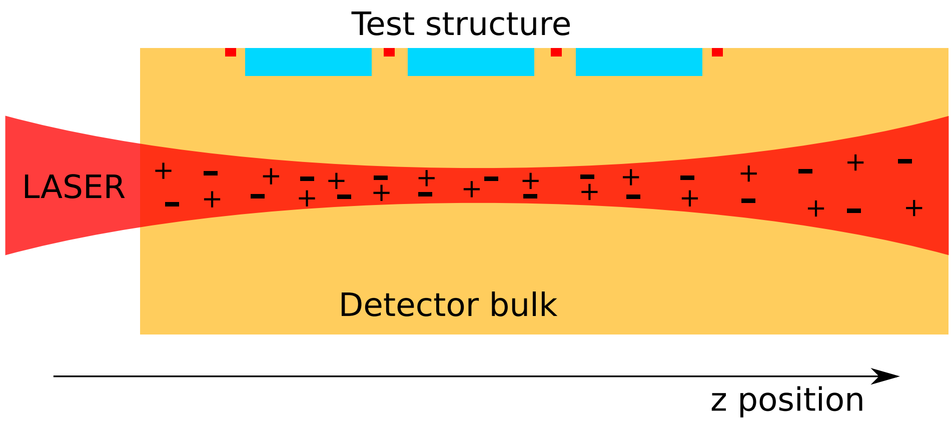

FIGURE 7.15: Sketch of the charge generation inside the silicon: charge is generated along the laser beam, not just in the focus point.

Characterisation of the non irradiated samples

Edge TCT measurements are carried out to estimate the depletion depth as a function of the bias voltage on all available substrate resistivities. After focusing the laser, a two-dimensional scan is taken at different reverse bias voltages (0 to 100 V, in 10 V steps). The scan is performed with 1 µm steps in the y direction from the implants down inside the bulk, where maximum precision is required for the measurement of the depth, and 5 µm steps in the x direction, parallel to the long edge of the pixels. For each point of the scan, a full current waveform (obtained averaging 40 measurements to decrease noise) is saved. An example of the current waveform inside the depletion region is shown in Figure 7.16.

To obtain the collected charge, each waveform is integrated over an 8 ns time window, highlighted as a vertical band in the plot. Figure 7.17 shows a 2D histogram of the charge collection map obtained with this procedure: each bin of the histogram is filled with the integral of the waveform recorded while pointing the laser at the indicated (x, y) coordinate. Then, the estimate of the depletion depth is obtained from these measurement by taking the profile along the y direction of

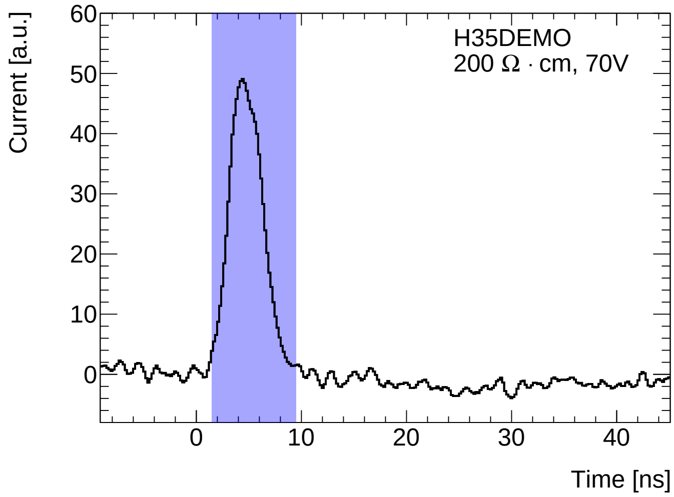

FIGURE 7.16: Example of an amplified current waveform collected in the depletion region. The vertical band highlights the integration window used to measure the collected charge.

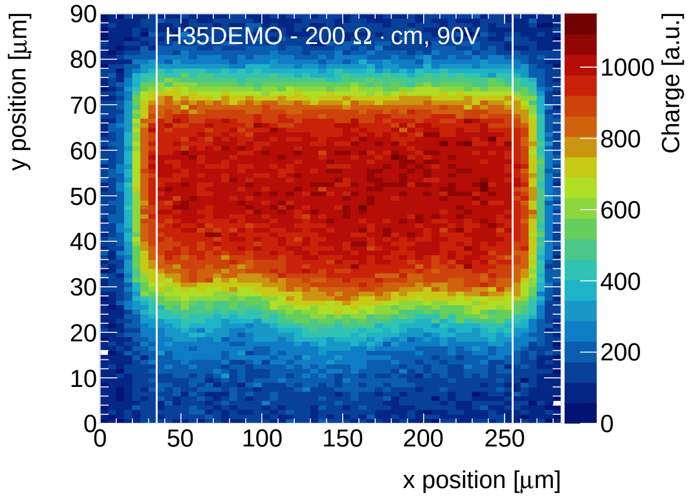

FIGURE 7.17: Distribution of the collected charge as a function of the position of the laser, for a 200 $\Omega \cdot$ cm sample at 90 V bias voltage. The vertical lines represent the range used to estimate the depletion region.

the collected charge distribution and then calculate the FWHM. Examples of these profiles, at different bias voltages, are shown in Figure 7.18.

In order to obtain an accurate estimation of the depletion depth, it is necessary to remove the profiles which are too close to the lateral edge of the pixel, where the laser beam is not fully contained. To do so, the average charge of each profile is calculated and if it is smaller that 0.85 times the maximum average charge, it is not considered. The profiles selected in this way designate the fiducial range and are situated between the white vertical lines in Figure 7.17.
In case of the 1000 $\Omega \cdot$ cm sample (Figure 7.18, on the right), a peak appears in the otherwise flat charge collection profile when the reverse bias voltage exceeds 20 V. This is due to the shape of the electric field lines inside the sensor bulk, as illustrated in Figure 7.19: when electron-hole pairs are generated deeper inside the bulk (depletion depth greater than $\sim$ 80 μm), part of the charge created below the outermost pixels of the test structure is collected by the central pixel,

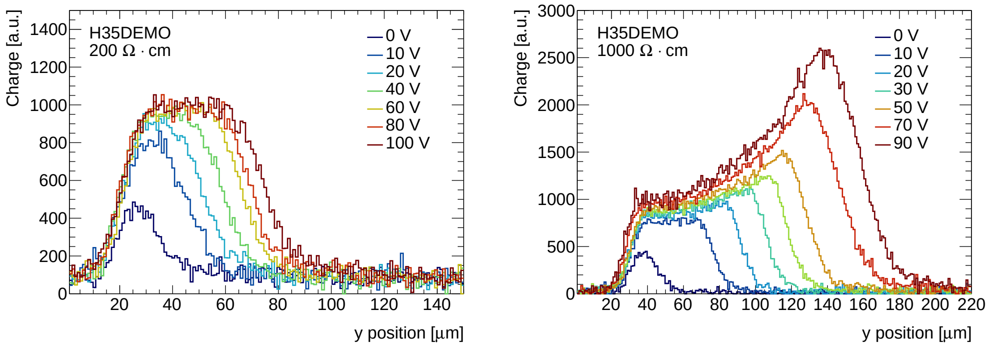

FIGURE 7.18: Projections, perpendicular to the sensor surface, of the collected charge for a $200\ \Omega \cdot \text{cm}$ sample (left) and for a $1000\ \Omega \cdot \text{cm}$ sample (right).

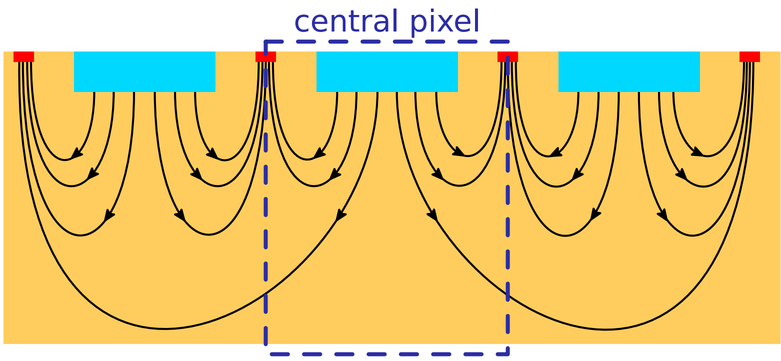

FIGURE 7.19: Sketch of the electric field in the depletion region. The lines give a qualitative trend of the electric field.

producing the peak in the charge collection profile. This is confirmed by the charge collection profile of the pixel frame, which features a dip corresponding to the charge excess observed in the central pixel. A flat charge collection profile is obtained by summing the two.

The peak produced by the charge generated in the neighbouring pixels can produce a bias in the evaluation of the FWHM [117]. Therefore, to separate the different contributions, each profile is fitted with the following function:

$$f(y) = \frac{A}{4}\left[\text{erf}\left(\frac{y - y_1}{\sigma_1}\right) + 1\right] \cdot \text{erfc}\left(\frac{y - y_2}{\sigma_2}\right) + B \cdot \text{Gaussian}\,(y, \mu, \sigma) + C \tag{7.6}$$

The combination of the error functions represents the profile of the charge collected in the depletion region: y_1 and y_2 are the beginning and the end of the region respectively, while σ_1 and σ_2 describe the smearing of the charge profile due to the size of the beam spot, and, in the case of σ_2, the effect of the decreasing electric field inside the bulk. The gaussian (and its normalisation B) represents the position, the width and the amplitude of the peak due to charge sharing and C a possible offset of the baseline current. The parameter A, which normalises the error functions and represents the charge collection maximum in absence of charge sharing, is used for the FWHM estimation.
When the depletion depth is comparable with the laser beam width, the charge collection profile has a gaussian shape and in this case the maximum is obtained from the global fitted function. An example of the fit behaviour on two the different kind of profiles is presented in Figure 7.20.

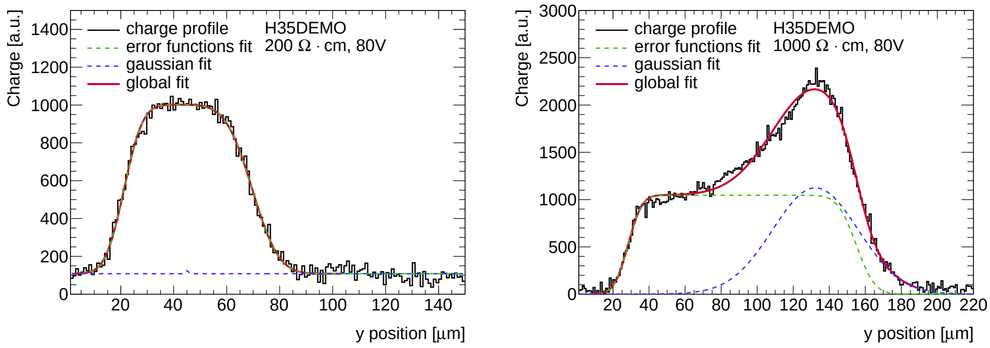

FIGURE 7.20: Examples of the charge profile fitted with the function defined in Equation 7.6, for a 200 $\Omega \cdot$ cm sample (left) and for a 1000 $\Omega \cdot$ cm sample (right). In the former, the charge sharing is negligible and the only contributions to the fit come from the error functions, while in the latter the charge sharing contribution is modelled with a Gaussian.

Once the maximum is calculated, the FWHM of the global fit profile is extracted. This procedure is repeated for each x position in the fiducial range: the depletion depth is obtained from the average of the distribution of these values. The error on each point is evaluated combining the contribution of the charge sharing and the standard deviation of the formerly mentioned values. This estimation of the depletion depth is not accurate when the depth is comparable to, or smaller than, the laser width at its focus: in those cases, since the charge collection profile is a convolution of the laser shape and of the depletion depth, when the latter is small, the estimation is dominated by the laser width. To correct for this effect, the proportionality between the fraction of the laser contained in the depleted region and the total charge collected inside the sensor is exploited. Each depletion depth value is thus reweighted with the ratio obtained from the charge maximum obtained for each bias voltage (parameter A from Equation 7.6), divided by the charge maximum obtained when the laser is fully contained.

Figure 7.21 shows the evolution of the depletion depth measured in this way, as a function of the bias voltage. The evolution of the depletion depth as a function of the bias voltage is fitted with the following function in order to extract the resistivity of the substrate:

$$d(V) = 0.3 \left[\mu\text{m}/\sqrt{\Omega \cdot \text{cm} \cdot \text{V}}\right] \cdot \sqrt{\rho(V + V_{\text{bi}})} \tag{7.7}$$

where d is the depletion depth, ρ is the substrate resistivity, V the bias voltage and V_{bi} the built-in voltage [118]. Since the value of V_{bi} is measured for non irradiated samples, this parameter has been constrained in the range $0.2 - 0.6$ V in the fit.

The fitted values are reported in Table 7.3. It is important to notice that the sensors are biased from the top and therefore the charge is collected along non-straight field lines. In particular for high bias voltages, the approximations considered in Equation 7.7 is no longer accurate and the fit tends to overestimate the depletion depth. The resistivity values obtained from the fit are consistent with the tolerance declared by ams for the 20, 80 and 200 $\Omega \cdot$ cm samples, despite the fact that the formula used for the fit is an approximation and assumes the sensors to be back-biased. The estimated resistivity of the 1000 $\Omega \cdot$ cm sample is not compatible with the declared resistivity values, but this behaviour has already been observed in previous measurements [117].

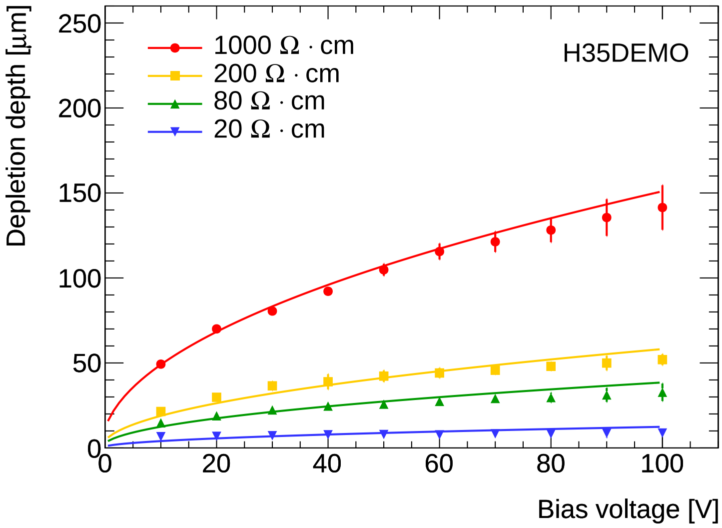

FIGURE 7.21: Evolution of the depletion depth as a function of the bias voltage. The four curves show the behaviour of samples with different resistivity: 20, 80, 200 and 1000 $\Omega \cdot$ cm. The dots represent the measured points, while the lines are the fitted curves according to Equation 7.7. The increase of the relative uncertainty with the depletion depth is related to the increase of the charge sharing effect: the extra charge has the effect of making the fit less stable and the measurements less precise.

Nominal ρ [$\Omega \cdot$ cm]	Declared ρ [$\Omega \cdot$ cm]	Fitted ρ [$\Omega \cdot$ cm]
20	15 – 25	17 ± 2
80	50 – 100	112 ± 8
200	200 – 400	306 ± 11
1000	600 – 1100	2518 ± 25

TABLE 7.3: Resistivity values obtained from the fit, along with the resistivity ranges of the wafers declared by ams AG. The declared resistivity values are the ranges of resistivities provided by the manufacturer, while the nominal resistivity is the value used to identify a given range.

Irradiation campaign

The sensors have been irradiated with 16.7 MeV and 24 GeV protons, in order to study the effect of the damage induced by charged hadrons. This kind of damage is particularly interesting because it is expected to be the major contribution to the total radiation damage in the outermost layers of the ATLAS tracker for the HL-LHC upgrade [100].

A first set of sensors was irradiated at the Bern cyclotron [119], in the facility described in Section 7.2. The benefit of having an in-house irradiation facility, allowed to irradiate many samples up to a fluence of 19×10^{14} 1 MeV n_{eq}/cm^2, in several steps, and to perform the measurement after each irradiation.

A second set of samples was irradiated at the CERN PS east area IRRAD facility [120]. PS IRRAD operates with 24 GeV protons, delivered from the PS accelerator in spills of about 400 ms (slow extraction), at a frequency of $\sim$ 0.1 Hz. The online monitoring of the dose is provided by a copper-based beam profile monitor [121]. An additional offline measurement of the dose is performed through γ-spectroscopy of thin aluminium films irradiated together with the samples [122]. In this case, the samples were exposed to a fluence up to 20×10^{14} 1 MeV n_{eq}/cm^2. In both irradiation facilities the samples have been irradiated at room temperature. At the Bern cyclotron a dose rate of $\sim 1 \times 10^{13}$ 1 MeV n_{eq}/cm^2 per minute was achievable so each irradiation step would take from 10 minutes to one hour, depending on the dose required at a given step. At the CERN PS IRRAD facility instead, the achievable dose rate was $\sim 1.8 \times 10^{13}$ 1 MeV n_{eq}/cm^2 per hour, so the irradiation time ranged from 5 to 77 hours.

Characterisation of the irradiated samples

The samples are characterised after each irradiation step as described for the non irradiate ones. The results of the measurement of the depletion region are shown in Figure 7.22 for the samples irradiated with protons of 16.7 MeV and in Figure 7.23 for the samples irradiated with protons of 24 GeV.

For all the cases considered, the depletion depth follows the same evolution with the increasing fluence: a strong growth is observed at low fluences, reaching values between 140 µm and 200 µm, depending on the resistivity, and then it shrinks again with the increase of the fluence. This effect has been observed before in sensors with *p*-doped substrates [123–125] and can be explained using a combination of two different effects: proton irradiation causes the introduction of deep acceptors, which lead to a decreased depletion region, and, at the same time, shallow acceptors are removed. In this context the term "shallow" is used to indicate that the energy levels are close enough to the valence band to be fully ionised at room temperature. At lower fluences the latter effect dominates, resulting in the observed initial increase of the active area while the former occurs at higher fluences.

The maxima of the depletion region are reached at different fluence levels for the different resistivities, with higher resistivity samples having a faster evolution than the lower ones: the larger depletion depth is observed at a fluence of around 5×10^{14} 1 MeV n_{eq}/cm^2 for the 20 $\Omega \cdot$ cm sample, while it is already reached before 1×10^{14} 1 MeV n_{eq}/cm^2 in case of the 1000 $\Omega \cdot$ cm resistivity.

Since the sensors are biased from the top, the charge is collected along non-straight field lines, and in particular when the larger depletion depths are obtained, the approximations considered in Equation 7.7 no longer hold and the fit fails to accurately describe the data. For this reason it was not possible to perform a quantitative study on the evolution of the resistivity.

By comparing the results obtained with protons of different energies, it is possible to observe that the evolution trend is similar, but the initial increase in depth due to the 24 GeV protons is less intense, and in general a smaller depletion region is measured with respect to the samples irradiated with 16.7 MeV protons. The H35DEMO prototypes were also characterised with similar techniques after neutron irradiation, in the work presented in [117]; this allows for an interesting comparison of the different effects of the non-ionising energy released by neutral and charged hadrons. Figure 7.24 shows the evolution of the depletion depth as a function of the fluence for a fixed reverse bias voltage (80 V), in the three irradiation campaigns: the 16.7 MeV and 24 GeV protons presented in this thesis and the nuclear reactor neutrons from [117]. While the proton irradiated samples show a similar behaviour, the neutron samples demonstrate a lower increase of the depletion region for all the tested resistivities. This is due to the different nature of the interaction of the charged and neutral particles inside the silicon bulk.

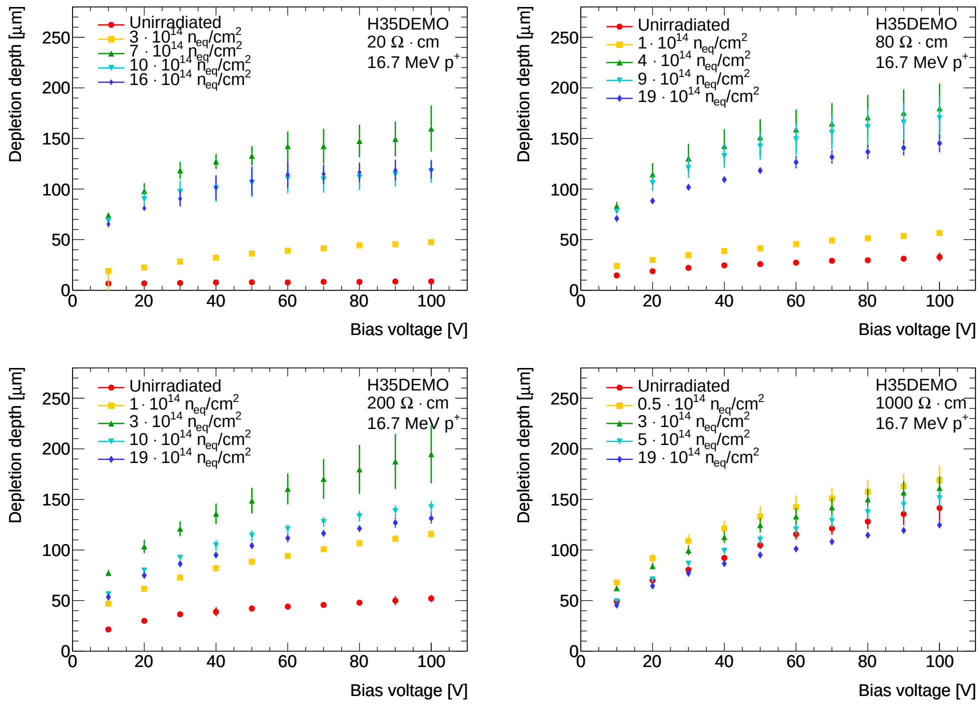

FIGURE 7.22: Evolution of the depletion depth as a function of the bias voltage, for the samples irradiated with protons of 16.7 MeV. The four plots show the behaviour of samples with different resistivities: 20, 80, 200 and 1000 $\Omega \cdot$ cm. The increase of the relative uncertainty with the depletion depth is related to the increase of the charge sharing effect: the extra charge has the effect of making the fit less stable and the measurements less precise.

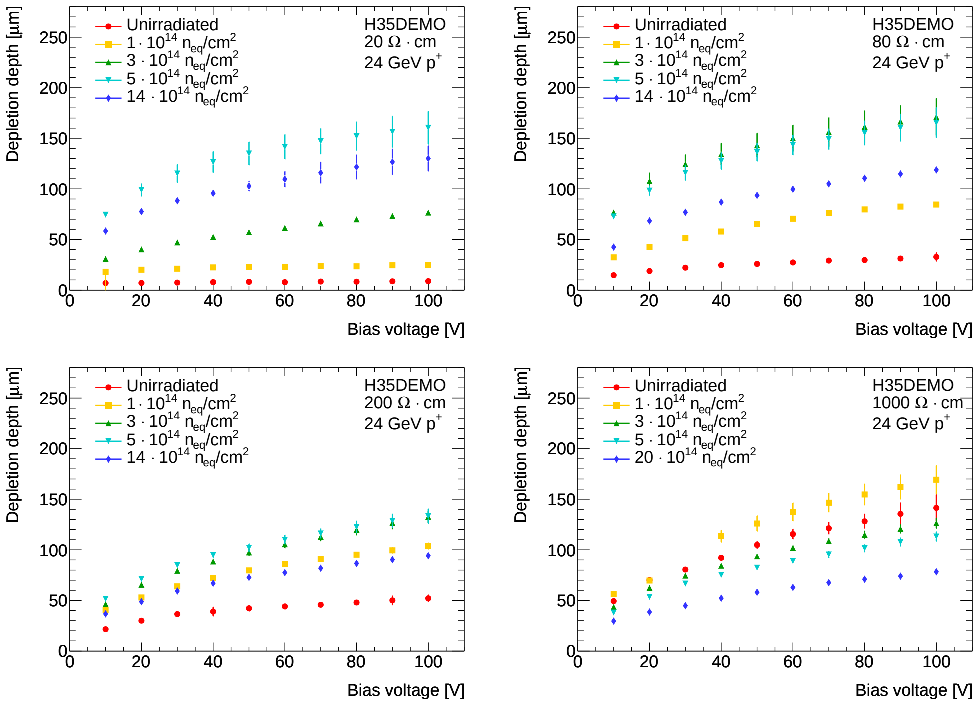

FIGURE 7.23: Evolution of the depletion depth as a function of the bias voltage, for the samples irradiated at 24 GeV. The four plots show the behaviour of samples with different resistivities: 20, 80, 200 and 1000 $\Omega \cdot$ cm. The increase of the relative uncertainty with the depletion depth is related to the increase of the charge sharing effect: the extra charge has the effect of making the fit less stable and the measurements less precise.

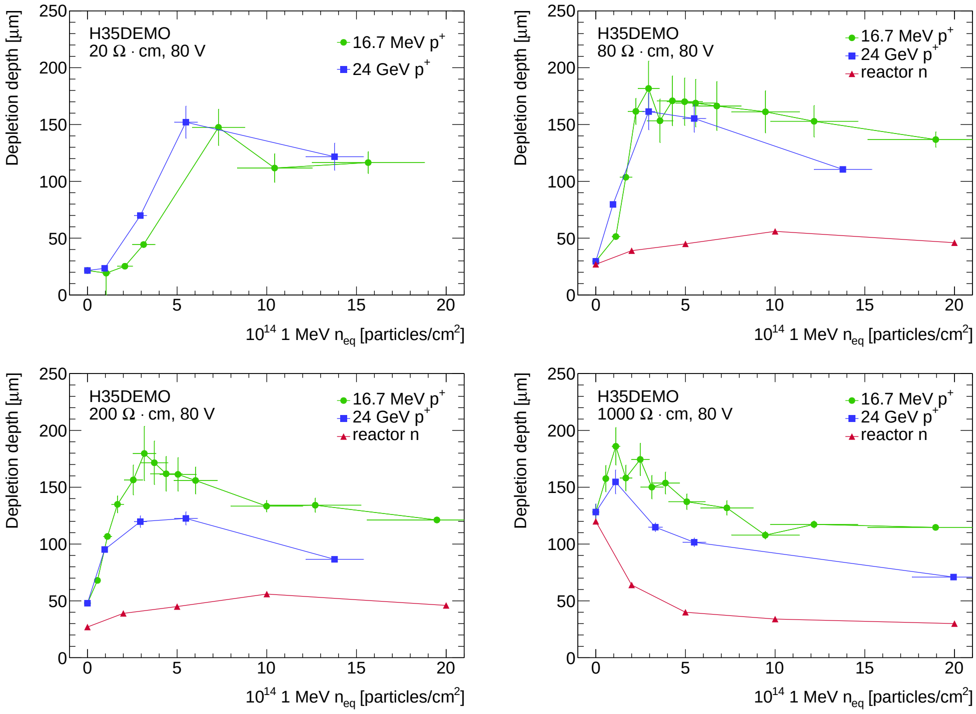

FIGURE 7.24: Evolution of the depletion depth (at −80 V bias voltage) as a function of the fluence, comparing the damage arising from different particles: 16.7 MeV (circles) and 24 GeV (squares) protons and reactor neutrons (triangles). The uncertainty on the fluence given by the 16.7 MeV protons takes into account the cumulative irradiation steps. The neutron irradiation measurements are taken from [117]. The four plots show the behaviour of samples with different resistivities: 20, 80, 200 and 1000 $\Omega \cdot$ cm.

Results

With the goal of studying the effect of radiation on silicon sensors designed for the HL-LHC, an irradiation facility was developed at the Bern cyclotron. This facility allows to irradiate the samples under study with low energy protons, mimicking the damage obtained during the HL-LHC data taking.
With the aid of this facility, the depletion depth of the H35DEMO prototype has been measured before and after proton irradiation on samples of four different substrate resistivities. All measured samples display a strong increase of the depletion depth after the initial irradiation steps, reaching a maximum between 1×10^{14} and 3×10^{14} $1\,\text{MeV}\ n_{eq}/cm^2$, when irradiated with 16.7 MeV protons, and between 1×10^{14} and 6×10^{14} $1\,\text{MeV}\ n_{eq}/cm^2$ when irradiated with 24 GeV protons. The increase of the depletion depth at low fluence can be attributed to the removal of shallow acceptors. The depletion depth is then measured to decrease slowly with the increasing fluence. A striking different effect in the charge collection properties after the irradiation of a p-type silicon bulk with neutrons and protons is observed. Comparison of these results with the measurements obtained after neutron irradiation [117] shows a strong difference in the effect of the two particles. While the depletion region exceeds 100 µm after proton irradiation for all the resistivities, it does not exceed 60 µm in the case of neutron irradiation. Furthermore, the growth of the depletion region after neutron irradiation continues up to higher fluences compared to proton irradiation, for the 80 and 200 $\Omega \cdot$ cm samples. The differences between protons with different energies are not as pronounced and the trend is similar. Still, the effect of high energy protons is smaller than the low energy ones.

Chapter 8

Prospects for SUSY searches exploiting the ITk

This chapter presents the prospect sensitivity for a search for electroweakino production in nearly mass degenerate scenarios at the HL-LHC. The sensitivity is evaluated assuming an integrated luminosity of 3000 fb^{-1} collected with centre-of-mass energy $\sqrt{s} = 14$ TeV proton-proton collisions. The instantaneous luminosity of the HL-LHC is expected to be around $L = 7.5 \times 10^{34}\,\mathrm{cm}^{-2}\mathrm{s}^{-1}$, leading to an average number of interactions per bunch crossing of approximately 200: these conditions will provide a very challenging environment for physics analysis and it is important to estimate the performances of the upgraded detector in such circumstances. Since the tracking detector will be changed completely, it is particularly important to assess the physic potential of the new system by studying prospective results of analyses which strongly rely on tracking performances.

This search investigates scenarios where the $\tilde{\chi}_1^{\pm}$, and $\tilde{\chi}_1^0$ are almost mass degenerate, leading to a long lifetime for the $\tilde{\chi}_1^{\pm}$ which decays after the first few layers of the tracking detector, leaving a track in the innermost layers of the detector. The chargino decays as: $\tilde{\chi}_1^{\pm} \rightarrow \pi^{\pm}\tilde{\chi}_1^0$; the $\tilde{\chi}_1^0$ escapes the detector and the pion has a very low energy and is not reconstructed, leading to the disappearing track signature, as shown in Figure 8.1. The unconventional final state targeted by this search makes it the perfect benchmark to study the tracking performance of the ITk.

This signature has already been explored with part of the Run 2 dataset and the latest ATLAS results for this scenario [126] using the 2015–2016 dataset of the LHC *pp* run at a centre-of-mass energy of $\sqrt{s} = 13$ TeV, excluded wino masses below 430 GeV with a chargino lifetime, $\tau(\tilde{\chi}_1^{\pm})$, of 0.2 ns.

8.1 Targeted models

In anomaly-mediated supersymmetry breaking (AMSB) scenarios [127, 128], the supersymmetric partners of the W bosons, the winos, are the lightest gaugino states. In this case, the lightest chargino ($\tilde{\chi}_1^{\pm}$) and the lightest neutralino ($\tilde{\chi}_1^0$), are both largely composed of the wino eigenstates and are nearly mass-degenerate. Due to this small mass difference, the $\tilde{\chi}_1^{\pm}$ can have a long enough lifetime such that it decays inside the detector. AMSB scenarios naturally predict a pure wino LSP, which is a dark-matter candidate.

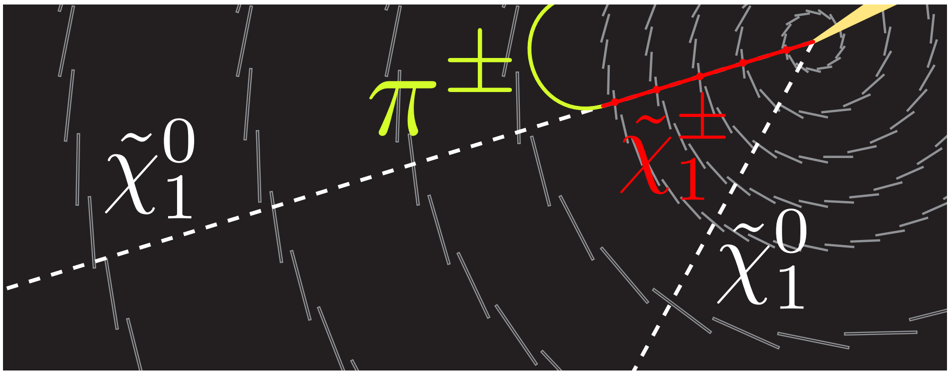

FIGURE 8.1: Schematic illustration of a $pp \to \tilde{\chi}_1^\pm \tilde{\chi}_1^0 +$ jet event in the HL-LHC ATLAS detector, with a long-lived chargino.

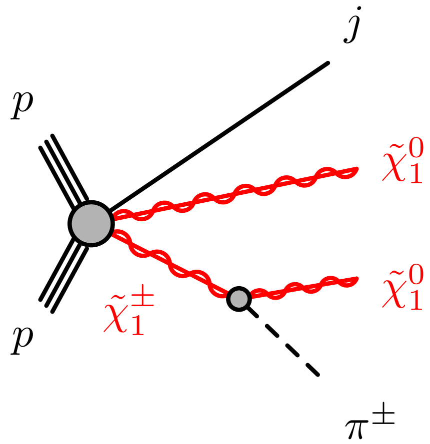

FIGURE 8.2: Diagrams depicting the $\tilde{\chi}_1^\pm$ $\tilde{\chi}_1^0$ production.

Further scenarios, which follow from naturalness arguments [13, 14], suggest that the absolute value of the Higgsino mass parameter μ is expected to be near the weak scale such that the higgsinos should be light, with masses below one TeV [129, 130], while the magnitude of the bino and wino mass parameters, M_1 and M_2 can be significantly larger, i.e. $|\mu| \ll |M_1|, |M_2|$. This results in the three lightest electroweakino states, $\tilde{\chi}_1^0$, $\tilde{\chi}_1^\pm$ and $\tilde{\chi}_2^0$ being dominated by the Higgsino component. In this scenario, the three lightest electroweakino masses are separated by hundreds of MeV to tens of GeV depending on the composition of these mass eigenstates, which is determined by the specific values of M_1 and M_2 [131].
The signals models considered in this search feature the electroweak production of $\tilde{\chi}_1^0$, $\tilde{\chi}_1^\pm$, as shown in Figure 8.2, and of $\tilde{\chi}_1^+$, $\tilde{\chi}_1^-$. They are generated assuming the minimal AMSB model with the ratio of the Higgs vacuum expectation values at the electroweak scale set to $\tan\beta = 5$, the sign of the higgsino mass term set to be positive, and the universal scalar mass set to $m_0 = 5$ TeV. The SUSY mass spectrum, the branching ratios and decay widths are calculated using ISASUSY version 7.80 [132]. The mass parameters are varied to consider $m(\tilde{\chi}_1^\pm)$ between 100 and 1500 GeV, and life-times ranging from 1 ps up to 10 µs.

The signal samples are generated with up to two extra partons in the matrix element using MG5_aMC@NLO 2.3.3 [133] at leading order (LO) interfaced to PYTHIA 8.186 [104] for parton showering, hadronisation and SUSY particle decay. The NNPDF2.3LO [134] parton distribution function (PDF) set was used. Renormalisation and factorisation scales are determined by the default dynamic scale choice of MG5_aMC@NLO. The CKKW-L merging scheme [135] was applied to combine tree-level matrix elements containing multiple partons with parton showers. The scale parameter for merging was set to a quarter of the mass of the wino or higgsino depending upon the signal scenario. The A14 [136] set of tuned parameters with simultaneously optimised multiparton interaction and parton shower parameters was used for the underlying event together with the NNPDF2.3LO PDF set. The cross-sections are calculated at next-to-leading order (NLO) in the strong coupling constant using PROSPINO2 [137].

For the interpretation considering higgsino-like electroweakinos, the same signal samples are considered, reweighted with the appropriate cross-section. In this case, the cross-sections are calculated to next-to-leading order (NLO) in the strong coupling, and next-to- leading-logarithm (NLL) accuracy for soft-gluon resummation using RESUMMINO v2.1.0 [138–140].

For both signal scenarios the nominal cross-section and its uncertainty are taken from an envelope of cross-section predictions using different parton distribution function sets and factorization and renormalization scales, as described in Ref. [141].

8.2 Event reconstruction in the high luminosity conditions

Jets are reconstructed with the anti-k_t algorithm with a radius parameter of 0.4. They are selected with $|\eta| < 2.8$ and the jet energy is smeared according to a Gaussian.

The magnitude of the missing transverse momentum is computed as the vectorial sum of the true momenta at the particle level of neutral weakly-interacting particles (neutrinos and neutralinos). It is then smeared, according to a Gaussian, to simulate the detector response, with a function parameterised as a function of the average number of interactions per bunch crossing μ and the scalar sum of energy in the calorimeter $\sum E_{\mathrm{T}}$.

The method to resolve overlaps between different reconstructed particle is similar as the one adopted for the the analyses performed with the current dataset and it is defined as follows: candidate jets are required to be separated from candidate electrons by $\Delta R(e, \mathrm{jet}) > 0.2$; if a jet and electron are within 0.2, then the jet is removed and the electron is kept; after this step, leptons (both e and μ) are removed if they are within $\Delta R < 0.4$ of a remaining jet.

Candidate leptons, which are used only to veto events, are selected with p_{T} larger than 20 GeV and $|\eta| < 2.47$ (2.7) for electrons (muons).

Tracklet reconstruction

The main feature of the signature relevant for this search is a short track, denoted as “tracklet”, which is reconstructed in the inner layers of the detector and subsequently disappears.

Tracklet reconstruction is performed in two stages. Firstly “standard” tracks, hereafter referred to as tracks, are reconstructed. Afterwards the track reconstruction is rerun with looser criteria, requiring at least four hits in the pixel detector. This second reconstruction step uses as inputs only detector hits which are not associated with previously reconstructed tracks. The tracklets are then extrapolated to the strip detectors, and any compatible hits are assigned to the tracklet candidate.

To reduce contributions from tracklets arising from background processes, the following requirements are applied.

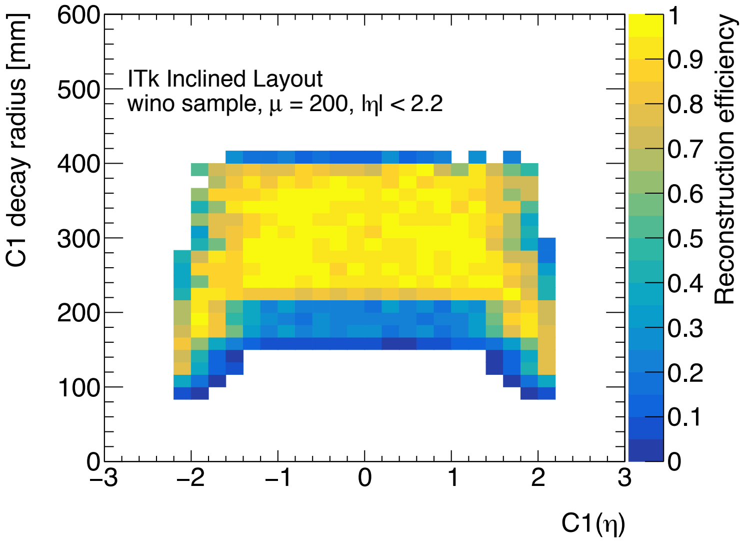

FIGURE 8.3: Tracklet reconstruction efficiency for simulated charginos as a function of the decay radius the direction of flight (η).

- **Isolation and p_T requirement**
  The separation in ΔR between the tracklet and any jet with $p_T > 20$ GeV must be greater than 0.4. The tracklet is then defined as isolated when the sum of the p_T of all standard tracks with $p_T > 1$ GeV in a cone of $\Delta R = 0.4$ around the tracklet, divided by the tracklet p_T, is smaller than 0.04. Finally, the candidate tracklet must have $p_T \geq 20$ GeV.

- **Geometrical acceptance**
  The tracklet must satisfy $0.1 < |\eta| < 1.9$.

- **Quality requirement**
  The tracklet is required to have hits on four or five pixel layers, with no holes between layers. The number of low-quality pixel hits, where the position uncertainty is large or the hit position is far from the reconstructed tracklet, associated with the tracklet must be zero. Furthermore, tracklets must satisfy the following requirements on impact parameters: $|d_0|/\sigma(d_0) < 2$ and $|z_0 \sin(\theta)| < 0.5$ mm.

- **Disappearance condition**
  The number of hits in the strip detector associated with the tracklet must be zero.

The tracklet reconstruction efficiency for charginos is estimated using simulated samples of $\tilde{\chi}_1^{\pm}$ pair production with $m(\tilde{\chi}_1^{\pm}) = 600$ GeV, featuring the HL-LHC pile up conditions and the ITk layout. The reconstruction efficiency obtained in this way is presented in Figure 8.3. This methods allows to achieve a reconstruction efficiency close to 100% for charginos which decay between 200 and 400 mm from the interaction point, a region which corresponds to the gap between the fourth pixel layer and the first strip layer. Some efficiency is recovered for lower radius when η is grated then 1.5: this happens thanks to the possibility of having multiple hits on the same layer in the inclined part of the layout.

8.3 Event selection

Events are selected containing zero charged leptons (electrons or muons), large $E_{\mathrm{T}}^{\mathrm{miss}}$ and at least one tracklet. All the events are reweighted by the expected efficiencies of tracklet reconstruction. Since the $\tilde{\chi}_1^{\pm}$ and $\tilde{\chi}_1^0$ have similar masses, they are often produced back to back and this yields little $E_{\mathrm{T}}^{\mathrm{miss}}$. Hence, it is necessary to select events where the system is boosted by recoiling against one or more jets from initial state radiation (ISR). The minimum azimuthal angular distance, $\min\{\Delta\phi(\mathrm{jet}_{1-4}, E_{\mathrm{T}}^{\mathrm{miss}})\}$, between the first four jets ordered in p_{T} and the $E_{\mathrm{T}}^{\mathrm{miss}}$ is required to be greater than one, in order to reject events with mis-measured $E_{\mathrm{T}}^{\mathrm{miss}}$.

Variable	SR Selection
Lepton veto p_{T} [GeV]	>20
$\min\{\Delta\phi(\mathrm{jet}_{1-4}, E_{\mathrm{T}}^{\mathrm{miss}})\}$	> 1
$E_{\mathrm{T}}^{\mathrm{miss}}$ [GeV]	> 300
Leading jet p_{T} [GeV]	> 300
Leading tracklet p_{T} [GeV]	> 150
$\Delta\phi(E_{\mathrm{T}}^{\mathrm{miss}}, \mathrm{trk})$	< 0.5

TABLE 8.1: Summary of the search selection criteria for the disappearing track SR.

Different kinematic variables are used in the search to separate the signal from the SM background, such as the leading jet p_{T}, the $E_{\mathrm{T}}^{\mathrm{miss}}$, the leading tracklet p_{T} and the azimuthal angle $(\Delta\phi(E_{\mathrm{T}}^{\mathrm{miss}}, \mathrm{trk}))$ between the tracklet and the $E_{\mathrm{T}}^{\mathrm{miss}}$. The final SR selection is optimised using two signal models: one with $m(\tilde{\chi}_1^{\pm}) = 800$ GeV and a lifetime of 1 ns and the other with $m(\tilde{\chi}_1^{\pm}) = 200$ GeV and a lifetime of 0.04 ns.
The set of selections which define the SR is presented in Table 8.1. Figure 8.4 shows the the $E_{\mathrm{T}}^{\mathrm{miss}}$ and the leading tracklet p_{T} distributions in events passing this selection, a part from the requirement on the plotted variables. The backgrounds distributions are compared with the ones obtained for two expected signal models, taken as example to demonstrate the difference in shape. The dominant background in the SR is arising from fake tracklets, similarly to the Run 2 version of the search [142]. The methods employed for the background estimation are described in the following.

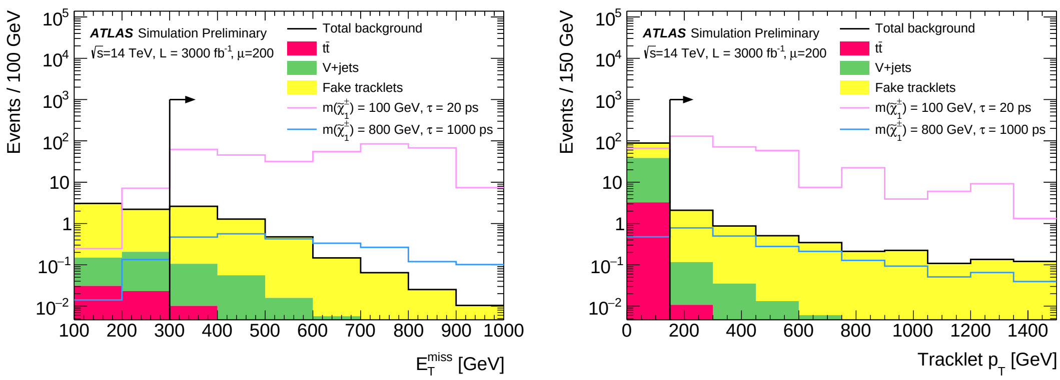

FIGURE 8.4: Kinematic variables for the disappearing track search: $E_{\mathrm{T}}^{\mathrm{miss}}$ distribution on the left and tracklet p_{T} on right. Both plots contain events passing the full SR selection, aside from the selection on the variable under consideration.

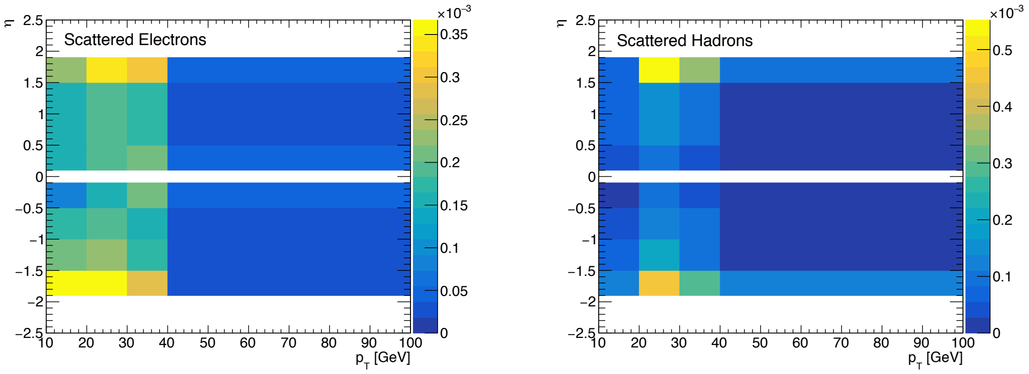

FIGURE 8.5: Probability of an electron (left) or a hadron (right) to leave a disappearing track signature, calculated as a function of η and momentum of the particle.

8.4 Background estimation

MC simulated event samples are used to predict the backgrounds from SM processes in the SRs. In simulated events, the detector response is parameterised based on studies performed with GEANT 4 [78] simulations of the upgraded detector in high luminosity conditions [143, 144]. All simulated events are overlaid with additional pp interactions in the same and neighbouring bunch crossings simulated with the soft QCD processes of PYTHIA 8.186 using the A2 set of tuned parameters [145] and the MSTW2008LO [146] PDF set. The pile-up conditions of the HL-LHC are assumed to follow a Poisson distribution with an average of 200 additional interactions.
Events containing a W or Z boson with associated jets (W+jets and Z/γ^*+jets) are produced using the SHERPA v2.2.1 generator with the NNPDF30NNLO PDF set at $\sqrt{s} = 13$ TeV with up to two extra partons in the matrix element. In both cases cross-section and PDF reweighting are applied to match the $\sqrt{s} = 14$ TeV conditions. For the production of $t\bar{t}$ the POWHEG-BOX V2 generator interfaced to PYTHIA8 parton shower with the ATLAS A14 tune is used. The sample is generated at $\sqrt{s} = 14$ TeV and a parton level filter requiring $E_{\mathrm{T}}^{\mathrm{miss}} > 100$ GeV is applied. The top-quark pair-production contribution is normalised to approximate next-to-next-to-leading-order calculations (NNLO) [147]. In addition, a series of dedicated "particle gun" samples are used to assess the probability of an isolated electron or hadron leaving a disappearing track in the detector.
The search presents two main background contributions: SM particles that are reconstructed as tracklets, and events which contain fake tracklets. The SM particles reconstructed as tracklets are typically hadrons scattering in the detector material or electrons undergoing bremsstrahlung. The probability of an isolated electron or hadron to leave a disappearing track is calculated using samples of single electrons or pions passing through the current ATLAS detector layout, and is then scaled to take into account the ratio of material in the current ATLAS inner detector and the upgraded inner tracker. The results are presented in Figure 8.5. The probability for hadrons and electrons to be reconstructed as tracklet is then applied to a template of simulated $t\bar{t}$ and V+jets events.

The second background contribution arises from events which contain "fake" tracklets (accidental alignment of hits in the pixel detector). These events arise from $Z \to \nu\nu$ or $W \to \ell\nu$ (where the lepton is not reconstructed) and are scaled by the expected fake tracklet probability:

$$p^{\mathrm{ITk}}_{\mathrm{fake,tight}} = p^{\mathrm{Run-2}}_{\mathrm{fake,tight}} \times \frac{R^{\mathrm{ITk}}_{\mathrm{fake,loose}}}{R^{\mathrm{Run-2}}_{\mathrm{fake,loose}}} \times \frac{\epsilon^{\mathrm{ITk}}_{z_0}}{\epsilon^{\mathrm{Run-2}}_{z_0}}. \tag{8.1}$$

In this equation, $p^{\mathrm{Run-2}}_{\mathrm{fake,tight}}$ is the fake rate of the current Run-2 analysis [148], computed using a d_0 sideband for the track reconstruction, $R^{\mathrm{ITk}}_{\mathrm{fake,loose}}$ is the fake rate in the same d_0 sideband for ITk computed with a neutrino particle gun sample, such that all tracks are purely a result of pile-up interactions, $R^{\mathrm{Run-2}}_{\mathrm{fake,loose}}$ is the fake rate in the d_0 sideband for Run 2 computed on data, $\epsilon^{\mathrm{ITk}}_{z_0}$ is the selection efficiency of the tracklet z_0 selection in ITk, and $\epsilon^{\mathrm{Run-2}}_{z_0}$ is the selection efficiency of the tracklet z_0 selection in Run 2. The ratio of the fake rates in the ITk and Run 2 is found to be ≈ 200, as the fake rate depends strongly on pile-up, whilst the ratio of the tracklet selection efficiencies is ≈ 0.12, which takes into account the differences in tracklet selection between the new search and the Run 2 analysis.

8.5 Systematic uncertainties

Systematic uncertainty projections have been determined starting from the systematic uncertainties studied in Ref. [142], and evolving them to a level which the ATLAS and CMS collaborations have agreed to consider as a sensible extrapolation to 3 ab^{-1} of proton-proton collisions. The theory modelling uncertainties are expected to halve, considering the possible improvements in calculation at higher orders and the constraints obtained with the Run 2 measurements. The recommendations for the experimental uncertainties are dependent upon the systematic uncertainty under consideration and are scaled appropriately from the Run 2 analysis [144]. When setting exclusion limits, an additional systematic uncertainty of 20% is applied to account for the theoretical systematic uncertainty on the models under consideration.
In this search, the dominant uncertainty arise from the modelling of the fake tracklet component, and the total uncertainty on the background yield is extrapolated to be 30%.

8.6 Results

Table 8.2 presents the expected yields in the SR for each background source, corresponding to an integrated luminosity of 3000 fb^{-1}. As seen in the table the dominant background source is events with a "fake" tracklet arising from spurious hits, consisting predominantly in $Z \to \nu\nu$ events with an ISR jet and high $E_{\mathrm{T}}^{\mathrm{miss}}$.

Total SM	4.6 ± 1.3
V+jets events	0.17 ± 0.05
$t\bar{t}$ events	0.02 ± 0.01
Fake tracklets	4.4 ± 1.3

TABLE 8.2: Expected background yields in the SR. The errors shown include the systematic uncertainties.

Prospect for limits at 95% CL on the chargino lifetime are shown in Figure 8.6 as a function of the $\tilde{\chi}_1^{\pm}$ mass. In the Figure, the yellow band shows the 1σ region of the distribution of the expected limits, while the red line presents the current limits from the Run 2 analysis and the hashed region is used to show the direction of the exclusion.

The potential for the full HL-LHC dataset is expected to be able to exclude at the 95% CL chargino lifetimes, assuming a wino-like (higgsino-like) LSP, of between 7 ps (10 ps) and 4 μs (1.5 μs) for light charginos with a mass of 100 GeV. Heavier wino-like (higgsino-like) charginos are expected to be excluded up to m($\tilde{\chi}_1^{\pm}$) = 1100 GeV (750 GeV) for lifetimes of 1 ns. The discovery potential of the analysis would allow for the discovery of wino-like (higgsino-like) charginos of mass 100 GeV with lifetimes between 20 ps and 700 ns (30 ps and 250 ns), or for a lifetime of 1 ns would allow the discovery of wino-like (higgsino-like) charginos of mass up to 800 GeV (600 GeV). In the pure-wino scenario, the chargino lifetime as a function of the chargino mass are calculated at the two loop level [149], as shown by the dashed grey line in Figure 8.6. In the pure-higgsino scenario the mass-lifetime relation is shown by the dashed grey line and is calculated at the one loop level [150]. Comparing the results to the theoretical prediction, would allow for the exclusion at 95% CL of signals with masses up to 850 GeV for the pure wino scenario and 250 GeV for the pure higgsino scenario. The discovery potential would be up to 450 GeV for the pure wino scenario and 150 GeV for the pure higgsino scenario.

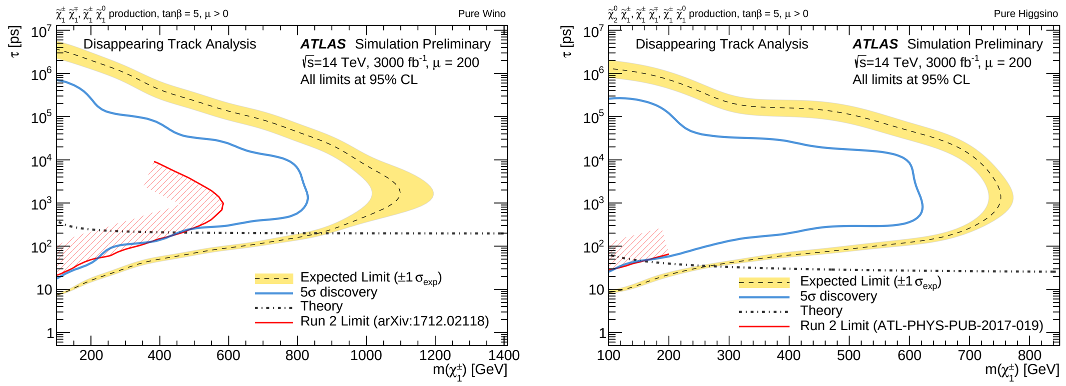

FIGURE 8.6: Expected exclusion limits at 95% CL, using 3000 fb^{-1}of 14 TeV proton-proton collision data as a function of the $\tilde{\chi}_1^{\pm}$ mass and lifetime. Simplified models including both $\tilde{\chi}^{\pm}\tilde{\chi}^{\mp}$ and $\tilde{\chi}^{\pm}\tilde{\chi}^{0}$ are considered assuming pure-wino scenarios (left) and pure-higgsino scenarios (right).

Figure 8.7 presents the 95% compares the expected exclusion sensitivity in the $\tilde{\chi}_1^0, \Delta m(\tilde{\chi}_1^{\pm}, \tilde{\chi}_1^0)$ mass plane, with the sensitivity obtained with a complementary search, looking for prompt decay of the electroweakinos with two low energy muons in the final state. The yellow contour shows the expected exclusion limit from the disappearing track search, with the possibility to exclude $m(\tilde{\chi}_1^{\pm})$ up to 600 GeV for $\Delta m(\tilde{\chi}_1^{\pm}, \tilde{\chi}_1^0) < 0.2$ GeV, and could exclude up to $\Delta m(\tilde{\chi}_1^{\pm}, \tilde{\chi}_1^0) = 0.4$ GeV for $m(\tilde{\chi}_1^{\pm}) = 100$ GeV. This search is mostly sensitive for very small mass splitting, which allows for charginos with longer lifetimes and consequently higher reconstruction efficiency. On the contrary, the search targeting soft leptons, represented by the blue curve, could exclude up to 350 GeV in $m(\tilde{\chi}_1^{\pm})$, and for a light chargino mass of 100 GeV would exclude mass differences between 2 and 15 GeV. This search relies on the reconstruction and identification of the muons and it is therefore more sensitive to models with larger mass splitting and more energetic decay products. The Figure also presents in pink the limits on direct chargino production obtained analysing LEP data [151].

It is important to state that these results are prospects, produced with the current available techniques and newly developed improvements may further enhance the sensitivity to these models. For example the sensitivity of the disappearing tracks search can be enhanced by optimising the tracking algorithms used for the upgraded ATLAS detector allowing for an increase in tracklet efficiency, the possibility of shorter tracklets produced requiring 3 or 4 hits, and further suppression of the fake tracklet component. The dilepton search sensitivity would be expected to improve by increasing the reconstruction efficiency for low p_{T} leptons. The addition of the electron channel would also further enhance the search sensitivity.

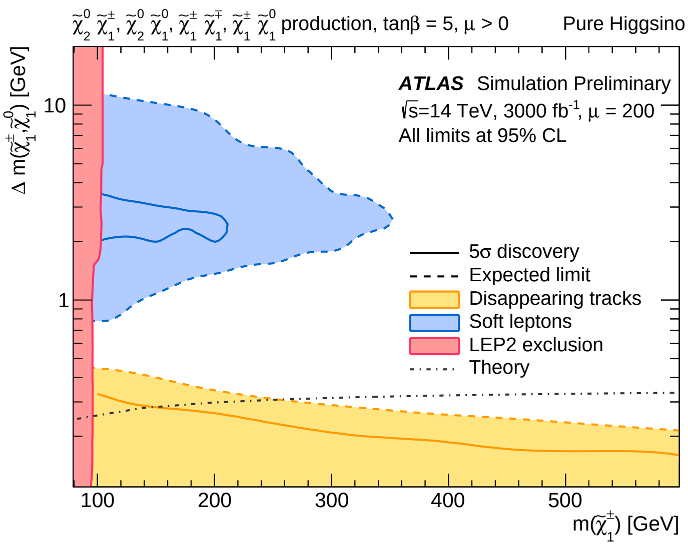

FIGURE 8.7: Expected exclusion at the 95% CL from the disappearing track and dilepton searches in the $\Delta m(\tilde{\chi}_1^{\pm}, \tilde{\chi}_1^0)$, $m(\tilde{\chi}_1^{\pm})$ mass plane. The blue curve presents the exclusion limits from the search with soft muons. The yellow contour presents the exclusion limit from the disappearing track search. The relationship between the masses of the chargino and the two lightest neutralinos in this scenario is $m(\tilde{\chi}_1^{\pm}) = \frac{1}{2}(m(\tilde{\chi}_1^0) + m(\tilde{\chi}_2^0))$.

Conclusions

During my PhD, I have focused most of my research activity on direct searches for new phenomena with the data collected by the ATLAS detector, being able to set world-leading constraints on several supersymmetric models, greatly extending the sensitivity from previous searches.
Specifically, I analysed the data collected by the ATLAS detector during the Run 2 of the LHC, to look for Supersymmetry and Dark Matter in multi-lepton final states and I published the results in the following journal articles:

- ATLAS Collaboration, *Search for direct top squark pair production in final states with two leptons in* $\sqrt{s} = 13$ *TeV pp collisions with the ATLAS detector*, Eur. Phys. J. C 77 (2017) 898
- ATLAS Collaboration, *Search for direct top squark pair production in events with a Higgs or Z boson, and missing transverse momentum in* $\sqrt{s} = 13$ *TeV pp collisions with the ATLAS detector*, JHEP 08 (2017) 006
- ATLAS Collaboration, *Search for dark matter produced in association with bottom or top quarks in* $\sqrt{s} = 13$ *TeV pp collisions with the ATLAS detector*, Eur. Phys. J. C 78 (2018) 18

This Thesis presents two closely related searches for top squark pair production. Both searches consider signatures with two or more charged leptons (electrons or muons) and missing transverse energy. As consequence, similar analysis strategies are developed and some of the techniques for the background estimate are shared.
The first analysis presented consists in a search for direct top squark pair production in final states containing two opposite-charge leptons and large missing transverse momentum, based on a 36.1 fb^{-1} dataset recorded during 2015 and 2016. Good agreement was found between the observed data and the expected Standard Model yields; consequent model-independent 95% CL upper limits on the visible cross-section for new phenomena entering the analysis selection were found to be 0.48 fb. The results are also interpreted in terms of simplified models assuming a range of top squark and lightest neutralino masses, with the former decaying into the latter via a four-body decay. In this hypothesis, top squark masses are excluded up to 400 GeV for $m_{\tilde{t}_1} - m_{\tilde{\chi}_1^0} = 40$ GeV. This result extends the coverage of previous searches by more then 100 GeV and it was reported in a peer review paper published in December 2017 in The European Physical Journal C (EPJC) [90]. This result marks the best coverage by ATLAS in such challenging models, with higher sensitivity with respect to other searches targeting the same models with different strategies [152].
The second search targets direct top squark pair production in events with a leptonically decaying

Z boson. The analysis uses 139 fb^{-1} of proton–proton collision data recorded during the full Run 2. No excess over the SM background predictions is observed, and exclusion limits are presented on a selection of simplified models. Limits exclude at 95% confidence level $\tilde{t}_1$ masses up to 1140 GeV in models featuring $\tilde{t}_1$ production and $\tilde{t}_1 \to t\tilde{\chi}_2^0$ with $\tilde{\chi}_2^0 \to Z/h\tilde{\chi}_1^0$ decays, extending the mass parameter space exclusion by up to 200 GeV in $\tilde{t}_1$ mass. For models featuring $\tilde{t}_2$ production and $\tilde{t}_2 \to Z\tilde{t}_1$ with $\tilde{t}_1 \to bff'\tilde{\chi}_1^0$ decays, $\tilde{t}_2$ masses up to 875 GeV have been excluded, placing the first limits on these particular kind of models at the LHC. Such results were presented at major international conferences during the spring of 2019:

- ATLAS Collaboration, *Search for top squarks in events with a Z boson using 139 fb^{-1} of pp collision data at $\sqrt{s} = 13$ TeV with the ATLAS detector*, ATLAS-CONF-2019-016

and are being collected in a peer review paper in preparation.

The analyses presented in this Thesis are an important extension of the already wide LHC program for SUSY searches: they exploit their characteristic signatures to gain sensitivity to complex scenarios, often neglected by traditional searches. Until now, many of the simplest scenarios have been thoroughly explored and the sensitivity for such models is not expected to improve drastically with the data that will be collected in the next few years, until the end of Run 3 of the LHC. For this reason, we must invest even more in the exploration of the energy frontier. Improvements in the analysis techniques can allow for a more accurate reconstruction of proton-proton collisions, enabling the detection of more particles, such as lepton with even lower energies. Precision measurements of the SM processes, especially in the Higgs sector, may suggest new hints for the searches for new physics, and in parallel allow to constraint the systematic uncertainties. Finally, with the statistical combinations of different searches it will be possible to exploit the LHC dataset at its best, and don't leave any holes behind.

In parallel, the physics community is preparing for the High Luminosity upgrade of the LHC, which will achieve instantaneous luminosities a factor of five larger than the LHC nominal value. During this period the size of the dataset collected by ATLAS is expected to reach a total of approximately 3000 fb^{-1}, providing an unprecedented opportunity to explore the energy frontier and possibly leading to new physics beyond the SM. However, the increased luminosity will come with some costs and the ATLAS detector will have to sustain an unprecedented level of radiation, especially in its inner layers. The final Chapters of this thesis present my contribution to the understanding on the radiation damage effect to the charge collection properties in silicon sensor prototypes, designed for the ATLAS Inner Tracker upgrade (ITk). For this study, the depletion depth of the prototype has been measured on samples presenting different doping, before and after proton irradiation. All measured samples display a strong increase of the depletion depthat low fluences, which can be attributed to the removal of shallow acceptors. Comparing these results with the measurements obtained after neutron irradiation, shows a strong difference in the effect of the two particles. These original results have been published in a peer review paper:

- J. Anders et al., *Charge collection characterisation with the Transient Current Technique of the ams H35DEMO CMOS detector after proton irradiation*, Journal of Instrumentation 13 (2018) P10004

and will be key to improve the modelling of this processes in simulations for the HL-LHC dataset, and to guide the design of the silicon sensors for the next generation of experiments. Having a deep understanding of the low-level operation of the detector is necessary to reach the level

precision required in the HL-LHC physic program.
Finally, I assessed the performance of the future detector producing a prospects of the sensitivity for direct chargino and neutralino production in highly compressed mass scenarios, with the HL-LHC dataset. The search investigates scenarios where the chargino has a sizeable life-time and decays to a neutralino within the innermost layers of the tracking detector. I demonstrated that it is possible to significantly extend the reach for these scenarios beyond the current Run 2 limits, thanks to an improved analysis strategy, to the increased dataset and to the excellent tracking performances of the ITk, motivating the effort for searches for new physics at the HL-LHC. This result was considered by the community as one of the highlight of European Particle Physics Strategy [153].
All the efforts carried out until now don't show any direct evidence of new physics, but all the inconsistencies of the SM are still there. Thanks to the HL-LHC we have the opportunity to keep investigating the energy frontier and shad light on the mystery of nature. Let's keep searching!

Acknowledgments

Reaching this goal was a long journey, which influenced and shaped any part of my life in the last four years. For this reason I would like to acknowledge all the people who accompanied me on this route, making it as exciting as it has been.

I will start with Michele and Antonio, who welcomed me at LHEP and in the Bern ATLAS Team. Thank you for creating such a fruitful environment and for teaching me how to always look at the big picture.
Thank you Federico, Antonello and John, for following my work on a daily bases. During all the time we spent together you have taught me much more than just physics and I will always be grateful for that.
I want extend this to all the members of the Bern family: Mari, Stefania, Marco, Tom, Geoffrey, Yves, Gabriele, Armin, Dean, Laura and Megh (and of course Fede, Anto and John again :)). People come and go from this group all the time, but the contribution from all of you is so important that in the end no one ever leaves for real. A special mention goes also to Ciro, Marcella, Alessia and Fabio, as you created the roots from which our family could grow.

Going back to the work presented in the thesis, none of this would have been reality without the outstanding contribution from all the members of the Stop2L and the StopZh analysis teams, and of the whole 3g group.
A special thanks goes then to the conveners, sub-conveners and analysis contacts who helped me producing meaningful science, and to my fellow PhD students with whom I shared this path.
Between all the great people I had the opportunity to work with, I particularly want to name Ximo, Priscilla, Rosa, Tommaso, Marilea and Luigi. Thank you Zach for your precious career advices, and for agreeing to review yet another document! And thank you Sonia and Lorenzo, I don't even have to say why.

For my time at CERN, which apart from science has been filled up with skiing, hiking, climbing and especially a lot of food, in R1 and beyond, I want to thank my friends who either work or worked in the past in the Milano group. Thank you Ettore, Giacomo, Giulia, Chiara, Giuseppe, Carlo, Maria Giulia, Davide, Alessandra, Stefano, Cristina, Enrico and again Sonia, Lorenzo and Federico. Having you around always made me feel at home.

Finally, grazie a mamma e papa', for always supporting my choices, even when they take me far away.

Bibliography

[1] P. J. Mohr, B. N. Taylor and D. B. Newell, *CODATA recommended values of the fundamental physical constants: 2010*, Rev. Mod. Phys. **84** (4 2012) 1527, URL: https://link.aps.org/doi/10.1103/RevModPhys.84.1527.

[2] G. W. Bennett et al., *Measurement of the Positive Muon Anomalous Magnetic Moment to 0.7 ppm*, Phys. Rev. Lett. **89** (10 2002) 101804, URL: https://link.aps.org/doi/10.1103/PhysRevLett.89.101804.

[3] ATLAS Collaboration, *Observation of a new particle in the search for the Standard Model Higgs boson with the ATLAS detector at the LHC*, Phys. Lett. B **716** (2012) 1, arXiv: 1207.7214 [hep-ex].

[4] CMS Collaboration, *Observation of a new boson at a mass of 125 GeV with the CMS experiment at the LHC*, Phys. Lett. **B716** (2012) 30, arXiv: 1207.7235 [hep-ex].

[5] Y. A. Golfand and E. P. Likhtman, *Extension of the Algebra of Poincare Group Generators and Violation of p Invariance*, JETP Lett. **13** (1971) 323, [Pisma Zh. Eksp. Teor. Fiz.13,452(1971)].

[6] D. V. Volkov and V. P. Akulov, *Is the Neutrino a Goldstone Particle?*, Phys. Lett. B **46** (1973) 109.

[7] J. Wess and B. Zumino, *Supergauge Transformations in Four-Dimensions*, Nucl. Phys. B **70** (1974) 39.

[8] J. Wess and B. Zumino, *Supergauge Invariant Extension of Quantum Electrodynamics*, Nucl. Phys. B **78** (1974) 1.

[9] S. Ferrara and B. Zumino, *Supergauge Invariant Yang-Mills Theories*, Nucl. Phys. B **79** (1974) 413.

[10] A. Salam and J. A. Strathdee, *Supersymmetry and Nonabelian Gauges*, Phys. Lett. B **51** (1974) 353.

[11] S. P. Martin, *A Supersymmetry primer*, (1997), [Adv. Ser. Direct. High Energy Phys.18,1(1998)], arXiv: hep-ph/9709356 [hep-ph].

[12] ATLAS Collaboration, *Measurement of the Higgs boson mass in the $H \to ZZ^* \to 4\ell$ and $H \to \gamma\gamma$ channels with $\sqrt{s} = 13$ TeV pp collisions using the ATLAS detector*, Phys. Lett. B **784** (2018) 345, arXiv: 1806.00242 [hep-ex].

[13] R. Barbieri and G. F. Giudice, *Upper Bounds on Supersymmetric Particle Masses*, Nucl. Phys. B **306** (1988) 63.

[14] B. de Carlos and J. A. Casas, *One loop analysis of the electroweak breaking in supersymmetric models and the fine tuning problem*, Phys. Lett. B **309** (1993) 320, arXiv: hep-ph/9303291 [hep-ph].

[15] R. Barbieri and G. Giudice, *Upper bounds on supersymmetric particle masses*, Nuclear Physics B **306** (1988) 63, ISSN: 0550-3213, URL: http://www.sciencedirect.com/science/article/pii/055032138890171X.

[16] G. Hinshaw et al., *NINE-YEARWILKINSON MICROWAVE ANISOTROPY PROBE(WMAP) OBSERVATIONS: COSMOLOGICAL PARAMETER RESULTS*, The Astrophysical Journal Supplement Series **208** (2013) 19.

[17] Y. Akrami et al., *Planck 2018 results. I. Overview and the cosmological legacy of Planck*, (2018), arXiv: 1807.06205 [astro-ph.CO].

[18] G. R. Farrar and P. Fayet, *Phenomenology of the Production, Decay, and Detection of New Hadronic States Associated with Supersymmetry*, Phys. Lett. B **76** (1978) 575.

[19] H. Goldberg, *Constraint on the Photino Mass from Cosmology*, Phys. Rev. Lett. **50** (1983) 1419, [Erratum: Phys. Rev. Lett.103,099905(2009)].

[20] J. R. Ellis, J. S. Hagelin, D. V. Nanopoulos, K. A. Olive and M. Srednicki, *Supersymmetric Relics from the Big Bang*, Nucl. Phys. B **238** (1984) 453.

[21] S. Weinberg, *A Model of Leptons*, Phys. Rev. Lett. **19** (21 1967) 1264, URL: https://link.aps.org/doi/10.1103/PhysRevLett.19.1264.

[22] S. L. Glashow, *Partial Symmetries of Weak Interactions*, Nucl. Phys. **22** (1961) 579.

[23] N. Sakai, *Naturalness in Supersymmetric Guts*, Z. Phys. C **11** (1981) 153.

[24] S. Dimopoulos, S. Raby and F. Wilczek, *Supersymmetry and the Scale of Unification*, Phys. Rev. D **24** (1981) 1681.

[25] L. E. Ibanez and G. G. Ross, *Low-Energy Predictions in Supersymmetric Grand Unified Theories*, Phys. Lett. B **105** (1981) 439.

[26] S. Dimopoulos and H. Georgi, *Softly Broken Supersymmetry and SU(5)*, Nucl. Phys. B **193** (1981) 150.

[27] J. H. Schwarz, *Introduction to superstring theory*, NATO Sci. Ser. C **566** (2001) 143, arXiv: hep-ex/0008017 [hep-ex].

[28] C. Rovelli, *Loop Quantum Gravity*, Living Reviews in Relativity **11** (2008) 5, ISSN: 1433-8351, URL: https://doi.org/10.12942/lrr-2008-5.

[29] P. Fayet, *Supersymmetry and Weak, Electromagnetic and Strong Interactions*, Phys. Lett. B **64** (1976) 159.

[30] P. Fayet, *Spontaneously Broken Supersymmetric Theories of Weak, Electromagnetic and Strong Interactions*, Phys. Lett. B **69** (1977) 489.

[31] A. Djouadi et al., 'The Minimal supersymmetric standard model: Group summary report', *GDR (Groupement De Recherche) - Supersymetrie Montpellier, France, April 15-17, 1998*, 1998, arXiv: hep-ph/9901246 [hep-ph], URL: https://inspirehep.net/record/481987/files/arXiv:hep-ph_9901246.pdf.

[32] M. Papucci, J. T. Ruderman and A. Weiler, *Natural SUSY Endures*, JHEP **09** (2012) 035, arXiv: 1110.6926 [hep-ph].

[33] W. Beenakker, C. Borschensky, M. Krämer, A. Kulesza and E. Laenen, *NNLL-fast: predictions for coloured supersymmetric particle production at the LHC with threshold and Coulomb resummation*, JHEP **12** (2016) 133, arXiv: 1607.07741 [hep-ph].

[34] ATLAS Collaboration, *ATLAS Run 1 searches for direct pair production of third-generation squarks at the Large Hadron Collider*, Eur. Phys. J. C **75** (2015) 510, arXiv: 1506.08616 [hep-ex].

[35] M. W. Cahill-Rowley, J. L. Hewett, A. Ismail and T. G. Rizzo, *The Higgs Sector and Fine-Tuning in the pMSSM*, Phys. Rev. **D86** (2012) 075015, arXiv: 1206.5800 [hep-ph].

[36] N. Arkani-Hamed, A. Delgado and G. F. Giudice, *The Well-tempered neutralino*, Nucl. Phys. **B741** (2006) 108, arXiv: hep-ph/0601041 [hep-ph].

[37] J. Alwall, M.-P. Le, M. Lisanti and J. G. Wacker, *Searching for Directly Decaying Gluinos at the Tevatron*, Phys. Lett. B **666** (2008) 34, arXiv: 0803.0019 [hep-ph].

[38] J. Alwall, P. Schuster and N. Toro, *Simplified Models for a First Characterization of New Physics at the LHC*, Phys. Rev. D **79** (2009) 075020, arXiv: 0810.3921 [hep-ph].

[39] D. Alves, *Simplified Models for LHC New Physics Searches*, J. Phys. G **39** (2012) 105005, ed. by N. Arkani-Hamed et al., arXiv: 1105.2838 [hep-ph].

[40] CMS Collaboration, *Search for top-squark pair production in the single-lepton final state in pp collisions at* $\sqrt{s} = 8$ *TeV*, Eur. Phys. J. C **73** (2013) 2677, arXiv: 1308.1586 [hep-ex].

[41] CMS Collaboration, *Search for direct pair production of supersymmetric top quarks decaying to all-hadronic final states in pp collisions at* $\sqrt{s} = 8$ *TeV*, Eur. Phys. J. C **76** (2016) 460, arXiv: 1603.00765 [hep-ex].

[42] CMS Collaboration, *Searches for third-generation squark production in fully hadronic final states in proton–proton collisions at* $\sqrt{s} = 8$ *TeV*, JHEP **06** (2015) 116, arXiv: 1503.08037 [hep-ex].

[43] CMS Collaboration, *Search for direct pair production of scalar top quarks in the single- and dilepton channels in proton–proton collisions at* $\sqrt{s} = 8$ *TeV*, JHEP **07** (2016) 027, arXiv: 1602.03169 [hep-ex].

[44] CMS Collaboration, *Search for top squark pair production in compressed-mass-spectrum scenarios in proton–proton collisions at* $\sqrt{s} = 8$ *TeV using the* α_T *variable*, Phys. Lett. B **767** (2017) 403, arXiv: 1605.08993 [hep-ex].

[45] CMS Collaboration, *Search for supersymmetry in events with soft leptons, low jet multiplicity, and missing transverse energy in proton–proton collisions at* $\sqrt{s} = 8$ *TeV*, Phys. Lett. B **759** (2016) 9, arXiv: 1512.08002 [hep-ex].

[46] ATLAS Collaboration, *Summary of the ATLAS experiment's sensitivity to supersymmetry after LHC Run 1 — interpreted in the phenomenological MSSM*, JHEP **10** (2015) 134, arXiv: 1508.06608 [hep-ex].

[47] S. Myers, *The LEP Collider, from design to approval and commissioning*, John Adams' Lecture, Delivered at CERN, 26 Nov 1990, CERN, 1991, URL: https://cds.cern.ch/record/226776.

[48] C. Lefèvre, 'The CERN accelerator complex. Complexe des accélérateurs du CERN', 2008, URL: https://cds.cern.ch/record/1260465.

[49] ATLAS Collaboration, *The ATLAS Experiment at the CERN Large Hadron Collider*, JINST **3** (2008) S08003.

[50] ATLAS Collaboration, *ATLAS detector and physics performance: Technical Design Report, 1*, Technical Design Report ATLAS, CERN, 1999, URL: https://cds.cern.ch/record/391176.

[51] ATLAS Collaboration, *Track Reconstruction Performance of the ATLAS Inner Detector at $\sqrt{s} = 13$ TeV*, ATL-PHYS-PUB-2015-018, 2015, URL: https://cds.cern.ch/record/2037683.

[52] B. Abbott et al., *Production and integration of the ATLAS Insertable B-Layer*, JINST **13** (2018) T05008, arXiv: 1803.00844 [physics.ins-det].

[53] M. Backes, *The ATLAS Trigger System : Ready for Run-2*, tech. rep. ATL-DAQ-PROC-2015-041, CERN, 2015, URL: https://cds.cern.ch/record/2058618.

[54] T. Cornelisen *et al.*, *The new ATLAS track reconstruction (NEWT)*, J. Phys. Conf. Ser **119** (2008) 032014.

[55] ATLAS Collaboration, *Reconstruction of primary vertices at the ATLAS experiment in Run 1 proton–proton collisions at the LHC*, Eur. Phys. J. C **77** (2017) 332, arXiv: 1611.10235 [hep-ex].

[56] W. Lampl et al., *Calorimeter Clustering Algorithms: Description and Performance*, tech. rep. ATL-LARG-PUB-2008-002. ATL-COM-LARG-2008-003, CERN, 2008, URL: https://cds.cern.ch/record/1099735.

[57] M. Cacciari, G. P. Salam and G. Soyez, *The Anti-k(t) jet clustering algorithm*, JHEP **04** (2008) 063, arXiv: 0802.1189 [hep-ph].

[58] ATLAS Collaboration, *Jet Calibration and Systematic Uncertainties for Jets Reconstructed in the ATLAS Detector at $\sqrt{s} = 13$ TeV*, ATL-PHYS-PUB-2015-015, 2015, URL: https://cds.cern.ch/record/2037613.

[59] ATLAS Collaboration, *Jet energy scale measurements and their systematic uncertainties in proton–proton collisions at $\sqrt{s} = 13$ TeV with the ATLAS detector*, Phys. Rev. D **96** (2017) 072002, arXiv: 1703.09665 [hep-ex].

[60] ATLAS Collaboration, *Performance of pile-up mitigation techniques for jets in pp collisions at $\sqrt{s} = 8$ TeV using the ATLAS detector*, Eur. Phys. J. C **76** (2016) 581, arXiv: 1510.03823 [hep-ex].

[61] ATLAS Collaboration, *Tagging and suppression of pileup jets with the ATLAS detector*, ATLAS-CONF-2014-018, 2014, URL: https://cds.cern.ch/record/1700870.

[62] ATLAS Collaboration, *Optimisation and performance studies of the ATLAS b-tagging algorithms for the 2017-18 LHC run*, ATL-PHYS-PUB-2017-013, 2017, URL: https://cds.cern.ch/record/2273281.

[63] ATLAS Collaboration, *Secondary vertex finding for jet flavour identification with the ATLAS detector*, ATL-PHYS-PUB-2017-011, 2017, URL: https://cds.cern.ch/record/2270366.

[64] ATLAS Collaboration, *Topological b-hadron decay reconstruction and identification of b-jets with the JetFitter package in the ATLAS experiment at the LHC*, ATL-PHYS-PUB-2018-025, 2018, URL: https://cds.cern.ch/record/2645405.

[65] ATALS Collaboration, *ATLAS b-jet identification performance and efficiency measurement with $t\bar{t}$ events in pp collisions at $\sqrt{s} = 13$ TeV*, (2019), arXiv: 1907.05120 [hep-ex].

[66] ATLAS Collaboration, *Performance of b-jet identification in the ATLAS experiment*, JINST **11** (2016) P04008, arXiv: 1512.01094 [hep-ex].

[67] ATLAS Collaboration, *Measurement of b-tagging efficiency of c-jets in $t\bar{t}$ events using a likelihood approach with the ATLAS detector*, ATLAS-CONF-2018-001, 2018, URL: https://cds.cern.ch/record/2306649.

[68] ATLAS collaboration, *Electron and photon performance measurements with the ATLAS detector using the 2015-2017 LHC proton-proton collision data*, (2019), arXiv: 1908.00005 [hep-ex].

[69] ATLAS Collaboration, *Muon reconstruction performance of the ATLAS detector in proton–proton collision data at $\sqrt{s} = 13$ TeV*, Eur. Phys. J. C **76** (2016) 292, arXiv: 1603.05598 [hep-ex].

[70] ATLAS Collaboration, *Muon reconstruction performance in early Run II*, ATL-PHYS-PUB-2015-037, 2015, URL: http://cds.cern.ch/record/2047831.

[71] ATLAS Collaboration, *E_T^{miss} performance in the ATLAS detector using 2015–2016 LHC pp collisions*, ATLAS-CONF-2018-023, 2018, URL: https://cds.cern.ch/record/2625233.

[72] ATLAS Collaboration, *Performance of missing transverse momentum reconstruction with the ATLAS detector using proton–proton collisions at $\sqrt{s} = 13$ TeV*, Eur. Phys. J. C **78** (2018) 903, arXiv: 1802.08168 [hep-ex].

[73] A. collaboration, *ATLAS luminosity measurements during Run 2*, 2019, URL: https://twiki.cern.ch/twiki/bin/view/AtlasPublic/LuminosityPublicResultsRun2 (visited on 30/09/2019).

[74] G. Avoni et al., *The new LUCID-2 detector for luminosity measurement and monitoring in ATLAS*, JINST **13** (2018) P07017.

[75] S. Frixione and B. R. Webber, *Matching NLO QCD computations and parton shower simulations*, JHEP **06** (2002) 029, arXiv: hep-ph/0204244.

[76] S. Frixione, P. Nason and B. R. Webber, *Matching NLO QCD and parton showers in heavy flavour production*, JHEP **08** (2003) 007, arXiv: hep-ph/0305252.

[77] J. Alwall et al., *The automated computation of tree-level and next-to-leading order differential cross sections, and their matching to parton shower simulations*, JHEP **07** (2014) 079, arXiv: 1405.0301 [hep-ph].

[78] S. Agostinelli et al., *GEANT4: A simulation toolkit*, Nucl. Instrum. Meth. A **506** (2003) 250.

[79] A. L. Read, *Presentation of search results: The CL(s) technique*, J. Phys. G **28** (2002) 2693.

[80] ATLAS Collaboration, *Search for pair-produced third-generation squarks decaying via charm quarks or in compressed supersymmetric scenarios in pp collisions at $\sqrt{s} = 8$ TeV with the ATLAS detector*, Phys. Rev. D **90** (2014) 052008, arXiv: 1407.0608 [hep-ex].

[81] ATLAS Collaboration, *Search for direct top-squark pair production in final states with two leptons in pp collisions at $\sqrt{s} = 8$ TeV with the ATLAS detector*, JHEP **06** (2014) 124, arXiv: 1403.4853 [hep-ex].

[82] ATLAS Collaboration, *Electron identification measurements in ATLAS using $\sqrt{s} = 13$ TeV data with 50 ns bunch spacing*, ATL-PHYS-PUB-2015-041, 2015, URL: https://cds.cern.ch/record/2048202.

[83] ATLAS Collaboration, *Electron reconstruction and identification in the ATLAS experiment using the 2015 and 2016 LHC proton–proton collision data at $\sqrt{s} = 13$ TeV*, CERN-EP-2018-273 (2019), arXiv: 1902.04655 [hep-ex].

[84] ATLAS Collaboration, *Topological cell clustering in the ATLAS calorimeters and its performance in LHC Run 1*, Eur. Phys. J. C **77** (2017) 490, arXiv: 1603.02934 [hep-ex].

[85] ATLAS Collaboration, *Data-Quality Requirements and Event Cleaning for Jets and Missing Transverse Energy Reconstruction with the ATLAS Detector in Proton–Proton Collisions at a Center-of-Mass Energy of $\sqrt{s} = 7$ TeV*, ATLAS-CONF-2010-038, 2010, URL: https://cds.cern.ch/record/1277678.

[86] ATLAS Collaboration, *Simulation of top-quark production for the ATLAS experiment at $\sqrt{s} = 13$ TeV*, ATL-PHYS-PUB-2016-004, 2016, URL: https://cds.cern.ch/record/2120417.

[87] ATLAS Collaboration, *Multi-Boson Simulation for 13 TeV ATLAS Analyses*, ATL-PHYS-PUB-2016-002, 2016, URL: http://cds.cern.ch/record/2119986.

[88] ATLAS Collaboration, *Modelling of the $t\bar{t}H$ and $t\bar{t}V$ $(V = W, Z)$ processes for $\sqrt{s} = 13$ TeV ATLAS analyses*, ATL-PHYS-PUB-2015-022, 2016, URL: http://cds.cern.ch/record/2120826.

[89] P. Kant et al., *HatHor for single top-quark production: Updated predictions and uncertainty estimates for single top-quark production in hadronic collisions*, Comput. Phys. Commun. **191** (2015) 74, arXiv: 1406.4403 [hep-ph].

[90] ATLAS Collaboration, *Search for direct top squark pair production in final states with two leptons in $\sqrt{s} = 13$ TeV pp collisions with the ATLAS detector*, Eur. Phys. J. C **77** (2017) 898, arXiv: 1708.03247 [hep-ex].

[91] ATLAS Collaboration, *Search for direct top squark pair production in events with a Higgs or Z boson, and missing transverse momentum in $\sqrt{s} = 13$ TeV pp collisions with the ATLAS detector*, JHEP **08** (2017) 006, arXiv: 1706.03986 [hep-ex].

[92] ATLAS Collaboration, *Search for direct top squark pair production in events with a Z boson, b-jets and missing transverse momentum in $\sqrt{s} = 8$ TeV pp collisions with the ATLAS detector*, Eur. Phys. J. C **74** (2014) 2883, arXiv: 1403.5222 [hep-ex].

[93] CMS Collaboration, *Search for top-squark pairs decaying into Higgs or Z bosons in pp collisions at $\sqrt{s} = 8$ TeV*, Phys. Lett. B **736** (2014) 371, arXiv: 1405.3886 [hep-ex].

[94] CMS Collaboration, *Search for top-squark pairs decaying into Higgs or Z bosons in pp collisions at $\sqrt{s}$=8 TeV*, Phys. Lett. B **736** (2014) 371, arXiv: 1405.3886 [hep-ex].

[95] ATLAS Collaboration, *Performance of the ATLAS Trigger System in 2015*, Eur. Phys. J. C **77** (2017) 317, arXiv: 1611.09661 [hep-ex].

[96] C. G. Lester and D. J. Summers, *Measuring masses of semiinvisibly decaying particles pair produced at hadron colliders*, Phys. Lett. B **463** (1999) 99, arXiv: hep-ph/9906349 [hep-ph].

[97] A. Barr, C. G Lester and P. Stephens, *A variable for measuring masses at hadron colliders when missing energy is expected; m T2: The truth behind the glamour*, J. Phys. G **29** (2003) 2343.

[98] ATLAS Collaboration, *New Small Wheel Technical Design Report*, tech. rep. CERN-LHCC-2013-006. ATLAS-TDR-020, ATLAS New Small Wheel Technical Design Report, 2013, URL: http://cds.cern.ch/record/1552862.

[99] ATLAS Collaboration, *Technical Design Report for the Phase-I Upgrade of the ATLAS TDAQ System*, tech. rep. CERN-LHCC-2013-018. ATLAS-TDR-023, Final version presented to December 2013 LHCC., 2013, URL: http://cds.cern.ch/record/1602235.

[100] ATLAS Collaboration, *Technical Design Report for the ATLAS Inner Tracker Strip Detector*, tech. rep. CERN-LHCC-2017-005. ATLAS-TDR-025, CERN, 2017, URL: http://cds.cern.ch/record/2257755.

[101] ATLAS Collaboration, *Technical Design Report for the ATLAS Inner Tracker Pixel Detector*, tech. rep. CERN-LHCC-2017-021. ATLAS-TDR-030, CERN, 2017, URL: http://cds.cern.ch/record/2285585.

[102] G. Casse, *Overview of the recent activities of the RD50 collaboration on radiation hardening of semiconductor detectors for the sLHC*, Nuclear Instruments and Methods in Physics Research Section A: Accelerators, Spectrometers, Detectors and Associated Equipment **598** (2009) 54, Instrumentation for Collding Beam Physics, ISSN: 0168-9002, URL: http://www.sciencedirect.com/science/article/pii/S0168900208011893.

[103] *Standard practice for characterizing neutron fluence spectra in terms of an equivalent monoenergetic neutron fluence for radiation-hardness testing of electronics*, ASTM, 2009, URL: https://cds.cern.ch/record/2103968.

[104] T. Sjöstrand et al., *An Introduction to PYTHIA 8.2*, Comput. Phys. Commun. **191** (2015) 159, arXiv: 1410.3012 [hep-ph].

[105] A. Ferrari, P. R. Sala, A. Fasso and J. Ranft, *FLUKA: A multi-particle transport code (program version 2005)*, CERN Yellow Reports: Monographs, CERN, 2005, URL: https://cds.cern.ch/record/898301.

[106] L. Adamczyk et al., *Technical Design Report for the ATLAS Forward Proton Detector*, tech. rep. CERN-LHCC-2015-009. ATLAS-TDR-024, 2015, URL: https://cds.cern.ch/record/2017378.

[107] S. I. Parker, C. J. Kenney and J. Segal, *3-D: A New architecture for solid state radiation detectors*, Nucl. Instrum. Meth. **A395** (1997) 328.

[108] D. Pitzl et al., *Type inversion in silicon detectors*, Nucl. Instrum. Meth. **A311** (1992) 98.

[109] I. Perić, *A novel monolithic pixelated particle detector implemented in high-voltage CMOS technology*, Nuclear Instruments and Methods in Physics Research Section A: Accelerators, Spectrometers, Detectors and Associated Equipment **582** (2007) 876, VERTEX 2006, ISSN: 0168-9002, URL: http://www.sciencedirect.com/science/article/pii/S0168900207015914.

[110] S. Braccini, *The new bern PET cyclotron, its research beam line, and the development of an innovative beam monitor detector*, AIP Conference Proceedings **1525** (2013) 144.

[111] J. F. Ziegler, M. D. Ziegler and J. P. Biersack, *SRIM - The stopping and range of ions in matter (2010)*, Nuclear Instruments and Methods in Physics Research B **268** (2010) 1818.

[112] F. W. T. Inc, *Dosimetric films calibration*, 2018, URL: http://www.fwt.com (visited on 30/09/2018).

[113] E. Vilella et al., *Prototyping of an HV-CMOS demonstrator for the High Luminosity-LHC upgrade*, Journal of Instrumentation **11** (2016) C01012, URL: http://stacks.iop.org/1748-0221/11/i=01/a=C01012.

[114] ams AG, *Tobelbader Strasse 30, 8141 Premstaetten*, Austria (), URL: http://ams.com.

[115] Particulars advanced measurements system, *Dragomelij 154, SI-1230 Donzale*, Slovenia (), URL: http://particulars.si.

[116] URL: https://www.psi.ch/drs/evaluation-board.

[117] E. Cavallaro et al., *Studies of irradiated AMS H35 CMOS detectors for the ATLAS tracker upgrade*, Journal of Instrumentation **12** (2017) C01074, URL: http://stacks.iop.org/1748-0221/12/i=01/a=C01074.

[118] K. A. Olive et al., *Review of Particle Physics*, Chin. Phys. **C38** (2014) 090001.

[119] P. Scampoli, K. von Bremen, S. Braccini and A. Ereditato, *The New Bern Cyclotron Laboratory for Radioisotope Production and Research*, Conf. Proc. **C110904** (2011) 3619.

[120] F. Ravotti, M. Glaser and M. Moll, *Upgrade scenarios for irradiation lines:: Upgrade of the Proton Irradiation Facility in the CERN PS EAST AREA*, (2014), URL: https://cds.cern.ch/record/1951308.

[121] B. Gkotse et al., *The Beam Profile Monitoring System for the IRRAD Proton Facility at the CERN PS East Area*, (2015), URL: https://cds.cern.ch/record/2235836.

[122] A. Curioni et al., *Single- and multi-foils 27Al(p,3pn)24Na activation technique for monitoring the intensity of high-energy beams*, Nuclear Instruments and Methods in Physics Research Section A: Accelerators, Spectrometers, Detectors and Associated Equipment **858** (2017) 101, ISSN: 0168-9002, URL: http://www.sciencedirect.com/science/article/pii/S0168900217304199.

[123] I. Mandić et al., *Charge collection properties of irradiated depleted CMOS pixel test structures*, (2018), arXiv: 1801.03671 [physics.ins-det].

[124] M. F. García, C. Gallrapp, M. Moll and D. Muenstermann, *Radiation hardness studies of neutron irradiated CMOS sensors fabricated in the ams H18 high voltage process*, Journal of Instrumentation **11** (2016) P02016, URL: http://stacks.iop.org/1748-0221/11/i=02/a=P02016.

[125] A. Affolder et al., *Charge collection studies in irradiated HV-CMOS particle detectors*, Journal of Instrumentation **11** (2016) P04007, URL: http://stacks.iop.org/1748-0221/11/i=04/a=P04007.

[126] ATLAS Collaboration, *Search for long-lived charginos based on a disappearing-track signature in pp collisions at* $\sqrt{s} = 13$ *TeV with the ATLAS detector*, JHEP **06** (2018) 022, arXiv: 1712.02118 [hep-ex].

[127] G. F. Giudice, M. A. Luty, H. Murayama and R. Rattazzi, *Gaugino mass without singlets*, JHEP **12** (1998) 027, arXiv: hep-ph/9810442 [hep-ph].

[128] L. Randall and R. Sundrum, *Out of this world supersymmetry breaking*, Nucl. Phys. B **557** (1999) 79, arXiv: hep-th/9810155 [hep-th].

[129] K. Inoue, A. Kakuto, H. Komatsu and S. Takeshita, *Aspects of Grand Unified Models with Softly Broken Supersymmetry*, Prog. Theor. Phys. **68** (1982) 927, [Erratum: Prog. Theor. Phys.70,330(1983)].

[130] J. R. Ellis and S. Rudaz, *Search for Supersymmetry in Toponium Decays*, Phys. Lett. B **128** (1983) 248.

[131] Z. Han, G. D. Kribs, A. Martin and A. Menon, *Hunting quasidegenerate Higgsinos*, Phys. Rev. D **89** (2014) 075007, arXiv: 1401.1235 [hep-ph].

[132] F. E. Paige, S. D. Protopopescu, H. Baer and X. Tata, *ISAJET 7.69: A Monte Carlo event generator for pp,* $\bar{p}p$*, and* e^+e^- *reactions*, (2003), arXiv: hep-ph/0312045 [hep-ph].

[133] J. Alwall et al., *The automated computation of tree-level and next-to-leading order differential cross sections, and their matching to parton shower simulations*, JHEP **07** (2014) 079, arXiv: 1405.0301 [hep-ph].

[134] NNPDF Collaboration, R. D. Ball et al., *Parton distributions for the LHC Run II*, JHEP **04** (2015) 040, arXiv: 1410.8849 [hep-ph].

[135] L. Lönnblad and S. Prestel, *Matching Tree-Level Matrix Elements with Interleaved Showers*, JHEP **03** (2012) 019, arXiv: 1109.4829 [hep-ph].

[136] ATLAS Collaboration, *ATLAS Pythia 8 tunes to 7 TeV data*, ATL-PHYS-PUB-2014-021, 2014, URL: https://cds.cern.ch/record/1966419.

[137] W. Beenakker, R. Hopker, M. Spira and P. Zerwas, *Squark and gluino production at hadron colliders*, Nucl.Phys. **B492** (1997) 51, arXiv: hep-ph/9610490 [hep-ph].

[138] B. Fuks, M. Klasen, D. R. Lamprea and M. Rothering, *Gaugino production in proton-proton collisions at a center-of-mass energy of 8 TeV*, JHEP **1210** (2012) 081, arXiv: 1207.2159 [hep-ph].

[139] B. Fuks, M. Klasen, D. R. Lamprea and M. Rothering, *Precision predictions for electroweak superpartner production at hadron colliders with Resummino*, Eur.Phys.J. **C73** (2013) 2480, arXiv: 1304.0790 [hep-ph].

[140] B. Fuks, M. Klasen, D. R. Lamprea and M. Rothering, *Revisiting slepton pair production at the Large Hadron Collider*, JHEP **01** (2014) 168, arXiv: 1310.2621 [hep-ph].

[141] C. Borschensky, M. Kramer, A. Kulesza, M. Mangano, S. Padhi et al., *Squark and gluino production cross sections in pp collisions at $\sqrt{s}$ = 13, 14, 33 and 100 TeV*, Eur. Phys. J. C **74** (2014) 3174, arXiv: 1407.5066 [hep-ph].

[142] ATLAS Collaboration, *Search for electroweak production of supersymmetric states in scenarios with compressed mass spectra at $\sqrt{s} = 13$ TeV with the ATLAS detector*, Phys. Rev. D **97** (2018) 052010, arXiv: 1712.08119 [hep-ex].

[143] ATLAS Collaboration, *The ATLAS Simulation Infrastructure*, Eur. Phys. J. C **70** (2010) 823, arXiv: 1005.4568 [physics.ins-det].

[144] ATLAS Collaboration, *Expected performance of the ATLAS detector at the HL-LHC*, (2018, in preparation), URL: http://cds.cern.ch/record/.

[145] ATLAS Collaboration, *Summary of ATLAS Pythia 8 tunes*, ATL-PHYS-PUB-2012-003, 2012, URL: https://cds.cern.ch/record/1474107.

[146] A. D. Martin, W. J. Stirling, R. S. Thorne and G. Watt, *Parton distributions for the LHC*, Eur. Phys. J. C **63** (2009) 189, arXiv: 0901.0002 [hep-ph].

[147] M. Aliev et al., *HATHOR: HAdronic Top and Heavy quarks crOss section calculatoR*, Comput. Phys. Commun. **182** (2011) 1034, arXiv: 1007.1327 [hep-ph].

[148] ATLAS Collaboration, *Search for long-lived charginos based on a disappearing-track signature in pp collisions at $\sqrt{s} = 13$ TeV with the ATLAS detector*, ATLAS-CONF-2017-017, 2017, URL: https://cds.cern.ch/record/2258131.

[149] M. Ibe, S. Matsumoto and T. T. Yanagida, *Pure Gravity Mediation with $m_{3/2}$ = 10-100 TeV*, Phys. Rev. D **85** (2012) 095011, arXiv: 1202.2253 [hep-ph].

[150] S. D. Thomas and J. D. Wells, *Phenomenology of Massive Vectorlike Doublet Leptons*, Phys. Rev. Lett. **81** (1998) 34, arXiv: hep-ph/9804359 [hep-ph].

[151] ALEPH, DELPHI, L3, OPAL Experiments, *Combined LEP Chargino Results*, http://lepsusy.web.cern.ch/lepsusy/www/inoslowdmsummer02/charginolowdm_pub.html.

[152] ATLAS Collaboration, *Search for top squarks in final states with one isolated lepton, jets, and missing transverse momentum in $\sqrt{s} = 13$ TeV pp collisions with the ATLAS detector*, Phys. Rev. D **94** (2016) 052009, arXiv: 1606.03903 [hep-ex].

[153] *Report on the Physics at the HL-LHC and Perspectives for the HE-LHC*, tech. rep. arXiv:1902.10229, Presented at The HL/HE-LHC Physics Workshop: final jamboree, 1 March 2019.: CERN, 2019, URL: https://cds.cern.ch/record/2651134.